Title

Shining Lights: Measurement of the 8B Solar Neutrino Flux with the SNO+ Detector and Research and Development Toward Next-Generation Optical Neutrino Experiments

Author

Smiley, Max Benjamin

Publication Date

2024

Shining Lights: Measurement of the ^{8}B Solar Neutrino Flux with the SNO+ Detector and Research and Development Toward Next-Generation Optical Neutrino Experiments

by

Max Smiley

A dissertation submitted in partial satisfaction of the

requirements for the degree of

Doctor of Philosophy

in

Physics

in the

Graduate Division

of the

University of California, Berkeley

Committee in charge:

Associate Professor Gabriel Orebi Gann, Chair
Professor Yury Kolomensky
Associate Professor Jessica Lu

Summer 2024

Shining Lights: Measurement of the ^{8}B Solar Neutrino Flux with the SNO+ Detector and
Research and Development Toward Next-Generation Optical Neutrino Experiments

Abstract

Shining Lights: Measurement of the ^{8}B Solar Neutrino Flux with the SNO+ Detector and Research and Development Toward Next-Generation Optical Neutrino Experiments

by

Max Smiley

Doctor of Philosophy in Physics

University of California, Berkeley

Associate Professor Gabriel Orebi Gann, Chair

This dissertation chronicles the role of optical photon-based detection technologies in the past, present, and future of neutrino physics. The initial chapters summarize the history of the field, following chapters explaining key areas of current research. The focus splits then splits, first covering studies with the current-generation, kiloton-scale SNO+ experiment, which has operated with significant amounts of liquid scintillator as its target since 2020. The next sections highlight work undertaken toward the development of a new paradigm known as "hybrid" detection, which aims to benefit from the two optical light emission mechanisms, Cherenkov radiation and scintillation, currently drawn on separately in today's experiments.

For SNO+, the experiment is described and this work explores the first demonstrations of α and instrumental background rejection on scintillator data, performed using likelihood-ratio-based classification with hit timing. These demonstrations provide powerful tools for a broad range of physics analyses in SNO+. Additionally, an analysis to determine the ^{8}B solar neutrino flux is performed on two datasets, one from when the SNO+ detector was only partially filled with liquid scintillator for an extended period of time due to the COVID-19 pandemic, and one from when the detector was completely full with the final scintillator cocktail for a period of over a year. The measured flux in both periods, $[5.13^{+1.29}_{-1.11}(\text{stat.})^{+0.45}_{-0.53}(\text{syst.})] \times 10^{6}$ cm^{-2} s^{-1} and $[5.74^{+0.84}_{-0.77}(\text{stat.})] \times 10^{6}$ cm^{-2} s^{-1} respectively, is consistent with theoretical predictions from leading Standard Solar Models. This gives confidence in the understanding of SNO+'s operations in this period and adds to the family of measurements made of this flux around the community.

Subsequent discussion introduces the hybrid paradigm and outlines the areas where this technology is maturing. This dissertation presents key explorations into the physics potential at large-scales of this technology using well-motivated modeling and reconstruction for the first time. The potential for neutrinoless double beta decay and CNO solar neutrino flux measurements are examined, with capabilities akin to or exceeding state of the art experiments in a range of scenarios. Also presented is the particle identification capability of the novel scintillating medium water-based liquid scintillator based on lab-measured timing and light yield properties, with substantial rejection power identified between α and β signals. These explorations provide a confirmation of the possibilities for hybrid detection and help pave the way for concrete realizations of these technologies at larger scales.

To my parents

For giving me the courage to embark on this damned-fool idealistic crusade in the first place

Contents

List of Figures

List of Tables

Acknowledgments

I want to thank the Academy... Wait a second, wrong achievement... It would be an understatement to say that my life, and the world around me, has evolved dramatically since my first visit to UC Berkeley and the Lawrence Berkeley National Laboratory in the Spring of 2018. At that point in time, the path seemed simple: pick a school, pick a group and do the research and at the end of the day, a doctorate I would have. There is no way I could have envisioned the twists and turns, most of them good and some of them less so, that graduate school had in store for me. From a global pandemic to political upheaval, and from establishing my life in an unfamiliar place far from friends and family to a six-week long strike, the journey to produce the work contained within these pages was far from straightforward both on a societal level and a personal level. I will do my best now to convey my appreciation for the help and support given to me in this endeavor by a broad away of colleagues, friends and family, though let me start out by apologizing to the many others who have shaped my journey that I have unconsciously omitted.

Firstly, I would like to express my deepest gratitude to my family, and especially my parents who have been on this journey with me every day even though they have been 3000 miles away. I would not have gotten to grad school at all had you not poured your love and support into raising me and encouraging me to pursue what I found most interesting in and outside of school. In many ways I feel like you almost never treated me like a child, and I think that was just what I needed to thrive. I'm excited that we are journeying into the next chapters of our lives at the same time, and I'm excited to continue exploring together. My other family back on the East Coast also has my heartfelt thanks for your confidence in me, especially given the fact that you suffered through my many tortured explanations of what exactly it is that I was doing on my trips back home or your trips here: Grandma Charlotte, Richard, Barbara, Marci, Jon, Brian, Eric, Drew, Sophie, Jeremy, and many others! I would also like to acknowledge my Grandpa Harry and Grandma Carole, who I know would be immensely proud of my achievements even though they left us long before I embarked on this chapter of my life, and Grandpa Howard and Molly, who helped me push off on this winding trip but sadly could not see the completion of this voyage.

Next, enough cannot be said about the wonderful Orebi Gann group at UCB and LBNL, headed by the Notorious GDOG (please forgive me!). I'm not sure I can adequately capture the importance of Gabriel's guidance on my career and development as a researcher, going back even before I arrived at Berkeley. No matter the day, no matter the hour, Gabriel was always open to talking through problems I was having or testing out a new idea. Her solution-oriented mentality has kept me going when faced with a multitude of challenges, and her ability to seek and find opportunities for our group (and me) has been remarkable to witness and to benefit from. She has taught me a great deal about the science itself and the science behind the science, so to speak, and I will carry that forward with me throughout my career.

I would also not be writing this document without the counseling of Javi Caravaca, who was instrumental in my growth as a physicist before and after I arrived at Berkeley and built my confidence as a researcher as we navigated several projects on SNO, SNO+ and hybrid detectors. From teaching me how to navigate my first peer review and write my first papers, to getting me to dig deep on understanding the statistics of likelihood fitting, Javi helped me get a firm footing as a grad student that has carried me forward to today. I am grateful that Javi has stuck around in the Bay Area and look forward to seeing him around the halls of LBL now that he has returned. Similarly, Morgan Askins put up with quite a bit of silliness from me and our collaborations, but made a lasting influence on my approach to physics and navigating the politics of Big Science. Also a great guy to play some soccer with. The dynamic duo of Zara Bagdasarian and Stephane Zsoldos brought our group some much-needed levity during troubling moments, in addition to their keen scientific prowess, though Stephane could use some work on his time management. It was a pleasure to work in that windowless office with Guang Yang, as well as enduring some exciting times during the initial Eos DAQ testing where it seemed like we had irreparably broken something, which mostly ended up not being the case. Tanner Kaptanoglu and Logan Lebanowski followed me from Penn (I forgive you) and it was pleasure to continue working alongside them after learning so much from them as an undergraduate. Leon Pickard brought some much needed additional English zest into our group as the intrepid Eos detector manager, and surprisingly taught me quite a bit about plumbing. Last but not least, it would be an extraordinarily grievous error to not sing the praises of Ed Callaghan, an esteemed physicist if ever there was one. A veritable font of knowledge and expertise, Ed always made himself available to troubleshoot a problem, in physics and in life. The number of times Ed helped resolve an issue I was having, prompted or unprompted, is likely immeasurable. I am so lucky to have overlapped with him in the OG Group and I am grateful to be continuing on as postdocs together at LBL.

For my collaborators on SNO+ and various hybrid optical detector projects, I have nothing but praise and would like to give a few specific callouts. Without the mentorship of Josh Klein while an undergrad at UPenn, I would not be producing this document at all, and I was privileged to maintain this connection through my PhD and continue to benefit from his acerbic wisdom. The rest of the Penn group also deserves some praise, for making me feel at times as though I never left, especially Tony Zummo, Meng Luo, and Sam Naugle (who pulled a reversal of my choice of post-secondary education). Very special shoutouts go to Ana Sofia Inacio and Daniel Cookman, who paralleled my journey with solar neutrinos on SNO+ and caught more than a few errors of mine. I have also had the pleasure of working with Richie Bonventre on a variety of projects. While at times I felt like a Mini-Me, inheriting from him or sharing with him quite a few roles and responsibilities greatly shaped my trajectory as a researcher. And I would be remiss of me to leave out Minfang Yeh and Milind Diwan, who graciously hosted me at Brookhaven National Laboratory and provided valuable insights to me as we worked on the cutting edge of optical detectors.

I could not leave out my many, many friends that I have made over the course of grad school, and the ones I made beforehand that helped to keep me sane. I am humbled by the fact that my neutri-bro Kenny Vetter and I made it six years living together and are finishing within days of each other. Hours-long conversations about everything from politics to logic puzzles, countless times barging into your bedroom to use our shared bathroom, partaking in perhaps a little too much festivities at a number of bars (including back alley moonshine), our friendship has seen it all. I wish you the best of luck at MIT and hope for a fantastic career ahead. Greg and Vanessa, I am not sure I would have continued in grad school, multiple times, without your love, patience and constant presence in my darkest moments, though I also have you to thank for getting me into this mess so I'll say you're even! Well, maybe letting me hang out with Wednesday and Zorro puts you back on the good side of things. Vikram and Burhan, you kept me sane in some dark moments as well and I have always been buoyed by your positivity and calmness. For my cohort-mates and classmates in Physics, Trevor, Daniel, Chris, Chi, Tomo, Lizzy, Gwen, Ella, Robin, Noelle, Olive, Aashrita, Greg KM, and others, there is no way I would've gotten through classes or quals, or had vibrant cultural experiences like museum visits, dinners (made collaboratively or enjoyed at restaurants), soccer matches, protests, movies and long hours of tabletop gaming. Many thanks also to my other roommates over the years here, Adam, Shumpei and Ben, for agreeing to share space with me of all people. Lastly, though my work with them certainly distracted from my research, I cannot leave out my UAW siblings: Jess, Leo, Diane, Jacob, Reed, Anjali, Tanzil, Mia, Christian, David, Daniel, Sarah, Hayley, Connor, Iris, Liz, Sam, Garrett, Kavitha, countless members of Physics OC over the last four years and many others who shaped our path toward a fairer UC and world. My experience in grad school and my outlook as a person would be wholly different had I not embarked on this work with you. I am so proud of what we have achieved together and what we will continue to work toward in the future.

Finally, I could not finish without thanking one more person: Maya. While you came into my life at the tail end of this experience, in many ways it feels like you have been here the whole time. You stuck with me through some trying times for me personally, professionally and socially, and introduced me to Tookie! You and I have built something wonderful together. Your love and support have kept me going as I have written this thesis and I am so excited to move into this next phase together with you (and hopefully some cats too).

Chapter 1

Introduction

Throughout the history of humankind, the search for understanding of the origins and structure of the Universe has always been central to the pursuit of knowledge. While many ancient thinkers developed similar theories of divisions of the world into smaller, fundamental pieces, we owe the familiar term "atom" to the Greek philosopher Democritus, who lived around 2500 years ago [2, 3]. These concepts were given a modern grounding by English scientist John Dalton and Russian chemist Dmitri Mendeleev in the 19th century [2, 4, 5], with the development of atomic theory and the periodic table of elements. Their work was carried forward over the course of the next 100 years, leading to, among others, the discovery of radiation and radioactivity by Wilhelm Roentgen, Henri Becquerel and the Curies and the discovery of sub-atomic particles like the electron by J.J. Thomson in 1897 and the nucleus by Ernest Rutherford in the 1910s [2]. This turn-of-the-century journey into the proverbial "microcosmos" generated in many ways more questions than answers, opening a Pandora's box of particles and possibility, but also leaving a dangerous and deadly legacy. In one small corner of this story, faced with peculiar patterns in the detection of β-decay, Wolfgang Pauli in 1930 proposed a solution in the form of a ghostly, little particle later dubbed the "neutrino" [6, 7]. It is here, within this ephemeral sliver of the set of fundamental rules governing the known universe called the Standard Model of Particle Physics, where we lay our scene.

This dissertation covers a slice of the world of neutrinos focused on their experimental detection at the MeV-scale: how they are produced, how they are detected, and what that means for the underlying physics, in the past, present and future, with a particular focus on solar neutrinos. This introduction serves as Chapter 1. A review of the relevant physics for neutrinos in the Standard Model of Particle Physics and beyond, as well as discussion of Standard Solar Models follows in Chapter 2. Chapter 3 discusses the detection principles for and history of optical neutrino experiments used to date and the phenomenology of neutrino detection with these detectors, again with a focus on solar neutrino detection. In Chapter 4, the state-of-the-art SNO+ optical neutrino experiment is detailed and the subsequent Chapter 5 describes the analysis of data from this detector to extract the ^{8}B solar neutrino flux while filled with liquid scintillator. With a view toward the future of this subfield, Chapter 6 contains an overview of so-called "hybrid" optical detection technology, which aims to broaden the horizons of capability for optical detectors for a variety of physics topics, and the following Chapter 7 features a subset of research and development work performed in pursuit of fleshing out this burgeoning area. Finally, the outlook for solar neutrino physics and hybrid detection is given in Chapter 8.

Chapter 2

The Physics of Neutrinos circa 2024 CE

The developments in fundamental physics in the past 150 years are nothing short of staggering. This chapter focuses on the developments in particle physics and solar physics that underpin the discussion of MeV-scale neutrino detection technology and analysis, particularly for solar neutrinos, that are discussed in the following chapters.

2.1 Standard Model of Particle Physics and Neutrinos

While Pauli postulated the “neutrino” in 1930 (though it was Fermi who popularized its name to juxtapose with Chadwick’s neutron [7]), and Cowan and Reines made the first detection at Savannah River in 1956 [8], the neutrino’s place in the jigsaw puzzle of particle physics only crystallized with the work of Glashow, Weinberg and Salam in the late 1950s and 1960s to formulate the theory of the electroweak (EW) interaction [9–11]. Taken together, with the addition of the quark model and quantum chromodynamics (QCD) [12–16] and the development of the Higgs mechanism [17–19], this was later developed into the Standard Model of Particle Physics. The Standard Model represents the summation of the current understanding of particle physics, with the notable exceptions of gravity and neutrino mass, as will be discussed later.

While there is plentiful content in QCD, for the purposes of exploring neutrino physics we can disregard the content of the $SU(3)_C$ gauge-invariant fields and focus on the Lagrangian formed by the $SU(2)_L \times U(1)_Y$ invariant fields. For the fermions, this can be written as [20]:

$$\begin{aligned}\mathcal{L}_F = &\sum_i \bar{\psi}_i\left(i\partial\!\!\!/ - m_i - \frac{m_i H}{v}\right)\psi_i - \frac{g}{2\sqrt{2}}\sum_i \bar{\mathbf{\Psi}}_i\gamma^\mu(1-\gamma^5)(T^+W_\mu^+ + T^-W_\mu^-)\bar{\mathbf{\Psi}}_i \\ &- e\sum_i Q_i\bar{\psi}_i\gamma^\mu\psi_i A_\mu - \frac{g}{2\cos\theta_W}\sum_i \bar{\psi}_i\gamma^\mu(g_V^i - g_A^i\gamma^5)\psi_i Z_\mu\end{aligned} \tag{2.1}$$

While this Lagrangian in some sense contains everything one needs to know to study neutrinos in the context of the Standard Model (the kinetic and mass terms in the first term, the charged current (CC) interactions in the second term, the electromagnetic interactions in the third term and the weak neutral current (NC) interactions in the fourth term), this formulation bears some additional explanation.

First, it is worth discussing some notational boilerplate. Where present, μ represents the spacetime index (i.e. t, x, y, z or some other transformation thereof), with γs representing the matrices used to perform Lorentz transformations on the spinors of the fields represented by ψ. γ^5 is a particular construction of γ matrices that enters the Lagrangian by way of the left-handed projection operator $P_L = \frac{1-\gamma^5}{2}$ in order to select the left-handed field component only in order to satisfy the transformation rules of $SU(2)_L$.

Addressing the field content, we have ψ_i representing the ith fermion field, and $\mathbf{\Psi}_i$ and representing the ith fermion doublet. As originally constructed, the admitted fermionic fields took the form of the three $SU(2)$ doublets $q_{L,i} = \begin{pmatrix} u_{L,i} \\ d_{L,i} \end{pmatrix}$ for $i = 1, 2, 3$ for the three generations of quarks corresponding to u and d, c and s, and t and b; three $SU(2)$ doublets of $\ell_{L,i} = \begin{pmatrix} \nu_{L,i} \\ l_{L,i} \end{pmatrix}$ for the three generations of leptons e, μ and τ; as well as the 9 right-handed $SU(2)$ singlets $u_{R,i}$, $d_{R,i}$, $l_{R,i}$ for the corresponding generations. Note that under the minimal Standard Model, there are no ν_R singlets. At the time of construction, neutrinos had only been observed in pure chiral states and they were believed to have zero mass, which the absence of the ν_R singlets conveniently allowed.

Further, the EW theory supposes the bosons W^i for $i = 1, 2, 3$ and B, produced as a result of the gauge symmetries, but those do not appear in the above due to the spontaneous symmetry breaking that results in the weak force and the electromagnetic force. $\tan\theta_W = \frac{g'}{g}$ defines Weinberg's weak mixing angle, with g being the dimensionless coupling strength of the $SU(2)$ fields and g' being the analogous constant associated with the $U(1)$ field. In turn, this angle describes the mixing of the neutral W^3 and B bosons present in the Standard Model that creates the physical Z and A bosons that represent the physical manifestations of the neutral current of the weak force and the electromagnetic force after spontaneous symmetry breaking. It is also convenient to rewrite W^1 and W^2. The relationships are given as

$$\begin{aligned} W^{\pm}_\mu &= \frac{W^1_\mu \mp i W^2_\mu}{\sqrt{2}} \\ A_\mu &= B_\mu \cos\theta_W + W^3_\mu \sin\theta_W \\ Z_\mu &= -B_\mu \sin\theta_W + W^3_\mu \cos\theta_W \end{aligned} \tag{2.2}$$

There are also associated good quantum numbers related to these bosons: the weak isospin T^3 (T^+ and T^- present in the Lagrangian are the weak isospin raising and lowering operators), weak hypercharge Y (which corresponds to the original B boson) and the electric charge Q (which exists as a result of the symmetry breaking down to $U(1)_{\text{EM}}$). The charges of the fermions under each are summarized in Tab. 2.1. Careful identification can be used to show that $Q = T_3 + \frac{1}{2}Y_W$, which is further explained by noting that e is defined as $g \sin\theta_W$, $g_V^i = T_i^3 - 2Q_i \sin^2\theta_W$ and $g_A^i = T_i^3$.

Particle Type	T^3	Y	Q
ν_L	$\frac{1}{2}$	-1	0
l_L	-$\frac{1}{2}$	-1	-1
l_R	0	-2	-1
u_L	$\frac{1}{2}$	$\frac{1}{3}$	$\frac{2}{3}$
u_R	0	$\frac{4}{3}$	$\frac{2}{3}$
d_L	-$\frac{1}{2}$	$\frac{1}{3}$	-$\frac{1}{3}$
d_R	0	-$\frac{2}{3}$	$\frac{2}{3}$

Table 2.1: This table summarizes the quantum numbers for the relevant fermion fields and quantum numbers. The quantum numbers for the three generations of leptons and quarks are identical.

The final piece to disentangle is H, which encodes the Higgs field and its interaction with the fermions. In the Standard Model, we consider the scalar potential for the Higgs field Φ, itself an $SU(2)_L$ complex doublet, with $Y = 1$ as such:

$$\begin{aligned} V(\Phi) &= \mu^2 \Phi^\dagger \Phi + \frac{\lambda^2}{2}(\Phi^\dagger \Phi)^2 \\ \Phi &= \begin{pmatrix} \phi^+ \\ \phi^0 \end{pmatrix} \end{aligned} \tag{2.3}$$

For $\mu^2 < 0$ and $\lambda > 0$, there is a non-trivial minimum at the vacuum expectation value of $v = \sqrt{2}\frac{|\mu|}{\lambda}$. We can rewrite the Higgs field as $H = \begin{pmatrix} 0 \\ \frac{v}{\sqrt{2}} + \phi \end{pmatrix}$, where we now consider fluctuations about this minimum. This gives rise to the Yukawa terms generating the fermion mass of the form $\propto \bar{l}_{e,L} H e_R$, and equivalents for the other charged lepton generations, and quarks. However, due to the lack of ν_R in this theory, no such terms can be constructed that give mass to the neutrinos.

2.2 Neutrino Mass and Oscillations

In discovering the neutrino, Cowan and Reines had only found the electron-type neutrinos ν_e, as these are the only flavor that can be produced in nuclear decays and fusion. While experimentalists built on their legacy and developments in accelerator physics to detect the ν_μ in 1962 [21] and ν_τ in 2001 [22], questions about the nature of neutrinos remain prominent. Eventually, the hypothesis of neutrino flavor change resolved the Solar Neutrino Problem (SNP) [23] (see Sec. 2.3.2) and associated discoveries made in the observation of atmospheric neutrino [24] and reactor neutrino [25] fluxes implied that the neutrinos must oscillate between flavors. These findings led to the conclusion that neutrinos, as with quarks and the Cabbibo-Kobayashi-Maskawa (CKM) formalism [26, 27], must, contrary to the Standard Model framework, be massive, as particles cannot experience time evolution without a mass. They must also have a misalignment between their flavor and mass eigenbases, such that the flavor state content evolves over time, as the interaction basis and propagating basis would otherwise remain aligned for all time. This has opened questions about where this mass comes from: whether neutrinos possess a Dirac mass (as with the other fermions, enabled by the addition of right-handed "sterile" neutrinos), a Majorana mass (in which case neutrinos and antineutrinos share the same field, enabled by being electrically neutral), or both. The absolute mass scale of neutrinos is also a free parameter that remains to be measured.

While the neutrino mass generation mechanism still remains elusive, the Pontecorvo–Maki-Nakagawa–Sakata (PMNS) formalism [28, 29] is the predominant mechanism to describe the mixing of neutrino mass states in vacuum, and is accompanied by the Mikheyev–Smirnov-Wolfenstein (MSW) effect [30, 31] to detail the modification to this picture in the presence of matter.

2.2.1 Neutrinos in Vacuum: PMNS Matrix

While the PMNS model is extensible to larger numbers of neutrino flavor states (for example, to models that include a 4th sterile neutrino used to explain anomalies in oscillation patterns to be discussed later), we will consider the currently accepted model of three light neutrino flavor states: ν_e, ν_μ and ν_τ. Supposing that the transformation between the mixture of pure flavor states and pure mass states should be unitary, in other words holding to the concept that there are only the three available states, we are left to consider the following:

$$\begin{pmatrix} \nu_e \\ \nu_\mu \\ \nu_\tau \end{pmatrix} = U_{\text{PMNS}} \begin{pmatrix} \nu_1 \\ \nu_2 \\ \nu_3 \end{pmatrix} = \begin{pmatrix} U_{e1} & U_{e2} & U_{e3} \\ U_{\mu 1} & U_{\mu 2} & U_{\mu 3} \\ U_{\tau 1} & U_{\tau 2} & U_{\tau 3} \end{pmatrix} \begin{pmatrix} \nu_1 \\ \nu_2 \\ \nu_3 \end{pmatrix} \tag{2.4}$$

In Eq. (2.4), ν_e, ν_μ and ν_τ represent the components in the flavor basis (interaction basis), ν_1, ν_2 and ν_3 represent that components in the mass basis (propagating basis) and U_{PMNS} is the unitary transformation matrix that maps between them, with U_{e1} and others representing the complex matrix elements. It is common to parameterize the PMNS matrix into "rotation" matrices considering the mixing of two of the mass states at a time (due to a complex phase that remains behind, these are not strictly rotations as we typically conceive of them) as follows:

$$U_{\text{PMNS}} = U_{23} U_{13} U_{12} = \begin{pmatrix} 1 & 0 & 0 \\ 0 & c_{23} & s_{23} \\ - & -s_{23} & c_{23} \end{pmatrix} \begin{pmatrix} c_{13} & 0 & s_{13} e^{-i\delta} \\ 0 & 1 & 0 \\ -s_{13} e^{i\delta} & 0 & c_{13} \end{pmatrix} \begin{pmatrix} c_{12} & s_{12} & 0 \\ -s_{12} & c_{12} & 0 \\ 0 & 0 & 1 \end{pmatrix} \tag{2.5}$$

Here, $c_{ij} = \cos\theta_{ij}$ and $s_{ij} = \sin\theta_{ij}$ where the angle is taken as the angle of rotation considering the two mass basis elements to appropriately map into the flavor basis, called the "mixing angle". Additionally, there is the complex phase $e^{i\delta}$, which enables CP-violation, an asymmetry between the mixing for neutrinos and antineutrinos. Generically, if the three neutrinos are Majorana particles, there will also be two immeasurable phases that are absorbed into the definition of the fields.

Now, it is simple to see that we can consider the time-evolving neutrino state, having been produced in a pure flavor state, as

$$|\nu_\alpha(t)\rangle = \sum_{i=1}^{3} U^*_{\alpha i} e^{-iE_i t} |\nu_i(0)\rangle \tag{2.6}$$

where α is the flavor basis index, i is the mass basis index, $U_{\alpha i}$ is the appropriate component of the PMNS matrix and E_i is the energy eigenstate. While this formalism is not Lorentz-invariant and additionally assumes propagation as a plane wave with definite momentum p, these simplifications are valid for most practical purposes, including applications explored in this dissertation. In the ultra-relativistic limit, we can take $E_i = \sqrt{p_i^2 + m_i^2} \approx p + \frac{m_i^2}{2E} = E + \frac{m_i^2}{2E}$, where we treat $p_i \approx p_j$ for all mass states and expand in $\frac{m_i}{E}$ as the small parameter. We can also assume $L \approx t$ (with $c = 1$), as it is experimentally convenient to consider the distance or "baseline" for the neutrino propagation, rather than the time elapsed from production. Then, applying the Born rule, the probability that the neutrino interacts in flavor β at time t is

$$\begin{aligned} P_{\alpha\beta}(t) &= |\langle \nu_\beta|\nu_\alpha(t)\rangle|^2 = U^*_{\alpha i} U_{\beta i} U_{\alpha j} U^*_{\beta j} e^{-i(E_i - E_j)t} = U^*_{\alpha i} U_{\beta i} U_{\alpha j} U^*_{\beta j} e^{-\frac{i}{2E}(m_i^2 - m_j^2)L} \\ &= \delta_{\alpha\beta} - 4\sum_{i<j} \mathrm{Re}\big\{U_{\alpha i} U^*_{\beta i} U^*_{\alpha j} U_{\beta j}\big\} \sin^2(\frac{\Delta m^2_{ij} L}{4E}) + 2\sum_{i<j} \mathrm{Im}\big\{U_{\alpha i} U^*_{\beta i} U^*_{\alpha j} U_{\beta j}\big\} \sin\left(\frac{\Delta m^2_{ij} L}{2E}\right) \end{aligned} \tag{2.7}$$

with $\Delta m^2_{ij} = m_i^2 - m_j^2$. Since the sign of the second term will change when exchanging neutrinos for antineutrinos under complex conjugation, this is the component of the oscillation probability that changes in the presence of a non-zero δ_{CP}. Given the chosen labeling of states and experimental data, m^2_{21} is known to be positive (i.e. $m_2 > m_1$), but as of yet m^2_{32} is free to either be positive or negative, as it is still to be experimentally determined. This gives rise to the potential for either a "normal" hierarchy, wherein $m_3 > m_2 > m_1$, or an "inverted" hierarchy, wherein $m_2 > m_1 > m_3$. If the produced and detected flavor are the same, as is the case for low energy detection of solar neutrinos and reactor neutrinos, for example (so-called "disappearance" experiments), this is reduced to

$$P_{\alpha\alpha}(L) = 1 - 4\sum_{i<j} \mathrm{Re}\big\{U_{\alpha i} U^*_{\alpha i} U^*_{\alpha j} U_{\alpha j}\big\} \sin^2(\frac{\Delta m^2_{ij} L}{4E}) = 1 - 4\sum_{i<j} |U_{\alpha i} U^*_{\alpha j}|^2 \sin^2(\frac{\Delta m^2_{ij} L}{4E}), \tag{2.8}$$

Note that the only parameters that will change based on the source and employed detection techniques are L and E. For very small $\frac{L}{E}$, as well as other particular values given the periodicity of sin, no oscillation will be observed. Meanwhile for circumstances where the neutrino production and detection spans a broad range of energy and distances (e.g. neutrinos of varied energy produced across a wide range in the Sun being detected on Earth), an averaging/washing-out effect will be apparent, as many different $\frac{L}{E}$ values will be observed, which makes it simpler to measure the mixing angles and the CP-violating phase. It is for this reason that experiments that seek to measure the mass splittings must precisely know the relevant $\frac{L}{E}$ for their setup, and typically will sample at values close to the maxima of sin.

Much experimental effort since the elucidation of the massive neutrino paradigm has been focused on measuring the above mentioned oscillation-related quantities: θ_{12}, θ_{23}, θ_{13}, δ_{CP}, Δm^2_{21}, and Δm^2_{32}, as well as the absolute neutrino mass scale and mass generation mechanism (see Tab. 2.2 for experimentally determined values). Several oscillation parameters are precisely measured [32, 33] but others remain to be definitively pinned down [34–38], with additional questions arising due to various observed "anomalies" [39, 40]. However, so far we have only discussed the phenomenology of neutrino mass and oscillations in the absence of matter. Matter has a significant influence on this picture, as will be seen in Sec. 2.2.2.

Table 2.2: The oscillation parameters and uncertainties obtained from the NuFit 5.3 evaluation [32], including the Super-Kamiokande atmospheric data, for both the normal and inverted mass orderings. Note that for the normal ordering, $\Delta m^2_{3\ell} = \Delta m^2_{31} > 0$ and for the inverted ordering, $\Delta m^2_{3\ell} = \Delta m^2_{32} < 0$.

Parameter	Normal Ordering	Inverted Ordering
θ_{12} (deg)	$33.67^{+0.73}_{-0.71}$	$33.67^{+0.73}_{-0.71}$
θ_{23} (deg)	$42.3^{+1.1}_{-0.9}$	$48.9^{+0.9}_{-1.2}$
θ_{13} (deg)	$8.58^{+0.11}_{-0.11}$	$8.57^{+0.13}_{-0.11}$
δ_{CP} (deg)	232^{+39}_{-25}	273^{+24}_{-26}
Δm^2_{21} (10^{-5} eV^2)	$7.41^{+0.21}_{-0.20}$	$7.41^{+0.21}_{-0.20}$
$\Delta m^2_{3\ell}$ (10^{-3} eV^2)	$2.505^{+0.024}_{-0.026}$	$-2.487^{+0.027}_{-0.024}$

2.2.2 Neutrinos in the Presence of Matter: MSW Effect

In the presence of normal, neutral matter containing electrons, neutrons, and protons, neutrinos can undergo coherent charged current forward scattering preferentially for the electron flavor, with a potential of the form

$$V = \begin{pmatrix} \sqrt{2}G_F n_e & 0 & 0 \\ 0 & 0 & 0 \\ 0 & 0 & 0 \end{pmatrix} \tag{2.9}$$

where G_F is the Fermi constant and n_e is the electron density, which may be position dependent and generally is. The potential takes this form due to lepton family number conservation, which disallows diagram contributions for electron scattering for ν_μ and ν_τ that are allowed for ν_e. Any enhancements due to the added neutral current interactions occur with a potential that is equal in strength for all flavors, so the contribution amounts to a phase shift that is not observable. Considering the scale of the potential as small relative to Δm^2_{31}, as is the case given the electron density in the Sun and Earth, we can consider only a two state system of mass states ν_1 and ν_2 with flavor states ν_e and ν_x, which represents some combination of ν_μ and ν_τ that functionally behaves identically to either flavor in a pure state given the conditions. This potential modifies the Hamiltonian to $H = H_{\text{vacuum}} + U^\dagger V U$, which can be re-diagonalized to remove the off-diagonal components from the potential term introduced by moving from flavor to mass basis via U_{PMNS}. This enables treatment as a kinetic-only Hamiltonian with new eigenvalues and eigenvectors modified from the vacuum case, leading to effective masses and a mixing angle given by [20]:

$$\begin{aligned}
\mu^2_{1,2} &= \frac{m_1^2 + m_2^2}{2} + E(V_e + V_x) \mp \frac{1}{2}\sqrt{(\Delta m^2 \cos 2\theta - 2E(V_e - V_x))^2 + (\Delta m^2 \sin 2\theta)^2} \\
\tan 2\theta_m &= \frac{\Delta m^2 \sin 2\theta}{\Delta m^2 \cos 2\theta - 2E(V_e - V_x)}
\end{aligned} \tag{2.10}$$

If the potential vanishes (or if the contribution for the two flavor states is identical), we see that this reduces to the vacuum case, as desired. So for small potentials, the propagation is essentially unmodified, or modified as a small perturbation on the vacuum case. We note that for $2E(V_e - V_x) = \Delta m^2 \cos 2\theta$, there is a resonance condition that drives θ_m to maximal value and the mass splitting ($\Delta\mu^2 = \mu_2^2 - \mu_1^2$) to be minimized. Noting that the sign flips about this condition, we also see that this has the effect of swapping the alignment of the predominant mass eigenstate associated with a particular flavor. In other words, if ν_e is predominantly ν_1 in vacuum, in the presence of matter of sufficient density, ν_{2m} will be the predominant mass state associated with ν_e. With high enough density, it is possible to drive the composition of the flavor state entirely into one of the effective mass eigenstates. And if the variation in density through a medium is slow, this composition can be maintained through to the vacuum case, meaning that the propagating state is the pure mass state; this is known as the adiabatic conversion. However, if the variation is strong enough, the effective mass eigenstates can mix with the change in the potential. Between the two extremes of the potential, especially in the non-adiabatic case, careful numerical treatment is required. These considerations are relevant to various sources of neutrinos, for example for production of solar neutrinos (to be discussed in Sec. 2.3.2) and passage of atmospheric and beam neutrinos through the Earth.

2.3 Standard Solar Models and Solar Neutrinos

The question of the nature of the Sun, and in particular how its light output is produced, has driven astrophysical research for centuries. After all, as the nearest star, the Sun represents the closest window we have into the workings of the stellar population writ large, as well as an explanation for how our solar system came to be the way that it is. With the advent of the revolution in physics related to atomic structure and radiation addressed in Chapter 1, Eddington proposed that the only process capable of sustaining the Sun was fusion [41], and later researchers were able to build on this hypothesis to devise viable pathways for this fusion reaction [42]. The generic process, regardless of the precise constituents to the reactions, involves the following reaction:

$$4p \rightarrow \alpha + 2e^{+} + 2\nu_e + \text{Energy}$$

where this energy can come in the form of photons or in the form kinetic energy of the reaction products [43]. In order to verify that fusion was the underlying process, and rigorously test whether our understanding of the Sun could form a self-consistent model, stellar and nuclear physicists developed Standard Solar Models (SSMs) in the mid-20th century, which predict outputs such as the luminosity in photons and neutrinos from given inputs such as the solar elemental composition and physical models for radiation transport. Among the most prominent researchers tackling this problem was John Bahcall [44–46], who forwarded the detection of neutrinos as the best, most direct probe of the fusion reactions occurring in the Sun. Many models have been produced over the years [47–50], with the most recent sets being produced in 2016 [51, 52] and 2023 [53, 54], using varied inputs to the elemental compositions, nuclear reaction models, radiative transfer mechanisms and other effects. With a decadal review of fusion cross sections just completed [55] and new composition determinations in the past several years [56, 57], the SSM space has been significantly refined in this latest round.

2.3.1 Production of Solar Neutrinos

The two processes that produce the solar energy output and, correspondingly, the fluxes of solar neutrinos, are the proton-proton (*pp*) chain and the CNO cycle, as shown in Fig. 2.1. The *pp* chain is the dominant mechanism, accounting for over 99% of the energy output, with the CNO cycle accounting for the remainder. A brief explanation of the two mechanisms follows, with a focus on discussion of the constituent reactions that produce neutrinos.

The *pp* chain is divided into a set of different pathways that all start from fusion of two protons (hence the name), and end with the production of an α particle. The starting step is either the *pp* reaction, which involves the direct fusion of two protons or, in a small minority of cases, the *pep* reaction, which involves an electron catalyzing the fusion process. Both of these reactions produce similarly named neutrino fluxes. An additional proton is then fused to the deuterium nuclei to create ^{3}He nuclei. From there the process proceeds through different possible reactions with varied probability based on the nuclear cross sections and stellar composition, density and temperature. The first is the *pp*-I chain, which yields no further neutrinos but accounts for the vast majority of solar fusion, and involves fusion directly to α particles (^{4}He nuclei). The next most often occurring reaction chain is the *pp*-II set, which involves fusion to ^{7}Be, which is unstable and decays to ^{7}Li, emitting a neutrino, before splitting into two α particles upon interaction with a proton. Alternatively, on the rarer chance that the ^{7}Be is fused with another proton to form ^{8}B before it decays, the ^{8}B can decay to ^{8}Be and in the process emit a neutrino, before fissioning into two α particles. Finally, there is also the possibility to engage in the *hep* reaction, which involves the ^{3}He nuclei fusing with a free proton rather than another ^{3}He or ^{4}He nucleus, which also produces a neutrino. In total, there are five distinct neutrino producing interactions in the *pp* chain, which are commonly referred to in reference to their antecedent reactions as: *pp*, *pep*, ^{7}Be, ^{8}B and *hep*.

In contrast to the *pp* chain, the CNO cycle, as the name implies, involves the fusion process being cyclically mediated by heavier elements (Carbon, Nitrogen, and Oxygen), as depicted in the right-hand panel of Fig. 2.1. In fact, the CNO cycle is composed of two overlapping samples, the CN cycle and the NO cycle, with the CN cycle being dominant. The strength of this dominance depends somewhat on the solar elemental composition, as does the prevalence of the entire CNO cycle, which presents a unique probe of the Sun's fraction of that are neither Hydrogen nor Helium, also known as the metallicity, or Z. The neutrinos of the CNO cycle are produced by the β^+ decay of ^{13}N, ^{15}O and ^{17}F.

As with all nuclear processes, the kinematics of these reactions and decays determine the energy spectra of the neutrinos, which are of particular interest in order to devise detection experiments. As can be seen from Fig. 2.2, the highest energy of these neutrinos is produced at just under 20 MeV, meaning that any interaction to be used for solar neutrino detection must have suitable cross sections at energies of this scale. The dominant flux, unsurprisingly from its presence at the start of the *pp* chain, is from the *pp* neutrinos, which represent the vast majority of the neutrinos produced in the Sun. The flux with highest endpoint is the *hep* neutrino flux, though due to the highly similar shape and lower total emission compared to the ^{8}B neutrino flux, it is as yet undetected, though several limits have been placed [58, 59]. Meanwhile, the remaining fluxes have been observed by various experiments [60–67], with the most recent breakthrough being the detection of CNO neutrinos for the first time [68, 69], though given the similar endpoints, the neutrinos from the different decay processes from this family of reactions have yet to be distinguished. The current leading SSM evaluations and the global fit accounting for these results is present in Tab. 2.3.

2.3.2 Solar Neutrino Problem

The picture for solar neutrinos was not always so clear. In fact, almost as soon as the first neutrinos from the Sun were detected by Ray Davis at Homestake in the 1960s [72], questions arose. The experiment operated on the principle of the following reaction:

$$^{37}\mathrm{Cl} + \nu_e \to {}^{37}\mathrm{Ar} + e^-.$$

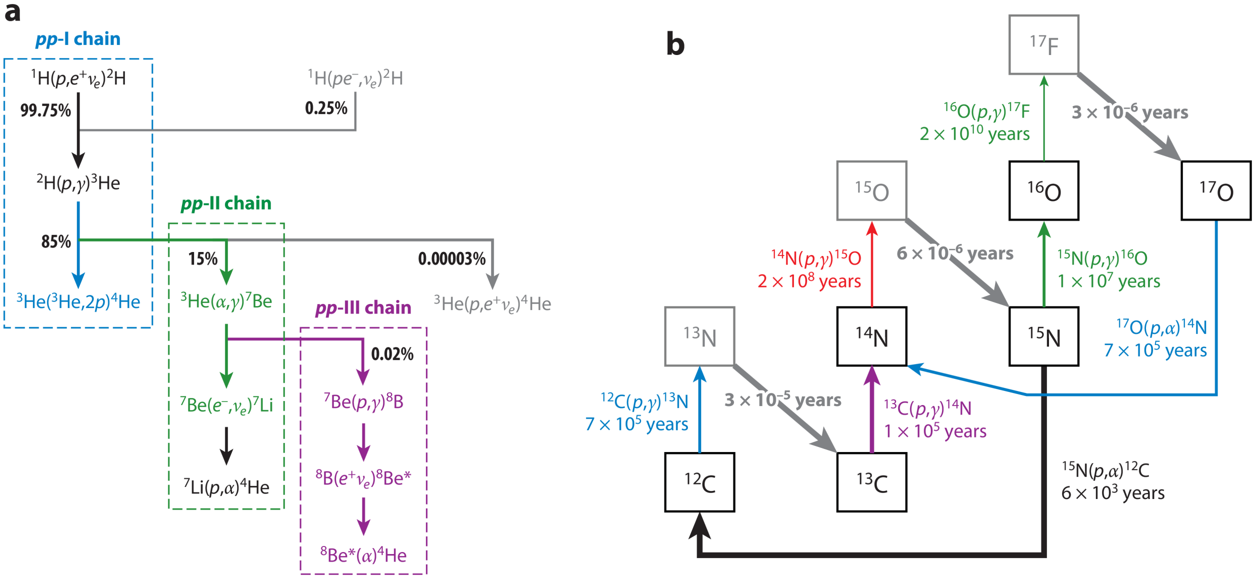

Orebi Gann GD, et al. 2021
Annu. Rev. Nucl. Part. Sci. 71:491–528

Figure 2.1: The nuclear reactions comprising the two principal fusion mechanisms in the Sun: the *pp* chain (**a** on left), and the CNO cycle (**b** on right). Reactions producing neutrinos are marked for the *pp* chain. For the CNO cycle, the neutrino-producing reactions are the indicated decays of ^{13}N, ^{15}O and ^{17}F. Figure reproduced from [43].

The experiment contained a large vat of tetrachloroethylene (dry-cleaning fluid), which was siphoned periodically to observe the electron capture decay of ^{37}Ar. The count rate of these decays was used to extrapolate the measured flux. From the results, it was observed that there was a significant tension with Bahcall's SSM prediction for the total solar neutrino flux, with the observed flux being substantially lower by roughly a factor of 3 [73]. This came to be known as the Solar Neutrino Problem.

Given the various complexities of the experimental method, despite various crosschecks, and the relatively high energy threshold, different experimental techniques were desired to serve as validations. This led to development of the Gallium experiments SAGE and GALLEX/GNO [61, 74]. These experiments operated on a similar radiochemical detection principle with ^{71}Ga instead of ^{37}Cl to achieve a lower energy threshold that was sensitive to

Table 2.3: Comparison of the computed solar neutrino fluxes in $\mathrm{cm}^{-2}\mathrm{s}^{-1}$ from the 2023 Barcelona Standard Solar Model evaluation [54], using the SF-III [55] reaction models and the low-Z AGSS09 [70] and AAG21 [56] and the high-Z GS98 [71] and MB22m [57] compositions, and the 2023 global experimental fit with the luminosity constraint (LC) [53]. With the exception of the *hep* flux, the global fit's preferred values are in reasonable agreement when accounting for errors, with the high-Z models currently favored.

Flux	GS98	AGSS09	AAG21	MB22m	Global Fit
pp ($\times 10^{10}$)	5.96 ± 0.03	6.01 ± 0.03	6.00 ± 0.03	5.95 ± 0.04	5.94 ± 0.02
pep ($\times 10^{8}$)	1.43 ± 0.02	1.45 ± 0.01	1.45 ± 0.02	1.42 ± 0.02	$1.42^{+0.02}_{-0.03}$
hep ($\times 10^{3}$)	7.95 ± 2.43	8.22 ± 2.50	8.16 ± 2.49	7.92 ± 2.43	$(3.0^{+0.9}_{-1.0}) \times 10^{1}$
^{7}Be ($\times 10^{9}$)	4.85 ± 0.36	4.43 ± 0.33	4.52 ± 0.33	4.90 ± 0.37	$4.93^{+0.10}_{-0.08}$
^{8}B ($\times 10^{6}$)	5.03 ± 0.63	4.14 ± 0.52	4.31 ± 0.54	5.13 ± 0.67	5.20 ± 0.10
^{13}N ($\times 10^{8}$)	2.80 ± 0.45	2.05 ± 0.29	2.22 ± 0.29	3.12 ± 0.46	$3.48^{+0.47}_{-0.40}$
^{15}O ($\times 10^{8}$)	2.07 ± 0.37	1.45 ± 0.24	1.58 ± 0.25	2.32 ± 0.40	$2.53^{+0.34}_{-0.29}$
^{17}F ($\times 10^{6}$)	5.35 ± 1.05	3.29 ± 0.57	3.40 ± 0.54	4.74 ± 0.76	$5.51^{+0.75}_{-0.63}$

pp neutrinos that are the most plentiful and that are produced in the simplest fusion reaction and therefore have the smallest uncertainties associated with their prediction. These experiments also observed a deficit, though this was found to be closer to 50% of the expected flux from the SSMs.

Another approach that was studied was to be able to more directly observe the neutrino interactions and their energy spectrum, rather than rely on the indirect counting methods of the radiochemical experiments. This was embodied in the KamiokaNDE [75, 76] experiment and later Super-Kamiokande [77], which were water Cherenkov detectors designed to do real-time observation of particle interactions occurring within their volume. More detail about this detection method will follow in Chapter 3. These experiments relied on the neutrino-electron elastic scattering (ES) interaction in order to detect neturinos, by observing the energy deposition of the outgoing electron via light production. Notably, the reaction

$$\nu + e^{-} \rightarrow \nu + e^{-}$$

occurs for all flavors, unlike the radiochemical experiments which solely happen for ν_e. However, the ν_e cross section for this interaction is enhanced by the presence of charged current interaction channels, rather than just the diagram mediated by the Z boson. With a higher energy threshold of several MeV, these "real-time" experiments were sensitive only to ^{8}B and *hep* contributions. These experiments also found a deficit compared to prediction. Super-Kamiokande will be discussed in further detail in Sec. 3.2.2.

Meanwhile, advancements in other areas of stellar observation gave confidence to the predictive power of the SSMs. Helioseismology, which is the study of the oscillation pattern of the Sun itself, helped provide insights into the properties of solar regions, including neutrino production areas. This was in much the same way that seismology can tell us about the

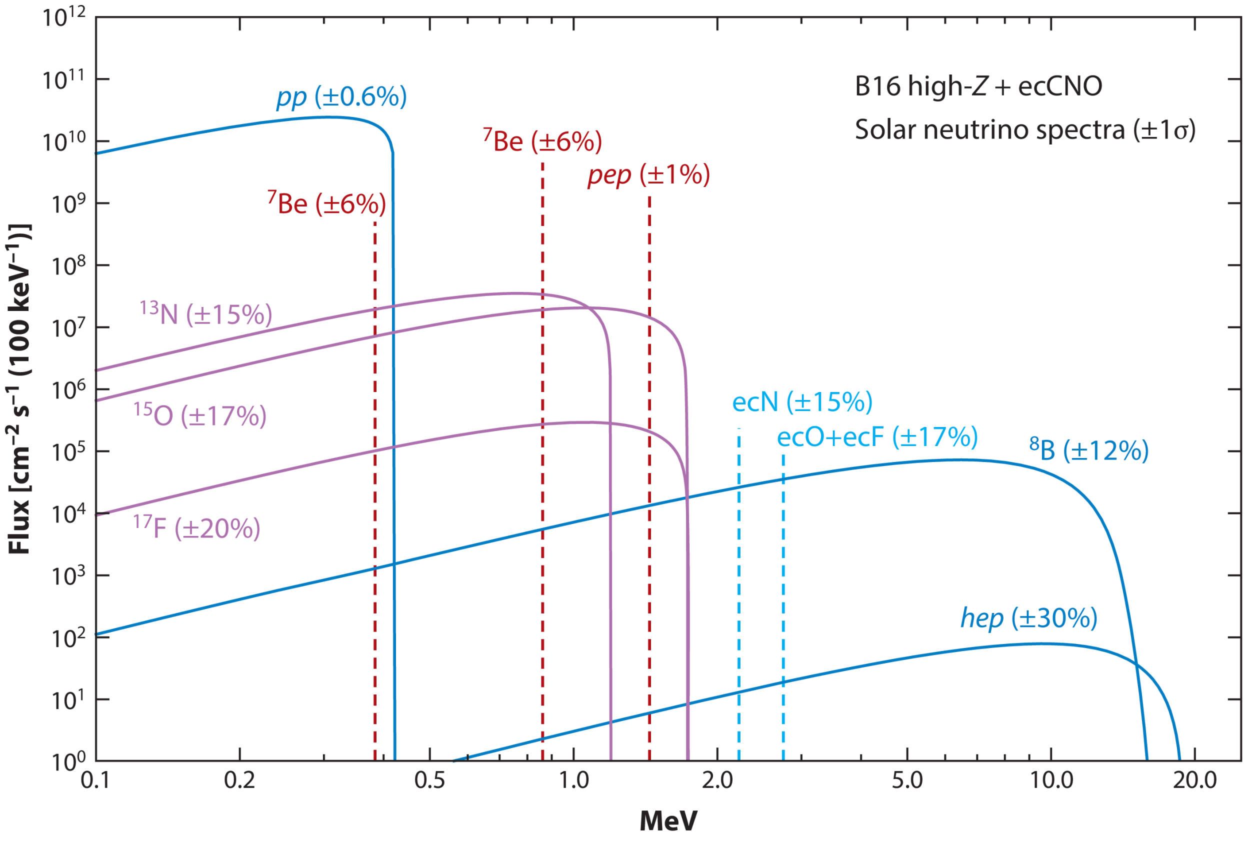

Orebi Gann GD, et al. 2021
Annu. Rev. Nucl. Part. Sci. 71:491–528

Figure 2.2: The neutrino energy spectra for the solar neutrino fluxes, scaled by the fluxes determined from the Barcelona 2016 high-Z model [52], and also including the electron capture CNO fluxes which are subdominant. Figure reproduced from [43].

Earth's structure (e.g. how we know about the Earth's core without having been able to directly probe it). The results from helioseismological studies contemporaneous with the work on solar neutrinos found that the properties predicted by the earlier SSMs and ones that incorporated helioseismological work yielded neutrino production characteristics that were in agreement, pointing to a neutrino physics explanation for the discrepancy [78].

The resolution to the problem came in the form of the Sudbury Neutrino Observatory (SNO), an experiment designed to detect solar neutrinos through multiple flavor-dependent channels [79]. SNO, like Super-Kamiokande, was a water Cherenkov detector, but more precisely, it was a *heavy water* Cherenkov detector. The substitution of D_2O for H_2O enabled access to the charged current and neutral current processes on the deuteron, namely:

$$\text{CC: } \nu_e + d \rightarrow e^- + p + p$$

$$\text{NC: } \nu + d \rightarrow \nu + p + n$$

The CC reaction is observable via similar means as the ES channel, while the NC interaction was observed via various means of neutron detection throughout the course of the experiment. These three channels allowed the flavor composition of the solar neutrino flux to be constrained for the first time, as shown in Fig. 2.3. So, while total solar neutrino flux, as observed by the NC channel, was actually in agreement with the theoretical prediction, somehow the neutrinos produced in these nuclear interactions, which should have been electron flavor, had been transmuted to other flavors.

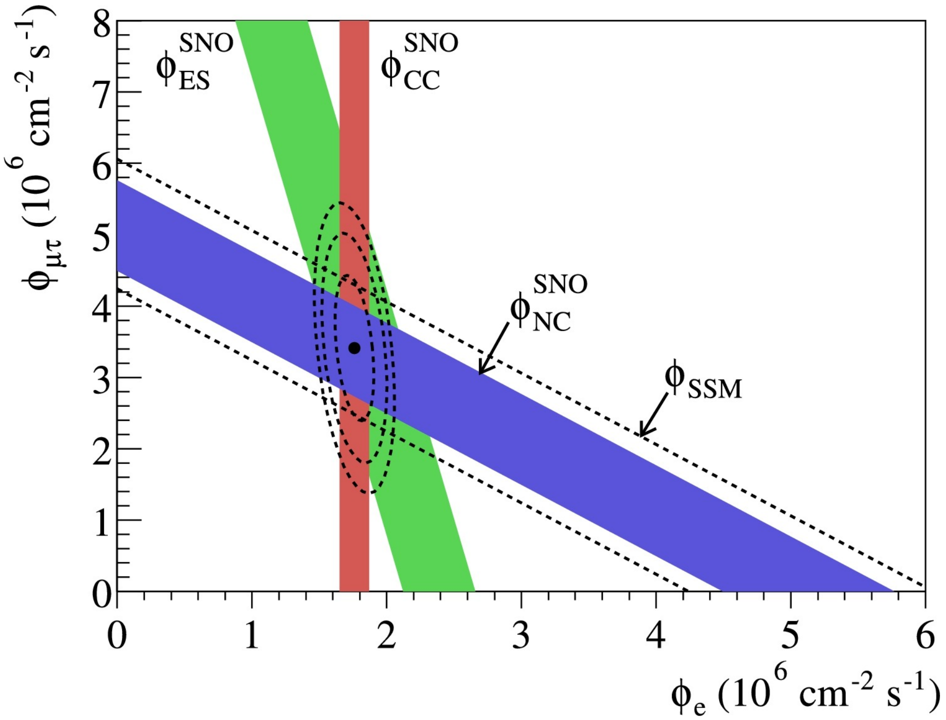

Figure 2.3: The flavor constraints on the observed flux from SNO using the ES, CC and NC channels, the Standard Solar Model constraint and the identified best fit point, reproduced from [79].

The processes explained in Sec. 2.2 provide the explanation for the observation of flavor change. SNO's results combined with Super-Kamiokande's observation of the atmospheric muon neutrino flux [24] and KamLAND's observation of reactor antinuetrinos [25] aligned with the presence of "large mixing angle" (LMA) oscillations and the above-discussed MSW effect in the presence of matter. This is otherwise known as the LMA-MSW solution to the phenomenon of neutrino flavor change.

To illustrate the combined effect, and the reason for the varied deficits observed, we consider two extreme cases of the low energy *pp* neutrinos and the higher energy ^{8}B neutrinos. For *pp* neutrinos, inspecting the effective masses in Eq. (2.10), one sees that for small E the contributions from the matter potential vanish, meaning that we are reduced to the vacuum oscillation case. Then the survival probability, i.e. the probability that a neutrino produced as an electron neutrino will be detected as an electron neutrino, P_{ee}, follows from Eq. (2.8). Because L, the Earth-Sun distance, is so large, with the production and detection points so distributed, the $\sin^2 x$ term will average out to $\frac{1}{2}$. Therefore, reading off

$$P_{ee} = 1 - 2\sum_{i<j} |U_{ei}U_{ej}^*|^2 = 1 - \frac{1}{2}\sin^2(2\theta_{13}) - \frac{1}{2}\sin^2(2\theta_{12})\cos^4(\theta_{13}) = 0.55 \tag{2.11}$$

where we have used the normal ordering results from Tab. 2.2. This explains why the Gallium experiments, which are sensitive to *pp*, saw a rise in the observed flux relative to theory compared to the high-energy sensitive Homestake.

Similarly, for high-energy ^{8}B neutrinos, referring back to the discussion in Sec. 2.2.2, it turns out that the electron density in the Sun is such that these neutrinos are produced in the pure ν_{2m} state due to the inversion caused by the potential, and then propagate adiabatically into vacuum, and transition into the ν_2 state. From reading off U_{PMNS}, this means that the survival probability looks like

$$P_{ee} = P_{e2} = \sin^2\theta_{12}\cos^2\theta_{13} = 0.30 \tag{2.12}$$

This explains the observation of the deficit in the Homestake experiment of about a third, given that the sensitivity was primarily to these higher-energy neutrinos.

With the solution to the SNP, the door has largely shut on the question of what processes are underlying the power output from the Sun, with direct confirmation via neutrinos in amounts that are consistent with the solar luminosity. However, several pressing questions remain.

2.3.3 Remaining Open Questions in Solar Neutrino Physics

In recent years, with Borexino's detection for the first time of CNO neutrinos [68], the subdominant CNO fusion process was finally found to occur in the Sun. This proof-of-principle has provided us with a pathway to solve the Solar Metallicity Problem or Solar Abundance Problem, which stems from disagreements between the internal structure predicted by SSMs and that observed from helioseismological measurements [43]. Lower Z models based on newer abundance extraction techniques amplified an already present tension for the higher Z models, calling into question their reliability. While various modeling revisions could be an explanation, pinning down the metallicity through direct measurement via CNO neutrino detection provides a promising road to explore and reduce the model space. While newer abundances with high Z have been produced [57], questions raised about their efficacy [80] put a finer point on the need to precisely measure the CNO flux, including the constituent components individually. The practicality of achieving such measurement is being explored by several experimental collaborations [1, 81–83].

Additionally, while the extremes of vacuum-dominated and matter-dominated regions of neutrino production in the Sun are thought to be fairly well-understood through experiment, the region in production energy from 2 MeV to 5 MeV is relatively unconstrained by data, as can be seen in Fig. 2.4. This leaves open the possibility that there are additional non-standard interactions (NSI) that could modify the shape of the survival probability, as well as other areas of neutrino physics [43]. Borexino [84], Super-Kamiokande [85] and SNO [63] have managed to explore this space to a degree, but fleshing out the NSI space and exploring other unaccounted for modifications to the survival probability will be the province of future experiments.

Finally, the determination of the *hep* flux and precision measurement of the previously measured fluxes enables further verification of solar models more generally. Pushing the current precision down to the percent level would represent a significant improvement on the ability to resolve issues in SSMs as well as for open questions in neutrino flavor physics. Because solar neutrinos are produced at various locations throughout the Sun over a broad range of energies, they continue to serve as an excellent probe, as detection technology and modeling techniques reach new heights.

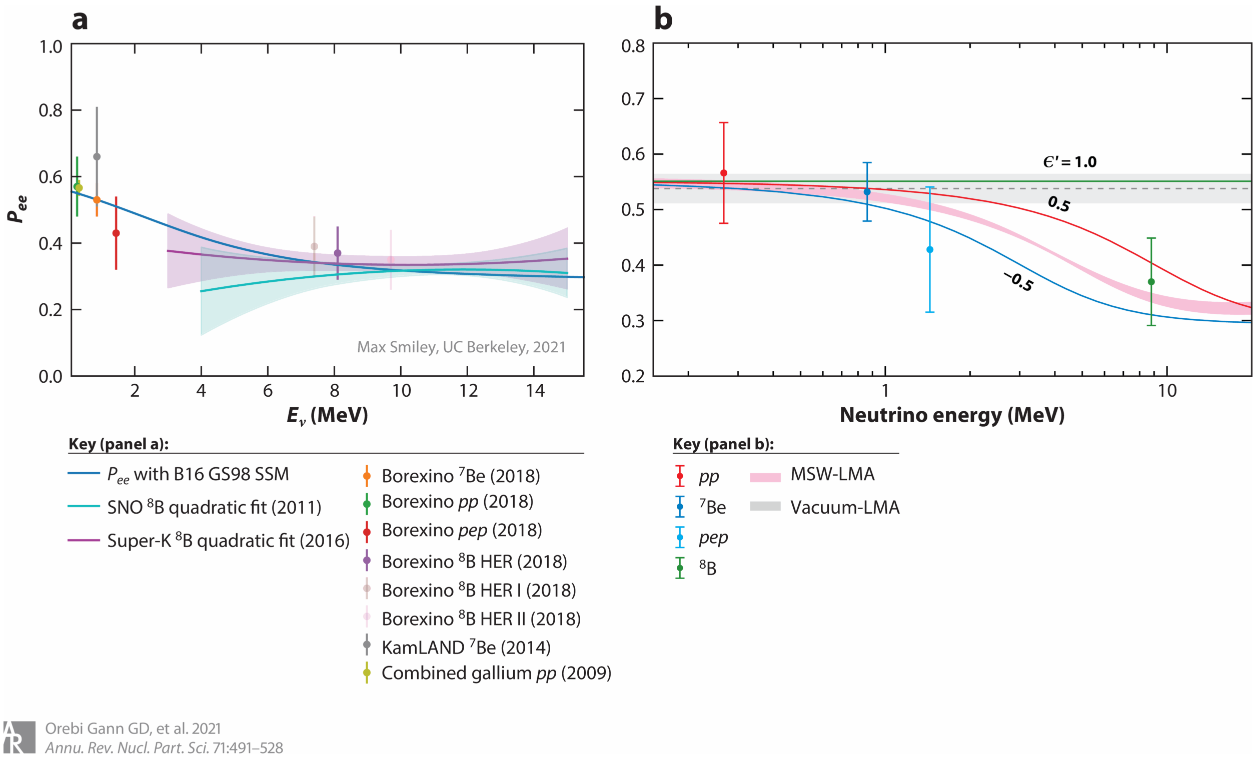

Figure 2.4: On the left in panel **a**, the survival probability P_{ee} as a function of neutrino energy E_ν in MeV, comparing measurements from a variety of solar neutrino experiments and calculation with the B16 GS98 SSM. On the right in panel **b**, a similar figure on a logarithmic scale on the energy axis, which shows the effect of non-standard interaction terms modifying the survival probability as function of the strength parameterized by ϵ'. Figure reproduced from [43]

Chapter 3

Principles of Optical Neutrino Detection

Now that we have explored the physics of neutrino interactions in Chapter 2, we turn our attention to discussion of how neutrinos are detected in practice. With the information collected using these detection techniques, one can work to confirm whether proposed physical models hold, or should be rejected. Several detection methods have been staples in previous eras such as the radiochemical techniques used in Homestake [60] and the Gallium experiments [61, 86]. Others have emerged to the forefront in the past few years such as noble liquid time projection chambers [87, 88], as employed first with ICARUS [89], more recently with MicroBooNE [90] and in the future with DUNE [91] among others. Not all detectors employ a liquid-phase target [92, 93] and some rely on division of sensitive area into smaller cells rather than maintaining a contiguous volume [94, 95] but that being said, the use of liquid-based large-volume unsegmented optical photon-based neutrino detectors has been a common thread throughout the history of neutrino detection. That through line spans from the days of Savannah River on to Super-Kamiokande and SNO and continues into the future, with currently constructing JUNO [34] and Hyper-Kamiokande [35], and next-generation concepts like THEIA [1] and JNE [83]. This chapter will focus on exploring the topic of optical photon detection for neutrino physics, with a strong focus towards detectors with these attributes though, in principle, many of the same concepts apply to solid-state, small-volume, or segmented detectors, where the goal is to detect optical photons.

3.1 Optical Radiation Detection in the Context of Neutrinos

In the simplest sense, there are three stages to all optical radiation detectors. The first of these is the production of the light itself, through various electromagnetic, atomic, and molecular processes depending on the material. As we are concerned with the optical part of the light spectrum, the targeted photons are produced between roughly 200 nm on the blue end and 800 nm on the red end in wavelength. The second step is the propagation of the produced light through the medium to wherever the active detectors may be. While typically propagation effects can be ignored on small scales due to small path lengths (assuming relative optical clarity for materials), in large-volume detectors path lengths can be on the scale of 1 m to 10 m, meaning that the effect of absorption and scattering can be significant. Finally, that light must be detected by light-sensitive detectors, typically photomultiplier tubes (PMTs), which as their name suggests amplify the signal produced by single photons to provide a detectable signal to be analyzed. Historically, these sorts of detectors are categorized as either water Cherenkov detectors, such as Super-Kamiokande and SNO, or liquid scintillator detectors, such as KamLAND and SNO+. As will be discussed in Chapter 7, in recent years, a significant focus has been put on bridging the divide.

3.1.1 Light Production

Because photons are the carriers of information in optical detectors, increasing the amount of light produced per unit of energy deposition in a material is fundamental. No amount of increased efficiency at later steps of the process can supply information on photons that are not there in the first place. As such, it is generally desirable to employ materials that produce large amounts of light when subject to particle interactions.

Now, it is reasonable to ask the question: “How do neutrinos produce light at all if they are only subject to the weak interaction, and not the electromagnetic interaction?”. Of course, the answer is that neutrinos may interact with other particles that are weakly charged, and *those* particles may produce light via electromagnetic interactions. In this way, all detection of neutrinos in optical detectors is done in an indirect fashion:

1. Neutrinos scatter or absorb on electrons or nucleons/nuclei in the target material of the detector;
2. Those electrons or nucleons/nuclei induce the production of photons in the target;
3. Those photons are detected in photodetectors viewing the target.

In fact, step two above may consist of many, many constituent sub-steps with many secondary particles produced, and in turn producing photons, that are then incident on the photodetectors.

While many processes emit photons, the Cherenkov and scintillation emission pathways are the two most responsible for the light observed in optical neutrino detectors. A brief discussion of the two mechanisms follows, and the key characteristics are summarized in Tab. 3.1. As a note, while almost always scintillation detectors will have the capacity for Cherenkov light production, the converse is not true, for reasons explored below.

3.1.1.1 Cherenkov Radiation

The Cherenkov effect is a process that occurs when a charged particle traverses a dielectric medium at a speed $v > c/n$, where c is the speed of light in vacuum and n is the index of refraction of the medium [20]. While the eponymous Cherenkov first detected this phenomenon [96], Frank and Tamm were the first to comprehensively describe this process [97]. The emission of light is caused by the relaxation of the dipoles induced by the traveling particle along its path, resulting in a characteristic emission angle

$$\cos\theta_c = \frac{1}{n\beta} \tag{3.1}$$

This characteristic angle results in conical emission patterns, which can be used to topologically identify light produced by highly relativistic particles crossing the material, i.e. this pattern is very suitable for use in detection of particle interactions. As an electromagnetic process, the relaxation of the dipoles is also essentially immediate, meaning that the light is produced very promptly.

Importantly, the energy/photon output is also easily described analytically by:

$$\frac{d^2N}{d\lambda dx} = \frac{2\pi\alpha z^2}{\lambda^2}(1 - \frac{1}{\beta^2 n^2(\lambda)}), \tag{3.2}$$

which is the number of photons output per unit wavelength, $d\lambda$, per unit length of travel, dx, for a particle of charge z. We note that the index of refraction is wavelength dependent, and that typically the $\propto \frac{1}{\lambda^2}$ leading dependence results in a wavelength spectrum that is peaked at the blue end and dips at longer wavelengths.

However, while the predictable emission topology, wavelength spectrum and production amount make the Cherenkov light an attractive avenue to leverage for studying particle physics, it is not without its drawbacks. Firstly, particles must be charged in order to produce Cherenkov radiation, as no dipoles can be induced otherwise. This means, for example, one cannot detect a neutron or neutral kaons moving through a detector solely through direct Cherenkov emission. Secondly, because particles must be relativistic in order to activate the Cherenkov effect, there is a mass-dependent energy threshold specific to each material, under which no light will be emitted. In other words, inspecting eq. (3.2) to see where it goes negative, $\beta_{\text{thresh}} = \frac{1}{n}$, and so:

$$E_{\text{thresh}} = \gamma_{\text{thresh}} m = \frac{m}{\sqrt{1 - \frac{1}{n^2}}}. \tag{3.3}$$

Since many common materials have an index of refraction around 1.2 to 1.5 at optical wavelengths, we can see that the energy threshold is at least a factor of a few times the rest mass. While achievable through nuclear processes for light particles like electrons, the kinetic contribution for any nucleons or nuclei will never reach these energies through a decay process or MeV-scale neutrino scattering. This also explains why observations of Cherenkov radiation were not initially in air, since $n = 1.0003$. This limitation means that energy deposition by heavier charged particles is typically not visible in the optical range for Cherenkov detectors focused on the MeV-scale.

3.1.1.2 Scintillation Emission

Moving beyond Cherenkov radiation, certain materials also exhibit optical light emission through the process called scintillation. This involves the excitation and/or ionization of electrons from molecules in the material via interaction with a traversing particle. The electrons then de-excite or recombine and in the process emit light in the visible spectrum. The seminal treatment of scintillators is by John Birks in the mid-20th century [98]. While scintillation can occur in a variety of contexts, such as in inorganic crystals, in organic plastics or in noble liquids, this discussion will be oriented towards the context of organic liquid scintillators, which have been widespread in neutrino detection contexts. Similar, but not exactly the same, concepts can be applied to other scintillating materials. These organic liquids are typically aromatics, and may be composed of a mixture that is tuned for desirable properties in terms of total emission, wavelength spectrum, clarity and more.

The energy deposition of particles as they pass through matter, i.e. the energy transfer that will excite/ionize the medium's electrons, is well-known and fairly simply rendered using formulae like the Bethe equation

$$\left\langle -\frac{dE}{dx} \right\rangle = Kz^2 \frac{Z}{A} \frac{1}{\beta^2} \left(\frac{1}{2} \ln \frac{2m_e c^2 \beta^2 \gamma^2 W_{\max}}{I^2} - \beta^2 - \frac{\delta(\beta\gamma)}{2} \right) \tag{3.4}$$

where K is a prefactor composed of various physical constants, z is the charge of the moving particle, Z and A are the atomic number and mass number of the matter, I is the ionization potential of the medium, $W_{\max}$ is a kinetic limit on energy transfer to an electron for heavy particles, and the final term is the "density correction" [20]. While there are numerous corrections for different circumstances, the kinematics are reasonably well-modeled through these formulae. However, once the energy is transferred to the electrons, the process by which those electrons return to the ground state and, in so doing, scintillate is still best modeled empirically.

The primary source of the emission is known to be the π-bonds found in organics, typically in the benzene-like compounds, which can have complex-level structures that lead to a variety of light emission channels. A schematic representation is shown in Fig. 3.1, as reproduced from [20]. Based on whether there is direct excitation or ionization and recombination, these electrons can populate "fast"-decaying singlet states or "slow"-decaying triplet states that determine the timing properties of the emission, which are typically found to be best modeled using an effective exponential model. Overall, the decays from any of these states occur on longer time scales than the Cherenkov emission. Because of the varied charge, mass, stopping power, and other particle-dependent properties, the tendency to excite to different proportions of states will subtly alter the emission time profile, opening up the possibility to differentiate types of particles based on the scintillation they produce [20].

Additionally, because scintillation deals with transitions between discrete energy states in comparison to Cherenkov radiation, the wavelengths of emissions are relatively combined

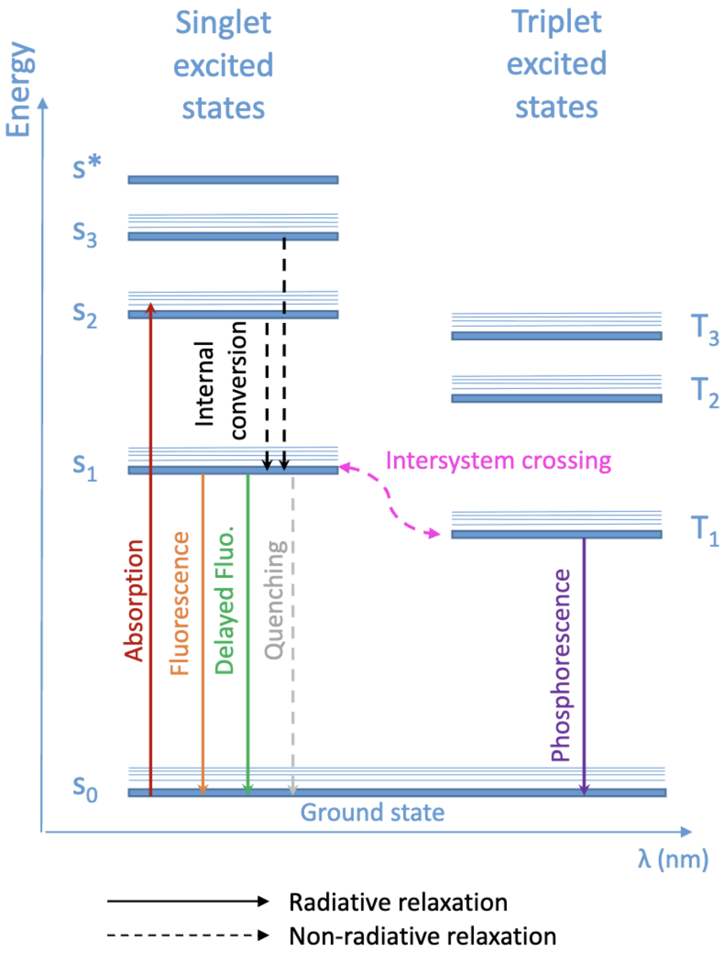

Figure 3.1: A schematic representation of the level diagram of a scintillator, featuring a multi-level system with singlet and triplet states. The fluorescence and delayed fluorescence process represent the "fast" and "slow" emission components depending on accessed levels, while the quenching process represents the non-radiative relaxation that occurs in scintillators without emission of optical photons. Inter-system crossing of energy from singlet to triplet states as depicted here results in delayed emission as phosphorescence due to the forbidden spin state transition to the singlet ground state from a triplet state, though energy may also transfer to a separate fluor compound, which is scintillating in its own right through its own additional level structure. Figure is reproduced from [20].

into a narrow band, which can be also be tuned depending on various dopants. There is also no preferred direction in the excitation and deexcitation involved for scintillation, so the emission is isotropically distributed (though particles traveling a cognizable distance will potentially cause a discernible aniosotropy to be induced).

The number of photons produced by scintillators per unit energy input, or the "light yield" as it is typically referred to, is usually substantially in excess of what is produced for Cherenkov emission, meaning that scintillators are exceptionally effective when used to perform calorimtery. Because the energy required to produce optical photons is on the order of 1 eV to 10 eV, the molecular excitations need only be of this order as well, meaning that any ionizing particle with any appreciable kinetic energy will be able to produce a scintillation output. In other words, scintillation emission, unlike Cherenkov radiation, has effectively no threshold. The other factor in the total emission is the phenomenon known as "quenching", where, as with the emission spectrum, the total light output can vary depending on particle type due to differences in how the different particles excite the molecular electrons. Several models exist to empirically reproduce this observed effect, but the predominant one is known as Birks' Law, and is given by

$$\frac{dL}{dx} = S\frac{\frac{dE}{dx}}{1 + k_{\text{Birks}}\frac{dE}{dX}} \tag{3.5}$$

where $\frac{dL}{dx}$ is the number of scintillation photons produced per unit length, S is the "scintillation efficiency" which can be thought of as the particle-independent light yield, $\frac{dE}{dx}$ is the energy deposition per unit length, and k_{Birks} is a particle-dependent constant. Typically, heavier and more charged species exhibit more drastic quenching effects, whereas Birks' Law can be effectively ignored in many media for electrons.

The scintillation properties of the primary compound may also be modified, such as to change the emission wavelength spectrum, boost the light yield or alter the timing using the addition of secondary and tertiary fluorophore compounds, or "fluors".

Table 3.1: Comparison of the properties of Cherenkov and scintillation emission.

Property	Cherenkov	Scintillation
Light Yield	Low (10s-100s per MeV)	High (1000s to 10000s per MeV)
Timing	Instantaneous	Slow (1 ns to 10 ns decay times or longer)
Emission Wavelength	Wideband over visible range	Confined
Threshold	Mass-dependent threshold	Effectively threshold-less
Topology	Characteristic cone	Isotropic

3.1.2 Light Propagation

In large-scale detectors, once light is produced, it will have a macroscopic path to travel before any photons can be detected. This presents the opportunity for effects to crop up over the course of that journey that hinder the collection of accurate information about the particle interaction, as the entrance of propagation effects can mask or blur information. As a general maxim, the longer the path from the point of photon creation to the point of photon detection, the more likely it is for a detected photon to have suffered from a propagation effect, and not be detected "directly". These effects primarily fall into three categories: absorption, scattering and reflection/transmission effects. Significant effort is put into understanding these effects, especially for liquid scintillator detectors where optics for particular cocktails are relatively unknown compared to, say, water [99–109]. This work is necessary as it is essentially impossible to properly model an experiment of substantial size without accounting for these effects, and they are both material-dependent and time-varying.

The first, and potentially the most dangerous, property to discuss is absorption. Just as molecules can emit photons of particular energies after excitation, they can also absorb photons. The probability of absorption is therefore dependent on wavelength, and at a given wavelength the probability will be exponentially dependent on the distance traveled, i.e. $\propto e^{-\frac{x}{l_{\text{abs}}}}$ where x is the path length and l_{abs} is the characteristic length scale, or absorption length. An example of measured absorption length of ultrapure water in SNO+ is shown in Fig. 3.2, and is found to be on the scale of 200 m from 300 nm to 450 nm before sharply dropping to around 40 m at 500 nm. Many of the photons that are absorbed will be converted into non-optical modes, meaning that the light is lost to the detector. As such, absorption serves to reduce the effective light yield that a detector can detect, meaning that the placement of any photodetectors should be optimized in order to preclude significant losses due to absorption. However, not all materials will simply absorb the photons and end the story there. In particular, because in scintillator much of the light absorbed comes directly from molecular excitations of the same molecules, the absorbed photons will be "re-emitted" with some probability as one or more photons at the same or longer wavelengths (conserving energy). This causes a smearing of the observed wavelength spectrum and timing, as the "re-emitted" photons will be redder and arrive at any photodetectors at later times than the "direct" scintillation counterparts. While a complication, the ability to preserve some information is a consolation.

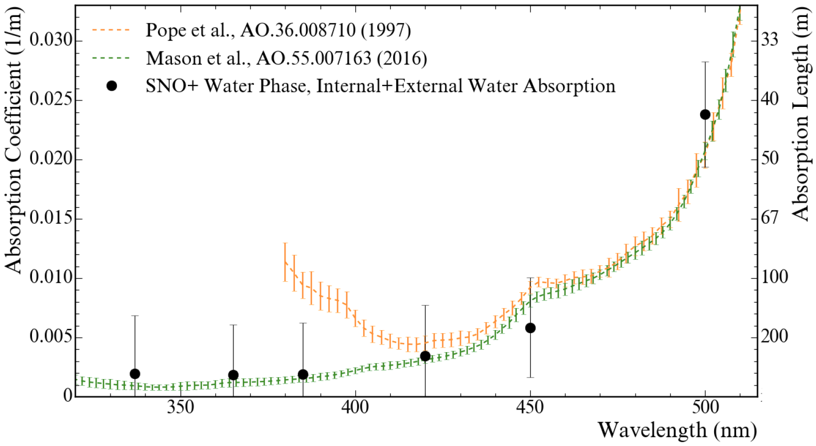

Figure 3.2: The absorption length of ultrapure water in SNO+, as measured at several wavelengths, in comparison to reference values. Figure is reproduced from [101].

The second optical effect to explain is scattering. This is the process by which a photon will be redirected (and, in certain cases, changed in energy) upon interacting with electrically charged matter along its path. Generally, materials in optical detectors are modeled as subjecting traversing light to Rayleigh scattering [110], though this is an idealization given limitations of the Rayleigh paradigm and the presence of other regimes like Mie scattering. Nevertheless, regardless of the mechanism, the effect of the scattering process is to complicate the picture by removing information about the origin point of a photon. While this is not a showstopper in the sense that scattered photons may still be detected, the value of photons "pointing" in a particular direction (as is useful for Cherenkov emission) is diluted with a rise in scattering. The scattering process is also wavelength-dependent (principally $\propto \frac{1}{\lambda^4}$, famously the source of our blue sky) and is associated with a similar characteristic length l_{scat} as to absorption. As such, similar to absorption, it is desirable to have media with long scattering lengths across a broad wavelength range, and to place photodetectors close enough to the detector medium to avoid significant loss of directional information from scattering.

The last optical effect to consider is from the refractive index of materials and associated effects related to transmission across boundaries (e.g. refraction and reflection). While common materials like water have tabulated references for their refractive index [111], scintillators and other materials must be measured [109]. The refraction of light across boundaries obviously obscures the directional information content for detected photons, but a greater issue arises from losses due to reflection at a boundary, total internal reflection or otherwise. These reflections can cause large distortions in the distribution of observed photon detections as a function of time, and also lead to increased path lengths, meaning that the effect of absorption and scattering is also enhanced. This leads to a strong impetus to well-match the refractive indices of the detector components, so that light will travel from its production to detection points without significant bending of the trajectory at interfaces and avoiding any strong reflections. Additionally, in order to reduce confusion from reflections off components that photons would not typically interact with on a direct path to a photodetector (e.g. support structures), it is common to make these components optically black to absorb stray photons.

3.1.3 Light Detection

The final step in the process is the actual detection of the light. To date, all large-scale detectors have used large-area photomultiplier tubes (PMTs) several inches in diameter for this purpose, though some modern advancements will be discussed in Chapter 7. The operating principle for these devices is that upon an incident photon striking the photocathode of the tube, a photoelectron will be emitted via the photoelectric effect. The photoelectron is then accelerated by an electric field, hitting several further stages known as dynodes that release more electrons, which exponentially create an observable electric signal that can be analyzed by readout electronics for timing and charge information [20]. This process has several efficiencies associated with it, principally the quantum efficiency, which represents the probability that an incident photon of a given wavelength will produce a photoelectron, and the collection efficiency, which encapsulates effects like the probability that the photoelectron is actually amplified to the final stage and does not get impeded in that process. Quantum efficiencies are typically between 10% and 30%, with newer models pushing toward the higher end. The wavelength-dependence is typically matched to the emission that the PMTs will observe, with peaks around 400 nm being fairly common. Quantum efficiency as a function of wavelength for several instances of the R1408 model from the manufacturer Hamamatsu, as used in SNO, can be found in Fig. 3.3, while the quantum efficiency for the modern R14688 tubes used in Eos are shown in Fig. 3.4.

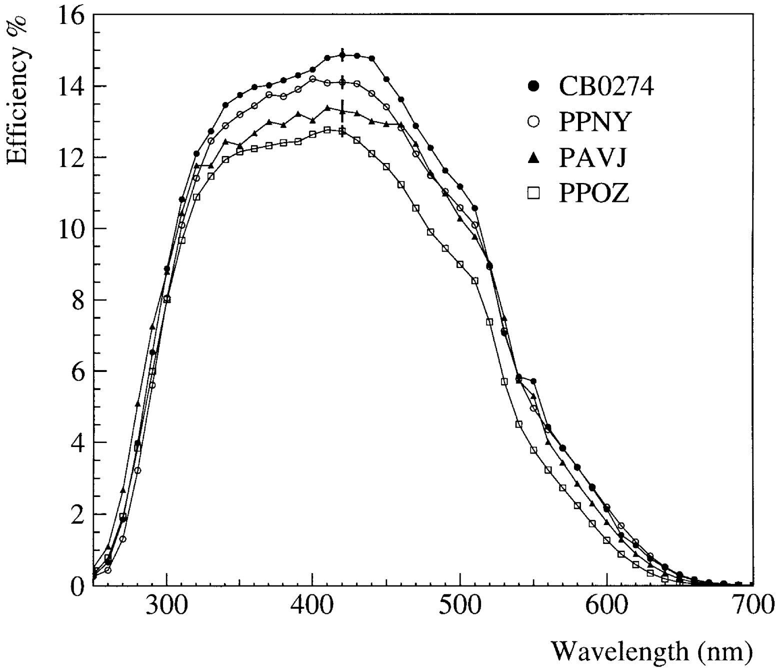

Figure 3.3: Measured quantum efficiencies for four R1408 Hamamatsu PMTs, which are the model used by SNO [112]. Their peak efficiency is located around 425 nm, ranging between 12% to 15% depending on the given tube. The alphanumeric strings represent the serial number for the corresponding measured PMT. Figure is reproduced from [112].

Another critical aspect of PMTs is their time response. Ideally, the signal response is quite fast in order to make multiple incident photons differentiable and imrpove the precision of timing-based reconstruction. However, maintaining a strong, uniform electric field over a large volume is difficult, meaning that the larger PMT models typically have a broader timing response than their smaller cousins. The response over the entire face of the PMT is also typically not uniform, with performance typically peaking at the center and varying with the angle of incidence. Because of this, and to increase light collection in general, some experiments opt to use "concentrators", essentially a set of mirrors, to augment the capability of the PMTs by reflecting more light onto their faces and make up for losses suffered due to drops in efficiency across the face, as well as from photons that are otherwise lost outside of the field of view of the PMTs.

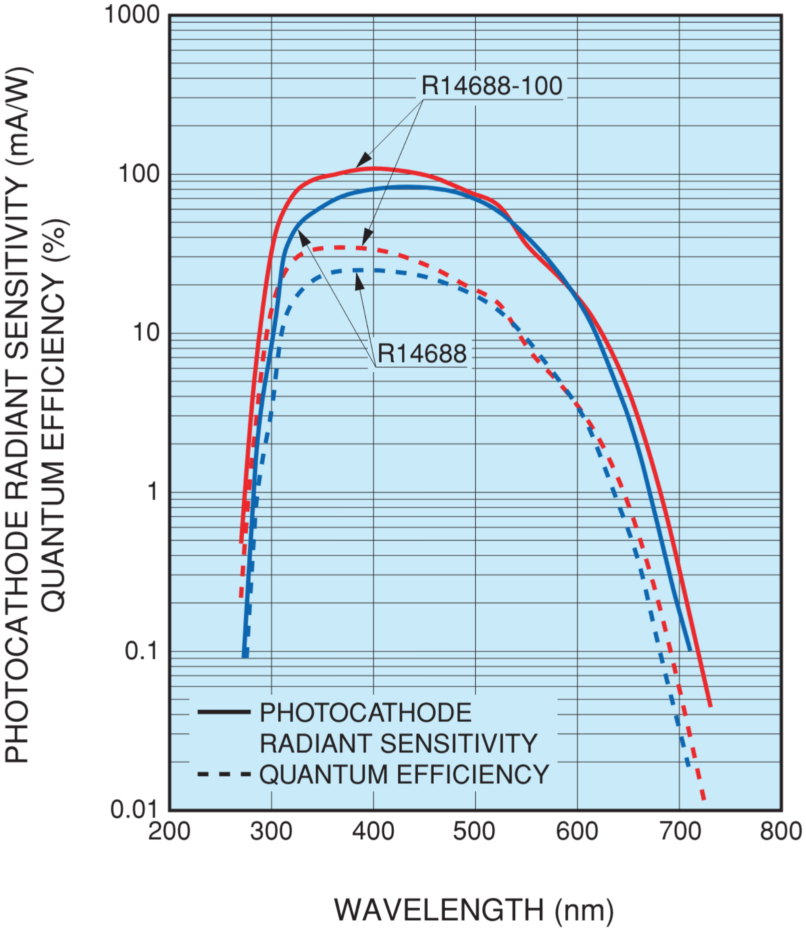

Figure 3.4: Typical quantum efficiencies for the R14688 (blue) and R14688-100 (red) Hamamatsu PMT model in dashed lines, as reported by Hamamatsu on the model datasheet [113] and reproduced here, which are the same model used by Eos [114, 115]. The quantum efficiency of the R14688-100 model is higher overall, achieving over 30% efficiency, with especially good performance at bluer wavelengths. The radiant sensitivity is also shown in solid lines, which is a related quantity that relates the more-easily measurable photocathode current output to the incident light power. The radiant sensitivity is convertible to quantum efficiency at a particular wavelength by multiplying by photon energy in eV.

Additionally, as they operate using strong electric fields, PMTs are vulnerable to the effects of magnetic fields, including the Earth's, which can lessen the efficiency and broaden the timing. As such, some experiments like Daya Bay [116] have used specially developed materials to shield out individual PMTs from magnetic field effects, whereas others like SNO have used Helmholtz coils to compensate the entire detector for geomagnetic effects. Because PMTs suffer from thermal dark noise, detectors, which often submerse PMTs in liquids to optimize optics performance (see Sec. 3.1.2), chill the liquids to below room temperature to minimize this effect and increase the sensitivity to true incident photons. Given the need for robust understanding of PMT response, rigorous study of the gain/charge, timing and noise characteristics, among others, is typically performed before deployment, and sometimes even before full procurement [115, 117–122].

With a distinguishable signal from an incident photon acquired through the amplification of the PMT, experimentalists design a wide array of options to record the output pulses. These stem from simple integrating circuits, to record an integral of a pulse or threshold-hold crossing time, to complex digitization electronics that record waveforms in exceptional detail. The complexity of the readout required is determined by physics needs and costs (as well as the age of the experiment), though in recent years there has been a push to record signals in as much detail as possible to allow for robust reanalysis at the most basic levels. Typically, the data acquisition system (DAQ) will also include an event trigger, which uses some criteria, such as number of PMT signals within a certain period of time, in order to segment the observed signals into discrete events corresponding to presumed particular physics interactions. Triggering algorithms have also become more complex with the march of progress of computing power and electronics sophistication, allowing highly configurable conditions suited for specialized searches [123].

3.1.4 Production, Purity and Shielding

Beyond light production, there are a few other considerations worth mentioning. The first of these is the production process for materials, which is closely linked to the question of purity. Secondly, there is the consideration of shielding the experimental setup from outside effects.

Specialized production processes are used for target media, as well as to ensure that the supporting components, like the tank/container materials and PMTs, are free from contaminants [20, 124–131]. For water Cherenkov detectors operating in the MeV-scale regime, removing radioactive contaminants such as radon from the medium is essential to ensure that the background from these radioisotopes does not swamp the signal, leading to robust purification and measurement systems and processes. This is made all the harder considering given liquid water's proficiency as a solvent. Similar purification processes occur for liquid scintillator detectors, which have the added challenge of needing to design and manufacture a scintillator concktail that suits the needs of the experiment, tuning to photodetector sensitivity, light yield constraints and optical clarity, among others. Detector components like the PMT glass and structural steel or aluminum will also be screened to prevent highly radioactive components from being present in the detector [132, 133]. Beyond radioactivity, dust and other macroscopic particulate matter can severely hinder the optical clarity of target media by increasing absorption and scattering, so detectors may often be sited in clean room facility.

Once an experiment is deployed, the effects stemming from the surroundings need to be mitigated. Primarily, the consideration of cosmic rays, and particularly muons, which can produce showers of particles through the detector as well as activate long-lived cosmogenic isotopes. At the surface, this can make searching for rare processes like neutrino interactions prohibitively difficult, which motivates the location of most optical neutrino detectors underground with a significant overburden of rock as a passive shield. Muon flux measurements and calculations, in addition to studies of cosmogenic activation, are critical pieces of information to inform the suitability of a location depending on the physics goals of an experiment [134, 135]. The muon flux at various underground sites is shown in Fig. 3.5. Many detectors also make use of an active veto region exterior to their targets, providing a buffer where muons and high energy gamma rays may interact *before* interacting within the area of interest. Typically these are water-filled, lightly-instrumented regions that ideally are optically separated to prevent intrusion of unwanted light into the target volume. Other forms of backgrounds may also make there way into the detector through less direct means. Often, separation systems such as a cover gas may be used to prevent the ingress of radioactive gases like radon from external locations. There may also be outgassing or leaching from components that are in direct contact with the liquid media.

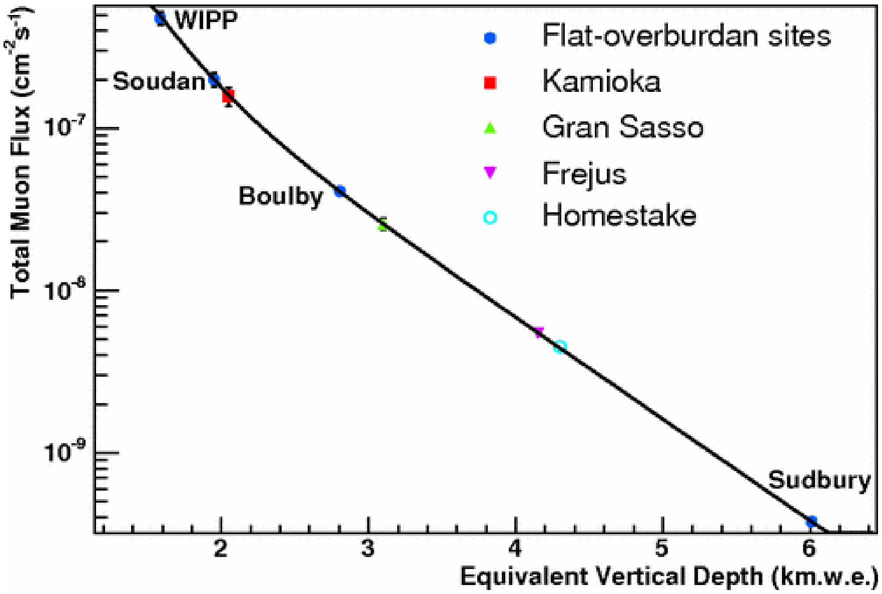

Figure 3.5: The total muon flux as measured at various laboratories, as a function of the overburden in kilometers water equivalent (km.w.e.), as reproduced here from [134]. Kamioka, home to Super-Kamiokande and KamLAND is relatively shallow and muon-rich, whereas Sudbury, home to SNO and SNO+ is very deep and benefits from significant suppression of the muon flux relative to the surface.

Finally, some consideration must also be given to shielding to maintain stable temperatures. Because scintillators have been to found to have noticeably varied performance with temperature [136] and controlled temperatures can avoid biological growth and convection of backgrounds that would otherwise be confined to specific locations [137, 138], much work goes into ensuring that the temperature profile is known and appropriate to experimental needs. This is along with the previously mentioned temperature considerations related to

PMTs, and often goes along with the need for a veto region, as the larger, exterior buffer volume can be used to cool the potentially isolated inner regions.

3.1.5 Designing an Optical Detector

With the above considerations, we can see how optical detectors take the forms that they do. First, in order to observe weakly-interacting neutrinos, do so in sufficient number to be able to make a statistical claim and do so on a time scale compatible with human life, detectors must be appreciably large. Given limitations in engineering and funding, up to today, this has meant mostly building at or around the kiloton scale, with SuperK being the prime example at the multi-kiloton scale, with future experiments JUNO (20 kt) and HyperK (250 kt) to finish construction and produce results before the end of the decade. As discussed, detectors must also be isolated as best as possible from the outside world, leading to placements in deep underground laboratories to mitigate the effect of cosmics, sourcing of radiopure materials to build the detector with and devising of complex control systems to ensure liquid stability and purity. Otherwise, a surface level optical detector could be swamped with cosmic ray induced backgrounds or detector components could produce so much radioactivity from contamination that any measurement of the signal of interest would be impossible. Since these interactions emit very little light in general (after all, a simple digital camera does not suffice), it is desirable to have an ample amount of photodetectors viewing the target volume. While 100% coverage is not practical for a host of reasons, experiments typically strive to instrument as much of the solid angle phase space as possible to avoid missing crucial information.

These are general considerations that apply for optical detectors no matter whether they fall into the water Cherenkov category or the liquid scintillator category. How then to choose which avenue to pursue? Water Cherenkov detectors have the benefit of scalability over scintillator detectors, given the abundance of water, well-known optical properties and clarity, safe handling characteristics compared to the high cost of manufacturing bespoke chemical products, complex, often understudied and difficult to measure emission and absorption, and flammability and toxicity risks associated with oils.

On the more physics-motivated side, considerations depend on which event observables (e.g. vertex position, time, energy, direction, particle type) are to be studied and how well they need to be known. Any physics search requiring exquisite vertex and energy resolution will likely require use of liquid scintillator, given that these detectors are subject to the mercy of Poisson statistics and scintillators can produce vastly more light. There is of course some tradeoff, since the sharper timing and the conical shape of Cherenkov can also provide an anchor point for improved vertex reconstruction. Meanwhile, if the direction of particle travel is valuable (for example in observing the correlation with solar direction), the Cherenkov cone's presence compared to the isotropic pattern of scintillator may trump other considerations. Depending on the analysis, the threshold of Cherenkov detectors can also serve as a blessing, by avoiding backgrounds from low energy, high mass particles like αs, or a curse, by losing the information that can be gleaned from them. In contrast, scintillation detectors have been demonstrated to have robust particle identification potential at low energies. This ability is limited to high energy for Cherenkov detectors, where the patterns of the ring or rings provide glimpses into the constituent particles of an interaction.

3.2 Select Historic Large-Scale Optical Detectors

While a variety of optical detectors at different scales have been used to detect neutrinos, the focus of this section will be on the subset of large-volume, unsegmented, liquid-based detectors that have predominantly been used for MeV-scale detection. Other neutrino detectors of interest that may not be covered by this section that have conceptual similarities are segmented scintillation calorimeter detectors like MINOS [139] and NoVA [140], extremely-large-volume detectors like IceCube [92] and KM3Net [141] (with IceCube being solid state),and a variety of smaller-scale segmented experiments mainly focused on near-field nuclear reactor observation [94, 142] as well as a host of benchtop and lab-scale setups at institutions around the globe to support these larger efforts.

3.2.1 Early Examples: Savannah River, KamiokaNDE and IMB

While not actually unsegmented in a sense, the earliest detector of neutrinos, deployed by Cowan and Reines at Savannah River in 1956 [8] falls into this category. The operating principle was based on the inverse beta decay (IBD) reaction of the electron antineutrinos on protons:

$$\bar{\nu}_e + p \rightarrow n + e^+$$

Cowan and Reines devised the experiment by using a layered setup of three liquid scintillator filled PMT-instrumented volumes sandwiching two water-filled chambers. The water-filled targets additionally had the salt cadmium chloride dissolved inside. Upon an IBD interaction in the water, the positron annihilates causing back-to-back emission of gamma rays, detected in the two opposite layers of the scintillator tanks. Due to the high neutron absorption cross section of the dissolved cadmium, there was also a delayed gamma ray signal that was detected in the scintillator volume some time after the prompt gamma ray detection. This use of a delayed coincidence signal has been replicated many, many times in subsequent neutrino experiments, as it provides a very powerful background reduction tool.

In the 1980s, the scale of optical neutrino experiments began to steadily grow, including the Irvine-Michigan-Brookhaven (IMB) [143] and Kamioka Nucleon Decay Experiment (KamiokaNDE) [75, 76, 144] experiments. IMB ran from 1982-1991, in three stages, and KamiokaNDE ran from 1983-1995, also in three stages. As KamiokaNDE's name suggests, these detectors were primarily designed to search for nucleon decays, but as interest began to grow in resolving the SNP, the focus on neutrino detection grew. KamiokaNDE consisted of about 2 kilotons of water instrumented by roughly 1000 20-inch PMTs arranged in a cylindrical shape located in Kamioka, Japan. IMB was a rectangular prism filled with about 7 kilotons of water viewed by over 2000 PMTs located in Ohio, USA. Both detectors were water Cherenkov detectors and made observations of solar and atmospheric neutrinos, as well as the supernova neutrinos from supernova 1987A, the only supernova from which neutrinos have been detected [145, 146]. These experiments laid the groundwork for the technology that continues pushing the bounds of neutrino physics even today.

3.2.2 Building Bigger: Super-Kamiokande

The evolution of KamiokaNDE came in the form of Super-Kamiokande, which was again located in Kamioka, Japan, but raised the stakes to the 50-kiloton scale and over 10000 20-inch PMTs, while still a water Cherenkov detector in cylindrical form. Super-KamiokaNDE began operation in 1996 and has operated in a variety of phases up to the present day, with the latest being a gadolinium-loaded phase to enhance the capacity to detect neutrons geared towards tagging neutrons from atmospheric neutrino interactions and searching for astrophysical events [147, 148]. The choice of gadolinium was used due to the high neutron capture cross section, as well as the appreciable kinetic energy of the de-excitation gammas. Like its predecessor, SuperK has focused on measurements of atmospheric neutrinos [24, 149], solar neutrinos [62, 150] and nucleon decay [151, 152]. Super-Kamiokande has also served as the far detector for the accelerator-based K2K [153] and T2K [154] experiments, which have sought to measure neutrino oscillation parameters using neutrino beams.

3.2.3 Triple Threat: Sudbury Neutrino Observatory

As discussed earlier, SNO operated as a heavy water Cherenkov detector from 1999 to 2006, detecting solar neutrinos via the three distinct channels [79]. As with its predecessors, SNO involved an approach with several phases: the first operating as a pure heavy water detector; the second operating with dissolved sodium chloride to access a chlorine gamma cascade upon neutron capture; and the last operating with ^{3}He proportional counters to detect neutrons. These phases served as important cross checks of the detected normalization for the NC interaction of the solar neutrinos on the deuteron, which underpinned the entire experiment. SNO operated with a spherical target volume housed in a 6 m-radius acrylic vessel (AV), with an inner capacity of 1 kiloton of heavy water. While smaller than SuperK, the photocoverage was fairly high, with roughly 9500 8-inch PMTs and associated light concentrators providing an effective coverage of 54%. While the primary physics aims for SNO were to engage in precision measurement of the solar neutrino flux as discussed in Sec. 2.3.2 and it subsequently made measurements of the solar mixing angle, mass splitting and survival probability features [63], it was also able to detect atmospheric neutrinos and other physics topics[155–157].

3.2.4 Anomalous Antineutrinos: LSND and MiniBooNE

The first large-scale scintillator detectors for neutrino physics, the aptly-named Liquid Scintillator Neutrino Detector (LSND) [158, 159] and its spiritual successor MiniBooNE [160–162], still focused quite heavily on using Cherenkov light, as their deployed scintillator was low-light-yield mineral oil (with a fluor in the case of LSND). LSND was a rectangular prism containing 167 tons of scintillator, instrumented by 1220 8-inch PMTs, giving close to 25% coverage. The experiment was located in the beamline at the Los Alamos Meson Physics Facility in Los Alamos, New Mexico, United States and operated from 1993 to 1999. The intent was to use the neutrino flavor components from the beam, stemming from muon decay at rest and pion decay in flight, though the results found an excess of $\bar{\nu}_e$ in the $\bar{\nu}_\mu$ beam that was incompatible with the oscillation parameters favored by other experiments. MiniBooNE was a similar mineral oil experiment constructed at Fermilab outside Chicago, Illinois, United States, in order to follow up on these results. The experiment was located in the Booster Neutrino Beam with an 800-ton sphere of mineral oil viewed by nearly 1300 8-inch PMTs and operated from 2002-2019. While constructed in order to address the questions raised by LSND, MiniBooNE came to similar conclusions, and the so-called short baseline anomaly is being targeted by the SBN program to definitively determine whether the anomaly is due to mismodeling or physical sterile neutrinos [163].

3.2.5 Observing Oscillations: KamLAND

Meanwhile, in Japan, in the old KamiokaNDE cavern right next door to SuperK, the Kamioka Liquid Scintillator Antineutrino Deetctor (KamLAND), began taking data in 2002 [164]. KamLAND was designed to take advantage of the infrastructure to make detections of antineutrinos from the many distant nuclear reactors of Japan, in order to measure the antineutrino spectrum, and observe the oscillation pattern. The experimental design enabling this was the usage of 1 kiloton of high light-yield scintillator mixture dodedcane, pseudocumene (PC) and 2,5-diphenyloxazole (PPO) suspended in a $13 - $m-diamter nylon balloon, viewed by nearly 2000 PMTs, a mixture of 17-inch and 20-inch models. Leveraging the IBD delayed coincidence technique, KamLAND was able to favorably identify the LMA parameter space with less than a years worth of data. KamLAND has also made a groundbreaking steps in providing evidence for the detection of geoneutrinos, the antineutrinos produced by nuclear decays in the Earth's mantle [165], and solar neutrino measurements [64, 65]. KamLAND has since transitioned to the neutrinoless double-beta decay focused KamLAND-Zen [166] experiment, which suspends Xe-doped liquid scintillator within the main target volume.

3.2.6 Solar Sailor: Borexino

Of particular interest for this work, Borexino [167] was a pioneering liquid scintillator detector that operated from 2007 to 2021, with the primary goal of studying solar neutrinos [66, 69], situated in Gran Sasso National Laboratory in Italy. Borexino was filled with 200 tons of pseudocumene (PC) loaded with 2,5-diphenyloxazole (PPO) in its main target, and dimethylphthalate (DMP) in its buffer regions. This PC-PPO admixture had a very high light yield, on the order of 10000 photons per MeV of energy deposited, which allowed for precision energy measurements. While spherical, instead of using an acrylic vessel like SNO, the inner volume was contained by a nylon vessel similar to KamLAND. Borexino used over 2000 8-inch PMTs to survey its volume. Borexino was able to perform robust spectroscopy of the solar neutrino fluxes, with the first real-time detections of the ^{7}Be and *pep* fluxes [66] and the previously mentioned detection of the CNO flux that confirmed that that process occurred in the Sun. Borexino also made the first conclusive observations of geoneutrinos, this time in Europe [168].

3.2.7 Reactor Reality: Double Chooz, Daya Bay and RENO

While KamLAND observed the reactor neutrino spectra from far away, several experiments sought to measure from closer by to establish the θ_{13} mixing angle. These include Double Chooz in France [169], Daya Bay in China [170] and RENO in South Korea [171]. The basic concept is the same across the three experiments, employing an array of gadolinium-doped liquid scintillator detectors at differently-situated sites from reactor cores on the kilometer-scale to observe the IBD interactions, and deduce oscillation information from the distortion between the two near and far detector spectra. The gadolinium is used to increase the efficiency of neutron captures to improve the capabilities of the delayed coincidence technique. In the course of their operation, several unexplained features in the observed spectra led to the identification of a Reactor Antineutrino Anomaly (RAA), which upon further experimental and theoretical investigation appears to primarily arise from deficiencies in the model used to predict the spectrum and understanding of reactor core elemental composition rather than new fundamental physics [172].

Chapter 4

The SNO+ Detector

The SNO+ detector is an optical photon-based, large-scale, liquid-phase neutrino experiment that is the successor the Sudbury Neutrino Observatory (SNO) with a focus on MeV-scale physics, joining a generation of detectors including Borexino, Daya Bay and KamLAND Zen. A kiloton-scale experiment, SNO+ aims to make advancements in the hunt for neutrinoless double beta decay ($0\nu\beta\beta$), as well as explore a variety of other neutrino and beyond the Standard Model (BSM) physics topics, including among others reactor antineutrino and geoneutrino detection, supernova neutrino detection, nucleon decay searches, dark matter searches and most importantly for this work, solar neutrino physics. This chapter will explain the goals, infrastructure and operations of SNO+.

4.1 The SNO+ Experiment

Located near Sudbury, Ontario, Canada, SNO+ [173] reuses much of the infrastructure of SNO [79], with several upgrades to modernize the detector electronics and accommodate target media different from heavy water. The development from SNO has enabled the knowledge transfer of lessons learned from that experiment to SNO+ through the participation of collaborators on both projects, with the additional opportunity to build out new capabilities with further generations of scientists and technicians. SNO+ is operated by a multinational team of more than 100 collaborators and additional support staff from nearly 10 countries. While SNO was initially located in a standalone facility, the SNOLAB complex [174] that developed around it is now home to SNO+ and numerous experiments investigating topics from particle physics to seismology to biology. This is all housed in a Class 2000 clean room with an overburden providing 6010 meters water equivalent of shielding that results in amongst the lowest muon rates in an underground lab around the world. A diagram of the facility is shown in Fig. 4.1. The operating plan for SNO+ involves a phased approach using different target media to target different physics signals and constrain backgrounds from phase to phase.

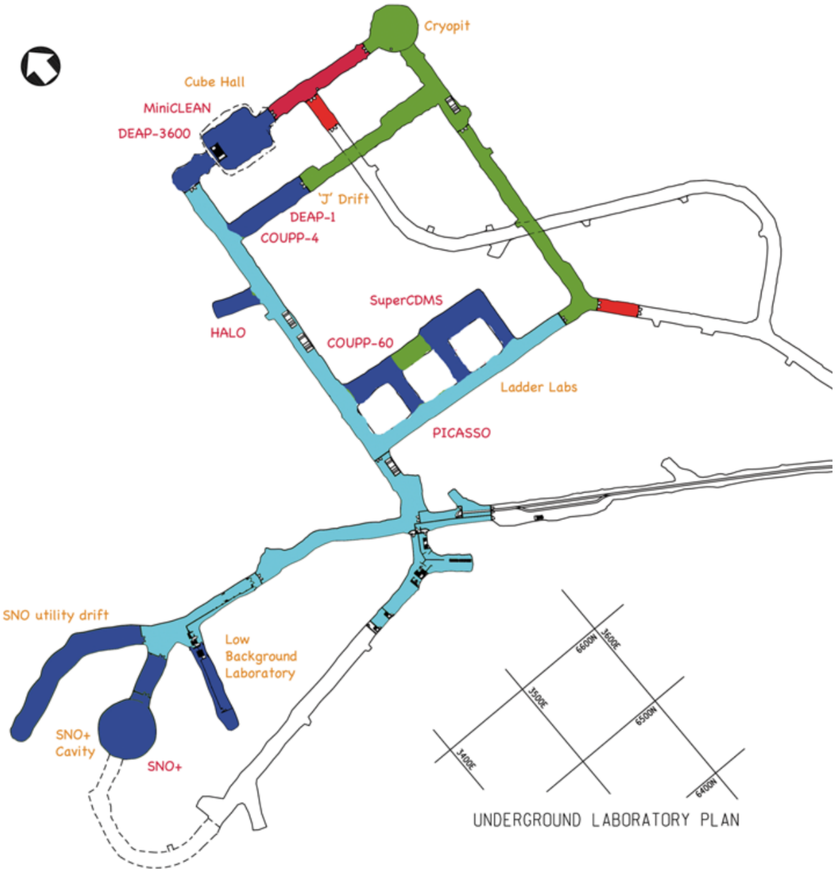

Figure 4.1: The layout of the SNOLAB underground laboratory with the locations of experiments as of 2012, reproduced from [174]. SNO+ is found in the bottom left corner of the figure.

4.1.1 Experimental Goals and Phased Approach

SNO+ is primarily designed as a $0\nu\beta\beta$ experiment using ^{nat}Te-loaded liquid scintillator, searching for one of the most elusive processes in particle physics. In order to best leverage the opportunity presented by the infrastructure in place, SNO+'s operating plan involves 3 primary phases. These are

1. **Water Phase:** SNO ceased data taking data in 2006, with the heavy water being returned to the supplier. Subsequently, the detector infrastructure was unused and empty for several years. The goal of the water phase was to operate the detector as a water Cherenkov detector akin to SNO, but using a target of 1 kt ultrapure water (UPW) instead of heavy water. The purpose of this was twofold. Firstly, background levels from detector components would be more easily studied and able to be constrained for future phases, given the ability to leverage directional information from

the Cherenkov emission. Secondly, as water acts a universal solvent, the target medium would "clean" the disused detector components of contaminants at some level and leave behind a cleaner detector for future phases. A tertiary benefit includes the ability to do additional physics with this dataset, such as examinations of nucleon decay, as will be discussed later in this section. The Water Phase began in May 2017 and lasted until July of 2019, when scintillator filling commenced.

2. **Scintillator Phase:** The energy resolution at the Q-value of the $2\nu\beta\beta$ process required for studying $0\nu\beta\beta$ is much finer than that which can be provided by Cherenkov emission. This, among other reasons, means that one could not simply dump isotope into water as had been done with the NaCl during SNO. Instead, a new liquid scintillator cocktail was developed with exquisite light yield properties and optical clarity, along with loading techniques. Additionally, while the framework from SNO had previously been used for optical photon detection, the setup had never been used to observe scintillation emission. Because the scintillator was both new to the community and to the detector, the Scintillator Phase was designed to calibrate the optical model for the scintillator and the associated detector response, and to evaluate the background levels of the raw liquid in its unloaded state, as inputs to the $0\nu\beta\beta$ investigation. The Scintillator Phase is also geared towards having the added benefit of enabling other MeV-scale neutrino physics topics, such as solar neutrino detection. The detector was completely filled with LAB by May 2021, while the primary fluor PPO was added to its maximal level of $2.2\,\mathrm{g\,L^{-1}}$ by May 2022. The scintillator phase continued for over a year before the addition of more additives in July of 2023, which will be discussed in further detail in Sec. 4.3.

3. **Tellurium Phase:** Finally, the isotope along with additional additives to provide solution stability and clarity of optics will be added in order to conduct the $0\nu\beta\beta$ search. The initial target is for a 0.5% loading of natural tellurium by mass, though other isotopes were explored in the past such as neodymium, and there is great interest in increasing the loading fraction to increase the exposure, as long as long-term stability and transparency at that level of concentration is proven. As will be discussed, a novel process to load the isotope was developed [175] and the scintillator cocktail will be optimized with several additives to ensure stability and optical transparency. This phase of the detector's operation will use the lessons learned and constraints found from the previous phases to focus in on the $0\nu\beta\beta$ measurement, along with other measurements related to the $2\nu\beta\beta$ process. The capacity to do other MeV-scale physics will be limited by the high $2\nu\beta\beta$ rate, though coincidence-based analyses will still be possible such as continued probing of reactor antineutrinos and geoneutrinos using IBD, as will searches with an energy region of interest solidly above the $Q_{\beta\beta}$ of ^{130}Te.

Incidentally, there was also a brief "Air Fill" phase conducted prior to Water Phase in order to commission the new detector electronics, which will be discussed in Sec. 4.4. Additionally, the transition periods between phases are not instantaneous, and give rise to a continuum of smaller phases while the target medium is being changed and optimized.

The most predominant of these for the purposes of this discussion is the so-called "Partial Fill" phase that resulted from a pause in scintillator filling between the Water Phase and Scintillator (or Full Fill) Phase due to the COVID-19 pandemic. When filling commenced prior to this, due to its lower density, pure LAB was added from the top of the detector while water was withdrawn from the bottom so as to not disturb the interface between the two materials and cause mixing. When the pause that enabled the partial fill phase occurred, this left two stratified zones in the detector, with a water volume on the bottom and scintillator on top. This period lasting from March to October of 2020 with the detector approximately half-filled with scintillator and half-filled with water, after which filling resumed. More details about this phase will be provided in Chapter 5. While the Water Phase provided valuable information about the operation and characteristics of the detector and physics results, this chapter will focus on the performance and operation of the detector pertaining to the scintillator-filled periods.

The different detector phases, as mentioned above, lend themselves to different physics aims. For the water phase, as the machinery for analysis in the SNO/SNO+ infrastructure was redeveloped, the main goal was to determine external background rates for use in future physics analyses, but the phase also yielded a plethora of interesting fundamental physics results [67, 176–178] and calibrations [101, 179]. Among these are several leading limits for "invisible" decay modes of protons, neutrons and pairs thereof, by leveraging the high quantity of ^{16}O present in UPW and the impressive depth of SNOLAB to mitigate confounding background signals from muogenic isotopes. These invisible modes do not result in energy deposit directly from decay products and instead can only be observed through de-excitation of nuclei that the decays occur within (^{16}O provides a host of states to transition to with relatively high energy de-excitations). An example of the fit used to recover the lifetime limit for one of the decay modes is shown in Fig. 4.2 and the 90% confidence level (CL) limit for all of the studied decay modes, achieved using the full data set, are shown in Tab. 4.1, as achieved in [177]. Leveraging the water Cherenkov detector's capabilities to pinpoint direction, and the high correlation between ingoing neutrino and outgoing electron directions for neutrino-electron elastic scattering, SNO+ was also able to determine the ^{8}B solar neutrino flux to be $\Phi_{^8\mathrm{B}} = [5.95^{+0.75}_{-0.71}(\mathrm{stat.})^{+0.28}_{-0.30}(\mathrm{syst.})] \times 10^6\ \mathrm{cm}^{-2}\ \mathrm{s}^{-1}$ using 69.2 kt d of exposure during the water fill [67], with a forthcoming update using the full exposure. Chapter 5 will provide an analogous measurement using the scintillator exposure, rather than water. SNO+, due to the achievement of an incredibly low energy threshold (1.4 MeV at the center of the detector) and aided by the rigorous measurement of neutron capture in the detector [179], is also the first unloaded water Cherenkov detector to observe reactor antineutrinos, with 3.5σ evidence [178].

Despite the ability to do groundbreaking physics, the measurement of backgrounds from external-to-target detector components like the PMTs and acrylic vessel was paramount for this phase. By leveraging the directional reconstruction capabilities enabled by the Cherenkov effect, using a judicious set of event selection cuts to hone in on particular backgrounds and combining that with simulation of the detector and modelled backgrounds, SNO+ collaborators were able to measure background rates associated with particular detector regions

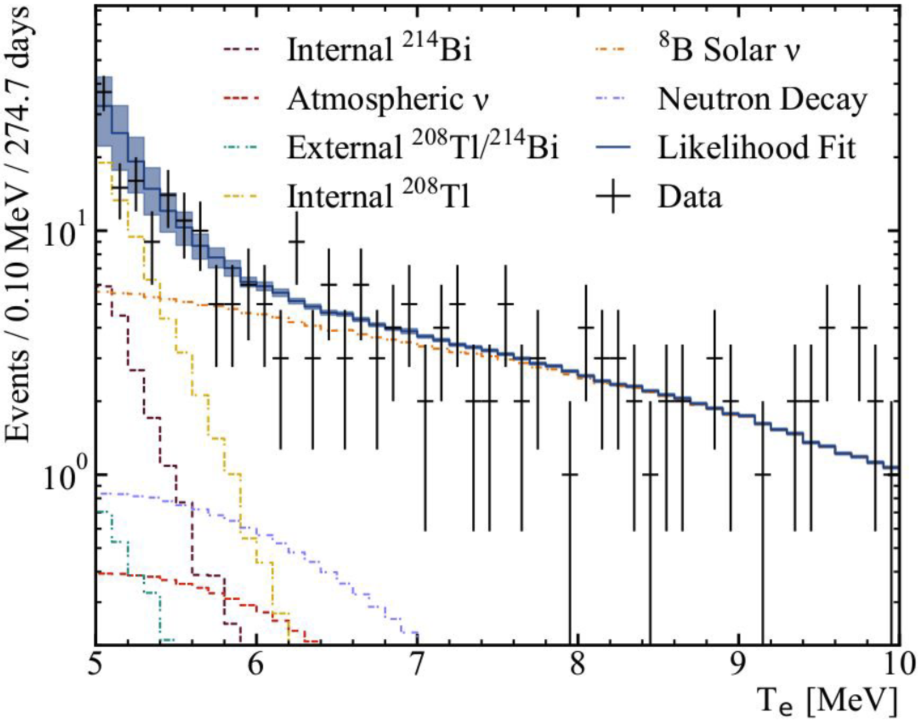

Figure 4.2: The reconstructed energy spectrum and fitted components for the full water phase dataset in the energy region of interest for single neutron decay. The shaded band on the fit represents the total uncertainty on the fit. Figure is reproduced from [177].

Table 4.1: The 90% CL limit in years for the "invisible" decay mode listed, as determined by SNO+ in [177].

Decay Mode	Partial Lifetime Limit
n	9.0×10^{29} y
p	9.6×10^{29} y
pp	1.1×10^{29} y
np	6.0×10^{28} y
nn	1.5×10^{28} y

and components. The observed events can be found in Fig. 4.3, with the computed fractional rates compared to the expected background contributions are found in Tab. 4.2.

While a somewhat unexpected development, the Partial Fill Phase did provide a valuable testbed for understanding and assessing the scintillator optical model and backgrounds and what the detector's capabilities actually were with a scintillator, as well as the opportunity for more physics results. The most promising result achieved was the leveraging of the unique detector configuration and scintillator mixture of LAB with $0.6\,\mathrm{g\,L^{-1}}$ PPO to enable direc-

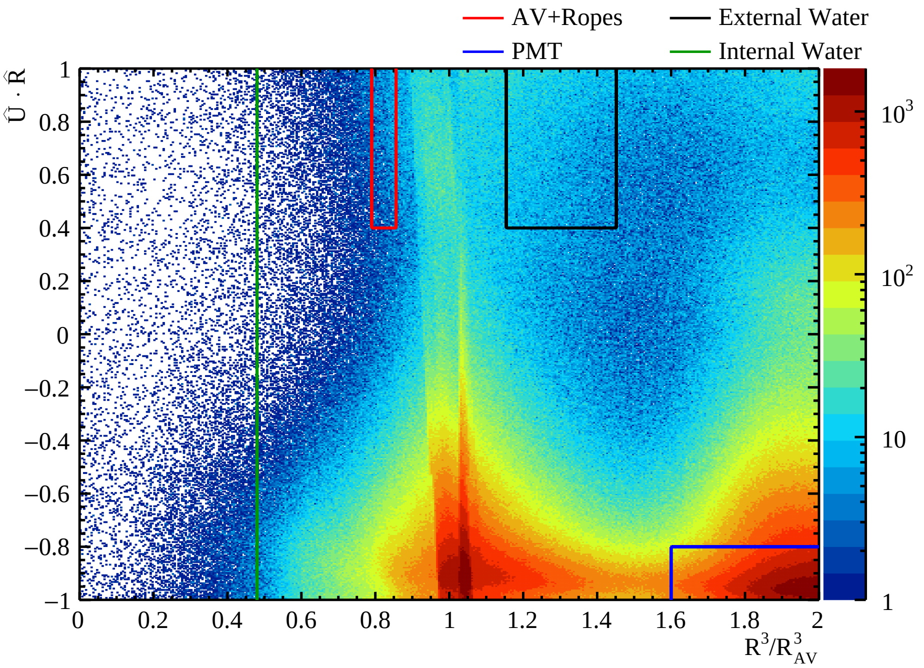

Figure 4.3: The observed spectrum in $\hat{U}\cdot\hat{R}$ and $\frac{R^3}{R^3_{\mathrm{AV}}}$ in the SNO+ detector, subject to additional event selection cuts. $\frac{R^3}{R^3_{\mathrm{AV}}}$ is the reconstructed radial position of an event, normalized by the radius of the acrylic vessel and transformed to respect volume weighting. $\hat{U}\cdot\hat{R}$ is an angular variable defined as the normalized component of the fitted event direction relative to the radial direction, i.e. the cosine of the angle between the event direction and the radial direction. The boxes show regions known to be associated with backgrounds from particular components with high confidence from simulation and other studies, as shown. "AV+Ropes" represents the contribution from the acrylic vessel (AV), and all supporting ropes. "External Water" represents the contribution of the water volume between the acrylic vessel and the photodetectors. "PMT" represents the total contribution from all PMTs. More about the detector geometry will be discussed in Sec. 4.2. Figure is reproduced from [180].

tional detection of solar neutrinos at the event-by-event level for the first time in a scintillator detector [183]. The results of this analysis are shown in Fig. 4.4 and this has a substantial impact for future detector development as will be discussed in Chapter 7. The intrinsic backgrounds in the scintillator were also found to be consistent with requirements needed for the background budget for the $0\nu\beta\beta$ phase [184], and many aspects of the scintillator model such as the timing, light yield and absorption were tuned in support of various analyses by leveraging internal contamination such as BiPo coincidence decays and externally deployed calibration sources. Preliminary investigations of the ^{8}B solar neutrino flux were also made in [184], with an alternative approach discussed in Chapter 5, and a measurement of the

Table 4.2: The determined event rate compared to the nominal expectation for the external backgrounds from the listed detector components. The rate is found by integrating the events within the boxes defined from Fig. 4.3 in data and Monte Carlo, where the Monte Carlo count corresponds with expectation. The first error shown is the statistical error, while the second is the systematic error. The nominal rates were assigned from measurements by SNO [181, 182] for the external water and acrylic bulk or by assay using Germanium detectors at SNOLAB [180] for the ropes and PMT glass.

Background from Detector Component	Rate (Fraction of Nominal)
AV+Ropes	$0.21 \pm 0.009^{+0.64}_{-0.21}$
External Water	$0.44 \pm 0.003^{+0.32}_{-0.27}$
PMTs	$1.48 \pm 0.002^{+1.65}_{-0.60}$

reactor antineutrino flux was also demonstrated in this phase [185], marking the first time a single detector has made antineutrino measurements using substantially different targets.

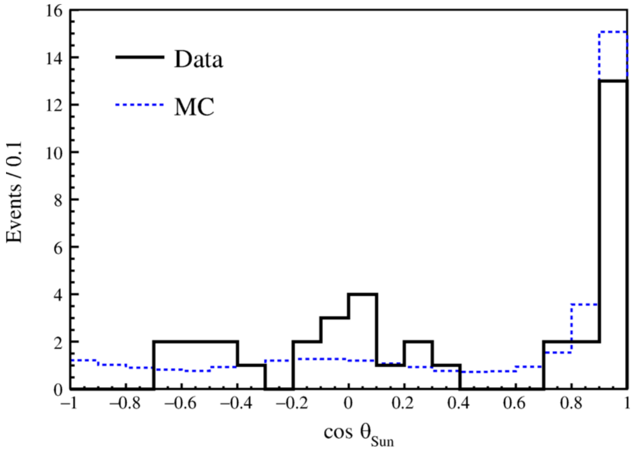

Figure 4.4: The observed spectrum in $\cos\theta_{\mathrm{Sun}}$, the angle between the fitted event direction and the the direction between the Earth and the Sun, for the selected solar neutrino events in the data and Monte Carlo simulation for the partial fill phase, as determined in [183]. In large part due to a pronounced forward peak, a likelihood ratio test comparing to a flat distribution (as expected from isotropic sources) yields a p-value with 5.7σ. Figure is reproduced from [183].

Eventually, when filling of the detector with scintillator completed and the final PPO loading of $2.2\,\mathrm{g\,L^{-1}}$ was reached, a quiescent phase of scintillator datataking began that lasted more than a year from April 2022 to July 2023, when the cocktail was further optimized with an eye towards the isotope loading for $0\nu\beta\beta$. This period marked the “true”, fully-filled Scintillator Phase, and will be the focus of the ^{8}B solar neutrino flux analysis presented in Chapter 5. This period also involved significant contributions to the tuning of the detector model, with investigation into the scattering profile [186] and more tuning and calibration of timing, other optical model parameters and the broader detector response via similar means as the partial fill. Background studies have shown that the levels are still within the acceptable bounds for the $0\nu\beta\beta$ requirements. This phase also provided the opportunity for further antineutrino detection studies as well as a solar oscillation parameter analysis [186], among others.

The physics goal for the Tellurium Phase is unsurprisingly to make a world-leading $0\nu\beta\beta$ measurement that pushes into the inverted hierarchy region. SNO+ is currently exploring a range of loading scenarios to enable a deployment configuration that produces the best possible result. Sensitivity projection and comparison to other experiments with several common nuclear matrix elements (NMEs) for different exposures and percents by mass can be found in Fig. 4.5. The projected sensitivity at the initial targeted loading of 0.5% by mass in 3 years yields a half-life sensitivity of 2×10^{26} years, with well-founded expectation to be able to push to at least 3% by mass for greater sensitivity in the future. This phase will also see continued work in solar neutrino and antineutrino physics.

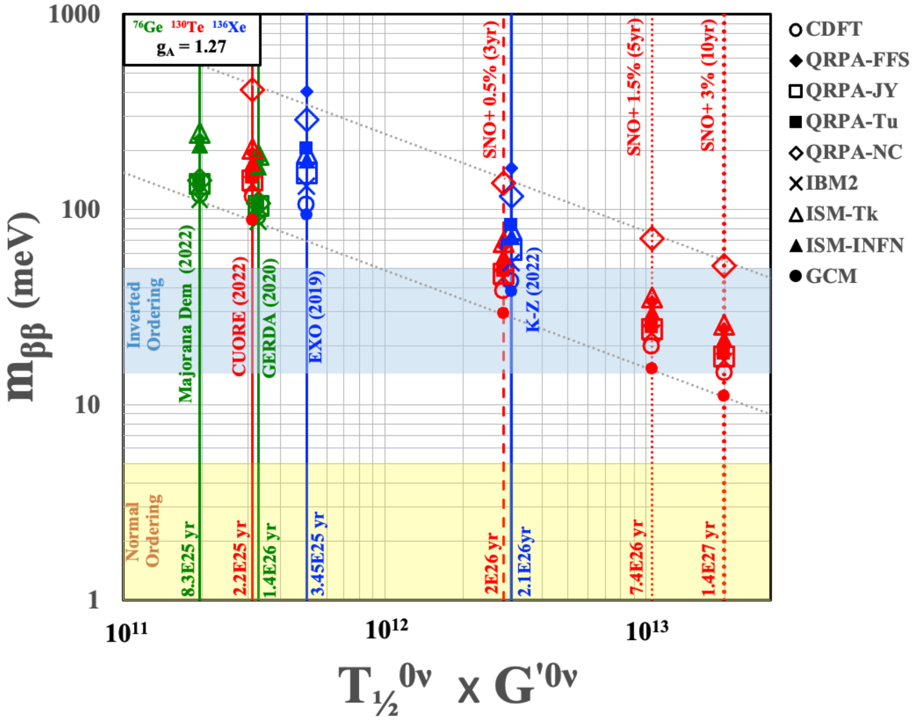

Figure 4.5: The estimated sensitivity of SNO+ for three loading and exposure scenarios, as a function of the calculated half-life and phase space factor, and $m_{\beta\beta}$, for several commonly used NMEs. Comparison is made to results from the Majorana Demonstrator, CUORE, GERDA, EXO and KamLAND-Zen experiments. Even for a modest datataking period and mass loading, sensitivity predictions show decent coverage of the inverted ordering region. Figure is reproduced from [180].

4.2 Detector Geometry and Materials

As discussed above, as the inheritor of SNO, SNO+ resides in the same cavern, and also reuses the PMTs, support structures, acrylic vessel (AV) and many other physical subcomponents. The target-holding spherical acrylic vessel, 12 m diameter, is suspended below an experimental deck and surrounded by a PMT support structure (PSUP) formed in a geodesic sphere 17.8 m in diameter. The PSUP holds the 9362 inward-facing PMTs, the predominant model being the reused-from-SNO Hamatsu R1408, approximately 8.35 m from the center of the AV. The inner PMTs are ringed by light concentrators to enhance photocollection. There are approximately 100 outward looking tubes that observe light between the cavity walls and the PSUP to serve as a veto, with the medium filling the space between the AV and PSUP, and PSUP and cavity, being approximately 7 kt of UPW. There are also two sets of ropes that perform structural roles: the hold-up ropes inherited from SNO that suspend the AV below the deck and the hold-down ropes that are designed to compensate for the buoyant force acquired during the scintillator fill (the SNO+ scintillator is less dense than water). A diagram of the detector can be found in Fig. 4.6. More details about the detector can be found in [173].

4.3 The SNO+ Scintillator

Strictly speaking, there is no one cocktail that can be called the SNO+ scintillator, due to evolving fill conditions and proliferation of additives on the way to the final cocktail for the Tellurium phase. However, the basic cocktail is composed of linear alkyl benzene (LAB) as the solvent with 2,5-diphenyloxazole (PPO) as the fuor, commonly referred to as LAB+PPO. The formulation and characterization of the scintillator is detailed in [127]. While other experiments had used formulations of liquid scintillators that would be otherwise suitable to achieving the physics goals for SNO+, it was desired to utilize a less hazardous and toxic alternative to, for example, pseudocumene, which has had a troubled history with leaks into the surrounding environment [187]. Eventually, on comparison with diversity of solvents, LAB won out with PPO as the fluor given its widespread use in industrial applications, high yield and cost advantages over other fluors. The targeted concentration was for 2.0 g/L, though the concentration during the partial fill was 0.6 g/L and the final concentration ended up at 2.2 g/L. The density determined for the final cocktail is 0.857 g/cm^3 at 20 deg, with the variation with temperature shown in Fig. 4.7. A light yield of nearly 12000 photons per MeV was found for the fully-PPO-loaded cocktail, as shown in Fig. 4.8, and exquisite optical clarity was achieved, better than the baseline pure LAB, as shown in Fig. 4.9. The timing characteristics were determined by measuring the time profiles associated with intrinsic radioactive contaminants and tuning simulation to match. The timing allows for the classification of events by particle type. This will be discussed more in subsequent sections. While the analyses presented in this thesis cover work during the periods of LAB loaded with varying amounts of PPO only, it bears mentioning the next steps for the scintillator formulation moving forward.

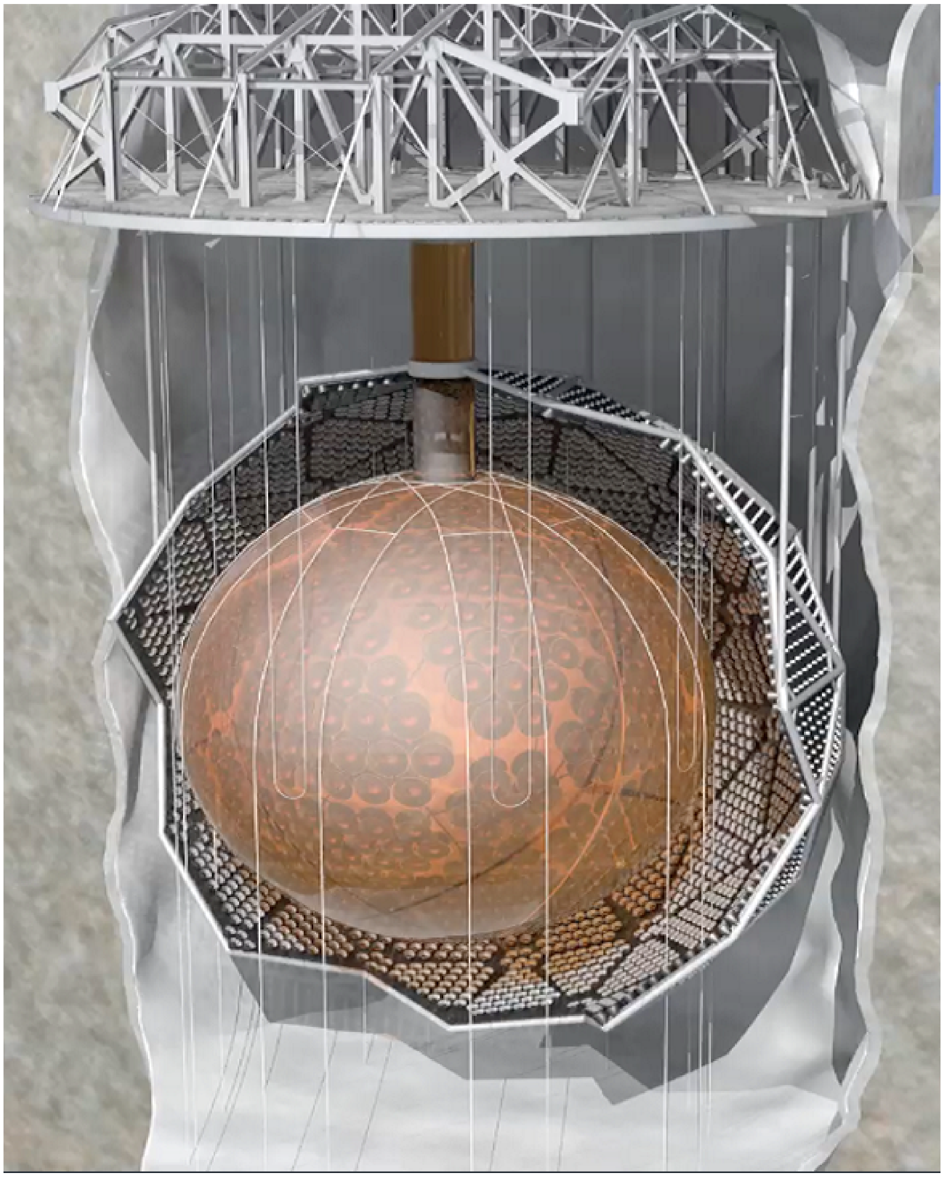

Figure 4.6: A rendering of the SNO+ detector with a cutaway on the PSUP to display the internal sections. Figrue is reproduced from [180].

Additional additives explored to preserve and improve the optics include butylated hydroxytoluene (BHT), an antioxidant to reduce the potential for increased absorption with aging, in 2023 and 1,4-Bis(2-methylstyryl)benzene (bisMSB), a secondary fluor that further shifts the wavelengths of light toward the peak of the PMT quantum efficiency and away from the self-absorption of PPO, in 2023 and 2024. These additives were mainly implemented with a view towards long-term operations for the loaded scintillator, but represent additional pure scintillator cocktails, with different extended periods of loading for each before the campaigns

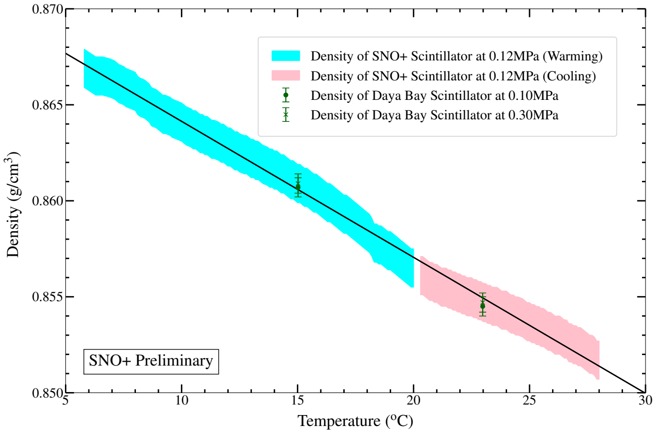

Figure 4.7: The density measured for the 2.2 g/L SNO+ scintillator as a function of temperature, compared to Daya Bay's scintillator. Figure is reproduced from [180].

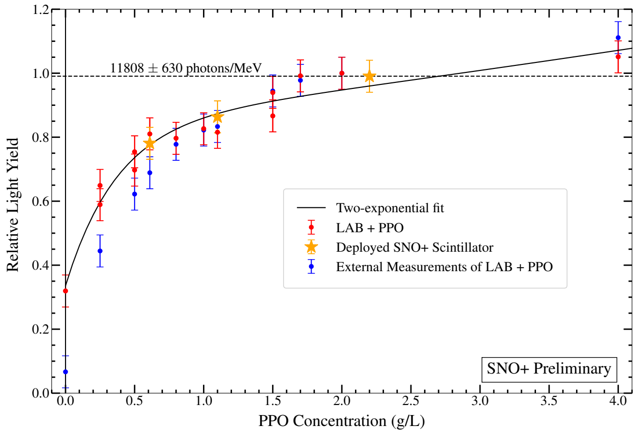

Figure 4.8: The light yield for the LAB+PPO at a range of concentrations, with the deployed samples indicated. The absolute light yield is determined by comparing results from a benchtop setup to Geant4-based simulations. Figure is reproduced from [180].

concluded. Incidentally, the final loading for bisMSB was for 2.2 *mg*, an amusing symmetry with the PPO loading. In principle, given long enough duration and sufficient confidence in the model and calibration, similar analyses as the other pure scintillator phases could be performed with any of the data generated during these periods.

A separate question revolved around how to load the Tellurium into the scintillator in a way that did not compromise the properties that had just been optimized below the point

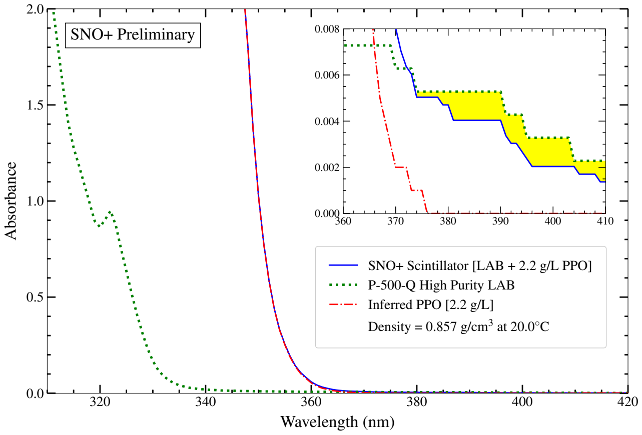

Figure 4.9: The absorption spectra of the pure LAB precursor as well as the final scintillator cocktail, obtained via ultraviolet-visible spectroscopy. The inferred PPO absorption curve referencing the fully-loaded scintillator to pure LAB is also shown. The yellow band represents the improvement in the absorption (i.e. the increase in the absorption length) in the PPO-loaded scintillator over the pure LAB used as input. Figure is reproduced from [180].

which the experiment could not be performed, and to stably keep the isotope in solution. A robust testing regime was developed, resulting in a novel method to load the Tellurium isotope [175]. In short, telluric acid $Te(OH)_6$ is reacted with 1,2-butanediol (BD) with N,N-dimethyldodecylamine (DDA) as a stabilizing agent to form compounds that are soluble and stable in LAB, with verification of stability over 5 years at the nominal loading fraction. Construction and testing of the production and deployment systems associated with this synthesis is underway underground at the time of writing.

4.4 Readout, Triggering, and Data Acquisition

Once a PMT registers and amplifies a photoelectron caused by an incident photon, this signal is channeled into SNO+'s data acquisition (DAQ) system, and the detector may be triggered to record the observed energy deposition, subject to certain conditions. The readout electronics and trigger system for SNO+ reuse many of the components from SNO, with a few updated facets designed to handle the higher light collection and event rate of multiple kHz inherent to scintillator and to add functionality, especially for the trigger. The full chain is shown in Fig. 4.10.

The channels for SNO+ are grouped into 19 crates, each of which contain a set of PMT interface cards (PMTICs) and front-end cards (FECs) with 4 constituent daughterboards (DBs) that carry 8 PMT signals each. The PMTICs are responsible for supplying high voltage to the PMTs, as well as separating out the PMT signal from the high voltage, as a single cable is used to transmit both. The PMTICs pass the signals to the FECs via the DBs, which upon application of the charge threshold to avoid sub-PE noise, will record time (via a time-to-amplitude converter, or TAC) and charge values associated with the observed pulse. These are used to define the characteristics of an individual PMT "hit". The charge values consist of integrations over short or long time windows, with varied gains, though typically the high-gain, short-integration value is referred to as the "charge". If a channel crosses threshold, the FEC generates channel trigger signals that propagate to the crate trigger card (CTC), which sums the output from channels across a crate. The CTC sends the summed signal off to a set of boards called analog master trigger cards (MTCA+) that create a sum over the entire detector determine whether to issue a global trigger. The reason for the "+" is that the initial cards used by SNO could not handle the power resulting from the higher rate in the detector with scintillator, and so had to be replaced with models that would withstand this. The upgrade also included modifications to allow for programmable logic in the summing and triggering process. Once an MTCA+ issues a trigger, this is propagated to the digital master trigger card (MTCD), which logs a Global Trigger (GT) that has an associated ID (GTID) and timestamp, and then requests that recorded hit information is saved as an "event", by propagating back through the chain. Information from 180 ns before to 220 ns after a trigger signal are saved, for a total trigger window of 400 ns. The total number of hits recorded within the trigger window is known as the *Nhit* or N_{hit} for the event. A trigger utility board is present to perform additional functions related to triggering the detector, such as the use of trigger inputs from signals other than the PMTs, like from calibration sources. A fast digitizer is also present to record the trigger signals associated with a global trigger, and this is saved to disk alongside the corresponding event.

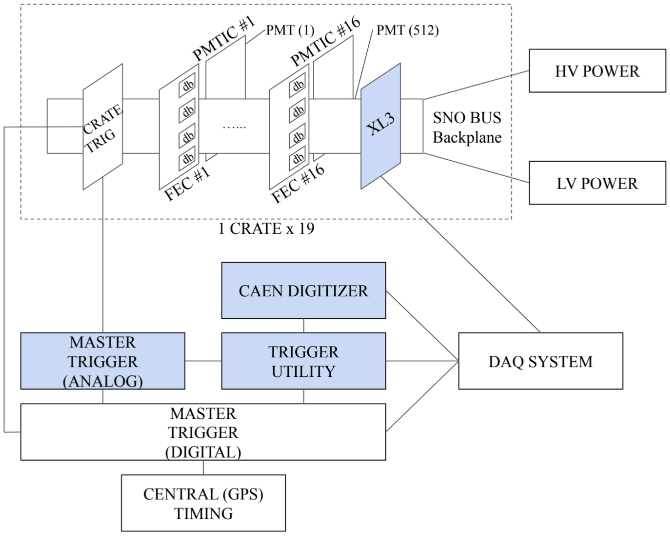

Figure 4.10: A schematic featuring the electronics readout chain for SNO+, with the upgrades from SNO featured in blue, as reproduced from [173].

On the software side, SNO+ collects events into (typically) hour-long "runs" that are grouped together based on the detector conditions, which may be configurable through the software or dependent on external factors. Typically, normal running is done in "Physics" mode, with other modes such as "Deployed Source" (for datataking with deployed calibration sources) and "Maintenance" (used most often for debugging detector issues), among others. While these conditions are assessed at the outset of a run, they may also be compromised during datataking, for example, due to failure of electronic components. The highest quality runs, which have conditions that remain well within the acceptable bounds for a wide set of criteria, are referred to as "gold" runs, while less acceptable runs may be classified as "silver" or "bronze". Runs are then grouped into run lists according to which set of criteria they satisfy, as a way to keep track of which periods of datataking should be used for particular purposes (e.g. for publishable physics analyses). It is important to note that for practical purposes to avoid dealing with large file sizes, one run is split into 1 GB chunks in files called "subruns", which each contain some subset of the events in a run.

4.5 Calibration

Calibration of the detector focuses on determining detector-specific aspects of the PMT response, optical properties of detector components, and the overall detector performance in relation to event characteristics. The electronics/PMT calibration, optical calibration and deployed source systems are described in detail in [173].

PMT and electronics calibrations are key to understanding how to convert the recorded time and charge values to meaningful quantities in physical units rather than the otherwise arbitrary units native to the electronics, for accounting for electronics noise and for understanding the efficiency with which hits are registered by the PMTs. Some of the electronics calibrations are carried out with regularity, as they simply involve forcing the electronics to record time and charge information absent an actual PMT signal to measure the baseline or "pedestal". Others, such as the detailed optical calibration performed in the water phase using the laserball, a deployed source that uses a diffuser ball to shine light into the detector [101], are more complicated and require a great deal of care. These calibrations are essential for both understanding PMT response to light and the properties of the media through which light travels in the detector, particularly the absorption and scattering characteristics. Beyond the laserball, SNO+ is also equipped with several fiber-based systems embedded in the PSUP, which are able to shine lasers and LEDs of different wavelengths into the detector from different vantages, collectively known as the Embedded LED/Laser Light Injection Entity (ELLIE) systems.

There are also several deployed radioactive sources that SNO+ operates to precisely learn how the target media responds to energy deposition in order to better model and analyze data by exploiting interactions of known energies. While a host of deployed sources are described in [173], the two of primary interest for scintillator operations are the AmBe and ^{16}N sources. The first involves α decay of ^{241}Am, which is then absorbed by ^{9}Be to create ^{12}C, either in the ground state or an excited state that releases a 4.4 MeV γ, and a neutron.

The neutron can thermalize and capture in the target volume inside the AV, particularly on ^{1}H, and the de-excitation γ, if present, may also scatter within the AV and deposit its energy. The ^{16}N source primarily provides a 6.1-MeV γ coming from the β decay to ^{16}O in an excited state, though other γs are also possible. This source also has the benefit of being taggable by virtue of observing the light from the decay β within the source enclosure. By comparing the events observed from these sources in data and simulation, the detector model can be tuned to better match observed patterns.

The final calibration source of note for the purposes of this thesis comes from the internal radioactive contamination within the scintillator. ^{238}U and ^{232}Th are the parent isotopes of decay chains that contain a multitude of daughters that can be leveraged for the purposes of calibration, in addition to proving to be backgrounds for MeV-scale neutrino physics. These primordial isotopes can enter the AV through suspension in the scintillator in the form of dust or other particulate matter, as well as through the ingress of radon gas from external sources or outgassing of components. In particular, the pair of daughters ^{214}Bi and ^{214}Po from the ^{238}U chain, and to a less extent ^{212}Bi and ^{212}Po from the ^{232}Th chain, have been used extensively by SNO+ to tune the light production modeling of the scintillator, enabling tuning of the overall light yield and quenching for β and α particles and the emission timing. This is enabled by the fast decay times of ^{214}Po ($t_{1/2} = 164\,\mu\text{s}$) and ^{212}Po ($t_{1/2} = 0.3\,\mu\text{s}$) providing a mechanism to use coincidence tagging to identify the decays and obtain a highly pure selection of events. Other leveraged isotopes include ^{210}Po from the ^{238}U chain and ^{14}C, the same isotope used in radiocarbon dating, which is present amongst the numerous carbons in the scintillator.

4.6 Modeling, Simulation, and Software

SNO+ relies on a `GEANT4` -based [188] simulation and analysis framework called `RAT`, a successor to `GLG4Sim` [189] codebase developed out of KamLAND. `RAT` handles all aspects of the Monte Carlo simulation, from generation of event vertices for a broad array of physics, to light production, to propagation of particles (including optical photons) through the fully-simulated detector geometry, and finally through the full detection and readout chain. `RAT` is also used to perform event reconstruction and analysis tasks for both real data and MC, with a plethora of utilities and tools to aid in complex tasks and a flexible database structure known as `RATDB` to hold information related to simulated and real datataking conditions. The information in `RATDB` includes the PMT light collection, scintillator, and radioactive decay properties, to name a few, all of which have been included from careful review of literature, benchtop measurements external to the detector or *in-situ* measurements taken during operations. `RAT` is also heavily reliant on the CERN `ROOT` library [190], which is the source of the predominant file formats for the experiment that are based on the `TTree` and `TChain` paradigms known as `RATDS` and `ntuple`, with the former containing hit-level and diagnostic-level information with the latter containing only higher order event and run information. Since `RAT` is constantly evolving like any highly used software, keeping track of the version number used is important for reproducibility of any result. For collaboration-wide endeavours, data is processed and Monte Carlo is produced centrally using the same `RAT` version, which should then also be used for the analysis.

4.7 Reconstruction

Converting, or "reconstructing", from information from individual hit PMTs to the overall event quantities such as the location of the particles within the detector is necessary to interpret and analyze data for physics. Event reconstruction in scintillator for SNO+ roughly falls into three sets of routines: vertex (position/time) reconstruction, energy reconstruction and event classification. For the scintillator fill, these routines are grouped into an overall framework called `scintFitter`, while for the partial fill, the combined fitter was known as the `partialFitter`. While other methods like track reconstruction for muons and direction reconstruction (such as in [183]) are also explored by SNO+, these are non-standard and are typically not run over events in central processing by default. Since most events of interest for low-energy neutrino physics are point-like in character and involve only one outgoing particle of interest (almost always an electron or positron), more time-intensive track-based, direction-based and multi-vertex approaches are typically safe to relegate to a la carte processing.

While primitive algorithms based solely on hit timing and position exist to seed more robust methods, the primary class of vertex reconstruction techniques (as well as event classifiers) relies on a quantity known as the hit time residual, defined as:

$$t_{\text{res}} = t_{\text{hit}} - t_{\text{event}} - t_{\text{tof}} = t_{\text{hit}} - t_{\text{event}} - \sum_i t_{\text{tof},i} = t_{\text{hit}} - t_{\text{event}} - \sum_i \frac{\ell_i}{c_i} \tag{4.1}$$

where t_{res} is the hit time residual, or time residual for a given hit on a PMT that occurs at time t_{hit}. t_{event} is the proposed time for the event the hit is within, and t_{tof} is the time-of-flight between the proposed event position and the hit PMT, which can be broken down by detector volumes traversed. That can be broken down into the length traveled within that volume ℓ_i, as well as the speed of light in the medium of that volume c_i (because we have no wavelength information from hits, this is taken as a nominal value of 400 nm based on the emission spectrum of scintillator and the PMT QE). The t_{tof} is calculated in `RAT` with the aid of a utility that is able to identify the probable path the light took between its emission point and the PMT (including reflection and refraction at interfaces). Relying on the time residual allows the transformation of events into a common reference frame (centered on the emission time), whereas raw hit time distributions vary wildly depending on where in the detector events may occur. The most prominent vertex reconstruction method relies on tabulating from simulation the time residual distribution for electrons in the detector within an energy range into a probability distribution. Then, for given events, the likelihood is computed for a hypothesized event vertex, and this is iteratively maximized such that the most-likely position and time are found, which are then taken as the fitted vertex. Because the likelihood can be determined more precisely with additional hits, the performance of the vertex reconstruction increases with energy (at least within the approximation that the event is still point-like). At energies and positions relevant to the analyses in Chapter 5, the resolution on position is well below 1 cm.

The standard energy reconstruction routines for SNO+, which at typical energies primarily operates with a single photoelectron per hit PMT, exploits a conversion between the number of hits N_{hit} to event energy. While there are corrections applied to account for multi-PE hits, this stands opposed to using one of the charge values such as QHS as the basis for converting to energy. This is eschewed due to limitations with the charge calibration and the fact that SNO+ operates below saturation ($N_{\text{hit}} < N_{\text{PMT}}$) at MeV-scale energies. The precise conversion between N_{hit} and MeV is determined through calibration, with assorted corrections, gleaned from calibration and simulation, applied to account for variation in the number of detected hits. These variations in the conversion are dependent on event characteristics, such as with position due to optical effects like absorption. The conversion used by SNO+ is also assumed to be in "electron-equivalent energy deposited", so the true energy of particles like αs are not reconstructed and instead are mapped onto the electron energy space. Below saturation, the response of the detector in N_{hit} is taken as Poissonian, meaning that the precision of the energy reconstruction roughly improves by $\sqrt{N_{\text{hit}}}$.

The final aspect of the reconstruction routines lies in event classification. This is a broad set of processes developed to differentiate classes of events from each other. The categories to be separated can be fairly abstract or very concrete. For example, separating events that have hits concentrated in particular areas of the detector from ones that do not, or separating events that are broadened in time due to the existence of multiple points of energy deposition from ones that only have single points of energy deposition. Commonly, these classifiers have as their output a likelihood-ratio test statistic comparing the two event classes as hypotheses. Often, these are based on the time residual distributions, similar to the position reconstruction, since different event classes will have somewhat different distributions in time (e.g. due to the differing excitation of scintillator depending on particle type). More simplified approaches also exist, such as simple fractions of hits subject to some condition like the ratio of hits inside a time window compared to the total number of hits. The primary purpose of these classifications is to provide background rejection power and enhance purity of event selection, since the classifiers enable single vertex vs. multi-vertex discrimination, particle identification (PID), and differentiation of instrumental backgrounds. The author has helped to shape event classification in SNO+ in several ways, as is detailed in Sec. 4.8.

4.8 Case Study: Event Classification in SNO+

The following two subsections examine the development and testing by the author of two related methods to discriminate between event classes, as discussed in Sec. 4.7. The first of these, relayed in Sec. 4.8.1, covers discrimination of interactions involving β particles from those involving α particles. The second, relayed in Sec. 4.8.2, covers discrimination between instrumental backgrounds known as flashers that stem from faulty behavior in the PMTs and normal physics interactions, e.g. decays and scatters within the target medium.

4.8.1 α/β Discrimination

Because of differing particle characteristics (e.g. mass, charge and characteristic energy deposition) and properties of SNO+'s LAB+PPO scintillator tuned during its development, light emission changes significantly between excitation by α and β particles, enabling the development of PID techniques that may reject α backgrounds. Neutrino interactions typically result in electron-like signals at the MeV level.

One such technique that has been developed for SNO+ is the BerkeleyAlphaBeta classifier, which relies on the time residuals from recorded events and compares these observed distributions in a likelihood ratio test with α and β hypotheses determined from MC simulation of the detector model. The classifier forms its two hypotheses from time residual distributions, generated from ^{210}Po α Monte Carlo simulations and β simulations at the energy that the ^{210}Po quenches to, as the basis for the likelihood ratio test. ^{210}Po is the most numerous α background observed in SNO+ and presents a significant hindrance to searches accessing the region below 1 MeV, such as low energy solar neutrino searches, hence the choice of energy scale. The β is simulated at comparable quenched energy (the effective amount of energy converted into light, which is different depending on particle type) to the α in order to account for differences in the light production and detection at different energies, for example in the multi-PE response that may shift the time distribution. This ensures the comparison between α and β events take place under the most similar conditions.

Considering all hits as independent, the classifier result is the sum over the hits in the difference in log-likelihood of having a hit at time residual t_i for the two hypotheses, i.e.:

$$c = \sum_{i=0}^{N_{\text{hit}}} (\ln P(t_i|\alpha) - \ln P(t_i|\beta))$$

where c is the classifier value, N_{hit} is the number of hits in the event, $P(t_i|\alpha)$ is the probability of having a time residual at t_i given the event is caused by an α and $P(t_i|\beta)$ is analogously defined for βs. The result of the classifier is thus a discriminant that should ideally separate events caused by α and β, and enable selection cuts to be deployed in an analysis depending on criteria of sample purity, accuracy of selection, etc. The more positive the classifier result is, the more β-like an event is, whereas more negative results are more α-like.

Because the discriminant is applied across a range of N_{hit} values and there is a running observed as the number of hits increases due to the varied number of samplings, it is often helpful to define the N_{hit}-normalized classifier value

$$c' = \frac{c}{N_{\text{hit}}}$$

c' allows for more easy comparison across a range of N_{hit}, as it removes the running while maintaining separation between α and β in classifier-space.

The performance of the BerkeleyAlphaBeta classifier in SNO+ has been evaluated using data taken during the partial fill phase, as well as simulation from the same detector setup and from simulation of the detector fully-filled with liquid scintillator. The results are presented using the Youden's J statistic, a common metric in classification problems that captures the separability of outcomes (usually positive and negative, here α and β), as the means to define a cut threshold. Here,

$$J = N_\beta(c')/N_{\beta,\text{tot}} - N_\alpha(c')/N_{\alpha,\text{tot}} \tag{4.2}$$

with a value close to 1 being optimal. $N_\beta(c')$ means the number of β events selected by the cut, with $N_{\beta,\text{tot}}$ being the total number in the class for the event sample, and analogously for αs. Several metrics are identified as a function of position in the detector to better understand uniformity, including the fraction of β (signal) events accepted and the fraction of α (background) events rejected.

^{214}BiPo decays in the detector are identified as an event sample from the detector data, having been processed with `RAT` 6.18.9. The sample used consists of BiPo coincidences from the golden runs from 257669 to 259062, with the following cut selection:

1. $r < 6\,\text{m}$ (prompt and delayed)
2. $0.85\,\text{m} < z < 6\,\text{m}$ (prompt and delayed)
3. Prompt $N_{\text{hit, cleaned}}$ between $(330, 1050)$
4. Delayed $N_{\text{hit, cleaned}}$ between $(170, 320)$
5. Δt between $(4000\,\text{ns}, 1\times10^6\,\text{ns})$
6. $\Delta r < 1\,\text{m}$

This selection follows tagging criteria developed by J. Wang and used by I. Morton-Blake for the timing parameter tuning for the partial fill period [180]. Due to the selection criteria cleanly separating the classes by N_{hit}, the achieved separation is inflated compared to a comparison done at like energies, though it still serves as a proof of concept that the classification works on any level. The classifier performance is evaluated within equal-volume rings around the detector delineated by appropriately chosen coordinates in $(\frac{\rho^2}{\rho_{\text{AV}}^2}, z)$. For this data, Fig. 4.11 show the histograms for the distributions of identified maximum J ($J_{\max}$), classifier value at the maximum J (the cut value), α rejection, and β acceptance.

Given the same partial fill detector conditions, run-by-run Monte Carlo production for select runs was produced using `RAT` 6.18.9, and in order to compare data and the MC model, we perform the same procedure outlined above on the simulated ^{214}BiPo from this production. For this run-by-run production, Fig. 4.12 show the histograms for the distribution of $J_{\max}$, classifier value at $J_{\max}$, α rejection, and β acceptance.

While the identified cut value varies slightly between data and MC (likely due to gaps in the timing and optical models at this stage of development with a detector configured oddly in a geometric sense), both samples achieve $J_{\max} \sim 0.7$, α rejection $\sim 80\%$ and β

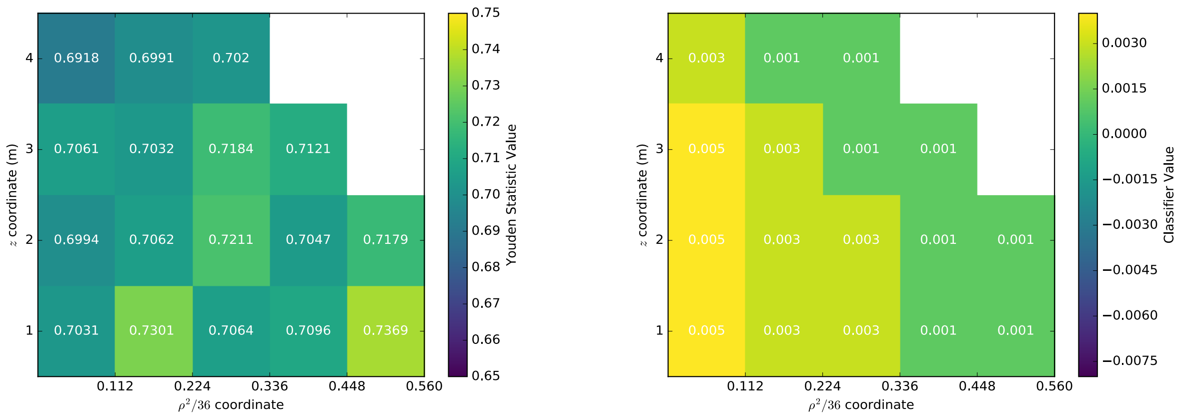

(a) J_{max} (b) Classifier Value at J_{max}

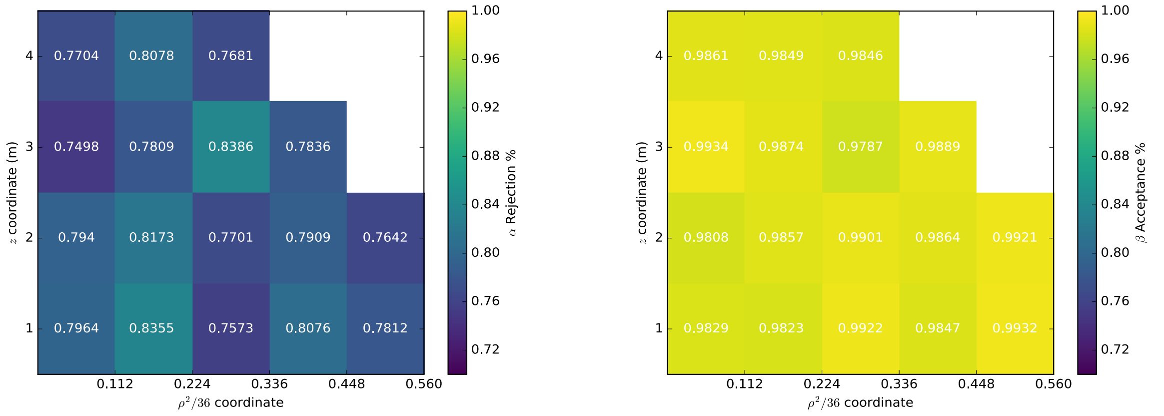

(c) α Rejection (d) β Acceptance

Figure 4.11: Plots showing the value achieved for each metric in the given position-based bin using the Youden's J test statistic on the BerkeleyAlphaBeta classifier distributions for data from the SNO+ partial fill.

acceptance $\sim 100\%$. As such, the low PPO loaded scintillator of the partial fill enabled fairly strong rejection, despite not having been a planned deployment, and despite the geometrical abnormality, performance was fairly uniform, as can be seen from the heat maps. While an overestimate of the true performance given the mismatched nature of the samples in energy space, this study was the first validation of timing-based α/β discrimination capabilities in deployed SNO+ scintillator.

For the full fill, as of writing, the data and MC have not been centrally reprocessed using the most recent iteration of the BerkeleyAlphaBeta classifier that incorporates the most recent optical model. However, small scale MC studies have been conducted to assess performance using the ^{210}Po α ($Q = 5.3\,\text{MeV}$) as the reference point. In the 2.2 g/L LAB+PPO

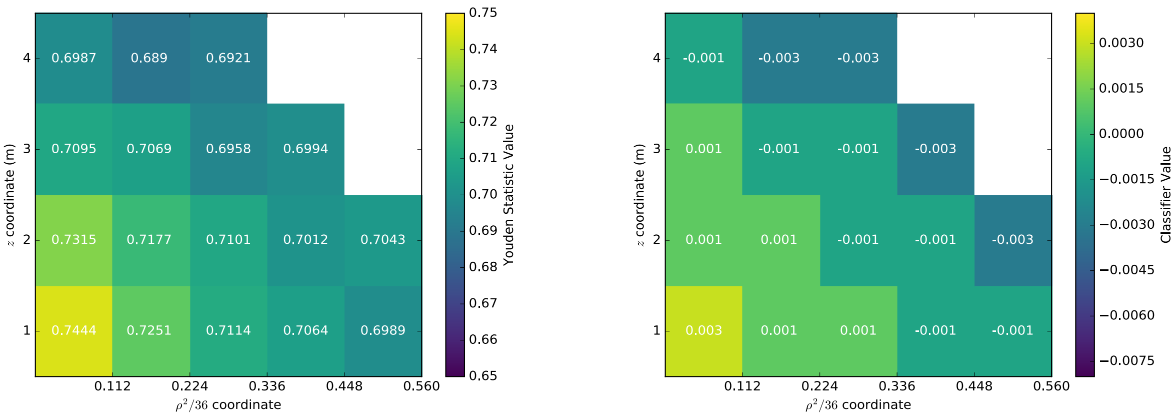

(a) Maximum J (b) Classifier Value at J_{max}

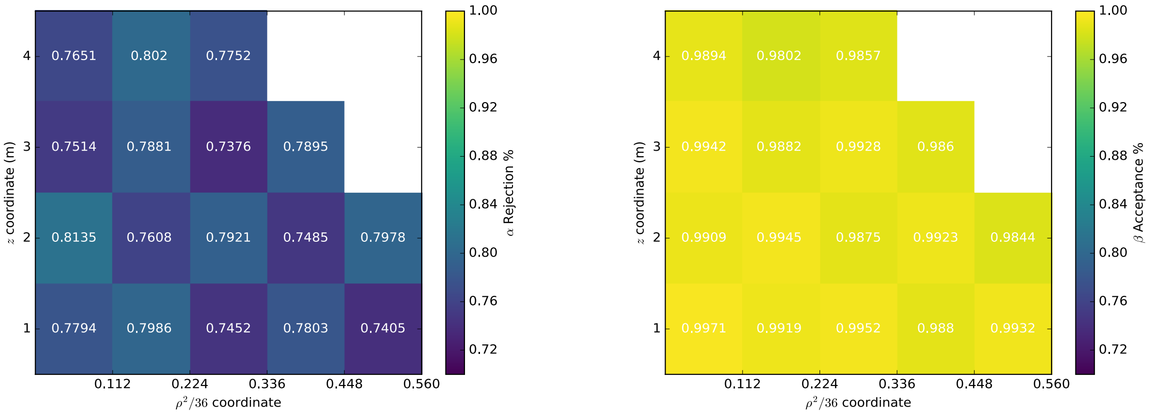

(c) α Rejection (d) β Acceptance

Figure 4.12: Plots showing the value achieved for each metric in the given position-based bin using the Youden's J test statistic on the BerkeleyAlphaBeta classifier distributions for run-by-run MC production for the SNO+ partial fill.

material, this corresponds to a β energy of 0.5 MeV. The distributions for a sample of events, the acceptance and rejection as a function of cut-on classifier value and the a version of the receiver operating characteristic are shown in Fig. 4.13. With this model, α rejection $\sim 80\%$ and β acceptance $\sim 80\%$ are achievable using a single cut throughout the entire volume. Previous studies in SNO+ [81] have suggested performance using a 2.0 g/L LAB+PPO formulation with correct identification of samples at better than 99% and Borexino achieved similarly with their PC+PPO mixture [191], though with different methodology. This suggests that unexpected features of the deployed scintillator and the precision of the optical model may be substantial factors as to the apparent departure from the expected performance. Future iterations of the optical model, as well as revisions to this classifier and other approaches, will likely yield improvements.

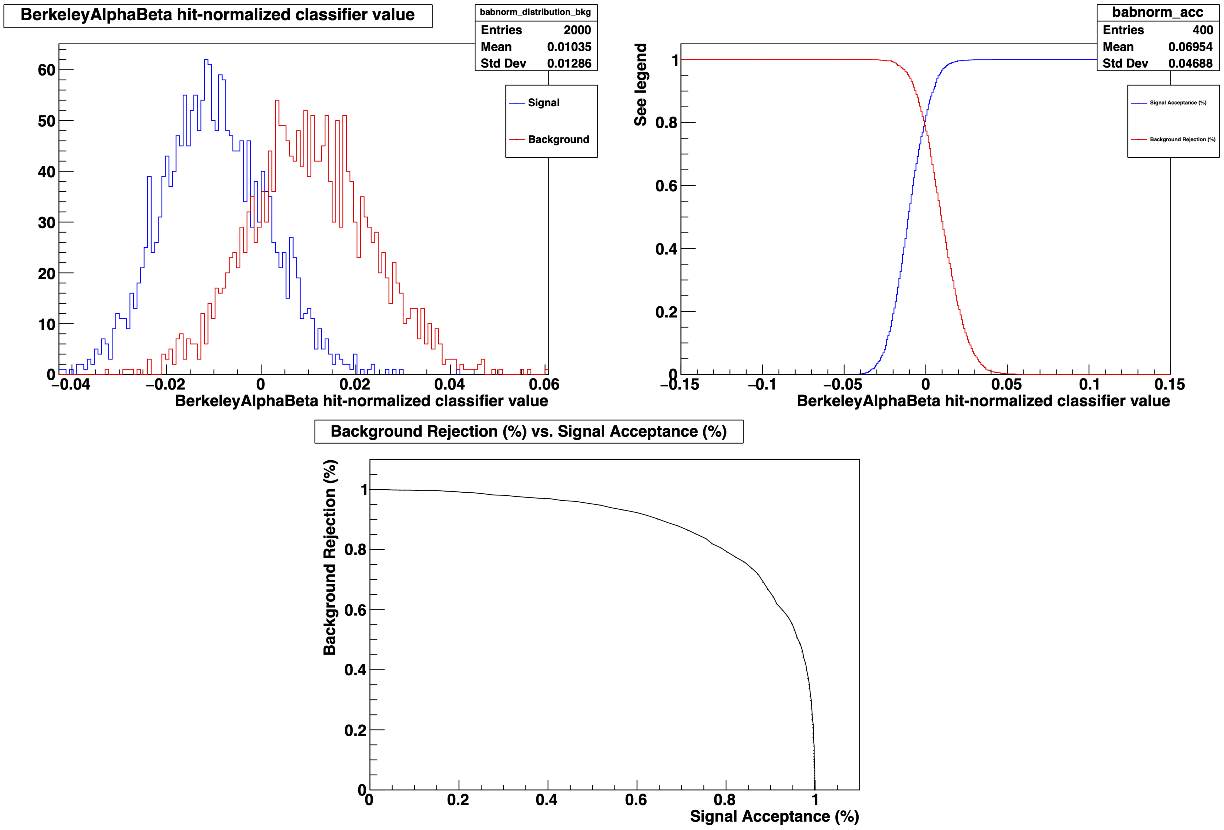

Figure 4.13: Results of the preliminary investigation of the α/β discrimination capability using simulation for the 2.2 g/L LAB+PPO optical model. The top left figure shows the distribution of a sample of events in classifier space, the top right plot shows the achieved α rejection and β acceptance as a function of the classifier value that is cut on, and the bottom plot shows the simultaneously achievable α rejections and β acceptances in the style of a receiver operating characteristic plot.

4.8.2 Flasher/Physics Discrimination

Discriminating between true physics events is not the only use this approach has, as certain backgrounds can stem from the experimental apparatus itself. These instrumental backgrounds contain features that “data cleaning” protocols attempt to leverage to remove from the data set to leave behind only real physics data. One such class of instrumental backgrounds observed in neutrino experiments employing PMTs including SNO+ are so-called “flashers”. Flashers occur when instead of detecting light from an interaction of interest in the target as is normal practice, a PMT emits light which propagates through the detector into other PMTs, mimicking detection of a particle interaction. While a dominant source of instrumentals, the exact cause of these flashers is not fully understood, nor is the wavelength distribution or emission timing of their light, leading to difficulties in mitigating them as a background source. Because the target material in SNO+ changed from water to a material with vastly different optical properties, the capacity of the established data cleaning cuts from SNO to eliminate flashers from data samples was not well-known during partial fill, and complementary tools were desired. Previous studies attempted to simulate the performance using a flasher generator that allows for multiple timing and wavelength profiles for the light given lack of certainty [192]. The work presented in Sec. 4.8.2 is the first flasher study with actual SNO+ scintillator data.

4.8.2.1 Overview of Flashers

While overall the ultimate cause of flashers and many of their characteristics remain unknown, some information is known about flashers from observation of clear candidate events in the detector. During SNO, roughly 50 flashers were expected to be observed per hour. While the number of hits in a flasher event covers a wide range of hits, primarily in 10s and 100s but extending to 1000s as shown in Fig. 4.14, the event topology associated with them in the heavy-water/water filled detector state is well-defined. Typically, a flasher will consist of a high charge PMT hit early in time (sometimes rolling over to negative charges), surrounded by cross talk hits. Then, later in time, once the light emitted by the flashing PMT has time to traverse the detector, an elliptical pattern of hits will occur on the opposite side of the detector from the flashing PMT.

In the past for SNO and SNO+, these hit patterns in physical and electronics space, as well as hit timing and charge have been used to discriminate flasher events from physics events. Several data cleaning cuts were developed in SNO and applied in SNO/SNO+ that removed flashers from the data set based on these patterns. These cuts relied on the promptness of the time distribution and ring-like structure of hits from Cherenkov light in comparison to the temporal and spatial topology of flashers. As such, their effectiveness for a scintillation-based detector is likely to be at least diminished somewhat, due to the different time scale and isotropy associated with scintillation light produced by interactions within the detector volume.

As mentioned, the exact wavelength distribution of light from flashers is not known, but some rough bounds can be established by considering the media light travels through in the

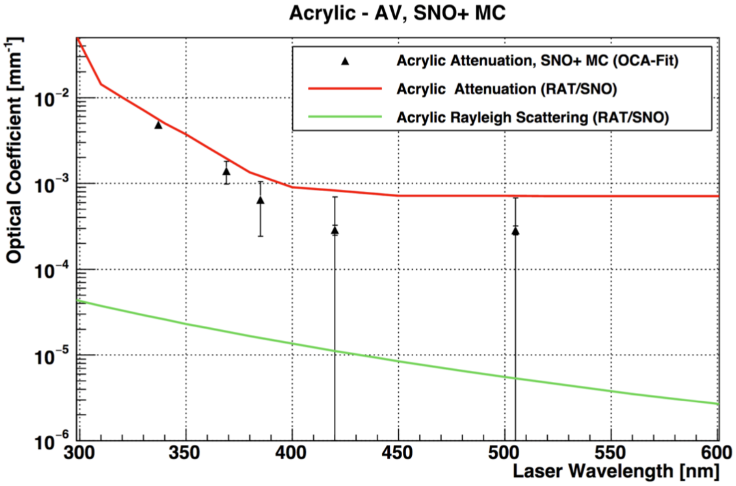

Figure 4.14: The N_{hit} distribution of observed flashers from the SNO D_2O salt phase, reproduced from [192]. This plot was generated by finding the N_{hit} of any events tagged by at least one flasher-focused data cleaning cut but not any non-flasher-focused data cut in SNO data.

detector and the scattering and attenuation associated with them. Due to the relatively large attenuation and large light travel distance in water at long wavelengths and the very large attenuation despite the short travel distance in acrylic at short wavelengths, most light from flashers observed in SNO must lie in the region between approximately 350 nm and 500 nm. The higher scattering at low wavelengths for water should not greatly affect the observed flasher topology.

Since the optics of the LAB+PPO scintillator employed by SNO+ are quite different compared to water, with more absorption and scattering, the flasher topology could be somewhat different in the scintillator-filled detector depending on the wavelengths at play. While the scintillator is relatively transparent at longer wavelengths as seen from Fig. 4.9, the steep rise in absorption on PPO around 370 nm may profoundly alter the appearance of flashers in the detector, which stands in contrast to water's transparency at these wavelengths as can be seen in Fig. 3.2. Fig. 4.16 uses simulation to show that the potential change in topology from a monochromatic 500 nm flasher with instantaneous emission in scintillator, which looks quite similar to the hit pattern for SNO flashers, compared to one at 350 nm, is quite apparent. The 350 nm flasher has a "flash-back" due to the absorption and subsequent reemission of low wavelength light, rather than a ring-like hit pattern on the opposite side of the detector. This would likely cause trouble for the standard flasher data cleaning that assumes the water geometry in physical and electronics space. Due to the uncertainty in the wavelength and timing distribution, only study of flashers in real scintillator data will reveal the topology actually present.

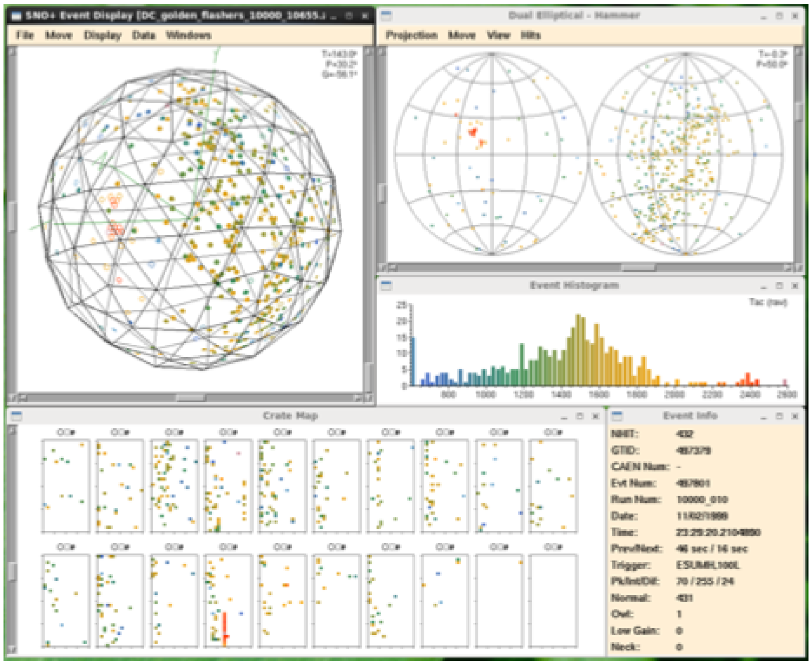

NHIT: 432
GTID: 497379
CAEN Num: -
Evt Num: 497801
Run Num: 10000_010
Date: 11/02/1999
Time: 23:29:29.2104850
Prev/Next: 46 sec / 16 sec
Trigger: ESUMH,100L
Pk/Int/Dif: 70 / 255 / 24
Normal: 431
Owl: 1
Low Gain: 0
Neck: 0

Figure 4.15: An event display of a typical flasher from SNO data, reproduced from [192].

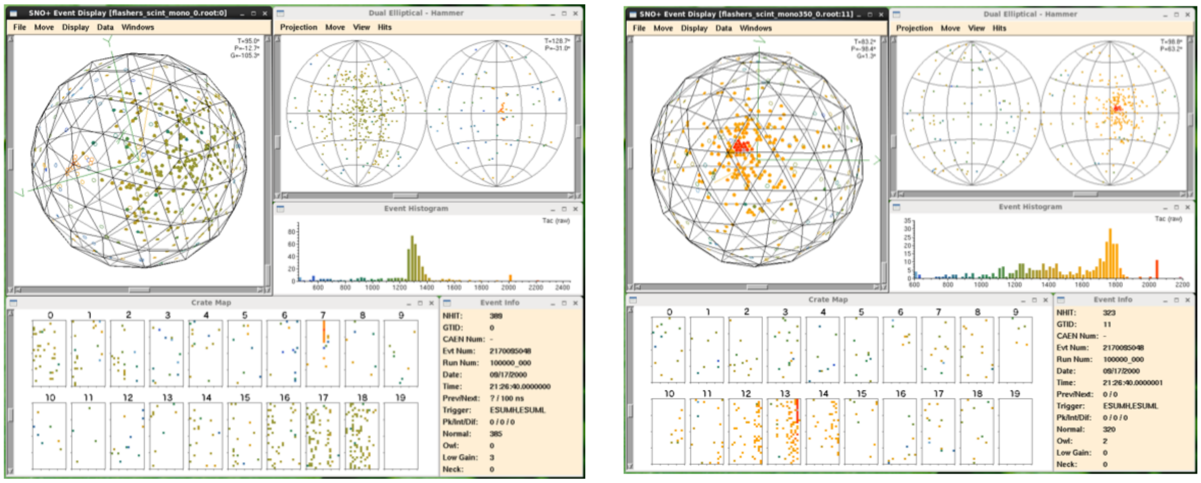

NHIT: 389
GTID: 0
CAEN Num: -
Evt Num: 2170085048
Run Num: 100000_000
Date: 08/17/2000
Time: 21:26:40.0000000
Prev/Next: ? / 100 ns
Trigger: ESUMH,ESUML
Pk/Int/Dif: 0 / 0 / 0
Normal: 385
Owl: 0
Low Gain: 3
Neck: 0

NHIT: 323
GTID: 11
CAEN Num: -
Evt Num: 2170085048
Run Num: 100000_000
Date: 08/17/2000
Time: 21:26:40.0000001
Prev/Next: 0 / 0
Trigger: ESUMH,ESUML
Pk/Int/Dif: 0 / 0 / 0
Normal: 320
Owl: 2
Low Gain: 0
Neck: 0

Figure 4.16: A monochromatic 500nm flasher with instantaneous emission in scintillator simulated in RAT (left) and a monochromatic 350nm flasher with instantaneous emission in scintillator simulated in RAT (right), shown from [192]. While the 500nm simulation appears similar in character to Fig. 4.15, the 350nm topology is vastly different

While the various properties of the light emitted by flashers is not known, it is quite likely that the time profiles of flasher events will not match that of physics events. This can be used to the advantage of data cleaning and instrumental background rejection, as an additional lever to identify and remove flashers from the dataset in addition to those developed for the water-filled detector iterations, which may have degraded capabilities. Based on the technique that has been developed for SNO+ with the BerkeleyAlphaBeta classifier as shown in Sec. 4.8.1, a flasher classifier can be created as an extension, which applies a similar likelihood-ratio test based on hit time residual PDFs with flasher and physics event hypotheses. For the purposes of this classifier, β events are used to create the physics hypothesis given the fact that most physics signals of interest in SNO+ are β-like, while several options motivated by the previous simulation studies and with a data-driven approaches are applied for flashers, as described below. For the physics hypothesis β sample, in the case of the explorations below, a tagged sample of ^{214}Bi decays is used, identified with the same criteria as in Sec. 4.8.1, in order to avoid mismodeling from simulation that might adversely impact discrimination against the instrumental events.

Considering all hits as independent, the classifier result is the sum over the hits in the difference in log-likelihood of having a hit at time residual t_i for the two hypotheses, i.e.:

$$c = \sum_{i=0}^{N_{\text{hit}}} [\ln P(t_i|\text{Flasher}) - \ln P(t_i|\text{Physics})]$$

where c is the classifier value, N_{hit} is the number of hits in the event, $P(t_i|\text{Flasher})$ is the probability of having a time residual at t_i given the event is caused by a flasher and $P(t_i|\text{Physics})$ is analogously defined for βs. Like with the BerkeleyAlphaBeta classifier, the more positive the classifier result is, the more flasher-like an event is, whereas more negative results are more β-like. A similar hit-normalization scheme also used.

4.8.2.2 Performance on Seismic-Correlated and Calibration Data in Partial Fill

Seismic activity is a known cause of instrumental backgrounds like flashers due to the physical disturbance of the sensitive electronics. While flashers exist through the detector running, a sample of flasher candidates can be identified by isolating events corresponding to seismic activity. A searchable tool providing the records of seismic activity can be found from Earthquakes Canada [193], which can be used to isolate seismic activity spatially and temporally near SNO+ during operating periods of interest; SNOLAB maintains a log of activity near the lab from this source. The Earthquakes Canada time is in UTC±00:00 while the SNOLAB time is in Sudbury local time. These database entries are correlated with SNO+ runs and then the relevant events are identified. All physics runs corresponding with seismic activity according to the SNOLAB-maintained listing during the stable partial fill period from March to October of 2020 can be found in Tab. 4.3.

Additionally, calibration data is used as the physics data with which to assess the data cleaning cuts and flasher classifier. For this analysis, externally deployed AmBe source and

Table 4.3: The runs corresponding to seismic activity registered in the SNOLAB database. The runlist label included is the highest quality runlist available. Runs with multipliers have multiple instances of seismic activity within their duration. Runs separated by a slash correspond to seismic activity that occurred close to the rollover between runs and so may fall in either run depending on consistency in the time between SNO+ and the seismic activity detector.

Run	Runlist
260058	Preliminary Partial Bronze
260097	None
260200	None
260264	Preliminary Partial Bronze
260685	None
260771	None
261150	Preliminary Partial Antinu
261363	None
261637 (x2)	Preliminary Partial Gold
261833 (x2)	Preliminary Partial Gold
262161	Preliminary Partial Bronze
262175	Preliminary Partial Bronze
262293	Preliminary Partial Bronze
262498	Preliminary Partial Bronze
262520	Preliminary Partial Bronze
263035 (x3)	Preliminary Partial Bronze
263250	Preliminary Partial Bronze
263413/263414	Preliminary Partial Bronze
263567/263568	Preliminary Partial Gold
263659	Preliminary Partial Gold
263701	Preliminary Partial Gold
263766	Preliminary Partial Nearline Selected
263868	Preliminary Partial Gold
263962	Preliminary Partial Gold
264027	Preliminary Partial Gold
264031	Preliminary Partial Gold
264111	Preliminary Partial Gold
264227 (x2)	Preliminary Partial Gold
264278 (x2)	Preliminary Partial Gold
264290	None
264312	Preliminary Partial Gold
264342	Preliminary Partial Gold

tagged BiPo data were used as physics calibration. The AmBe runs used for this analysis were the external deployment runs 261559, 261560, and 262243-262254 processed using the `Analysis_AmBe` module, using the time coincidence between the n-capture and de-excitation γ to select a high purity sample of physics events. The BiPo sample used consists of BiPos from the golden runs from 257669 to 259062, with the same selection cuts applied as in Sec. 4.8.1.

The time residual PDF for the flasher hypothesis used for this study was generated using simulation in the partial fill detector configuration using the flasher generator with the assumptions that flashers are monochromatic at 400 nm and emit instantaneously. The time residual PDF for the physics hypothesis used the *in-situ* time residual distribution extracted from the ^{214}Bi selection identified from the above sample. A data-driven PDF is used for the physics hypothesis with a MC-generated PDF for the flasher PDF as the study itself is largely data-driven due to the vast gap in understanding of flashers. As such, the "true" observed timing of physics events seen directly from data is more valuable for use with other data compared to the MC model's timing, and the MC-generated flasher PDF is merely a starting point due to the limited knowledge of flashers and general difficulty simulating instrumental backgrounds. The PDFs can be seen in Fig. 4.17. The significant early time component and sharper peak for the flasher PDF compared to the physics PDF presented a promising handle on separating these two classes of events.

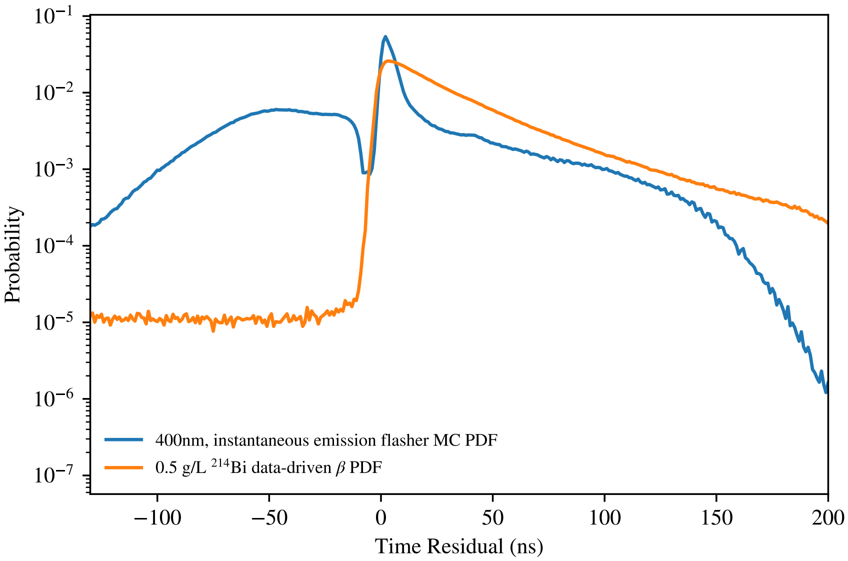

Figure 4.17: PDFs used for the flasher classifier analysis, normalized by area.

The performance of the classifier on the calibration data is examined to establish what physics data should look like subject to the classifier. A scatter plot of the N_{hit} -normalized classifier value plotted against N_{hit} is generated for 4 different classes of events: non-candidates; flasher candidates tagged by data-cleaning cuts only; flasher candidates tagged by the classifier only (with a nominal cut value at 0); and candidates tagged by both DC cuts and the flasher classifier. It is quite clear in all three sets of calibration data, as seen in Fig. 4.18, that while the flasher data cleaning cuts erroneously tag many physics events, the classifier does not. Also, as expected, the physics events are centered around a negative value for the classifier.

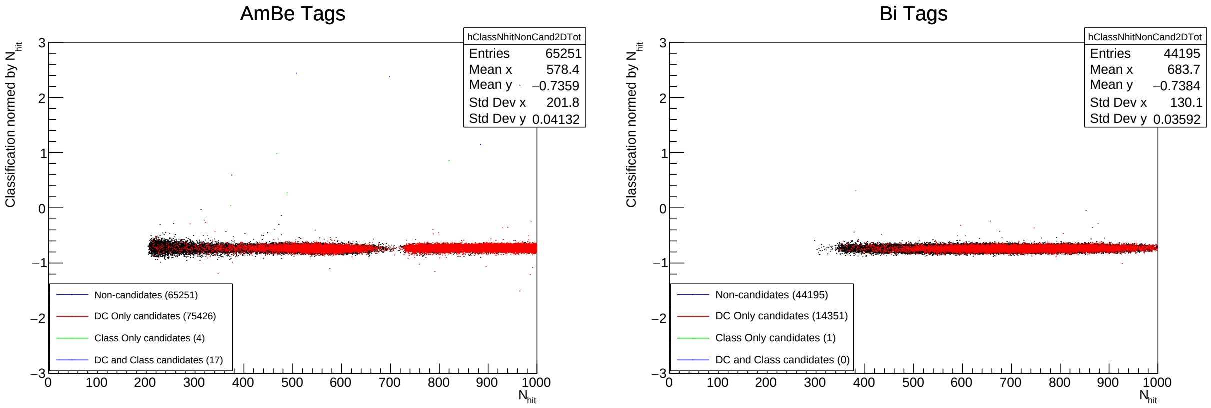

(a) AmBe (b) ^{214}Bi

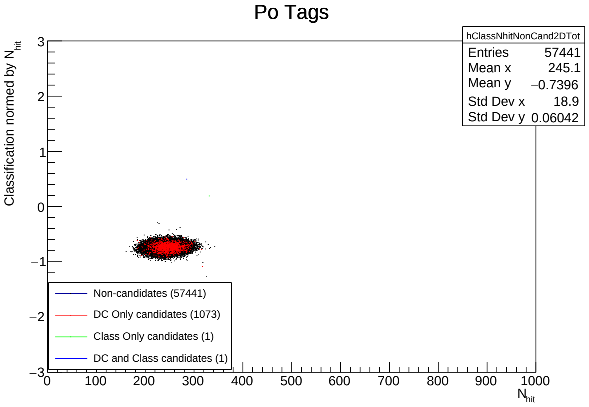

(c) ^{214}Po

Figure 4.18: The flasher tagging results for the data cleaning cuts and flasher classifier on different calibration datasets. The top left plot shows the results using events from the AmBe source, the top right plot shows the results using events from the tagged ^{214}Bi and the bottom plot shows the results using events from the tagged ^{214}Po.

After looking at calibration data, attention can be turned to data from normal physics running. For the runs of Tab. 4.3, the data is scanned to look for instances where the detector rate spikes. In one particular case, show in Fig. 4.19, two spikes in rate are clearly apparent at appropriate times spaced by an appropriate interval in time compared to the seismic activity recorded, giving confidence that the detector is sensitive to seismic events. Note that a spike is not always present for every instance of seismic activity, likely given the dependence on the strength and exact proximity of the event to the detector and the probability of PMTs to emit flashers at any given point in time. In this way, we identify "seismic-correlated" and "non-seismic" data in a given run. A comparison of the tag plots (akin to the ones presented for the calibration data) for seismic-correlated and non-seismic subruns from the same run can be seen in Fig. 4.20. The "banana" shape is only present above the main population in the seismic-correlated subrun, which occurs in a more positive area of classifier space compared to the physics data, as expected for flasher candidates. In order to ensure this population corresponds to the spike, the plot is trimmed to a period of time surrounding the spike, and the result is shown in Fig. 4.21. While some normal physics data is still present, the spike is mainly the banana shape, confirming the hypothesis that this is the flasher population. An event display of an example flasher candidate event from this spike can be seen in Fig. 4.22.

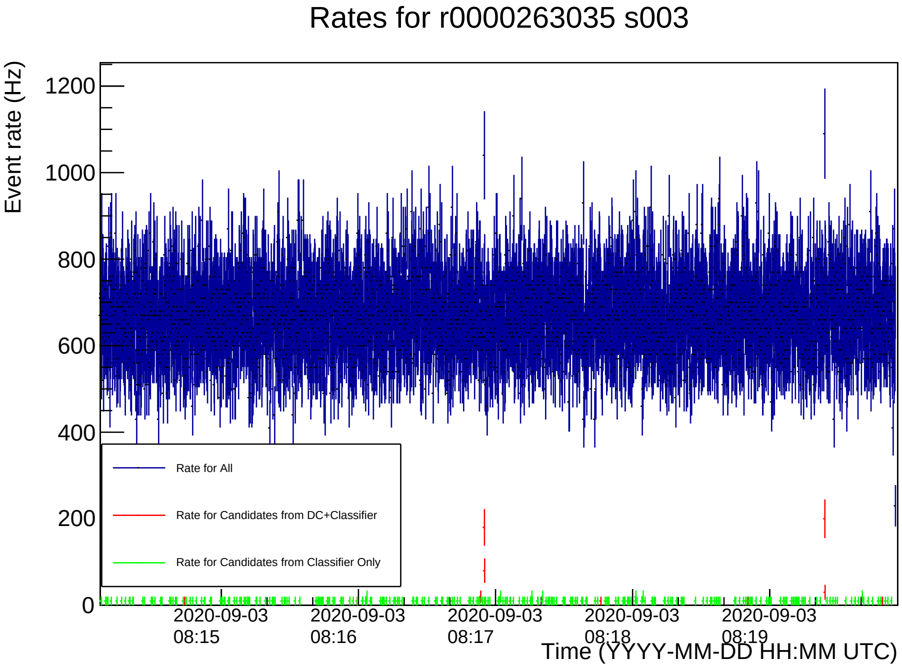

Figure 4.19: The rate of all events, flasher candidates tagged by the data cleaning cuts and the flasher classifier, and flasher candidates tagged by the classifier only for a subrun corresponding to seismic activity.

By compiling events from many of these spikes together, the time residual distribution of the candidate events tagged by both the data cleaning cuts and the classifier is observed, which can be seen in comparison to the PDFs used for the classifier in the left plot of Fig. 4.23. While the structure is somewhat different, including the bump toward 100 ns, similarity to the simulated flasher MC timing is readily apparent. Notably, the 100 ns bump disappears when considering only candidates from the seismic spikes, as shown in the right plot of Fig. 4.23. While the classifier is not highly efficient at tagging flashers on its own, its use in conjunction with the data cleaning cuts allows for the selection of cleaner samples of instrumental events.

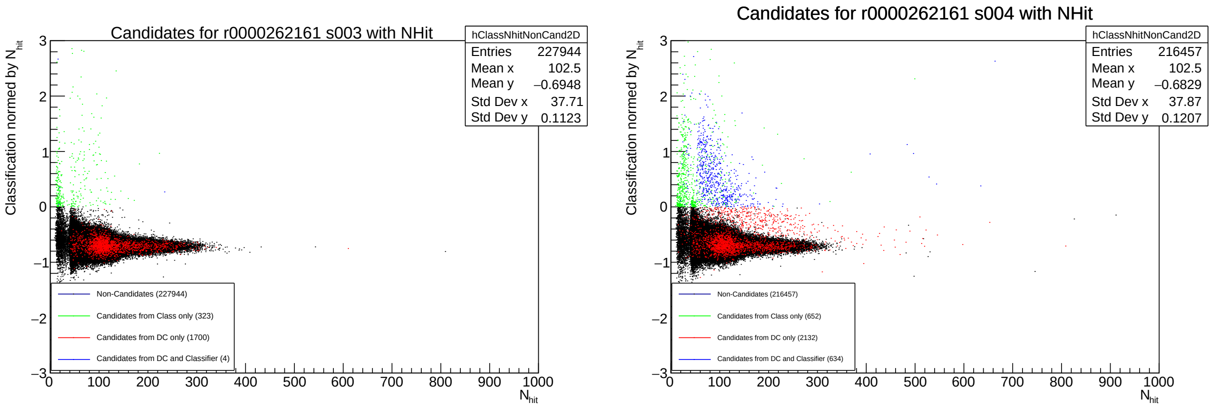

Figure 4.20: Flasher tagging for a subrun without seismic activity (left) and one with seismic activity, from the same run. Note the population present only in the seismic-correlated subrun in the banana-shaped region in the positive classifier value half-plane above the population of physics events observed in both subruns. These are the instrumental events.

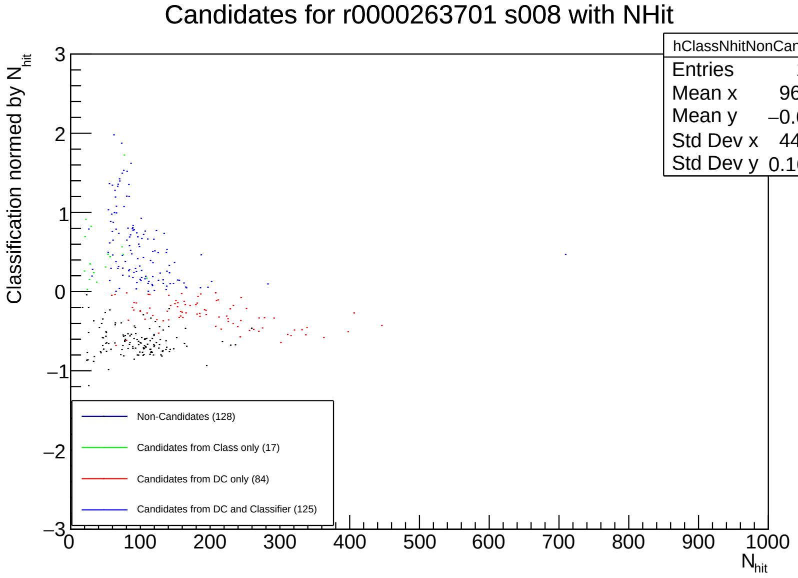

Figure 4.21: Tagging when considering only the region 0.15s around a rate spike, as defined bin-by-bin on the rate plots. In this case, the non-candidate event sample is reduced to be less than half of the flasher candidate sample, though this is not always the case. The method is somewhat crude but reproduces the expected behavior that the banana-shaped region contains the flasher candidates.

It is important to note that no constraint was imposed on this study related to the way the flashers would travel through the detector (i.e. whether they took paths predominantly

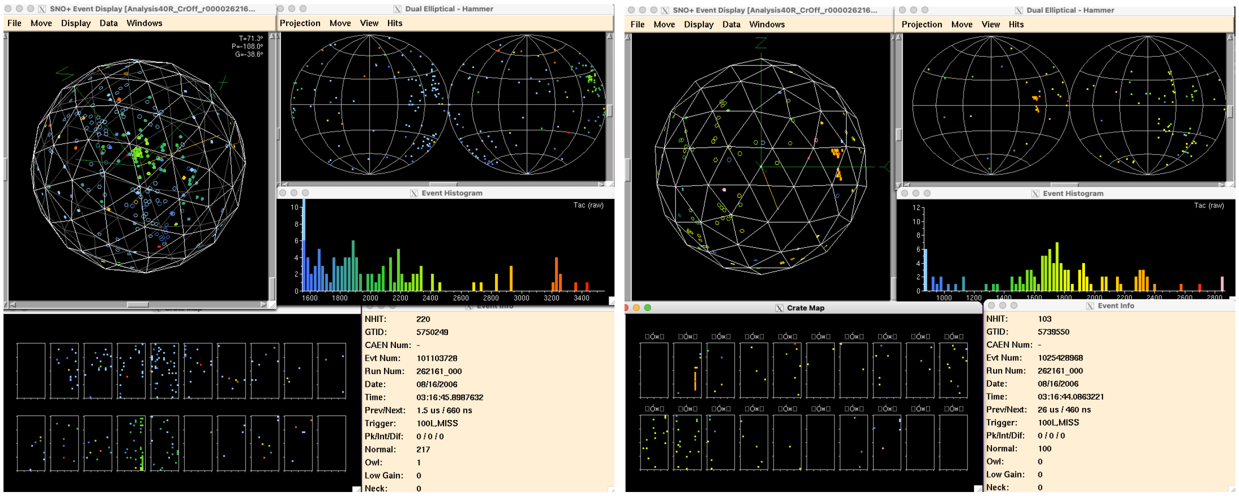

NHIT: 220
GTID: 5750249
CAEN Num: -
Evt Num: 101103728
Run Num: 262161_000
Date: 08/16/2006
Time: 03:16:45.8987632
Prev/Next: 1.5 us / 660 ns
Trigger: 100L,MISS
Pk/Int/Dif: 0 / 0 / 0
Normal: 217
Owl: 1
Low Gain: 0
Neck: 0

NHIT: 103
GTID: 5739550
CAEN Num: -
Evt Num: 1025428968
Run Num: 262161_000
Date: 08/16/2006
Time: 03:16:44.0863221
Prev/Next: 26 us / 460 ns
Trigger: 100L,MISS
Pk/Int/Dif: 0 / 0 / 0
Normal: 100
Owl: 0
Low Gain: 0
Neck: 0

Figure 4.22: Event displays of examples of flasher candidates from SNO+ Run 262161.

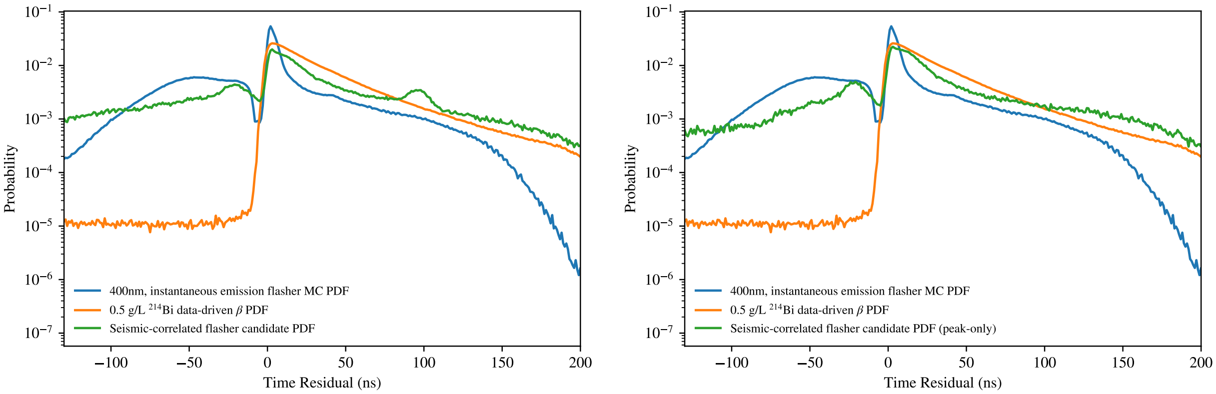

Figure 4.23: The extracted timing for flasher candidates in the seismic data compared with PDFs used for the flasher classifier analysis (left) with the extracted timing for flasher candidates in the seismic data restricted only to events in peak regions compared with PDFs used for the flasher classifier analysis (right). Normalization is by area for all curves in both plots.

through the scintillator or through the water in the partially-filled detector), though the calibration data is all within the scintillator volume. The next section, using full fill data (though with a lower PPO loading than the final scintillator phase cocktail), will address some of the concerns that might be raised about the efficacy of this methodology.

4.8.2.3 Performance on Instrumental-Heavy Data in Full Fill

After filling with LAB was completed, a period of anomalous running was identified as having a high probability of containing many flashers, based on known pathologies of instrumental problems during detector operations. The runs in question are 274179-274183 and 274186. Similar checks were performed as with the partial fill data, using the same PDFs as the partial fill period, despite the detector at this point in time being filled with scintillator. Luckily, similar behavior as in the seismic-correlated data is evident. This can be seen in the rate plots of Fig. 4.24 and the corresponding scatter plots of Fig. 4.25.

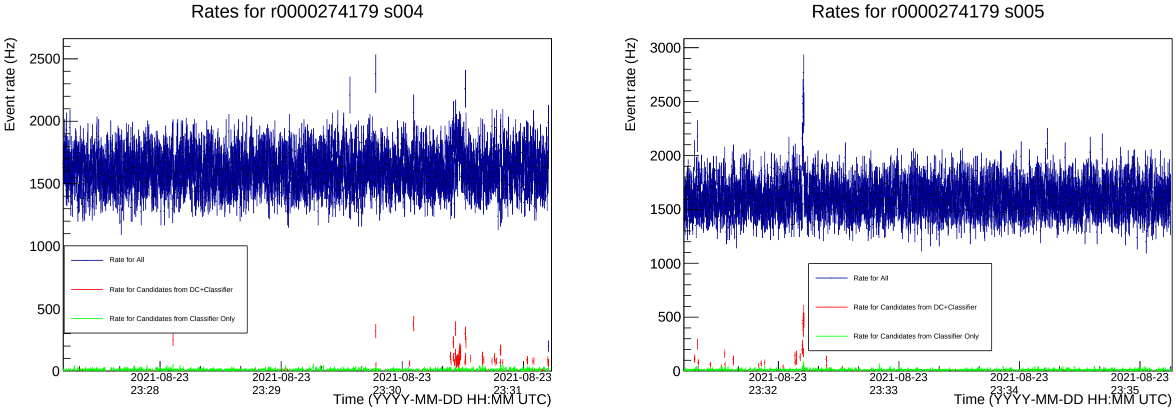

Figure 4.24: The rate of all events, flasher candidates tagged by the DC cuts and the flasher classifier, and flasher candidates tagged by the classifier only for two subruns in the period with known instrumental issues. The combination of the flasher classifier and data cleaning cuts picks out the anomalous behavior.

As such, it is clear that the flasher classifier still performs in the fully-filled detector, and the concerns raised earlier about whether the scintillator has impacted the flasher timing due to the partial fill geometry are mitigated. The time residual distribution for the candidate events tagged by both the data cleaning cuts and the classifier for this period of running can be found in the left plot of Fig. 4.26, which displays slightly different features from the timing in the partial fill detector. While it retains the bump at 100 ns and the early time structure, the area around $t = 0$ is distinct from the PDFs and also from the observed flasher timing in partial fill. Unlike the partial fill data, when restricting to regions with excessive tags, the 100 ns bump does not go away, which requires further study.

Even at this prototype stage, the flasher classifier has apparent value. It is not at this point highly efficient as is desirable, but it does allow the identification of events that are clearly flasher-like, especially when used in conjunction with the data cleaning cuts that no longer perform as well on their own. Due to the fact that instrumental backgrounds like flashers are hard to isolate and hard to simulate, it is not straightforward to provide a quantification of performance. With revisions to the scintillator optical model and the addition of charge information into the likelihood, the performance is nevertheless expected

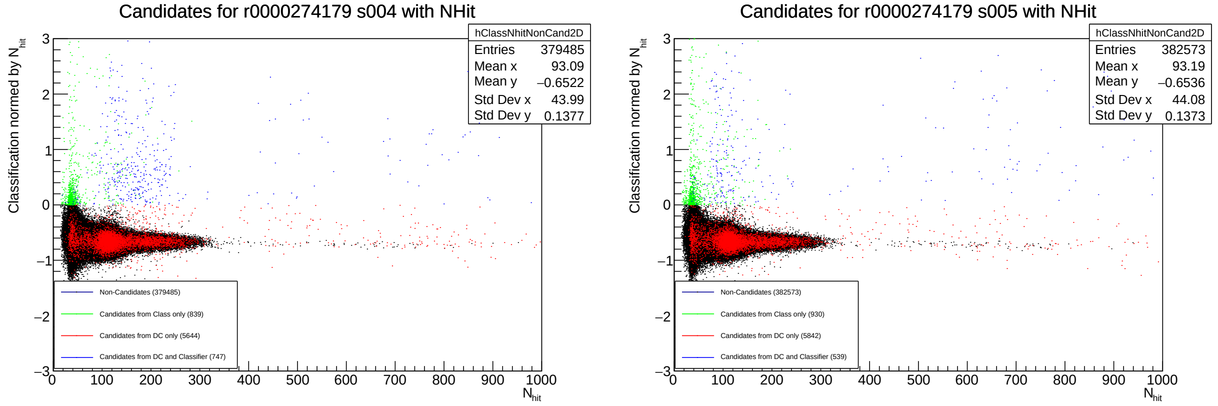

Figure 4.25: The tagging plots for two subruns in the period with known instrumental issues. The flasher classifier in conjunction with the data cleaning cuts picks out clear activity that are not good physics events.

to improve. The classifier is set to be deployed in conjunction with lower energy analyses to build on the proof-of-concept demonstration provided here.

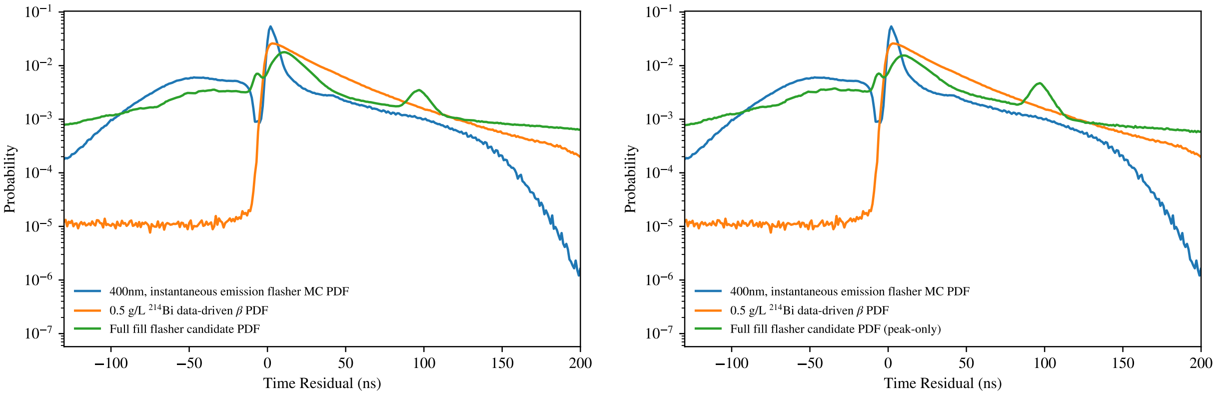

Figure 4.26: The extracted timing for flasher candidates in the anomalous full fill data compared with PDFs used for the flasher classifier analysis (left) with the extracted timing for flasher candidates in the anomalous full fill data restricted only to events in peak regions compared with PDFs used for the flasher classifier analysis (right). Normalization is by area for all curves in both plots.

Chapter 5

Measurement of the ^{8}B Solar Neutrino Flux with SNO+

Building on the previous chapter's discussion of the SNO+ detector, this chapter will discuss two related analyses to determine the ^{8}B solar neutrino flux using the varied scintillator exposures of the SNO+ dataset.

5.1 Solar Neutrino Flux Analysis Motivation

The ^{8}B solar neutrino flux has been directly measured with great success by previous optical neutrino detector experiments SNO [63], SuperK [62], Borexino [66] and KamLAND [65]. As discussed in the previous chapter, SNO+ has also measured this flux during its water phase [67], with an updated measurement using the full water phase dataset soon to be published. At the time of writing, the global experimental fit with the luminosity constraint [53] finds a flux of $\Phi_{^{8}\mathrm{B}} = (5.20 \pm 0.10) \times 10^{6}\,\mathrm{cm}^{-2}\mathrm{s}^{-1}$, for a fractional error of less than 2%. In that sense, SNO+ on its own will not shatter our current understanding of the Sun's ^{8}B neutrino production level, but the results discussed below serve to reinforce the set of measurements performed in similar detectors. Given the depth of SNOLAB, the good energy resolution of the SNO+ scintillator and SNO+'s size relative to previous scintillator experiments, a final measurement by SNO+ should be competitive with Borexino's in the long term, since SNO+ will be able to continue its sensitivity to the higher energy portions of the ^{8}B spectrum even into the Tellurium phase of experiment.

Beyond that, measurement of the ^{8}B flux in scintillator serves a valuable purpose for SNO+ as an experiment. Firstly, because the ^{8}B flux is so well-known, applying experimental techniques to measure this source can provide a benchmark for measurements of less well-understood signals such as lower energy solar neutrino fluxes as well as for deeper investigations of the ^{8}B solar neutrino spectrum including its shape and evolution over time. In this sense, the ^{8}B flux measurements serves as a calibration for other SNO+ scintillator analyses, in addition to being a physics measurement in its own right. Related, this measurement allows for the comparison of experimental methods as applied to the same source using two different target materials, by leveraging the water phase measurement. This serves as an important cross-check that the scintillator model is well-understood and no serious deviations in other systems have occurred that would manifest as significant systematic uncertainties. Finally, the ^{8}B flux is the contribution that accounts for the plurality of the $0\nu\beta\beta$ background budget. While constraints from the very precise global solar fit will obviously have the strongest affect on $0\nu\beta\beta$ measurements, possessing a sideband measurement of this source in the same detector gives substantial confidence to employing constraints from more precise determinations.

5.2 Detection Principle

The interaction of interest from the solar neutrinos in SNO+ is the neutrino-electron elastic scattering (ES) process, one of the three channels also exploited by SNO. In this process, the ingoing neutrino ejects an electron bound to an atom in the target material. The electron then will deposit energy in the target, which in this case is the scintillator. The scintillator then produces light, which traverses the detector media, and whatever of that light reaches the photodetectors, either directly or indirectly, is observed as the signal. By observing these events along with any present background signals and applying statistical techniques, the number of ES events over a dataset can be found. With the number of observed events and the corresponding expectation given an assumed flux, one can then recover the observed flux.

5.2.1 Signal

To determine the expected number of ES interactions occurring within the target volume of the detector as a function of detector datataking time (regardless of whether these interactions are detected), there are several factors to consider. Firstly, absent any information about the incoming neutrino content, the rate is governed by the underlying cross-section for this process, which, as discussed in Sec. 2.3.2, is flavor-dependent, as well as neutrino energy dependent. The atomic electrons are treated as at rest and unbound. Given the fact that in comparison to the MeV-scale of the solar neutrinos, the ionization energies are typically well below 1 keV, especially for the low-Z elements and molecules found in a scintillator target, this is a good approximation in this case. In his seminal work *Neutrino Astrophysics* [46], Bahcall finds the following integrated cross section for this process as a function of neutrino energy, without considering radiative corrections

$$\sigma(E_\nu) = \frac{2G_F^2 m_e^2}{\pi}\left(\frac{g_l^2 + g_r^2}{m_e}T_{\max} - \left(\frac{g_r^2}{E_\nu m_e} + \frac{g_l g_r}{2E_\nu^2}\right)T_{\max}^2 + \frac{g_r^3}{3E_\nu^2 m_e}T_{\max}^3\right), \tag{5.1}$$

where G_F is the Fermi coupling constant, $g_r = \sin^2\theta_W$ is the square of the sine of the Weinberg weak-mixing angle, $g_l = g_r \pm 1/2$, positive for ν_e and negative for ν_μ and ν_τ, m_e is the electron mass, E_ν is the incoming neutrino energy and $T_{\max}$ is the maximum allowed kinetic energy of an electron scattered by a neutrino with energy E_ν, that is

$$T_{\text{max}} = \frac{2E_\nu^2}{m_e + 2E_\nu}. \tag{5.2}$$

While not important for understanding the total interaction rate, the differential cross section with respect to outgoing electron energy T_e, valuable to understanding the observed energy spectra that will underpin the analysis, is convenient to introduce at this moment as well. Bahcall, again without radiative corrections finds

$$\frac{d\sigma}{dE_\nu dT_e}(E_\nu, T_e) = \frac{2G_F^2 m_e^2}{\pi}\left(g_l^2 + g_r^2\left(1 - \frac{T_e}{E_\nu}\right)^2 - \frac{g_l g_r m_e}{E_\nu^2}T_e\right). \tag{5.3}$$

There are radiative corrections associated with each of the three terms in the parentheses, denoted f_+, f_- and f_{+-} respectively, which depend on the ratio of T_e to E_ν, and the couplings g_r and g_l also develop an energy dependence. Note that the full treatment with radiative corrections is included when calculating the total and differential cross sections in RAT, which has the effect of changing the cross sections at the level of a few percent, depending on E_ν. These values are used throughout the analysis.

The second piece to consider is that of the flavor content of the incident flux of neutrinos. This encapsulates three separate pieces: the overall flavor-independent flux of ^{8}B solar neutrinos at Earth, the energy-dependent shape of the flux defined by the kinematics of the ^{8}B decay in the Sun, and the survival probability $P_{ee}(E_\nu)$ that governs the amount of the flux composed of electron flavor neutrinos compared to μ or τ flavor neutrinos (because ν_μ and ν_τ behave identically for the ES interaction at the relevant energies, the non-ν_e flux will be referred to as the ν_μ flux for simplicity). For the assumed flux, the B16 GS98 SSM flux of $\Phi_{^8\text{B}} = 5.46 \times 10^6\ \text{cm}^{-2}\text{s}^{-1}$ [52] is used. While more recent models exist [54], the majority of work on the foregoing analyses was completed before the release of the newer models, and given the fact that this value is an overall scale, any change simply enters as a multiplicative factor to the final result.

For the assumed energy spectra of the flux, the Winter spectrum [194] recommended by Solar Fusion II (SF-II) [195] is used, which gives an endpoint around 15.6 MeV. Reading Eq. (5.2), this corresponds to a maximum electron kinetic energy of 15.3 MeV, though the vast majority of scattered electrons will have a kinetic energy below this. To supplement the Winter spectrum, the newly released SF-III [55] suggests additional evaluation with respect to the newer Longfellow spectrum [196] for searches with sensitivity to the spectral shape. Because, unlike a search for *hep* neutrinos, this analysis is not overly sensitive to the exact choice of spectral shape, and because the bulk of this work was completed before the new recommendations were published, only the Winter spectrum is considered.

Finally, the survival probability of the neutrino events is calculated separately from the `PSelmaa` software package originally developed by Nuno Barros for SNO and now maintained by SNO+ [180], as a function of energy, using the B16 GS98 Standard Solar Model [52] and the best fit mixing parameters values from PDG20 [197], as given in tab. 5.1. `PSelmaa` uses the adiabatic approximation when determining the survival probability and accounts for the location of the nuclear reaction within the Sun, and so the P_{ee} result is also flux-dependent.

The code also includes regeneration effects, important for studying day-night asymmetry and other shape distortions, though for this analysis, only a representative P_{ee} curve irrespective of $\cos\theta_{\text{Sun}}$ is used given the weak dependence.

Table 5.1: The oscillation parameters to produce the P_{ee} and $P_{e\mu}$ curves with `PSelmaa`, from PDG20 [197]

Parameter	Used Value
Δm^2_{21}	7.53×10^{-5}
Δm^2_{31}	2.53×10^{-3}
$\sin^2\theta_{12}$	0.307
$\sin^2\theta_{13}$	0.0220

See fig. 5.1 for the produced curve, which is linearly interpolated for each neutrino scattering event based on the parent neutrino energy and source flux (as either P_{ee} for ν_e or $1 - P_{ee}$ for ν_μ). The simulation of solar neutrinos in RAT is produced according to the unoscillated neutrino energy spectrum and the unoscillated flux is assumed for the normalization so that a variety of survival probability models may simply be applied through weighting events by the parent neutrino energy. This approach is useful, for example when considering non-standard interactions that deviate from the current model. The numerical values used for the ^{8}B ν_e and ν_μ survival probabilities can be found in the appendix App. A.

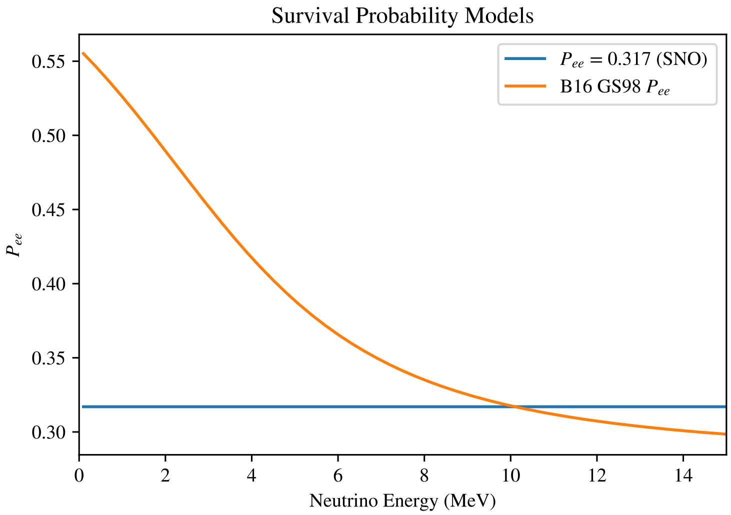

Figure 5.1: The survival probability P_{ee} as calculated in `PSelmaa` using the B16 GS98 Standard Solar Model and the PDG20 mixing parameters, as a function of neutrino energy. Also plotted is the best fit value for the flat contribution to the P_{ee} as measured by SNO [63].

The last piece to consider when calculating interaction rate is the number of expected targets within the detector, which in this case means identifying the number of electrons present in the scintillator mass, N_e. Because not all LAB molecules are the same length and therefore have different molecular weights and number of molecular electrons, careful treatment is needed. Relevant values are shown in Tab. 5.2, for a representative sample of LAB. The total mass of scintillator must also be known with some precision; though given the low concentration of PPO, that contribution is relatively safe to ignore.

Table 5.2: The expected LAB composition by chain, as well as the associated molar mass and electron number per molecule for each chain. The composition here is found from mass analysis of a representative sample of pure LAB. Variation on the few-percent level is expected based on the batch produced by the supplier, and the longest chains may be partially removed through the distillation process used to purify the scintillator.

LAB Chain	$C_{15}H_{24}$	$C_{16}H_{26}$	$C_{17}H_{28}$	$C_{18}H_{30}$	$C_{19}H_{32}$
Mass Fraction	0.012	0.204	0.432	0.334	0.018
Molar Mass (g/mol)	204	218	232	246	260
Electron per Molecule	114	122	130	138	146

Because we do not know the total mass of each scintillator chain, we define an effective molar mass and electron number per molecule based on the expected proportions of chains, such that

$$N_e = \frac{n_{e,\mathrm{LAB}} N_A M_{\mathrm{LAB}}}{m_{\mathrm{eff,\ LAB}}} \tag{5.4}$$

where $n_{e,\mathrm{LAB}}$ is the effective electron number per LAB molecule defined as a weighted average according to Tab. 5.2, $m_{\mathrm{eff,\ LAB}}$ is the effective molar mass defined in the same way, M_{LAB} is the total mass of scintillator in the detector and N_A is Avogadro's number. For these proportions, $n_{e,\mathrm{LAB}} = 131$ and $m_{\mathrm{eff,\ LAB}} = 234$ g/mol (using the proportions from a different batch of LAB yields $m_{\mathrm{eff,\ LAB}} = 235$). For the partial fill, M_{LAB} was found to be 365 t, whereas in full fill, this was 780 t, giving $N_e = 1.23 \times 10^{32}$ electrons and $N_e = 2.63 \times 10^{32}$ electrons respectively.

Then, integrating over the neutrino energy spectrum, the interaction rate is

$$R_{^8\mathrm{B}} = \int N_e \Phi_{^8\mathrm{B}} S_{^8\mathrm{B}}(E_\nu) \left(P_{ee}(E_\nu)\sigma_e(E_\nu) + (1 - P_{ee})\sigma_\mu(E_\nu)\right) dE_\nu, \tag{5.5}$$

where $R_{^8\mathrm{B}}$ is the interaction rate, N_e is the number of electron targets, $S_{^8\mathrm{B}}(E_\nu)$ is the spectral shape of the ^{8}B neutrinos, $P_{ee}(E_\nu)$ is the survival probability as function of neutrino energy and σ_e and σ_μ are the cross section for the ES interaction for ν_e and ν_μ respectively. Assuming the flux is constant over time, the total interaction during a period of datataking (or "livetime") of length t_{live} is then just

$$N_{^8\mathrm{B}} = t_{\mathrm{live}} \times R_{^8\mathrm{B}} \tag{5.6}$$

In truth, there is some variation due to the eccentricity of Earth's orbit, which is not perfectly circular, and because the solar activity is not constant over time, which would require a more careful integration with respect to time. These effects are small, and more impactful on analyses that are particularly sensitive to the shape of the observed spectrum, rather than the magnitude.

5.2.2 Backgrounds

To avoid being encumbered by a variety of radioactive backgrounds, as well as other solar neutrino signals, for little gain in sensitivity to the ^{8}B flux, the focus of the analysis in both phases is in a relatively pure energy region of interest. In this region with $E \gtrapprox 2.5\,\mathrm{MeV}$, the only backgrounds of importance arise from internal scintillator contamination from daughters of the ^{232}Th and ^{238}U chains, as well as gammas from these chains that ingress into the fiducial volume from external detector components.

5.2.2.1 Internal ^{232}Th and ^{238}U

^{232}Th and ^{238}U and their daughters can find their way into the scintillator through particulate matter, as well as outgassing from detector components and external sources in the form of radon. While the SNO+ scintillator has achieved high purity, contaminants from these chains still remain. In this region, the problematic backgrounds arise from the ^{208}Tl ($Q_\beta = 5.0\,\mathrm{MeV}$) decay of the Th chain and ^{214}Bi β-branch ($Q_\beta = 3.27\,\mathrm{MeV}$) and ^{210}Tl ($Q_\beta = 5.48\,\mathrm{MeV}$) decays of the U chain. While several α decays occur with kinetic energy in the energy ROI (for example ^{210}Po at $Q_\alpha = 5.4\,\mathrm{MeV}$), because of the α quenching of the scintillator, these do not present as a background here, with all of those decays falling to effective energies of $< 1.5\,\mathrm{MeV}$.

In principle, with no further information and purity reaching the level of sensitivity of external measuring devices, the background rates associated with these two decay chains would not be knowable outside of the measurement about to be performed. However, the ^{214}Bi background serves a dual role in that it can also aid in constraining the U chain contamination in sideband, due to the coincidence decay of ^{214}Po, the next decay in the U chain. While not serving as a background as its $Q_\beta = 2.25\,\mathrm{MeV}$ falls below the analysis energy threshold, the ^{212}Bi β-branch decay on the Th chain serves plays a similar role due to the coincidence this decay has with the ^{212}Po α decay. As discussed in Sec. 4.8.1, these BiPo decays can be isolated due to their time coincidence and energy properties, harkening back to techniques drawn on from the start of neutrino detection. Using careful modeling of the efficiencies of the selection criteria used, one can back out estimates for the concentration of the contaminants in the scintillator.

Unsurprisingly, the same technique can also be deployed to remove the problematic ^{214}Bi backgrounds from the dataset, rather than simply select for them. This requires a distinct tuning of the tagging cuts to reject as many coincidence candidates as possible without rejecting a significant amount of signal, whereas the sideband measurement configuration requires cuts that select only true BiPo decays with high probability, even if they do not isolate all of them.

Of course, this tagging procedure only works assuming that the BiPo decays occur in two separate triggered event windows. This is not always the case, especially for the faster ^{212}BiPo decay, which has the governing for the Polonium half-life $t_{1/2} = 294\,\mathrm{ns}$ being quite close to the trigger window length of 400 ns. This means that the Bi and Po decays may "pile-up" into the same triggered event window, and would no longer be discernible by the tagging procedure. These are referred to as "in-window" BiPo events, compared to "out-of-window" BiPo events, which can be tagged. This distinction is only relevant as SNO+ does not employ a continuous readout stream and instead chunks data into windows of fixed length based upon triggers. For a longer trigger window, more events would be in-window compared to out-of-window. One could even imagine a more flexible readout scheme that captures variable length event windows to better confine coincidences to the same chunk of data and do away with the distinction altogether (though the efficacy of such a system is dependent on the rate in the detector). All is not lost though: a separate technique has been developed for SNO+ based on the time residual distributions to classify events based on whether they have a multi-peak structure in their time spectrum. Single decay events in SNO+ will only have a prompt peak, centered around $t_{\mathrm{res}} = 0$, whereas events with two or more decays may display multiple peaks, depending upon the time proximity of the decays. This technique is called `alphaBeta` and has been tuned for rejection of both ^{212}BiPo and ^{214}BiPo backgrounds compared to electron-like signals using a likelihood-ratio test (n.b. this is not the same tool as the `BerkeleyAlphaBeta` technique designed to discriminate between α and β events).

Specifics for how these three mechanisms (i.e. coincidence tagging for sideband measurement, coincidence tagging for background rejection, and time-residual-based classification for pileup rejection) are employed in the distinct datasets is discussed further below.

5.2.2.2 External Backgrounds

The other primary background to the ^{8}B search comes from γ rays produced external to the scintillator volume ingressing and scattering inside the target. In particular, the 2.6-MeV γ from the ^{208}Tl decay presents a significant challenge, though γs from other isotopes such as ^{214}Bi contribute as well. As with the scintillator itself, the materials comprising the other detector components were procured with high radiopurity standards, but they still carry some non-zero contamination. As discussed in Sec. 4.1.1 and shown Tab. 4.2, the contributions from the external water, acrylic vessel, and supporting ropes and PMTs have all been measured during the water phase, providing an additional constraint.

The primary means with which external backgrounds can be reduced is by limiting the fiducial volume of the analysis to more central regions by applying a selection cut on the reconstructed radial coordinate. This is also the reason to add the radial dimension to the fit, as more information can be gleaned from the event distributions further afield that would otherwise be removed by a hard cut, though this has the downside of requiring more precise modeling in the more optically-complex outer regions. The motivation for this approach is the fact that these backgrounds are caused by γs, which can travel appreciable length scales before scattering electrons. The accompanying βs from the same decays do not observably travel, and produce very little light in the acrylic, other plastics in the ropes, cavity water and PMT glass. The effect of these γs can be limited by the fact their intensity diminishes due to attenuation $\propto e^{-\frac{x}{\ell}}$, where ℓ is the Compton scattering length. This exponential dependence means that distancing the fiducial volume from these external components can have a substantial effect. This attenuated intensity then shows up in the distribution of external background events with position, which tails off toward the center of the detector, in contrast with the uniform nature of the distribution with position for radioactive backgrounds from internal contamination and from the solar neutrino scatters.

The story, luckily, is not over there, as there are still ways for SNO+ to reject these backgrounds even if they enter a chosen a volume. Yet again, the time-residual distributions for events hold the key. Due to the kinematics of Compton scattering, events from external backgrounds typically contain multiple scatters within the same time window. While SNO+ does not currently employ a multi-vertex fitter to identify each of these locations, the time residual distribution under the single vertex hypothesis is still subject to broadening in the presence of multiple vertices occurring in a short period of time. This opens the door for an "external timing classifier" called `ext0NuTimeTl208AVNaive`, so named for its primary purpose of discriminating between $0\nu\beta\beta$ and ^{208}Tl gammas from the acrylic using timing, though its applicability is more generic. Additionally, there is also anisotropy for the earliest PMT hits relative to the reconstructed event position. Of the little light produced at the decay vertex, the closest PMTs to the decay will register hits first. Because inward going γ are most likely to be detected, the reconstructed position (defined from the center) will then point in the direction of the decay, and so in the direction of the early hit cluster as well. This is leveraged as an "external topological classifier" called `ext0NuAngleTl208AV`, for similar reasons.

5.2.2.3 Considerations for Other Sources

As discussed in Sec. 4.8.2, SNO+ and similar detectors are subject to a class of backgrounds that are produced by the detector electronics, which can confoundingly appear to be arising through particle interactions within the detector. These instrumental backgrounds typically reconstruct at low energies, if they validly reconstruct at all, though the low-level data cleaning cuts are still applied regardless of energy ROI, as the sacrifice to the signal is tuned to be quite low.

While SNO+'s depth means that its muon rate is minimal, and the rate of production of any muon-associated products is likewise small, steps are still taken to remove the muons and a subsequent period of data offline during analysis. This helps to avoid Michel electrons, short-lived spallation products, activated isotopes and other products from the muon. Even with a low rate, a veto of this nature has a strong impact on the livetime associated with the dataset, so careful consideration is given to calculation of the deadtime incurred. Historically, muon vetos in SNO+ rely primarily on the outward looking (OWL) PMTs that view the cavity external to the PSUP, but a more simplified high N_{hit} veto was also devised for the beginning of scintillator operations due to the observation of bursts of anomalous events believed to be caused by instrumentals.

Though most radioisotopes are plainly eliminated by either the energy threshold of the analysis or by vetoing after muon passage through the detector, due to pervasive presence of α decays, isotopes may also be activated in (α, n) reactions. The most common occurs when ^{12}C absorbs an α and produces ^{16}O and n. Depending on whether the ^{16}O nucleus is produced in an excited state, or how the outgoing neutron thermalizes, the resulting observation in the detector may be different, though there will be some form of a detectable prompt signal before the neutron captures within the volume on ^{1}H, providing a 2.2-MeV γ. This means that standard delayed coincidence rejection techniques can be employed and fortuitously given the comparable capture time for the neutron, the OOW tagging developed for removing BiPo events is strongly efficient at rejecting (α, n) candidates within the energy ROI. Similarly, atmospheric neutrino events with neutron followers may also be rejected on the same basis.

5.3 Analysis Method

In order to measure the flux, a binned maximum likelihood fit in energy (E) and radial position (R^3/R^3_{AV}) is performed, subject to Gaussian constraints, for the normalizations of the ^{8}B neutrino signal from elastic scattering interaction and the above-mentioned radioactive backgrounds. The fit dimension in energy provides information about the recovered spectral shape, important in leveraging known spectra information about the solar neutrino signal and radioactive decay backgrounds to aid in recovering the associated rates. The radial dimension differentiates the (assumed) uniformly distributed solar neutrino signal and internal backgrounds from the external backgrounds, which attenuate toward the center of the detector. Detection in any particular bin is considered to follow a Poisson process and, because the sum of Poissons is also a Poisson, the total rate should also follow a Poisson distribution. The precise details of the fit in each dataset are described in the sections below, though a general description follows here, informed by the frequentist methods of the Statistics section of the PDG [20]. The log likelihood takes the form

$$-\ln \mathcal{L}(\boldsymbol{\lambda}|\boldsymbol{n}) = \sum_{i=1}^{N_{\text{bins}}} \Big[\sum_{j}^{N_{\text{par}}} \lambda_j \mathcal{N}_{j,i} - n_i \ln \left(\sum_{j}^{N_{\text{signal}}} \lambda_j \mathcal{N}_{j,i} \right) - n_i + n_i \ln n_i \Big] + \sum_{k}^{N_{\text{par, constrained}}} \frac{(\lambda_k - \bar{\lambda}_k)^2}{2\sigma_k^2} \tag{5.7}$$

Here $\boldsymbol{\lambda}$ is the vector of normalization parameter values in the fit, N_{bins} is the number of bins, N_{par} is the number of individually floated parameters, $\mathcal{N}_{j,i}$ is the expected number of interactions occurring in bin i for parameter j (obtained from the PDF associated with this parameter), n_i is the number of observed data events occurring in bin i, $N_{\text{par, constrained}}$ is the number of parameters subject to constraint, $\bar{\lambda}_k$ is the considered externally measured value considered for the parameter λ_k, and σ_k is the externally measured parameter error. Usually, one discards the terms independent of the fit parameters in the likelihood, as they vanish in the derivative which is used in the minimization, as they are constants.

PDFs for the relevant signals and backgrounds are prepared by simulating each with detector conditions on a run-by-run basis using RAT. MC events are subjected to a variety of selection cuts, discussed further in Sec. 5.4 and Sec. 5.5, and binned into histograms that serve as the PDFs. Background PDFs give each passing event a weight of 1 and are normalized by the total number of simulated events. Signal PDFs from the solar neutrino simulation are given a weight corresponding to the survival probability associated with the parent neutrino energy (P_{ee} for ν_e and $1-P_{ee}$ for ν_μ) and are normalized by the total number of simulated events, in this way respecting both the oscillation of neutrinos and the selection cuts applied to the subsequent electron scattering events. Unless explicitly noted below, the same selection cuts and binning are also applied to the data.

In this sense,

$$\sum_{i=1}^{N_{\text{bins},E}} \sum_{j=1}^{N_{\text{bins},R^3/R^3_{\text{AV}}}} P(E_i,(R^3/R^3_{\text{AV}})_j) \leq 1 \tag{5.8}$$

Here, i specifies the energy bin and j specifies the radial bin, with $N_{\text{bins},E}$ $N_{\text{bins},R^3/R^3_{\text{AV}}}$ representing the total number of bins in the energy and radial dimensions.

For signals or backgrounds controlled by the same normalization parameter (such as ν_e and ν_μ for ^{8}B neutrinos, or daughters in a decay chain at secular equilibrium), their PDFs are combined weighted by their respective normalizations and scaled by the livetime t_{live} to create a single PDF for that parameter. In other words, we define,

$$N(E_i,(R^3/R^3_{\text{AV}})_j) = \sum_{\substack{\text{signals } k \\ \text{with same par.}\lambda}} t_{\text{live}} N_k P_k(E_i,(R^3/R^3_{\text{AV}})_j) \tag{5.9}$$

This definition ensures that the parameter λ associated with each signal PDF is conveniently equal to 1 in the nominal case (i.e. when the measure parameter value is equal to expectation) for all PDFs. To give a bit of further explanation, $N(E_i,(R^3/R^3_{\text{AV}})_j)$ is the number of events expected passing cuts controlled by a given parameter λ in the bin corresponding to E_i and $(R^3/R^3_{\text{AV}})_j$, in t_{live} years of running. This arises as t_{live} is the number of years, N_k is the number of expected events of signal k in one year, and $P_k(E_i,(R^3/R^3_{\text{AV}})_j)$ is the fraction of events of signal k passing cuts in the bin corresponding to E_i and $(R^3/R^3_{\text{AV}})_j$ out of the total number of events of signal k before cuts and in all bins. This process is justified as for instance, if the production rate of ^{8}B neutrinos increased in the Sun, the proportion of ν_e to ν_μ should remain fixed, and likewise if the ^{232}Th contamination in the detector was higher by some factor, all the daughters should also rise by the same factor (assuming secular equilibrium).

With the binned data and PDFs in hand, appropriately scaled according to the expected event rates and livetime, the likelihood can then be minimized in order to find best fit parameters and associated errors. The minimization procedure for the likelihood proceeds using various `MINUIT` algorithms available in `ROOT`. A first minimization is performed using `SIMPLEX`, then `MIGRAD` is passed the results, and the `MIGRAD` result is considered the final minimum. `MINOS` is then used to extract the 1σ errors. Parameter values, errors, covariances, biases, symmetric and asymmetric pulls are tracked, as are the likelihood value and best fits. In order to assess sensitivity, fake data sets are generated and fit against, as well.

5.4 Partial Fill Analysis

5.4.1 Fit Overview

The partial fill detector phase featured a roughly hemispherical mass of scintillator sharing the AV volume with a corresponding hemisphere of water below it. While the water phase had vigorously explored the capabilities of SNO+ with a water target, partial fill enabled the exploration of scintillator performance for the first time, though the odd configuration and limited deployed mass presented some challenges as reconstruction in this configuration was not contemplated previously and calibrations were limited. As a result, the fit used to determine the ^{8}B flux was designed to be fairly straightforward and avoid complexities that would best be tackled by the symmetric, fully-filled configuration. As a result, a fiducial volume is chosen to avoid dealing with reconstructions near the internal interface of the scintillator, and the analysis threshold is raised to strongly preclude external backgrounds from entering the fit. Since calibrations were limited, a robust energy reconstruction was not developed, and as such the energy dimension of the fit uses N_{hit} as a proxy with 30 equal-width bins between 1000 to 4000 N_{hit}. Given the fact that the threshold is so high and, hence, external background contribution is heavily minimized, the radial dimension of the fit is discarded, though the fit is performed with multiple radial cuts in order to monitor any position-dependent effects. The fit considers the normalizations of 1 signal parameter and 2 background parameters, one of which is fixed due to a strong constraint and high correlation with the other background. The fit parameters include the normalizations for:

- ^{8}B (ν_e and ν_μ components floated together, after accounting for flavor-dependent spectral effects)
- Uranium chain, which includes ^{238}U, ^{234}Th, $^{234\text{m}}$Pa, ^{234}U, ^{230}Th, ^{226}Ra, ^{222}Rn, ^{218}Po, ^{214}Pb, ^{214}Bi (alpha and beta branch), ^{214}Po, and ^{210}Tl
- Thorium chain, which includes ^{232}Th, ^{228}Ra, ^{228}Ac, ^{228}Th, ^{224}Ra, ^{220}Rn, ^{216}Po, ^{212}Pb, ^{212}Bi (alpha and beta branch), ^{212}Po, and ^{208}Tl

Due to the threshold at approximately 3 MeV, essentially the only contribution from the U chain is ^{210}Tl, with ^{208}Tl from the Th chain, though all signals are considered together for completeness. Of note, there is a small residual contribution from ^{214}Bi to U chain that survives the coincidence cuts, despite the fact that endpoint for this decay is over the analysis threshold. Secular equilibrium is assumed to hold for the listed decays.

5.4.2 Run Selection

This analysis uses the "Preliminary Partial Solar" run list, which spanned from April 5, 2020 to October 24, 2020, though only a subset is used. This time period spans from the settling and homogenization of PPO in the scintillator volume following the pause induced by the COVID-19 emergency, to the recommencement of scintillator filling operations in the fall. While SNO+ applies several run selection criteria (such as runs being an appropriate length) in order to place the runs in the list in the first place, an analysis-specific criterion was applied that all runs used had all electronics crates operating. The absence of any crates at high voltage significantly distorts the reconstructed energy spectrum, especially because we rely solely on N_{hit} for this analysis. A full breakdown of the data files used can be found in Tab. B.1. These files have been processed using `RAT` 6.18.9 using the Analysis40R and Analysis40RP modules and include a total of 2694 runs, starting with run 257693 and ending with run 264716. The raw livetime for this runlist is 2228.2 hours or 92.84 days. Subject to the veto discussed in Sec. 5.4.3 used to reject the time after muons transit the detector and other high N_{hit} phenomena, this will noticeably be reduced due to the muon rate at SNO+ and the deadtime for each vetoing of the detector is 20 seconds. It is important to note that the veto may span multiple runs and subruns and may be extended if another triggering event occurs within the original veto window. As a result, the calculation is not as simple as multiplying the number of vetoes by a fixed length. A routine to account for these cases provides a total deadtime over this period due to veto of 18.98 hours. This means the total livetime over the entire period is reduced to 2209.21 hours.

MC simulations from `RAT` are used as the basis of the model in the solar fit, in order to extract the PDFs used for the likelihood fit. The MC used in this analysis comes from the run-by-run partial fill production performed using `RAT` 6.18.9 for all backgrounds aside from the ^{8}B ν_μ simulation, which was performed using `RAT` 6.18.12. Only the ^{8}B ν_e and ν_μ solar neutrino signals and signals belonging to the ^{232}Th and ^{238}U chain internal backgrounds are considered in the analysis. A full breakdown of the MC used can be found in Tab. B.2. The remainder of the simulated signals to do not pass the event selection cuts with any appreciable efficiency, as discussed in Sec. 5.4.3.

5.4.3 Event Selection

Before building the PDFs and binning the data, the SNO+ standard ntuple files for the data and MC are skimmed into a bespoke ntuple format that removes unneeded information and then combined into a single file to allow easier access.

Due to a physical mismatch between the AV center and PSUP center, an AV offset of 131.8 mm is used to correct the reconstructed z coordinate for all data and MC events, such that $z_{\text{corrected}} = z_{\text{uncorrected}} - 131.8$. This is performed such that the corrected value is saved for the z coordinate, and is additionally accounted for in the radius calculation and any cuts relying on position (either in the coincidence tagging discussed below or when skimming the data).

For the Monte Carlo processing, only the first trigger is accepted (except in the case of BiPo events) and a valid `partialFitter` position result is required for the information on an event to be stored. If an event does not trigger the detector in simulation or if the event does not have a valid reconstruction result, dummy values are used to differentiate these cases from events that successfully reconstruct. Retriggers are ignored except in the case of ^{212}Bi and ^{214}Bi β decays in order to account for the coincident Po decay that may retrigger the detector if it does not fall in the same event window, per earlier discussion. The events that are simulated but do not trigger the detector and invalidly reconstructed events are kept in order to properly compute the normalizations when constructing PDFs, with dummy values used to prevent accidental inclusion of these events in the PDFs while also still retaining the MC truth information and other aspects. Retriggers can be ignored entirely as the normalization used is the number of simulated physics events, not the total number of triggers.

At this stage, tags are applied to flag BiPo coincidences and events following muons, in order to make applying the coincidence cuts easier when constructing the PDFs and binning the data. The muon tag is only applied in data. For the BiPo tags, the rate of accidental coincidences (i.e. coincidences of two non-BiPo events, a non-BiPo event and a Bi decay or a non-BiPo event and a Po decay that meet the criteria) being flagged is found to be negligible, so additional scalings accounting for accidentals are not required on other backgrounds. Coincidences and vetos are considered over time-adjacent subruns of data, given the fact that there could be satisfying events over two different files, especially for vetos. The BiPo coincidence cut also removes retriggers of physics events that occur due to late light triggering the detector a second time, which may be the case if a BiPo coincidence occurs in-window but the Po decay comes towards the end. The coincidence tagging cuts are shown in Tab. 5.3. The specified data cleaning mask was used across all partial fill analyses in order to simultaneously apply cuts for events in data with bad trigger IDs, multiple hits on the same channel (even for multi-PE hits, only one set of output values should be recorded per channel), indications of the periodic detector electronics monitoring activity, missing trigger digitizations and multiple hits on the outward looking PMTs. The `skyShine` classifier was a tool developed to coarsely differentiate events occurring in acrylic vessel's neck during the partial fill based on hit topology. The high N_{hit} veto rejects any event with a $\Delta t < 20\,\text{s}$ after an event with cleaned $N_{\text{hit}} > 5000$. The Δt for pairs of events is calculated using the 50 MHz clock onboard the MTCD.

The data and MC is then subject to a set of cuts detailed in Tab. 5.4. These are similar to the prompt coincidence tag cuts, though restrict the N_{hit} region of interest and fiducial volume differently. Multiple fiducial volumes are selected to understand the uniformity over the volume of the fit in a simplified way compared to a fully two dimensional fit. At high

Table 5.3: Cuts used in the coincidence tagging procedure for BiPo rejection for the partial fill ^{8}B flux analysis. A "-" in the table indicates the given cut is not applied to either the prompt or delayed event, as listed. Only one of the "Fast Coincidence" or "Slow Coincidence" cuts need be passed to be flagged as a potential coincidence, though both may be. Several bound sanity checks on N_{hit}, `skyShine`, `alphaBeta212`, `alphaBeta214` and Δr that are used to exclude bad events and numerical expressions are omitted for clarity.

Criteria	Prompt Event	Delayed Event
Trigger? (MC only)	✓	✓
Passes data cleaning mask `0x210000000242` (data only)	✓	-
Valid `partialFitter` result	✓	✓
`skyShine`	Value > 1.0	Value > 1.0
Cleaned N_{hit}	$N_{\text{hit}} > 300$	-
r coordinate	$r < 6\,\text{m}$	$r < 6\,\text{m}$
z coordinate	$z > 1\,\text{m}$	$z > 0.5\,\text{m}$
`alphaBeta212`	Value > 1.25	-
`alphaBeta214`	Value > 1.4	-
Fast Coincidence	-	$N_{\text{hit}} > 40$ $\Delta t < 505\,\text{ns}$
Slow Coincidence	-	$N_{\text{hit}} > 150$ $505\,\text{ns} > \Delta t 2\,\text{ms}$ $\Delta r < 2.5\,\text{m}$

radius, the impact of external backgrounds could become important, and the reconstruction is also poorest here due to the impact on light paths of proximity to the AV. For similar reasons, the internal liquid interface is also avoided by choice of z coordinate cut. However, a larger volume also improves statistics, so this tradeoff is explored here. An N_{hit} of 1000 roughly translates to 3 MeV, avoiding most backgrounds, and above 1500 N_{hit}, which should be almost entirely ^{8}B neutrinos, 20 candidates are found within the largest fiducial volume.

The efficiency of each cut at the step it is applied is calculated and written to file for each event type. The number of MC events considered when applying the event selection for the relevant signals and the total number of these events passing all cuts can be found in Tab. 5.5. The efficiencies after each cut can be found in App. C. With the level of statistics in the MC production, the PDFs are generally found to be smooth.

5.4.4 Expected Rates and Distributions

With the total livetime of 2209.21 hours and scintillator mass of 365 t, this corresponds to an exposure of 92.1 t yr. As mentioned in Sec. 5.2, the ^{8}B solar neutrino rate is calculated using the B16 GS98 flux of 5.46×10^{6} cm^{-2}s^{-1}, and `RAT` is used with the previously mentioned factors to determine annual rates for a fully filled detector, which are then scaled proportionally for the 92.1 t yr exposure. The internal ^{232}Th concentration is taken to be

Table 5.4: The cuts used in the event selection for the partial fill ^{8}B flux analysis. Several bound sanity checks on`skyShine`, `alphaBeta212`, `alphaBeta214` that are used to exclude bad events and numerical expressions are omitted for clarity.

Criteria	Value
Trigger? (MC only)	✓
Passes data cleaning mask `0x210000000242` (data only)	✓
Not vetoed by high N_{hit} veto	✓
Not tagged by fast coincidence prompt/delayed tag	✓
Not tagged by slow coincidence prompt/delayed tag	✓
Valid `partialFitter` result	✓
Cleaned N_{hit}	$1000 \leq N_{\text{hit}} \leq 4000$
r coordinate	$r < 4.5\,\text{m}$, $5.0\,\text{m}$, or $5.5\,\text{m}$
z coordinate	$1\,\text{m} < z < 6\,\text{m}$
`skyShine`	Value > 1.0
`alphaBeta212`	Value > 1.25
`alphaBeta214`	Value > 1.4

Table 5.5: The number of MC events generated for each relevant signal and the number of such events surviving all cuts for the 3 chosen fiducial volumes for the partial fill ^{8}B flux analysis. The overall efficiencies are shown in parentheses. For the ν species, the second percentage is the efficiency when including the survival probability, i.e. it is the efficiency for the oscillated spectra.

Signal	Simul. Events	Events in 4.5 m (eff.)	Events in 5.0 m (eff.)	Events in 5.5 m (eff.)
^{8}B ν_e	424324	66239 (15.6%/5.32%)	93604 (22.1%/7.51%)	124430 (29.3%/9.97%)
^{8}B ν_μ	225921	31280 (13.8%/9.13%)	44350 (19.6%/12.9%)	58919 (26.1%/17.2%)
^{208}Tl	1151077	303854 (26.4%)	416845 (36.2%)	509795 (44.3%)
^{210}Tl	1149803	220815 (19.2%)	307049 (26.7%)	385535 (33.5%)

$5.3 \times 10^{-17}\ \frac{\text{g}_{^{232}\text{Th}}}{\text{g}_{\text{LAB}}}$ obtained from sideband measurement throughout the entire partial fill period using ^{212}BiPo. The ^{208}Tl event rate is determined from the concentration by computing the specific activity for ^{232}Th (using a molar mass of $232\,\text{g}\,\text{mol}^{-1}$ and half-life of 1.4×10^{10} years), scaling by the associated concentration and total scintillator mass, and accounting for the branching ratio to ^{208}Tl (0.36). Meanwhile, the internal ^{238}U concentration is taken to be directly proportional to the number of ^{214}Bi tags found in the dataset used for the analysis. The reason for this is that any events from the ^{238}U chain that are sufficiently high in energy to affect this analysis (principally ^{210}Tl) will be daughters of ^{214}Bi and the coincidence tag is highly efficient. The ^{210}Tl rate is computed by scaling the number of coincidences by the ratio of the fraction of ^{214}Bi decays to ^{214}Po (0.9979) and the fraction of ^{214}Bi to ^{210}Tl (0.0021).

The spectral distributions of the PDFs in E for an exposure equivalent to one year in the fully filled detector, under the background expectations, are found in Fig. 5.2 for the 4.5-m fiducial volume, the 5.0-m fiducial volume and the 5.5-m fiducial volume, moving left to right. The expected normalization for the exposure of this data set for each PDF before and after cuts (and P_{ee} in the case of the neutrino signal) for the 3 choices of fiducial volume are found in Tab. 5.6, along with the number of events surviving in data. Note that though there is still a small contribution from ^{214}BiPo pileups after all cuts (on the level of 10% of the ^{210}Tl contribution), the U-chain contribution may be interchangeably referred to as the ^{210}Tl contribution for convenience. Because the shape of the ^{210}Tl spectrum and the ^{208}Tl spectrum are highly correlated, as can be seen from the PDFs, and the ^{210}Tl rate is heavily constrained from the tagging procedure, the ^{210}Tl rate is fixed in the fit. Some ^{212}BiPo coincidence may contaminate this rate from the tagging, but the contribution is small.

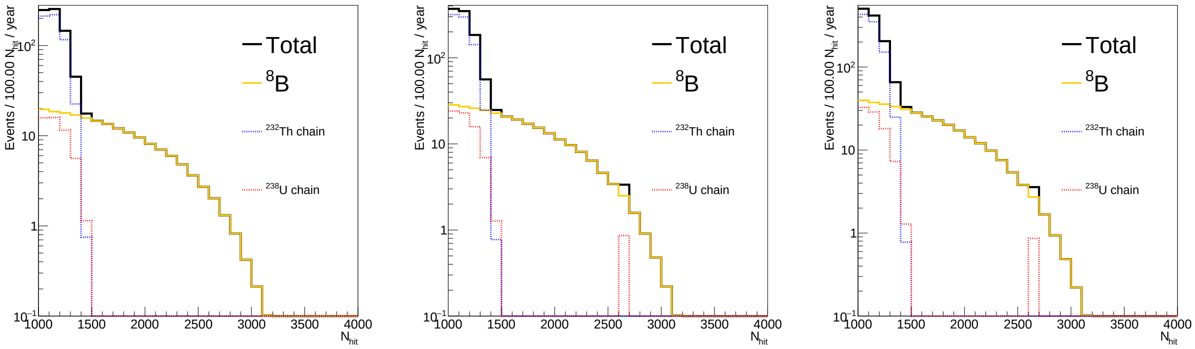

Figure 5.2: The PDFs for the partial fill ^{8}B flux analysis scaled to a 780 tyr exposure for the 4.5-m fiducial volume (left), the 5.0-m fiducial volume (center) and the 5.5-m fiducial volume (right). The anomalous bump near 2650 in N_{hit} arises from a rare decay mode involving an excited state.

5.4.5 Results

The fit is performed in 3 configurations corresponding to 3 different fiducial volumes, with $r < 4.5, 5, 5.5$m, with the aim of identifying non-uniformity. The resulting fit spectra are shown in Fig. 5.3 for each fiducial volume, and the extracted parameter values and corresponding rates with errors can be found in Tab. 5.7. The ^{8}B parameters are consistent with expectation in each case. Note there appears to be external contamination in the largest fiducial volume that inflates the ^{232}Th chain fitted normalization. There also appears to be a significant upward fluctuation in the number of events present in the data in the highest N_{hit} region of the fit, which is discussed further alongside similar events from the full fill period in Sec. 5.5.5.

To validate the fitter, fake data sets are generated by Poisson-fluctuating the PDFs on a bin-by-bin basis. Using the expected rates scenario and 10000 fake data fits, the pull

Table 5.6: The expected normalizations in events before and after cuts for all PDFs used in the fit, for the calculated exposure in the different fiducial volumes. The source normalizations for the U chain differ depending on the chosen fiducial volume, as indicated by the values separated by commas. The number of U chain events is scaled by the overall efficiency of the tag scheme taken from ^{214}BiPo MC. The number of expected events for the ν signal is oscillated only after cuts. The number of data events surviving cuts is also indicated.

Signal	Source normalization	Pre-cut rate (full volume)	Post-cut rate (4.5 m, 5.0 m, 5.5 m)
^{8}B ν_e	5.46×10^6 cm^{-2}s^{-1}	317.7	16.9, 23.9, 31.7
^{8}B ν_μ	5.46×10^6 cm^{-2}s^{-1}	56.7	5.18, 7.34, 9.76
^{8}B ν	5.46×10^6 cm^{-2}s^{-1}	–	22.1, 31.2, 41.4
^{232}Th chain (^{208}Tl)	$5.3 \times 10^{-17} \frac{\mathrm{g}_{232\mathrm{Th}}}{\mathrm{g}_{\mathrm{LAB}}}$	224.9	59.4, 81.4, 99.6
^{238}U chain (^{210}Tl)	39294, 58466, 80038 BiPo tags	28.7, 29.5, 29.5	5.51, 7.88, 9.88
^{238}U chain (^{214}BiPo)	39294, 58466, 80038 BiPo tags	136688, 140436, 140312	0.396, 0.611, 0.611
Data	—	—	97, 144, 210

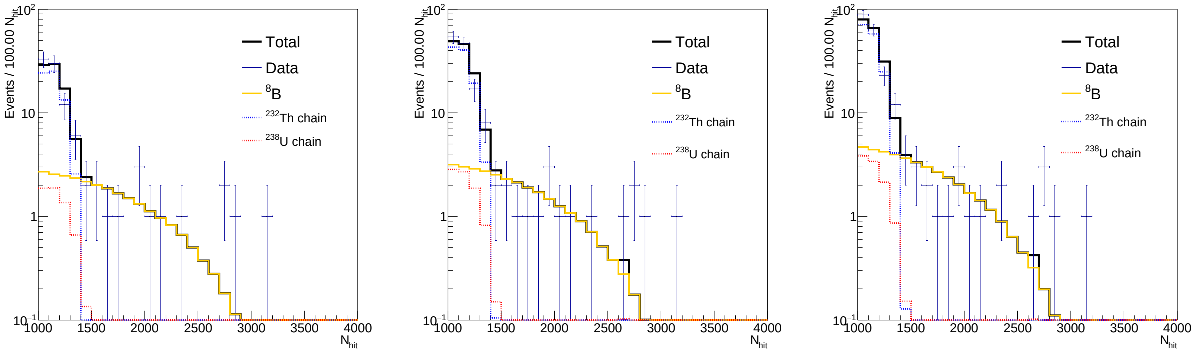

Figure 5.3: The best fit result plotted against the data for the partial fill ^{8}B flux analysis in the 4.5-m fiducial volume (left), the 5.0-m fiducial volume (center) and the 5.5-m fiducial volume (right).

Table 5.7: The fitted number of events for the partial fill ^{8}B flux analysis, with errors, and the corresponding fraction of the expected event rate for each signal and fiducial volume.

Signal	4.5 m	5.0 m	5.5 m
^{8}B	$25.70^{+6.85}_{-5.85}$ $(1.17^{+0.31}_{-0.27})$	$29.28^{+7.38}_{-6.36}$ $(0.94^{+0.24}_{-0.20})$	$41.25^{+8.76}_{-7.73}$ $(1.00^{+0.21}_{-0.19})$
^{232}Th chain	$65.48^{+9.53}_{-8.90}$ $(1.10^{+0.16}_{-0.15})$	$106.20^{+11.75}_{-11.11}$ $(1.30^{+0.14}_{-0.14})$	$158.10^{+14.21}_{-13.58}$ $(1.59^{+0.14}_{-0.14})$
^{238}U chain (fixed)	5.91 (1)	8.49 (1)	10.49 (1)

distributions, which should have mean of 0 and rms of 1 in the unbiased case, are found to be acceptable. The pull distributions from the 5.5 m FV fit are shown in Fig. 5.4.

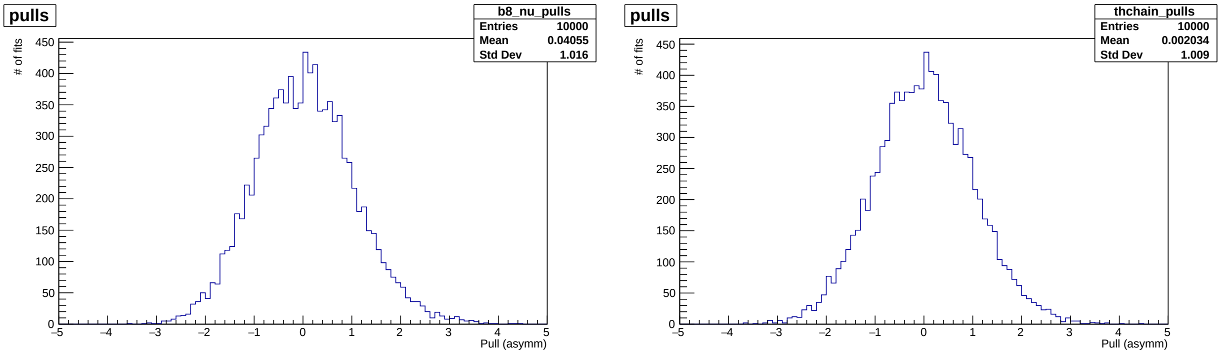

Figure 5.4: Pull distributions for the partial fill ^{8}B flux analysis for 10000 fake data fits for the ^{8}B (left) and the Th chain (right) parameters for the 5.5-m fiducial volume.

5.4.6 Systematics

The fit is also performed in slightly different configurations in order to evaluate systematics related to the N_{hit} response and the understanding of the fiducial volume.

5.4.6.1 Energy Systematics

In order to account for mismodeling of the N_{hit} response in simulation as compared to the actual patterns observed in data, the N_{hit} distributions of the Monte Carlo simulation are scaled and smeared via analytical functions dependent on position extracted from tagged ^{214}BiPo events, creating a new set of PDFs. The transformations applied to the data are as follows:

$$\begin{aligned} f_{\mathrm{mean}}(r) &= 0.858 + (1.24 \times 10^{-4})r - (3.65 \times 10^{-8})r^2 + (3.5 \times 10^{-12})r^3, \\ f_{\sigma^2}(r) &= -206744 + 208.433r - 0.0771985r^2 + (1.25054 \times 10^{-5})r^3 - (7.48268 \times 10^{-10})r^4 \end{aligned} \tag{5.10}$$

These are the results of fitting polynomials to the ratio of the mean and difference in the σ^2 parameters, respectively, between data and MC of Gaussian fits to the N_{hit} distribution of the BiPos in positional bins. The procedure for applying the smearing involves drawing the new N_{hit} value from the normal random variable $\mathcal{N}(N_{\mathrm{hit}} \times f_{\mathrm{mean}}(r), \sqrt{f_{\sigma^2}(r)})$ for an event with particular N_{hit} and r. The PDFs created from the transformed events are then fit against the unsmeared data, providing the results found in Tab. 5.8.

5.4.6.2 Fiducial Volume Systematic

The uncertainty on reconstructed positions found by comparing the reconstructed positions of tagged ^{214}BiPo events has been found to be roughly 45 mm, and so the fits are performed under fiducial volumes where the selection criteria has been expanded, $(r+45, z-45)$,

Table 5.8: The fitted number of events and corresponding fraction of the expected event rate for each signal and fiducial volume for the additional N_{hit} scaling and smearing scheme.

Signal	4.5 m	5.0 m	5.5 m
^{8}B	$25.84^{+6.88}_{-5.88}$ $(1.42^{+0.38}_{-0.32})$	$29.37^{+7.41}_{-6.39}$ $(1.07^{+0.27}_{-0.23})$	$41.28^{+8.78}_{-7.75}$ $(1.09^{+0.23}_{-0.20})$
^{232}Th chain	$66.42^{+9.55}_{-8.92}$ $(1.37^{+0.20}_{-0.18})$	$107.20^{+11.77}_{-11.13}$ $(1.52^{+0.17}_{-0.16})$	$158.90^{+14.23}_{-13.59}$ $(1.75^{+0.16}_{-0.15})$
^{238}U chain (fixed)	4.82 (1)	7.38 (1)	9.63 (1)

and restricted, $(r - 45, z + 45)$, by this same amount in data and Monte Carlo simulation. The results are provided in Tab. 5.9.

Table 5.9: The fitted number of events and corresponding fraction of the expected event rate for each signal and fiducial volume for the fiducial volume systematic. The values on top in each cell represents the result for the contracted fiducial volume and the values on the bottom represent the results for the expanded fiducial volume.

Signal	4.5 m	5.0 m	5.5 m
^{8}B	$22.82^{+6.50}_{-5.49}$ $(1.09^{+0.31}_{-0.26})$ $28.29^{+7.22}_{-6.22}$ $(1.21^{+0.31}_{-0.27})$	$26.28^{+7.04}_{-6.02}$ $(0.88^{+0.24}_{-0.20})$ $31.86^{+7.74}_{-6.71}$ $(0.97^{+0.24}_{-0.20})$	$38.42^{+8.50}_{-7.47}$ $(0.97^{+0.21}_{-0.19})$ $44.10^{+9.10}_{-8.06}$ $(1.02^{+0.21}_{-0.19})$
^{232}Th chain	$62.66^{+9.29}_{-8.66}$ $(1.11^{+0.17}_{-0.15})$ $70.34^{+9.93}_{-9.30}$ $(1.12^{+0.16}_{-0.15})$	$102.50^{+11.51}_{-10.87}$ $(1.32^{+0.15}_{-0.14})$ $0.14^{+2.81}_{-0.15}$ $(1.40^{+12.42}_{-11.79})$	$147.20^{+13.75}_{-13.12}$ $(1.52^{+0.14}_{-0.14})$ $167.80^{+14.67}_{-14.03}$ $(1.64^{+0.14}_{-0.14})$
^{238}U chain (fixed)	5.61 6.34	8.13 8.97	10.23 10.86

5.4.7 Results with Systematics

The systematic errors are found by taking the difference in fitted event rates between the nominal fit and the systematic fits. The N_{hit} systematic is assumed to be symmetric, while the larger and smaller fiducial volume fits correspond to the upper and lower errors for that systematic. Then, the systematics are assumed to be independent and are summed in quadrature to give the final set of results including both statistical and systematic uncertainties, as show in Tab. 5.10. The measured flux is compatible within errors with the theoretical value from the B16 GS98 model in all cases of fiducial volume, as shown in Tab. 5.11. The fitted flux in each fiducial volume is compared to the two leading theoretical predictions in Fig. 5.5.

The results of the binned maximum likelihood fit for the ^{8}B solar neutrino flux in the stable partial fill period of the SNO+ experiment are found to agree well with the theory prediction. The statistical uncertainties are dominant over the systematic ones, regardless of the fiducial volume chosen, which is unsurprising given the limited exposure. This analysis served as a proof of concept for future non-coincidence-based analyses in the SNO+ scintil-

Table 5.10: The fitted number of events with statistical and systematic errors, with the corresponding fraction of the expected event rate below in each cell, for each fiducial volume. The first set of uncertainties are statistical and the second are the combined systematic errors.

Signal	4.5 m	5.0 m	5.5 m
^{8}B	$25.70^{+6.85+2.59}_{-5.85-2.88}$ $(1.17^{+0.31+0.12}_{-0.27-0.13})$	$29.28^{+7.38+2.58}_{-6.36-3.00}$ $(0.94^{+0.24+0.08}_{-0.20-0.10})$	$41.25^{+8.76+2.85}_{-7.73-2.83}$ $(1.00^{+0.21+0.07}_{-0.19-0.07})$
^{232}Th chain	$65.48^{+9.53+4.95}_{-8.90-2.97}$ $(1.10^{+0.16+0.08}_{-0.15-0.05})$	$106.20^{+11.75+106.06}_{-11.11-3.83}$ $(1.30^{+0.14+1.30}_{-0.14-0.05})$	$158.10^{+14.21+9.73}_{-13.58-10.93}$ $(1.59^{+0.14+0.10}_{-0.14-0.11})$

Table 5.11: The resulting solar fluxes in each case in cm^{-2} s^{-1}. The theoretical value is $(5.46 \pm 0.66) \times 10^6$ cm^{-2} s^{-1} for the B16 GS98 prediction, and (4.50 ± 0.54) $\times 10^6$cm^{-2} s^{-1} for B16 AGSS09. The errors in the table are listed with the statistical error first and the systematic errors second, and the systematic errors do not include the uncertainty on the theoretical flux.

	4.5 m	5.0 m	5.5 m
^{8}B Flux (10^6 cm^{-2} s^{-1})	$6.36^{+1.69+0.64}_{-1.45-0.71}$	$5.13^{+1.29+0.45}_{-1.11-0.53}$	$5.44^{+1.15+0.38}_{-1.02-0.37}$

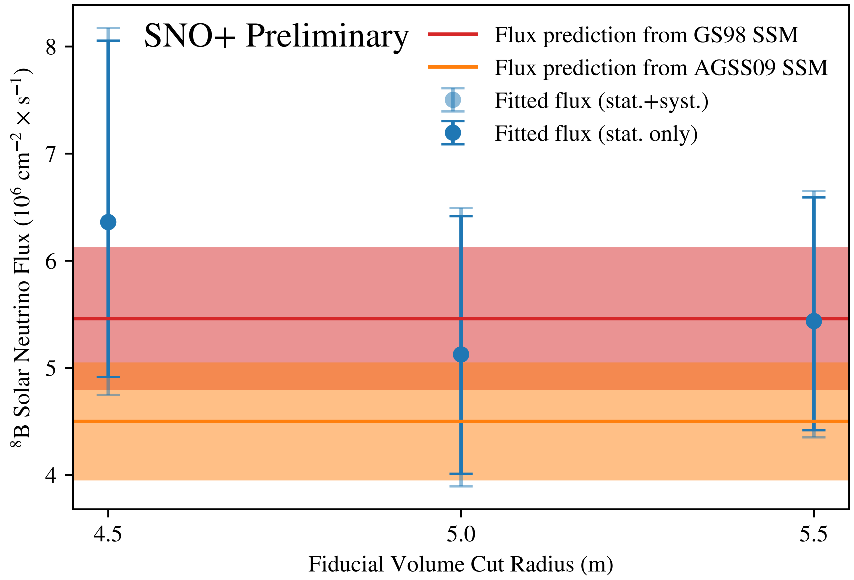

Figure 5.5: The solar flux fitted in each fiducial volume with statistical and systematic uncertainties, in comparison with the GS98 (5.46×10^6 cm^{-2} s^{-1}) and AGSS09 (4.5×10^6 cm^{-2} s^{-1}) flux predictions, and their uncertainties (both 12%).

lator, and solar neutrino analyses in the scintillator in particular, which leads to the next section.

5.5 Full Fill Analysis

5.5.1 Fit Overview

Once the pause in operations due to the COVID-19 pandemic ended, SNO+ began a campaign to finish filling the detector with LAB, and load to a nominal level with PPO. While there was ongoing datataking during this period, the short lengths and variable stability of any given period of this data mitigates the potential for the use of this data towards physics analysis. However, once the final PPO concentration of 2.2 g/L was reached, the detector entered a quiescent period designed to allow background counting and physics analyses, and development of the full suite of scintillator tools. These conditions form the backdrop for the dataset used in the full fill flux analysis. Building on the lessons learned and machinery devised for the partial fill version of the analysis, this analysis focuses on using the fully operational capabilities of the SNO+ detector to perform the fit. As a result, the fit used to determine the ^{8}B flux was designed to be fairly straightforward and avoid hiccups that would best be tackled by the symmetric, fully-filled configuration. Because energy reconstruction and calibration were now possible in the detector, the fit now uses the reconstructed energy estimator instead of N_{hit} as a dimension, with even-width binning of 0.5 MeV between a lower bound of 3 MeV and an upper bound of 14 MeV, for a total number of bins along this axis of 22. The radial dimension of the fit is restored given greater confidence in the position reconstruction and as a result externals are included in the fit. The fit is still performed in multiple fiducial volumes in order to monitor the impact of externals in a direct fashion, with 4 equal-width bins in r^3/r_{AV}^3 (a choice of coordinate that maintains linear volume scaling in the radial dimension) within each fiducial volume configuration. The fit then considers the normalizations of 1 signal parameter and between 3 and 5 background parameters depending on the configuration, with constraints on some parameters. The fit parameters include the normalizations for:

- ^{8}B (ν_e and ν_μ components floated together, after accounting for flavor-dependent spectral effects)
- Uranium chain, which includes ^{238}U, ^{234}Th, $^{234\mathrm{m}}$Pa, ^{234}U, ^{230}Th, ^{226}Ra, ^{222}Rn, ^{218}Po, ^{214}Pb, ^{214}Bi (alpha and beta branch), ^{214}Po, and ^{210}Tl
- Thorium chain, which includes ^{232}Th, ^{228}Ra, ^{228}Ac, ^{228}Th, ^{224}Ra, ^{220}Rn, ^{216}Po, ^{212}Pb, ^{212}Bi (alpha and beta branch), ^{212}Po, and ^{208}Tl
- ^{214}Bi and ^{208}Tl from AV and support ropes
- ^{214}Bi and ^{208}Tl from the water external to the AV
- PMT $\beta\gamma$

Alternatively, the last three can be combined into a single controlling parameter. With the revised threshold, the U chain sees contributions from both ^{214}Bi and ^{210}Tl, with ^{212}Bi and ^{208}Tl from the Th chain, unlike the partial fill phase, where this was not the case. As with the partial fill, all signals from both chains are considered together for completeness, and secular equilibrium is assumed to hold for the listed decays.

5.5.2 Run Selection

The detector data for this analysis uses a subset of the "Preliminary Scintllator Gold" run list, which lasted from April 29, 2022 to March, 10, 2023. This time period began with the final loading of a PPO batch into the scintillator, and ended with the addition of the BHT additive for Tellurium phase operations. The subset actually used for this analysis lasted from May 17, 2022 to November 30, 2022, which corresponds to run numbers 300733-306498. The period between the end of April to the middle of May in 2022 was found to have prohibitively high backgrounds associated with the decay of Rn from the Uranium and Thorium chains that entered the detector during loading operations, so this data was not used given the background situation was not stable. As with the partial fill runs used, detector stability criteria are applied for runs in order to be placed on the runlist, including that all crates are online. The list of all files and runs in this dataset can be found in Tab. D.1. These files have been processed using `RAT` 7.0.8 using the Analysis20R module. Several runs on the runlist that would otherwise be used had processing issues and were not part of the dataset though future attempts restored them to usability; these are 305589, 305590, 305592, 305593, 305594, 305596. The raw livetime for the 2132 processed runs in this period is 2114.1 hours, or 88.1 days. The same high N_{hit} event veto is used as in partial fill and in the full fill a specialized muon and muon follower veto is also used (with an identical window of 20 s). Considerations of overlapping veto periods are similarly made, with the choice made to extend the veto if events satisfying the criteria occur within an already active veto window, in order to conservatively exclude data. Accounting for this, the dataset loses 4.59 days of runtime. Reduced by this amount, the livetime of the dataset becomes 2003.9 hours, or 83.5 days.

Simulations occur similarly as they did in the partial fill analysis, serving as the basis of the model to fit against. This MC is the run-by-run full fill production performed using `RAT` 7.0.8 and `RAT` 7.0.9 for the standard set of backgrounds (some revisions to certain backgrounds were made between the versions). In addition to the signals considered in the partial fill analysis, the full fill analysis also includes the external background signals from all of the simulated sources. The corresponding breakdown of MC files used is prohibitively large due to the increased length of the run list and the larger number of backgrounds that are components of the fit, so this is not included as a table.

5.5.3 Event Selection

The same procedure is used to select events, bin the data and build the PDFs from Monte Carlo events as was used in the partial fill analysis, though some of the cuts used in the coincidence tagging and event selection procedures are changed due to the distinct geometry, light yield and optics of the full fill phase. No AV offset correction is required as this is now done implicitly in the event reconstruction unlike during the partial fill phase. The switch is also made from the `partialFitter` suite of reconstruction tools to the `scintFitter` collection, while the `skyShine` classifier is dropped due to the fact that it no longer functions with its desired effect in the full fill geometry, and no z cut is needed given the absence of the water volume below the scintillator. As mentioned, the high N_{hit} veto remains the same, rejecting any events that occur within the 20 s following a predecessor event with greater than 5000 N_{hit}. Additionally, the data cleaning mask of `0x2100000042c2` now includes the muon and muon follower veto logic that separately tags events as muons and rejects event within 20 s of those. The revised coincidence tagging cuts are shown in Tab. 5.12, and this time only one overall coincidence tag is used, rather than two for slow and fast coincidences, in order to reject a broader set of events. The restrictions on present on the time and position between prompt and delayed events in the partial fill are relaxed in order to remove more coincidences from the data set. N_{hit} is used for the tagging procedure instead of energy in order to provide looser tagging criteria, and avoid issues with misconstructions of delayed events (e.g. events caused by late light leaking from the previous event window that do not reconstruct properly).

Table 5.12: The cuts used in the coincidence tagging procedure for BiPo rejection for the full fill ^{8}B flux analysis. The "-" indicates the cut is not applied. Only one of the "Fast Coincidence" or "Slow Coincidence" cuts need be passed to be flagged as a potential coincidence, though both may be. Several bound sanity checks on N_{hit} and Δr that are used to exclude bad events and numerical expressions are omitted for clarity.

Criteria	Prompt Event	Delayed Event
Trigger? (MC only)	✓	✓
Passes data cleaning mask `0x2100000042c2` (data only)	✓	-
Valid `scintFitter` result	✓	✓
Cleaned N_{hit}	$N_{\text{hit}} > 150$	$N_{\text{hit}} > 100$
r coordinate	$r < 6\,\text{m}$	$r < 6\,\text{m}$
Coincidence	-	$\Delta t < 4\,\text{ms}$ $\Delta r < 2\,\text{m}$

The set of cuts used to identify passing events in data and MC is found in Tab. 5.13. As discussed, the use of multiple fiducial volumes is maintained from the partial fill in order to directly probe the effect of the radial dimension and maintain consistency with the partial fill fit, and the `skyShine` and z cuts are abandoned due to their lack of utility. The `alphaBeta212` and `alphaBeta214` are reoptimized for full fill, allowing a cut at 0. The external background rejection classifiers `ext0NuTimeTl208AVNaive` and `ext0NuAngleTl208AV` are included with values to maximize rejection will maintaining ^{8}B signal, achieving roughly 40% rejection with over 99% acceptance of signal. The in-time ratio (ITR) is also used to reject events that have abnormal time distributions. Originally a metric developed by SNO for Cherenkov emission, ITR is the ratio of the number of hits occurring within an asymmetric 7.5 ns window around the time residual distribution peak for an event to the number of hits in the entire event. While less heightened than with the very prompt Cherenkov light, a significant fraction of the SNO+ scintillator's emission also occurs within this window, meaning that events with less or more light within this window can be differentiated from signal-like events.

Table 5.13: The cuts used in the event selection for the full fill ^{8}B flux analysis. Several bound sanity checks that are used to exclude bad events and numerical expressions are omitted for clarity.

Criteria	Value
Trigger? (MC only)	✓
Passes data cleaning mask `0x2100000042c2` (data only)	✓
Not vetoed by high N_{hit} veto	✓
Not tagged by coincidence prompt/delayed tag	✓
Valid `scintFitter` result	✓
Reconstructed energy E	$3\,\text{MeV} < E < 14\,\text{MeV}$
r coordinate	$r < 4.5\,\text{m}$, $5.0\,\text{m}$, or $5.5\,\text{m}$
`alphaBeta212`	Value > 0
`alphaBeta214`	Value > 0
`ext0NuTimeTl208AVNaive`	Value > -0.007
`ext0NuAngleTl208AV`	Value > -4.7
ITR	$0.2 <$ Value < 0.3

As with the partial fill, the number of MC events considered when applying the event selection for the relevant signals and the total number of these events passing all cuts can be found in Tab. 5.14.Like with the partial fill, given the level of statistics in the MC production, the PDFs are generally found to be smooth.

5.5.4 Expected Rates and Distributions

With the total livetime of 2003.9 hours and scintillator mass of 780 t, this corresponds to an exposure of 178.4 t yr. The expected ^{8}B solar neutrino rate is found similarly to the partial fill analysis, scaling proportionally for the different exposure. The expected internal ^{232}Th concentration is assumed as $1.3 \times 10^{-16} \frac{\text{g}_{^{232}\text{Th}}}{\text{g}_{\text{LAB}}}$, based on sideband measurement using ^{212}BiPo. Unlike the partial fill analysis, due to the relaxed coincidence cut, the expected rates for the U chain contribution is not based on the tag rate from the anaylsis, but instead based on a sideband measurement performed using ^{214}BiPo as with the Th chain, which determined a concentration of $1.7 \times 10^{-16} \frac{\text{g}_{^{232}\text{U}}}{\text{g}_{\text{LAB}}}$. The higher concentration compared to partial fill implies are more significant ingress of radon during full fill operations as compared to the partial fill. In fact, studies have noted that the upper parts of the U and Th chain, above

Table 5.14: The number of MC events generated for each relevant signal and the number of such events surviving all cuts for the 3 chosen fiducial volumes for the full fill ^{8}B flux analysis. The overall efficiencies are shown in parentheses. For the ν species, the second percentage is the efficiency when including the survival probability, i.e. it is the efficiency for the oscillated spectra.

Signal	Simulated Events	Events in 4.5 m (eff.)	Events in 5.0 m (eff.)	Events in 5.5 m (eff.)
^{8}B ν_e	2554438	614025 (24.0%/8.28%)	836373 (32.7%/11.3%)	1098420 (43.0%/14.8%)
^{8}B ν_μ	1713050	378630 (22.1%/14.5%)	515130 (30.0%/19.7%)	677334 (39.5%/25.9%)
Internal ^{212}BiPo	5631255	3574 (0.0635%)	5348 (0.095%)	7654 (0.136%)
Internal ^{214}BiPo	4397913	458 (0.0104%)	1572 (0.0357%)	5376 (0.122%)
Internal ^{210}Tl	735417	217007 (29.5%)	298095 (40.5%)	395892 (53.8%)
Internal ^{208}Tl	736365	252233 (34.3%)	349060 (47.4%)	464820 (63.1%)
AV ^{214}Bi	24476706	14 (0.0000572%)	111 (0.000453%)	1330 (0.00543%)
Ropes ^{214}Bi	60919856	15 (0.0000246%)	147 (0.000241%)	1102 (0.00181%)
AV ^{208}Tl	3672283	150 (0.00408%)	1512 (0.0412%)	22646 (0.617%)
Ropes ^{208}Tl	5507089	172 (0.00312%)	1456 (0.0264%)	15014 (0.273%)
External Water ^{214}Bi	73401015	8 (0.0000109%)	63 (0.0000858%)	573 (0.000781%)
External Water ^{208}Tl	33013635	341 (0.00103%)	2785 (0.00844%)	23569 (0.0714%)
PMT $\beta\gamma$	3670151	1966 (0.0536%)	13414 (0.365%)	76329 (2.08%)

^{222}Rn and ^{220}Rn respectively, may be in disequilibrium with the lower parts, though the components of the chain in this section are all excluded from the event selection due to their lower energies. As a result, these backgrounds are treated as effectively sourcing from ^{238}U and ^{232}Th concentrations, even if the reality of the contamination source is somewhat more complicated. The external background nominal rates are based on the measurements done in the water phase, previously shown in Fig. 4.3.

The spectral distributions of the PDFs in E and r^3/r^3_{AV} for an exposure equivalent to one year in the fully filled detector, under the nominal background expectations are found in Fig. 5.6 and Fig. 5.7 for the 4.5-m fiducial volume, the 5.0-m fiducial volume and the 5.5-m fiducial volume, moving left to right. As with the partial fill, the expected normalization for the exposure of this data set for each PDF before and after cuts are found in Tab. 5.15, along with the number of events surviving in data. The PDFs are overall similar to what was observed in the partial fill, with the addition of the external component being apparent at higher radii, as expected. While the non-uniformity of the external background signal is expected, the ^{238}U signal is notably not flat, which is primarily driven by the radial dependence of the coincidence tagging and the fact that the PDF is dominated by the ^{214}BiPo contribution, especially in the larger fiducial volumes. The ^{232}Th PDF is flat, as the ^{208}Tl contribution dominates and there is not a heavily radially-dependent cut or tag applied (the ^{212}BiPo PDF alone displays some radial dependence, though less than the ^{214}BiPo PDF).

5.5.5 Results

The resulting fit spectra for the full fill are found in Fig. 5.8 for the projection in E and Fig. 5.9 for the projection in r^3/r^3_{AV} for each fiducial volume, and the extracted parameter values and corresponding rates with errors can be found in Tab. 5.16. The fit is performed

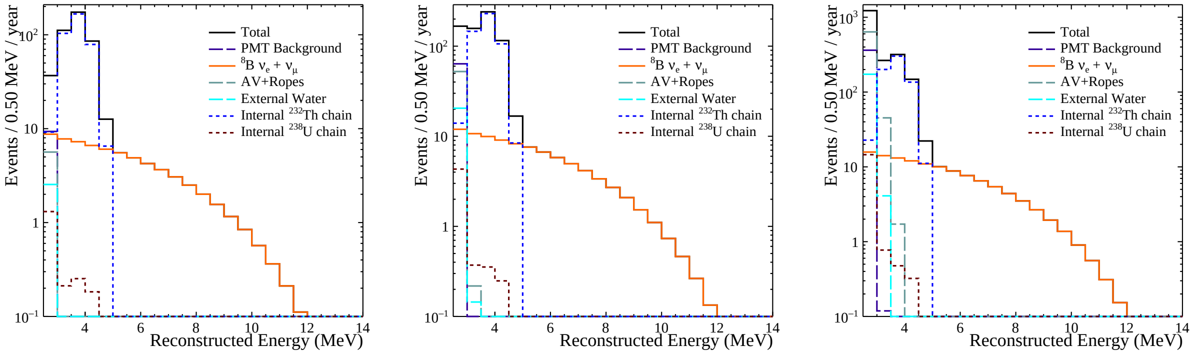

Figure 5.6: The PDFs in E for the full fill ^{8}B flux analysis scaled to a 780 t yr exposure for the 4.5-m fiducial volume (left), the 5.0-m fiducial volume (center) and the 5.5-m fiducial volume (right).

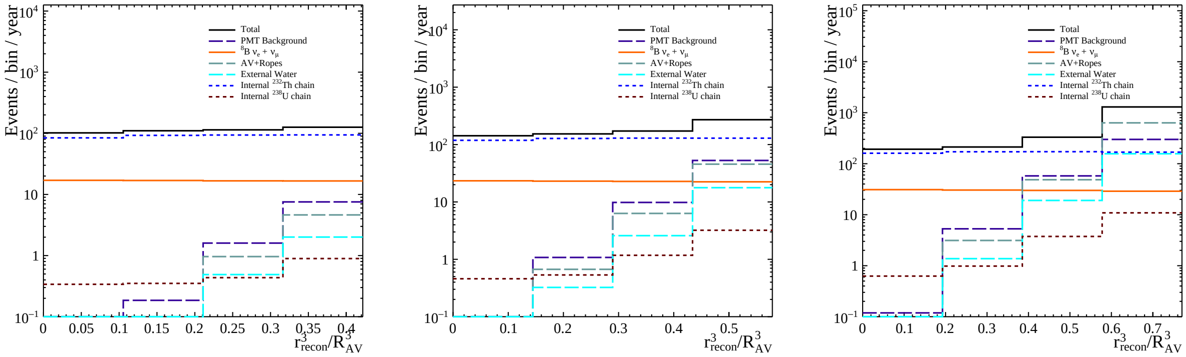

Figure 5.7: The PDFs in r^3/r^3_{AV} for the full fill ^{8}B flux analysis scaled to a 780 t yr exposure for the 4.5-m fiducial volume (left), the 5.0-m fiducial volume (center) and the 5.5-m fiducial volume (right).

with the external background parameters floated as three separate parameters for the PMT background, the AV and ropes background and the external water background, and also by using a single controlling parameter. The results for the ^{8}B normalization parameter remain consistent in either case, so the case where there is a single parameter is reported to enable brevity. This is the case even with constraints from the water phase measurement applied or not applied in the individual external parameter case, which is not particularly surprising given the constraints are quite open due to large systematic errors on the measurements. The fit is also performed with a 25% constraint on the value of the ^{238}U chain parameter, based on the tagging procedure, and with similar motivation as the fixing of this parameter in the partial fill due to the shape degeneracy with the ^{232}Th spectrum. The ^{8}B parameters are found to be consistent with expectation in all three cases.

Table 5.15: The expected normalizations in events before and after cuts for all PDFs used in the fit, for the calculated exposure in the different fiducial volumes. The number of expected events for the ν signal is oscillated only after cuts. The source normalization for the external backgrounds is given in fraction of the nominal rate, as determined from the water phase, since the direct concentrations are not particularly instructive. The number of data events surviving cuts is also indicated.

Signal	Source normalization	Pre-cut rate (full volume)	Post-cut rate (4.5 m, 5.0 m, 5.5 m)
^{8}B ν_e	5.46×10^{6} cm^{-2}s^{-1}	618.93	51.234, 69.789, 91.654
^{8}B ν_μ	5.46×10^{6} cm^{-2}s^{-1}	110.49	16.011, 21.784, 28.644
^{8}B ν	5.46×10^{6} cm^{-2}s^{-1}		
Internal ^{208}Tl (^{232}Th chain)	$1.3 \times 10^{-16} \frac{\mathrm{g}_{232\mathrm{Th}}}{\mathrm{g}_{\mathrm{LAB}}}$	1061.15	363.483, 503.016, 669.833
Internal ^{212}BiPo (^{232}Th chain)	$1.3 \times 10^{-16} \frac{\mathrm{g}_{232\mathrm{Th}}}{\mathrm{g}_{\mathrm{LAB}}}$	1886.48	1.197, 1.792, 2.564
Internal ^{210}Tl (^{238}U chain)	$1.7 \times 10^{-16} \frac{\mathrm{g}_{238\mathrm{U}}}{\mathrm{g}_{\mathrm{LAB}}}$	2.55	0.753, 1.034, 1.373
Internal ^{214}BiPo (^{238}U chain)	$1.7 \times 10^{-16} \frac{\mathrm{g}_{238\mathrm{U}}}{\mathrm{g}_{\mathrm{LAB}}}$	12145.40	1.265, 4.341, 14.847
AV ^{214}Bi	0.21	615014.00	0.352, 2.789, 33.418
Ropes ^{214}Bi	0.21	130700.00	0.032, 0.315, 2.364
AV ^{208}Tl	0.21	72072.00	2.944, 29.674, 444.449
Ropes ^{208}Tl	0.21	74685.80	2.333, 19.746, 203.616
External Water ^{214}Bi	0.44	4651050.00	0.507, 3.992, 36.308
External Water ^{208}Tl	0.44	197317.00	2.038, 16.645, 140.868
PMT $\beta\gamma$	1.48	17432.40	9.338, 63.713, 362.545
Data	—	—	316, 684, 3047

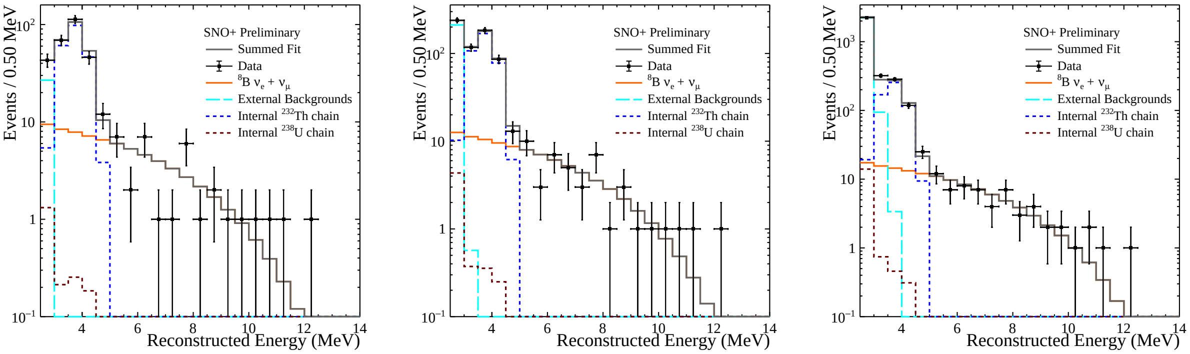

Figure 5.8: The best fit result plotted in the projection in E against the data for full fill ^{8}B flux analysis in the 4.5-m fiducial volume (left), the 5.0-m fiducial volume (center) and the 5.5-m fiducial volume (right).

The ^{8}B normalization parameter fits above the expectation by 8.1%, 5.2% and 10.1%, respectively for the progressively larger fiducial volumes. Given there is significant overlap in the datasets (the smaller volumes are subsets of the larger volumes), this is not particularly surprising. It is also interesting to note that the same pattern in the which the fitted

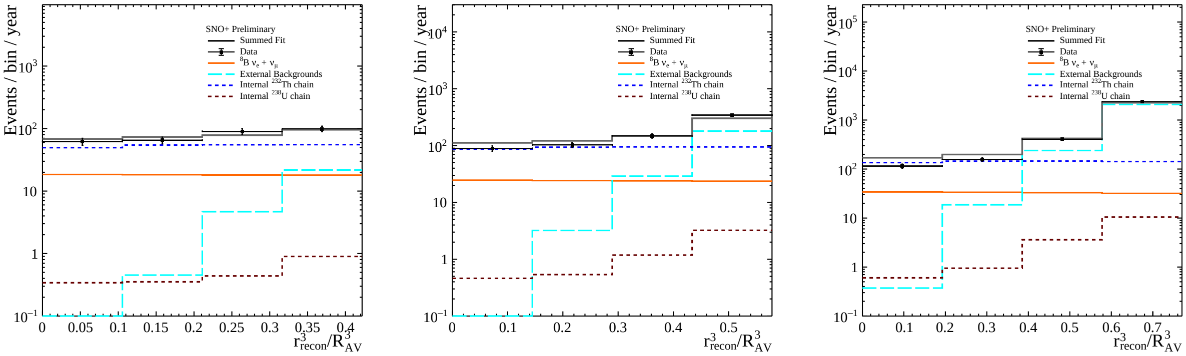

Figure 5.9: The best fit result plotted in the projection in r^3/r^3_{AV} against the data for full fill ^{8}B flux analysis in the 4.5-m fiducial volume (left), the 5.0-m fiducial volume (center) and the 5.5-m fiducial volume (right).

parameter drops in magnitude from the 4.5-m volume fit to the 5.0-m volume fit and then rises from the 5.0-m volume fit to the 5.5-m volume fit exists in the full fill and the partial fill. This suggests that the increased impact of the externals and potential mismodeling at higher radii (for example, in the uniformity of the internal backgrounds) may bias the fit in particular way dependent on the chosen fiducial volume. In the partial fill, the 5.5-m volume fit ends up at a best value that is essentially dead-on with expectation, though this may be a conspiracy of confounding factors rather than an indication that the expected value from the model is truly the underlying value in nature.

One additional factor worth discussing is the apparent excess of events toward the high energy end of the the region of interest. While present in the partial fill, there was not significant attention on this, but given its reappearance in the full fill, further investigation is warranted. Removing the region above 10 MeV from the fit results in fitted ^{8}B parameter values that are higher than expectation by only 2%, 1% and 6% respectively for each volume. While potentially an overfluctuation biasing the fit away from the expectation, the fact that this population appears in datasets from both phases discounts that hypothesis. Investigation is ongoing as to the nature of these events and whether there are instrumental or physics processes that could explain their presence.

Table 5.16: The fitted number of events for the full fill ^{8}B flux analysis, with errors, and the corresponding fraction of the expected event rate for each signal and fiducial volume.

Signal	4.5 m	5.0 m	5.5 m
^{8}B	$72.7^{+12.12}_{-10.98}$ $(1.081^{+0.1802}_{-0.1632})$	$96.37^{+14.01}_{-12.84}$ $(1.052^{+0.153}_{-0.1403})$	$132.4^{+16.4}_{-15.24}$ $(1.101^{+0.1364}_{-0.1267})$
^{232}Th ch.	$214.4^{+16.68}_{-16.04}$ $(0.5879^{+0.04574}_{-0.04399})$	$370.2^{+21.43}_{-20.79}$ $(0.7333^{+0.04244}_{-0.04118})$	$567.7^{+27.59}_{-26.91}$ $(0.8443^{+0.04103}_{-0.04002})$
^{238}U ch.	$2.031^{+0.4913}_{-0.5178}$ $(1.006^{+0.2434}_{-0.2566})$	$5.402^{+1.342}_{-1.344}$ $(1.005^{+0.2496}_{-0.2501})$	$15.62^{+4.052}_{-4.054}$ $(0.9623^{+0.2497}_{-0.2498})$
Externals	$26.86^{+6.391}_{-5.674}$ $(1.531^{+0.3643}_{-0.3234})$	$212^{+15.6}_{-14.93}$ $(1.549^{+0.114}_{-0.1091})$	$2332^{+49.73}_{-49.17}$ $(1.906^{+0.04065}_{-0.04019})$

The extracted ^{8}B flux values are shown in Tab. 5.17, and are compatible with the B16 GS98 prediction, favoring the high-Z model over the low-Z B16 AGSS09 prediction. This can also be seen in Fig. 5.10, which includes the global fit from 2016. Despite the fact the analysis was performed assuming this iteration of Standard Solar Models, it is also instructive to view them in light of the revisions published in 2023, as well as the newest global fit. While not a one-to-one comparison given the difference in model inputs that will cause variations in the model spectra, the dependence is weak enough (mainly factoring into the survival probability) that a comparison can still be made. This is shown in Fig. 5.11. Because the predicted flux from the SSMs decreased for the given abundance models, the 2023 SSM fluxes display more tension with the full fill result, though the result is still compatible with either of the high-Z models (the SSMs with GS98 and MB22m abundances). The 2023 global fit value is only shifted from its 2016 counterpart at the percent level so the place of this result in the global experimental picture is not impacted heavily by the revised global fit. Further, the results in the full fill are compatible with those from the partial fill discussed in Sec. 5.4.

The place of 5.0-m fiducial volume fit from the full fill analysis in the broader experimental context is shown in Fig. 5.12. Notably, the full fill result is compatible with the experimental results shown from the SNO+ water phase [198], SNO's three-phase analysis [63] and Borexino [59], which offer points of close comparison given the overlap in detection principle and experimental apparatus. The results in all experiments shown are slightly higher than the global fit and SSM values just as the full fill analysis result is, which helps to put concerns about model compatibility into a wider perspective. The global fit ^{8}B flux value from [53] is strongly driven by the very precise SNO result, though the fact that experimental results across all the solar neutrino fluxes and relevant oscillation parameters are included in the global fit causes a slight downward deviation.

Table 5.17: The resulting ^{8}B solar neutrino fluxes from the full fill analysis in each fiducial volume case in cm^{-2} s^{-1}. The theoretical value is $(5.46 \pm 0.66) \times 10^{6}$ cm^{-2} s^{-1} for the B16 GS98 prediction, and $(4.50 \pm 0.54)\ \times 10^{6}$cm^{-2} s^{-1} for B16 AGSS09. The errors in the table are the statistical errors from the fit and do not include systematic uncertainties or the uncertainty on the theoretical flux.

	4.5 m	5.0 m	5.5 m
^{8}B Flux (10^{6} cm^{-2} s^{-1})	$5.90^{+0.98}_{-0.89}$	$5.74^{+0.84}_{-0.77}$	$6.01^{+0.74}_{-0.69}$

Sensitivity estimations performed based upon the fitted values in the 5.0-m fiducial volume configuration with twice the livetime and additionally with a full year's worth exposure (roughly four times the exposure used in this analysis) show the error on the fitted flux decreasing from around 15% to around 10% and 7% respectively, in line with the expected behavior for a statistics-limited analysis assuming on Poisson statistics. This suggests that the additional exposure from the currently unexplored runs of the full fill dataset, and the possible addition of data from the bisMSB-loaded phase (which has a higher light yield and therefore improved energy resolution), will duly enable a more precise result for SNO+ in the

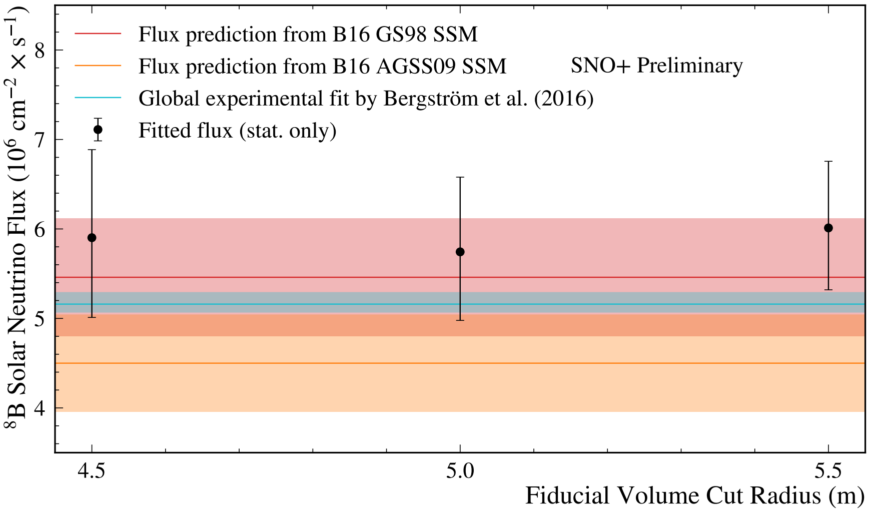

Figure 5.10: The ^{8}B solar neutrino fluxes from the full fill analysis in each fiducial volume case, in comparison with the B16 GS98 (5.46×10^6 cm^{-2} s^{-1}) and B16 AGSS09 (4.50×10^6 cm^{-2} s^{-1}) flux predictions, and their uncertainties, as well as the 2016 Bergström global fit [52]

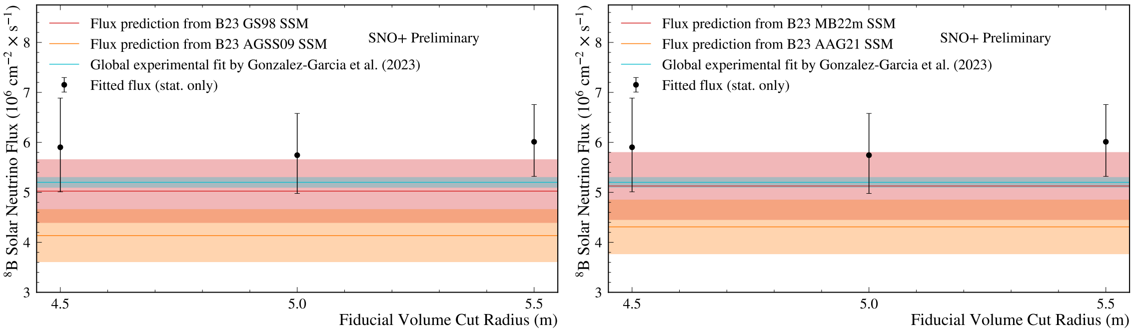

Figure 5.11: The ^{8}B solar neutrino fluxes from the full fill analysis in each fiducial volume case, in comparison with, on left, the B23 GS98 (5.03×10^6 cm^{-2} s^{-1}) and B23 AGSS09 (4.14×10^6 cm^{-2} s^{-1}) flux predictions, and their uncertainties, as well as the 2023 Gonzalez-Garcia global fit [53]. On the right, alongside the global fit the SSM predictions with the more recent compositions of B23 MB22m (5.13×10^6 cm^{-2} s^{-1}) and B23 AAG21 (4.31×10^6 cm^{-2} s^{-1}) are shown with their uncertainties.

future. This suggests a result with precision on par with or better than Borexino's, shown in Fig. 5.12, may be achievable.

Building on similar work from the partial fill, the first analysis toward a measurement of the ^{8}B solar neutrino flux in the fully-operational scintillator phase of the SNO+ detector has been performed. The results are in agreement with theoretical predictions, though there

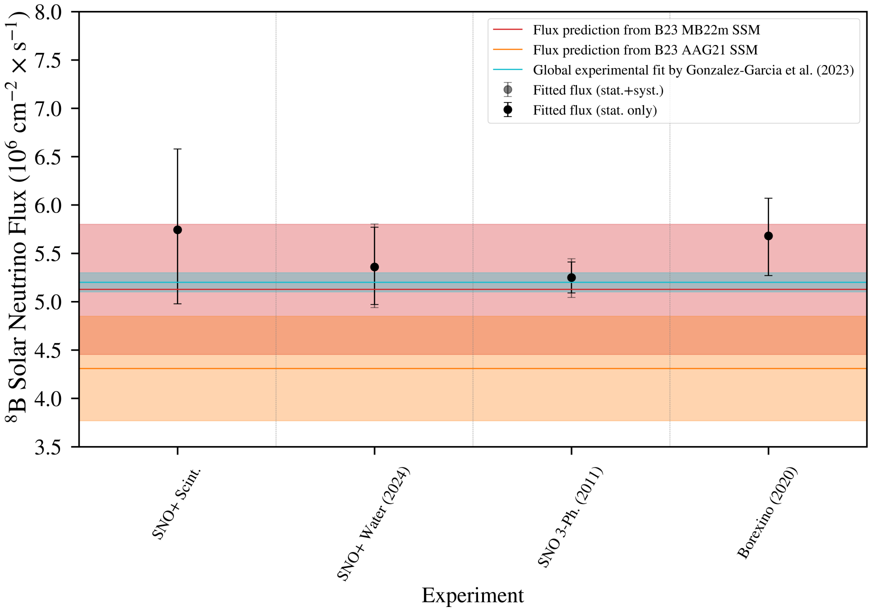

Figure 5.12: The fitted ^{8}B solar neutrino flux fitted in the 5.0-m fiducial volume is shown alongside results from other relevant experiments, as well as the flux from the B23 MB22m and B23 AAG21 SSMs and the most recent global fit evaluation. The other experimental results shown are the most recent fit from the SNO+ water phase using the full water phase dataset [198], the SNO combined three-phase fit [63], and the most recent result from Borexino [59]. These respectively represent the best result achieved in the same detector with a different target medium, the best result achieved in the precursor detector (which benefited from the ability to measure the flux in a more robust manner through additional interaction channels), and the best result achieved by an organic liquid scintillator detector to date.

are hints in the analysis of mismodeling that will be addressed as the scintillator phase model and analysis mature. The statistical limitations of the analysis will see substantial improvement with the addition of the rest of the scintillator phase dataset, as well as the potential for the analysis of data accumulated during periods of loading with subsequent scintillator cocktails and during the Tellurium-loaded phase of SNO+. This analysis has continued the development of solar neutrino detection with SNO+ and will serve as the benchmark and foundation for future efforts.

Chapter 6

Hybrid Detectors aka Optical Detectors: The Next Generation

As discussed in previous chapters, large-scale optical neutrino detectors have largely operated in distinct detection modes. That is, they either detect Cherenkov light from relativistic charged particles, or they detect scintillation light produced from excitations of the molecular orbitals of organic compounds. This has led to operations in two different regimes, with detectors that are optimized for the detection and reconstruction of different sets of event parameters at different precision. In recent years, much effort has gone into devising mechanisms to combine these approaches and enter a so-called "hybrid" regime that benefits from and exploits both production mechanisms to produce physics results that either scheme on its own would struggle to produce [199]. This chapter will discuss a variety of avenues that are currently being pursued.

6.1 A Unified Approach

In truth, charged particles traversing a scintillating medium may also produce Cherenkov light, but often the relative light yield makes discerning photons from the two sources (and thereby leveraging the distinct information provided from each) challenging. While this has previously been leveraged in LSND [158] and MiniBooNE [161] using low yield scintillator for 10s of MeV of energy deposited and beyond, only recently has progress been made to achieve such a feat in the high light yield scintillators used by experiments aiming to perform precision MeV-scale spectroscopy, such as Borexino [200, 201] and SNO+ [183]. Still, performing these analyses has stretched the limits of what is achievable with contemporary detector technology, necessitating leaps forward to reach the hybrid paradigm.

6.1.1 Novel Scintillating Media

Part of this effort has gone into developing new scintillating materials that may make separating the Cherenkov and scintillation signals easier than previously used substances, while still maintaining the benefits of each emission channel as well as overall optical clarity. Enhancing the properties of the two light production paradigms has been common place in optimization of scintillator cocktails [127, 202], and even for water Cherenkov detectors [203]. But, these efforts have previously focused on improving, say, the base light yield or wavelength response of the channel of interest, and not on harnessing both scinitllation and Cherenkov emission simultaneously. The development of water-based liquid scintillators and slow scintillators are precisely dedicated to this question.

6.1.1.1 Water-based Liquid Scintillator

The conceptual underpinning of water-based liquid scintillator (WbLS) is to combine water and scintillator, typically immiscible as scintillator is oil-based, into a material that exhibits the properties of both. Ideally, depending on the turn of the knob of how much scintillator is incorporated into the mixture, can act more like a pure water Cherenkov detector, more like a pure liquid scintillator detector, or end up somewhere in between depending on the physics needs [204]. This would allow one to maintain a relatively high light yield from the scintillator, while keeping the better optical clarity of water. Additionally, the relative abundance of water compared to scintillating compounds could aid in scalability due to procurement savings.

Chemically, this is achieved by emulsifying the liquid scintillator into the water using a surfactant that creates micelles containing the scintillator. The micelles are envelopes of the scintillator material protected from interfacing with the surrounding water by the surfactant layer, which contains a hydrophobic inner shell and a hydrophilic outer shell, enabling dissolution into the water. The prevalence of these micelles can be tuned to the users needs, and has been demonstrated to be stable at a wide spread of concentrations, up to 40%. Other properties at this extreme may falter, inclining deployments toward lower concentrations. Given the suitability of the properties of LAB as a solvent and PPO as a secondary fluor in standalone liquid scintillator contexts through the community, these components have also predominantly been used for the scintillator in WbLS. Different preparations of WbLS in comparison to pure scintillator can be seen in Fig. 6.1. Work on WbLS has been pioneered by Brookhaven National Laboratory (BNL), which in recent years has led efforts to characterize and model WbLS and demonstrate stability at the benchtop and ton scales [205–209].

Characterization of timing and light yield properties has been extensively studied beyond BNL, particularly at Lawrence Berkeley National Laboratory (LBNL) and University of California, Berkeley with the CHESS experiment [210]. CHESS uses an array of small-area, fast PMTs imaging a liquid target volume exposed to cosmic ray muons or radioactive sources in order to separate the Cherenkov and scintillation components via the pixelization and time response. This has been demonstrated with pure liquid scintillators [211], as well as with WbLS [212], and the timing and light yield have similarly been assessed at various concentrations using CHESS. Additional measurements for timing have been done using X-ray excitation [213].

There is also considerable interest in the particle identification (PID) capabilities for WbLS, given the advantages that leveraging both emission channels provides. For example, one could use the ratio of scintillation to Cherenkov light produced as a PID metric since heavy particles should be below threshold for MeV-scale interactions. Several studies have been undertaken toward that end [214, 215], benefited by the measurement of the proton light yield of WbLS under exposure to neutrons [216, 217]and measurements of the light yield and timing for α particles [215], to be discussed further in Sec. 7.2.

It should be noted however, that oil-based scintillators typically have a lower index of refraction than water, meaning that pure scintillators may actually produce more Cherenkov light than pure water. This additional light will still be swamped by the vastly larger scintillation response, which is what WbLS aims to rectify with its mixture. Another potential drawback exists in the sense that water, as a universal solvent, is remarkably harder to purify than oil-based compounds like scintillator, meaning radioactive background levels may be more substantial compared to what is achievable in a pure scintillator detector.

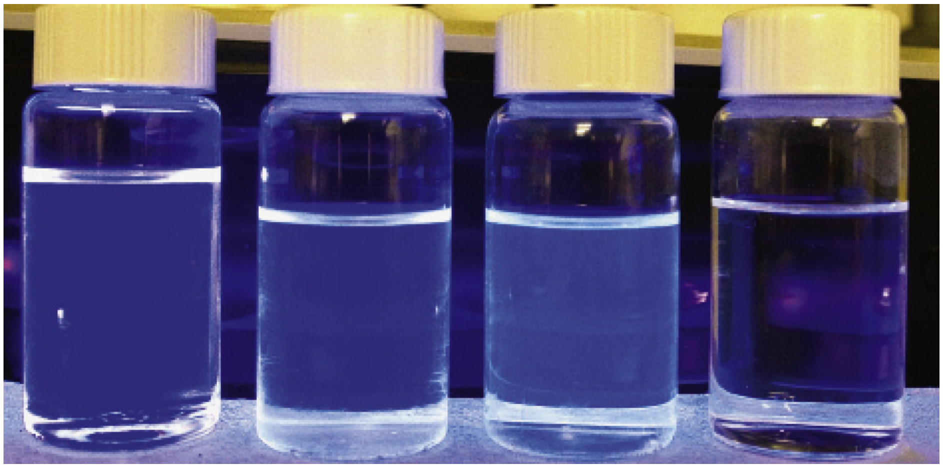

Figure 6.1: Samples of scintillating media illuminated by ultraviolet (UV) light. On the left is a pure LAB-based scintillator, whereas the midle two samples are distinct formulations of WbLS, with the rightmost sample being water loaded with a wavelength shifter that does not boost overall light production [216]. The rightmost sample does not visible illuminate under the application of the UV light because no scintillation photons are produced. Figure reproduced from [204].

6.1.1.2 Slow Scintillators

While separation of Cherenkov and scintillation light has been found achieved in pure scintillators at the benchtop scale at BNL and with CHESS and FlatDot [211, 218, 219] and with large-volume experiments as mentioned above, the situations in which this is achievable are often quite limiting, requiring high energy depositions or pre-knowledge about sources like muons that may not always be available. The evolution toward slow scintillators aims to accomplish this separation in pure scintillators and avoid sacrificing the light yield as occurs in WbLS. This is done by exploiting formulations where the scintillation emission is sufficiently delayed relative to the Cherenkov emission [220], as explored by collaborators at BNL and Chinese institutions. Oxford has explored this topic extensively, and has demonstrated both physics impacts through simulations as well as measurement of properties on the benchtop [221, 222]. Researchers in Germany have also extensively characterized slow scintillator of their own, including optimization of the solution and measurement of timing and emission characteristics, with a particular view towards pulse shape discrimination [223]. While the slow scintillator pathway may be hindered by issues with scalability, either due to cost or optical conditions, there are significant advantages to maintaining the scintillation yield while also achieving separable Cherenkov and scintillation lights.

6.1.1.3 Doping

The use of select dissolved isotopes in optical neutrino detectors dates back to the usage of cadmium in the Savannah River experiment, continued with chlorine in the salt phase of SNO and has expanded now with the widespread use of gadolinium and ^{6}Li in today's reactor experiments. These dopants primarily aid in neutron detection, but additional efforts have been made to load tellurium [175] and xenon [166] for neutrinoless double beta decay experiments in recent years. As a consequence of the strong community desire for enhancements provided by these isotopes [224, 225] and of the emergence of hybrid optical technology, there is a key need to maintain these capabilities with newly formulated materials, as well as explore how hybrid techniques can actually expand the options for isotope loading.

In particular, WbLS has been put forward as a pathway to loading a variety of metals with yearslong stability, in contrast to failures experienced with some pure scintillator doping strategies from the past [226]. A significant example of this can be found in the advancement of ^{6}Li-loaded scintillator for the PROSPECT experiment, which used techniques associated with WbLS production in order to effectively load the scintillator [227]. There has also been renewed interest in the use of ^{7}Li for solar neutrino physics, while using hybrid technology [228, 229]. An example of the target-weighted cross sections for the ^{7}Li charged current interaction and other interactions present for a 5% WbLS detector with 10% ^{7}Li loading by mass can be found in Fig. 6.2. Given the benefits of Gadolinium loading displayed in scintillator-based reactor experiments and in water with SuperK-Gd, the prospect of WbLS doped with Gd has produced significant interest, especially amongst the nonproliferation community with interest in reactor monitoring [230–232], as WbLS being water-based has scalability benefits and avoids handling and health hazards associated with large volumes of scintillator. In addition to doping particular isotopes, the potential for loading various forms of quantum dots has been explored for both liquid scintillator [233–235] and more recently for WbLS [236]. The quantum dot loading allows favorable tuning of light emission and absorption through the precise band structure.

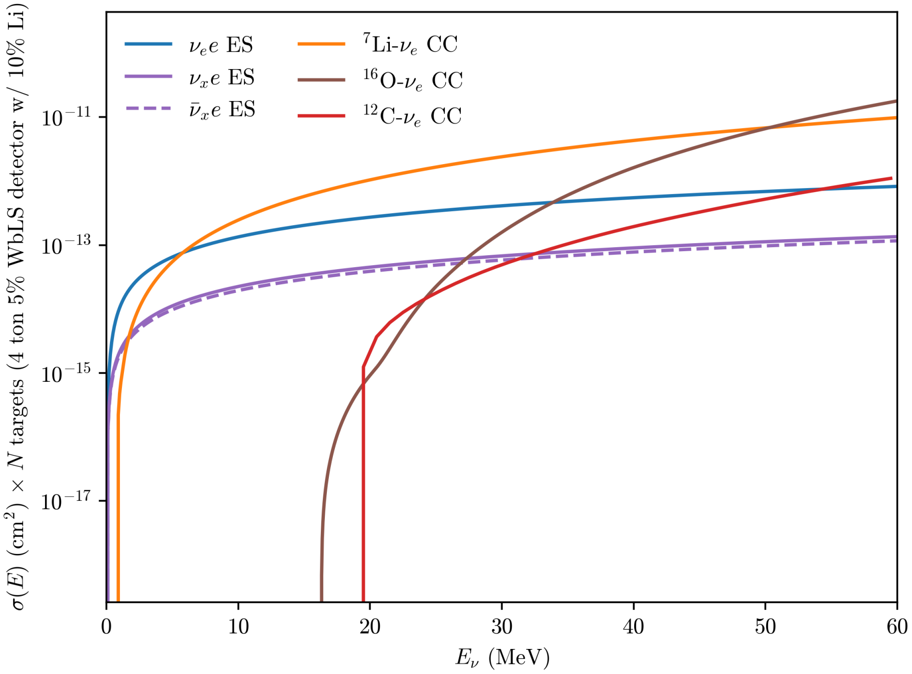

Figure 6.2: The cross sections as function of energy weighted for the number of targets in a 5% WbLS detector of 4 tons with 10% ^{7}Li loading by mass, for the ^{7}Li charged current interaction with ν_e, ^{12}C charged current interaction with ν_e present from the scintillator, ^{16}O charged current interaction with ν_e present from the water and to a much lesser extent the scintillator, and the neutrino-electron elastic scattering cross sections.

6.1.2 Fast, High Efficiency Photosensors

Beyond the target media advancements, there has been considerable work in the past decade to improve the performance of large-area PMTs, in terms of better time precision, high quantum efficiency, lower radioactivity, noise reduction, operating conditions and more. While technologies like silicon photomultipliers (SiPMs) have become favored in certain contexts [20], the need to realize high photocoverage over substantial volumes has led to the continued reliance on PMTs for optical neutrino detectors. For example, SiPMs require much colder operating temperatures to achieve survivable noise levels, which presents a substantial difficulty for use in detectors where the target is liquid at room temperature. Additionally, the tiling considerations required for high coverage that bring high costs along with them tip the balance in favor of large-area PMTs. If large-area PMTs attain exquisite time resolution, this potentially has a large impact in sorting Cherenkov signal from scintillation signal, given the differences in the emission processes.

A variety of standard technology PMTs that represent enhancements on the baseline performance have been evaluated in recent years [115, 119, 120, 237–239]. Timing resolutions have been demonstrated for 8-12-inch (20-inch) PMTs at around 1 ns (3 ns) or below, a substantial improvement from the SNO (SuperK) PMT models with 3 ns (6 ns or greater transit time spread (TTS). Efficiencies have also improved, with peak quantum efficiencies of near 30% now common across a range of models, combined with increased collection efficiencies.

Perhaps the most groundbreaking move forward in this space has been the innovation of the microchannel plate (MCP), which has allowed for the creation of the Large Area Picosecond Photodetector (LAPPD) and its cousin the MCP-PMT [240, 241]. MCPs are replacements for the dynode amplification stages in a typical photomultiplier, and consist of glass plates which are perforated by an array of cylindrical microchannels that photoelectrons pass through under an electric field and in so doing cause a cascade of further electrons to be released. LAPPDs are large format (side lengths of 20 cm) tile-shaped photodetectors that employ MCPs to achieve sub-100 ps timing [242], with potential for both strip-based and pixel-based readout. Building on the work of CHESS to measure WbLS properties, the LAPPD has also been used on the benchtop for characterization [243]. LAPPDs have also been succesfully deployed in the ANNIE experiment, representing a major milestone for the technology [244]. Meanwhile, MCP-PMTs, with capacity for similarly impressive time features, are being deployed by JUNO [119, 245].

6.1.3 Chromatic Sorting

Taking into consideration the difference in wavelength spectra between the Cherenkov and scintillation light, research has also explored the use of dichroic filters that selectively transmit or reflect certain wavelengths to optically sort photons [246]. This sorting ideally separates out the Cherenkov and scintillation components with some level of purity. Most prominently, this work has taken the form the “dichroicon”, which combines usage of dichroic filters with light concentrators, replacing the mirrors with filters [247]. In this way, long-wavelength or short-wavelength light can be focused onto individual PMTs, with a diversity of possible configurations based on wavelength cutoffs and PMT placements. There are significant limitations due to the efficiency of the filters especially as it relates to the sharpness of the transmission behavior with wavelength and angle of incidence and the complexity of manufacturing these devices, but work continues to demonstrate their efficacy.

6.1.4 Other Developments

There are a few other explorations in the realm of hybrid detection worth mentioning. First is the development of algorithms to exploit the topological and timing information of these detectors to leverage the added information, using both traditional [248–252] and machine learning (ML) [253–255] focused approaches. Secondly, in order to improve light collection, the wavelength shifting plates have been proposed as an alternative to classical light concentrators [256, 257]. These plates would better match the light to the PMT QE and also provide a larger area of coverage. Additionally, though most hybrid detector concepts retain the “standard” geometry of a large monolithic volume surrounded on all sides by photodetectors, the Stratified Liquid Plane Scintillator (SLIPS) concept proposes a layer-based design that takes advantage of reflections and clever photodetector placement to minimize costs, “dead” detector volume and complications from physical structures [258].

6.1.5 Consolidating and Scaling Up: Eos, Theia, and Others

With all of these concepts and advancements floating around, the space to draw from when designing next-generation experiments is almost overwhelming. As these concepts progress from the drawing board to the benchtop and then need to move to the next step, a host of technology testbed concepts have sprung up in recent years designed to pave the way for broader implementations. Brookhaven National Laboratory has focused largely on ensuring that the production of WbLS is scalable from the laboratory scale without losses to performance and that once WbLS is deployed that it remains stable both chemically and in terms of its emission and absorption properties. Currently this has been explored with a 1-ton detector with plans underway to operate a 30-ton detector for similar purposes [208, 209]. Meanwhile in the United Kingdom, concepts about deploying WbLS in the nonproliferation context [230–232, 259] have coalesced into the Boulby Underground Technology Testbed Observing Neutrinos (BUTTON) [260], another 30-ton device which would be the first to employ WbLS in a deep-underground context, along with demonstration of novel photodetector module technologies. The Accelerator Neutrino Neutron Interaction Experiment (ANNIE) at Fermilab [261–263] is a optical detector designed as the name would suggest to study neutron production from beam neutrinos as an aid to understanding the impacts for nucleon decay and neutrino oscillation analyses. However, as a bonus, ANNIE has also been used as a technology testbed to deploy LAPPDs [244] and, for the first time, detect neutrinos with WbLS [264].

The most ambitious of the testbeds is Eos [114], which aims to make good that the hybrid concept leads to improvements in reconstruction necessary to push the boundaries of physics results. The detector is a Lawrence Berkeley National Laboratory project located on the campus of UC Berkeley, and is a 20-ton detector with a 4-ton acrylic vessel (AV) to hold the target medium, which will be tuned between water and different concentrations of WbLS, surrounded by a water buffer. Nearly 250 PMTs of different models, including dichroicon assemblies, instrument the detector, taking advantage the high efficiency and exquisite timing performance of these newer models, with a rough overall coverage of approximately 50%. The readout electronics include fast digitizers from CAEN, and a custom, flexible trigger utility board designed to allow triggering on inputs from the detector, veto system or calibration sources.The Eos project has also motivated the development of the open-source RAT-PAC2 simulation and analysis framework for use in all experiments in the community [265, 266]. The evaluation of hybrid performance in reconstruction features at the heart of the project, with a diversity of deployed calibration sources being developed and brought to bear, including a novel, tagged directional source to test angular reconstruction precision. With a demonstration of the viability and precision of reconstruction that heavily relies on the hybrid nature of experiment and verification and tuning of the simulation models for hybrid detectors, Eos may provide the linchpin of support needed to confirm the benchtop and simulation studies and to move beyond the ton scale. As of June 2024, Eos has finished commissioning and begun collecting data.

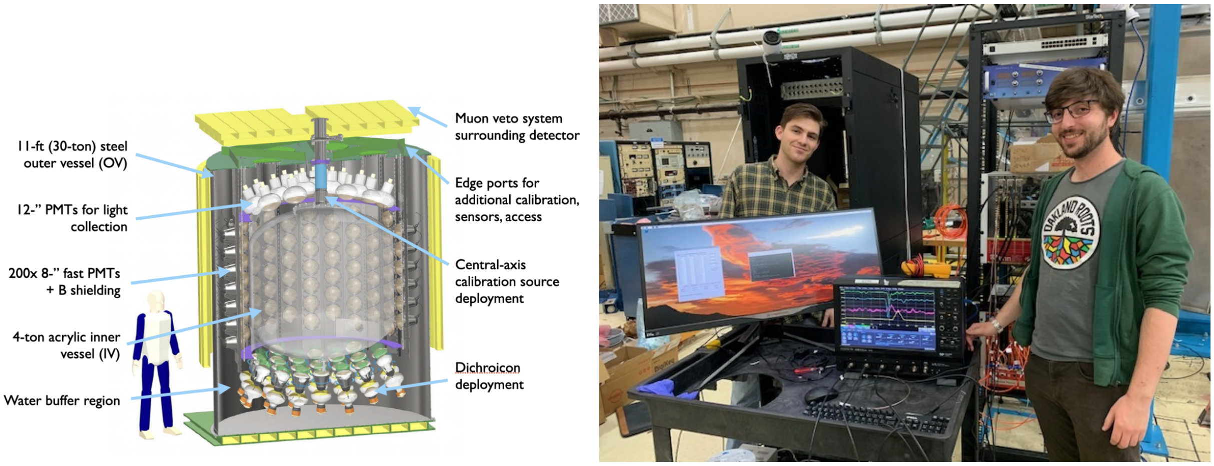

Figure 6.3: On left, a rendering of the Eos with various components labeled, reproduced from [114]. On right, the author (bespectacled) and collaborator B. Harris of the University of Pennsylvania show off the first PMT pulses read out from the Eos detector.

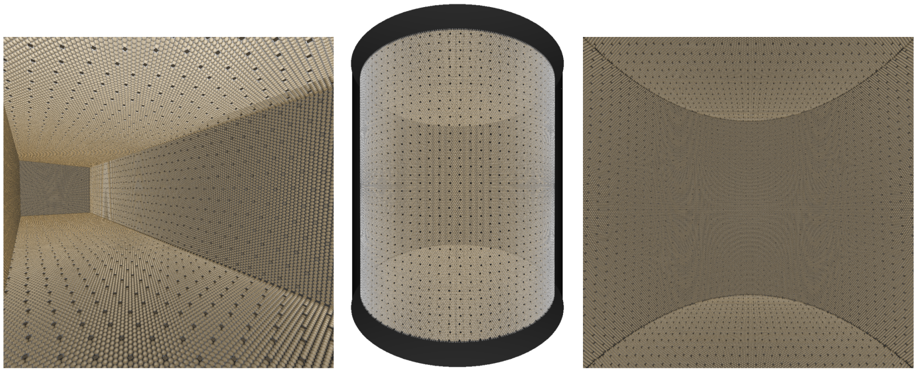

Figure 6.4: Renderings of Theia in the 25-kiloton configuration (left), and 100-kiloton configuration (center, right). Figure reproduced from [1].

Of course, while these testbeds are valuable proofs-of-concepts and intermediate sized detectors may yet be required, the main goal remains to operate hybrid detectors at the forefront of physics capabilities. Building off of the 50 kiloton liquid scintillator Low Energy Neutrino Astronomy (LENA) proposal [267, 268] and the similarly-sized Advanced Scintillator Detector Concept (ASDC) [228], Theia [1] is the conceptual endpoint for large-volume hybrid detectors that has gained broad community support across the basic and applied optical neutrino detection landscape [199, 259, 269]. The exact hybrid technologies to be deployed are still very much to be determined, but different concepts have assumed the 25-kiloton, 50-kiloton, and 100-kiloton scales with above 50% photocoverage of fast PMTs and a range of WbLS formulations. The current testbeds will help narrow this picture, though exact performance will vary depending on the exploited target and instrumentation. THEIA proposes accessing a broad physics program at both high and low energy regimes, with flexibility as to the final configuration. Example renderings of possible configurations can be found in Fig. 6.4, exhibiting the scale and high coverage. Projections show competitive capabilities to measure δ_{CP} to a DUNE module when placed in the same beamline, with complementarities to both HyperK and the liquid argon-based DUNE modules in terms of systematics that could prove illuminating. Beyond that, THEIA would achieve sub-10% precision on the CNO solar neutrino flux and make substantial contributions to geoneutrino and reactor antineutrino observations [270] and nucleon decay sensitivity. For the elusive diffuse supernova neutrino background (DSNB), THEIA presents an opportunity for 5σ results in only a few years of data-taking [271]. Given the size, the possibility of deploying a massive balloon of isotope-loaded scintillator to search for neutrinoless double beta decay $(0\nu\beta\beta)$ and reach into the inverted ordering region has been explored as well. Each of these capabilities is reliant on the hybrid nature of the detector, proving the value of these technologies.

Chapter 7

Explorations of Hybrid Detector Technology

Following from the previous chapter on the developments in hybrid detection technologies, this chapter summarizes some particular contributions to this research and development by the author. The focus in Sec. 7.1 is on assessing the impact of hybrid detection technology and reconstruction capability on MeV-scale physics topics, while Sec. 7.2 focuses on the potential for particle identification in hybrid detectors at large scales.

7.1 Case Study: Physics Impact of Reconstruction Performance in Hybrid Detectors

The following section details a study of the physics impacts for CNO solar neutrino detection and $0\nu\beta\beta$ limit setting given simulation of a nominal hybrid detector model and potential reconstruction techniques. This work originally appeared in Phys. Rev. D 103.5 052004 (2021) [252]. The modeling and reconstruction to which the author contributed in part are summarized for the benefit of the reader to the extent necessary to understand the final results in Sec. 7.1.1 and Sec. 7.1.2, while this author's direct contributions to the publication on the physics impacts are restated and expanded upon in Sec. 7.1.3. For additional context, work by the author from Eur. Phys. J. C 80 (2020) 5, 416 [1] is also incorporated in Sec. 7.1.3.

7.1.1 WbLS Modeling

Modeling of WbLS properties since its inception had proceeded on a fairly as-needed basis subject to what was under study, with other properties defined using approximations made under assumptions about how the optics of water and liquid scintillator would combine based on their properties as individual components. Given the complicated structure of WbLS, direct inputs from measurement were then well-motivated and necessary in order to build a self-consistent model. By the onset of this study, enough sophistication had developed in measurements of properties that creating a substantially realistic model became practical, though there was still some reliance on combination of characteristics.

The direct measurement of the light yield of 1%, 5%, and 10% WbLS in [212] as well as the emission profiles and time profiles measured in [213] in these specific formulations enabled the realistic modeling of light production in WbLS in simulation for the first time. A meticulous literature review was performed to account for the propagation effects. Newton's formula [272], along with input measurements for LAB+PPO [273] and the approved standard for water [111], is used to define the refractive index as a function of wavelength in the model, which hews closely to the water refractive index given the proportions of materials. For the absorption, the absorption coefficient (the inverse of the absorption length) was calculated by taking the sum of the absorption coefficient for each of LAB, PPO and water weighted by the molar concentration within the final mixture. The inputs came from internal measurements by SNO+ for LAB and PPO [180], while for water a combination of source from literature was used: the Pope and Fry measurement [274] above 380 nm and the Smith and Baker measurement [275] below 380 nm. Reemission probabilities were scaled according to the component's contribution to the overall absorption. Finally, scattering lengths were determined by taking the volume fraction weighted sum of the scattering coefficients (the inverse to the scattering length), again using internal measurements from SNO+ [180].

From the software perspective, the modeling relied on use of the open-source RAT-PAC simulation and analysis framework [276], the Geant4-based [188] community tool that has since evolved into RAT-PAC2 [266] in part as a consequence of this study, which also fleshed out the capabilities of RAT-PAC substantially. Important refinements to the software included the addition of the Rayleigh scattering module from the SNO+ collaboration [180] and revisions to the GLG4Scint module originally developed out of KamLAND to handle the scintillation and associated absorption and reemission of photons [189].

7.1.2 Reconstruction

In order to flexibly examinine reconstruction capabilities and physics impacts at a broad range of scale and detection configurations, a simplified framework was developed rather than employing a full simulation of the geometry with 10s of thousands of PMT objects. Advancements in computing and software since this study likely mean that one could repeat this study with full simulation today. Instead, electrons of energy 2.6 MeV, a single value that is of interest for reactor and solar neutrinos and for neutrinoless double beta decay, were simulated at the center of a large block of the material of interest, isotropically in direction. The materials surveyed were water, 1% WbLS, 5% WbLS, 10% WbLS, and pure liquid scintillator. The tracks for generated photons are stored, and then in order to simulate the photodetector boundary, the tracks are truncated at the distance from the center corresponding to where the photodetectors would be in a right cylinder of LAB+PPO with mass density $0.867\,\mathrm{gcm}^{-3}$. This corresponds to a radius of 10.4 m and 38 m for 1-kiloton and 50-kiloton detectors. Note that because water (which will not be focused on in the Sec. 7.1.3 as the physics targeted is not possible without any scintillation light at all) and WbLS at the concentrations of interest have very similar densities near $1.0\,\mathrm{gcm}^{-3}$, meaning that the simulated detector radius contains less than 1 and 50 kilotons of material. In this truncation, the track is counted as a hit subject to a coverage factor of 0.9, as well as a QE corresponding to the super bialkali formulation available from Hamamatsu for large-area PMTs [277]. In this way, 10% of the tracks are killed uniformly at random to simulate the fact that the entire surface area is not sensitive, and then an additional wavelength dependent efficiency is applied. The intersection point is taken as the hit position with perfect precision while a Gaussian smearing in time is applied according to four categories of photodetector:

1. "PMT" → 1.6 ns
2. "FastPMT" → 1.0 ns
3. "FasterPMT" → 0.5 ns
4. "LAPPD" → 0.07 ns

The *PMT* model is meant to emulate then industry-leading time sensitivity, while *FastPMT* corresponds to a similar time spread as today's R14688 models. *FasterPMT* invokes sub-nanosecond timing from PMTs, while *LAPPD* is meant to model the tiling of the detector with LAPPDs capable of achieving sub-100 picosecond response. While some effects are lost from this simplified approach (noise, reflections off of detector components, position uncertainty), the impact of these factors on reconstruction of events far from the detector boundary were found to be small.

The event reconstruction was developed with hybrid detection specifically in mind though is kept relatively simple, and relies on techniques that have been applied previously to scintillator and water Cherenkov detectors. Adaptations of this scheme have been used in later studies [114, 270]. The staged method used has three steps:

1. Vertex position and time is fit by finding the reconstructed position that maximizes the time residual likelihood, which here assumes straight line paths and monochromatic emission at 400 nm when accounting for the index of refraction. The quadrature sum of the fit residuals for the three position dimensions is taken as the position resolution.
2. Direction is fit by identifying the prompt photons using the vertex position and time identified in the first step, and then maximizing against the $\cos\theta_\gamma$ distribution between the hypothesized direction and the photon direction defined by the difference in the event position and hit position. The angular resolution is defined by integrating the reconstructed $\cos\theta$ (where here θ is defined by the angle between the true and reconstructed direction) distribution out to 68%. A variety of thresholds are used to define the prompt window, and the prompt threshold that results in the best angular resolution is taken as the angular resolution for a configuration when discussing this later.
3. The energy reconstruction relies on simple hit counting, with the mean and width of a fitted Gaussian defining the energy resolution.

Several diagnostic tools were used, including the photon statistics (within the Cherenkov ring and in total), as well as modifying the time profiles. The photon statistics checks helped to cross-check on a coarse level why the resolutions in different fitted dimensions evolved as they did, for example, by understanding the extent to which Cherenkov light in the ring dominated over other photons detected in the ring for different materials. Modifying the time profiles, such as shortening or lengthening the principal decay time, was used to explore how these parameters drive the reconstruction performance, signposting for future material development such as with slow scintillators. The results for the 1-kiloton and 50-kiloton detectors are presented in Fig. 7.1. While a simplified approach, this represented the first demonstration of reconstruction for large-scale hybrid detectors and showed that good precision was simultaneously achievable for position, direction and energy at the studied energy, with plenty of room to optimize and refine the approach.

7.1.3 Physics Impact

With the energy and angular resolutions evaluated, their effect on the rejection capability of the ^{8}B solar neutrino background in neutrinoless double beta decay searches, and the identification of signal events for CNO solar neutrino detection was examined. While in one case the directional solar neutrinos from elastic scattering interactions are the signal and in the other these neutrinos are the background, the focus remains on them.

Prior to this, detailed studies for a multi-kiloton hybrid detector had been performed both for CNO neutrinos and for neutrinoless double beta decay [1, 278]. For CNO neutrinos, in those cases, the studies examined the sensitivity of 25 and 50 kiloton WbLS detectors, and 25- and 100- kiloton WbLS detectors for CNO neutrinos for the earlier and latter works respectively, with the scale definition being based on the density of water (unlike this study) for radii of 15.85 m, 20.0 m and 50.3 m for 25-, 50-, and 100-kilotons respectively. For neutrinoless double beta decay, the work assumed a 50-kiloton detector with an 8 m radius balloon of pure liquid scintillator. As with this sensitivity study, 90% coverage is considered in both of those previous works. In those works, a number of simplifying assumptions were made, including an assumed vertex and angular resolution, and simplified approaches to energy reconstruction. In addition, that work was based on a less complete model of the optical properties for WbLS, whereas this is the first such study using a data-driven optical model for WbLS, a more realistic detector simulation at the single photon level, and full event reconstruction to inform the resolutions applied to analysis. This work therefore serves to validate the simpler assumptions made in the earlier studies and to support the results from that work.

As with previous studies [1, 278], this analysis made use of the RAT-PAC framework [276], including the neutrino-electron elastic scattering generator and the radioactive decay generator used by SNO [279] and SNO+ [177] as well as an implementation of Decay0 [280]. In simulation, the neutrino-electron elastic scattering differential cross section [281] is weighted by the neutrino energy spectrum [45, 194] for the different fluxes from the Sun and then sampled in outgoing electron energy and scattering angle, for both ν_e and ν_μ. The solar

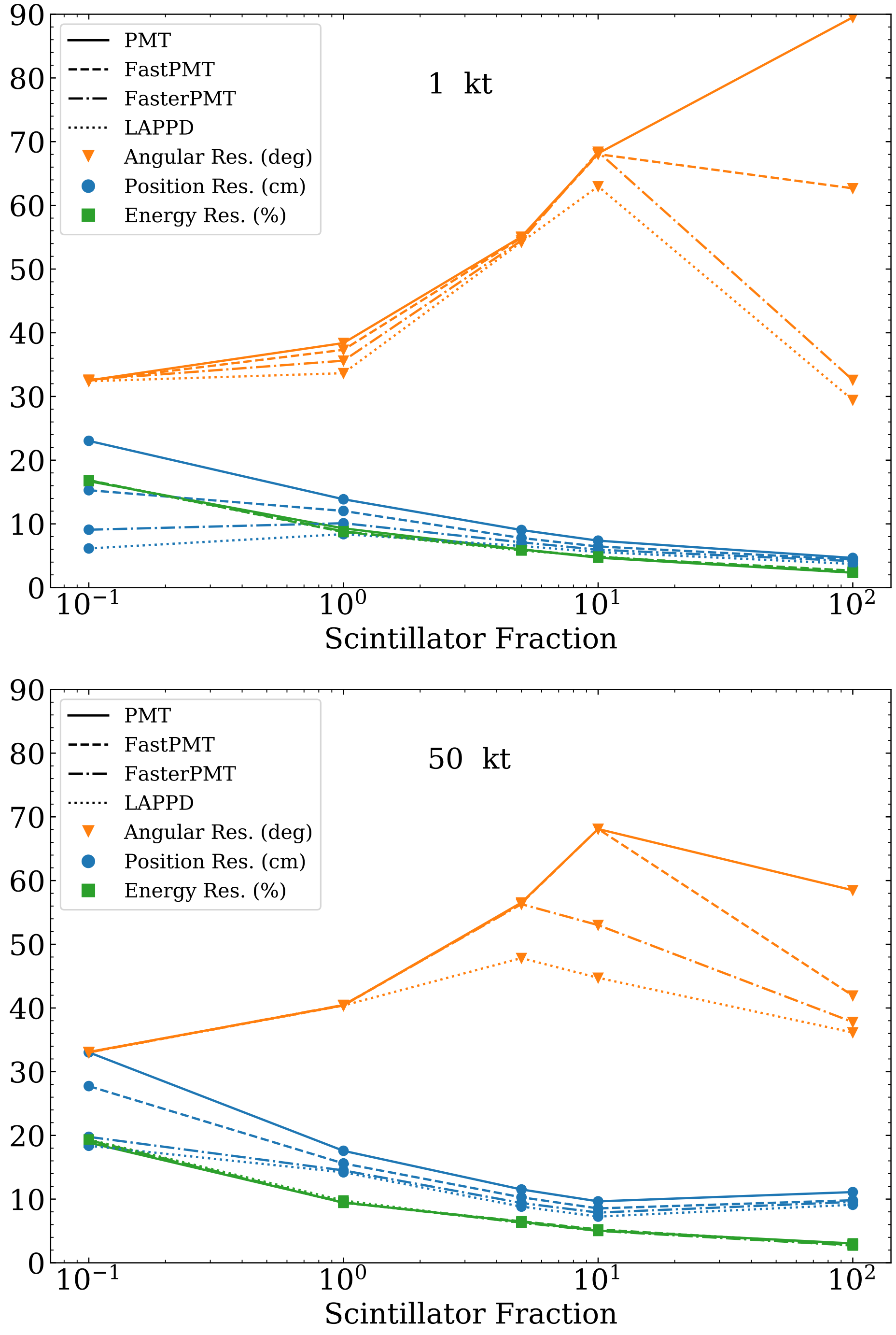

Figure 7.1: The achieved resolutions for position, direction and energy for the specified photodetector time response models and target materials, for the 1 kiloton and 50 kiloton scale detectors. Water is arbitrarily plotted with a scintillator fraction of 10^{-1} due to the axis's log scale.

neutrino fluxes from the BS05OP SSM were the assumed nominal values [282], for the sake of comparison despite the fact that these were outdated even at the time.

RAT-PAC is used for solar neutrino interactions and radioactive decays to simulate and extract the expected energy deposition in the target materials under consideration: 1% WbLS, 5% WbLS and 10% WbLS. After the simulation, solar neutrino event samples are weighted following the survival probability calculated in [283], again in order to maintain the ability for direct comparison.

The extracted angular resolution parameters from Sec. 7.1.2 are used to smear the scattering angle for solar neutrino events using a functional form

$$P(\theta) = Ae^{\frac{1}{\sigma}(\cos\theta - 1)} \tag{7.1}$$

taken from [278]. Radioactive and cosmogenic background events, as well as double beta decay events, were assumed to be isotropic and so their direction was not smeared by the resolution.

The decay energy spectra are also found for various backgrounds associated with the CNO energy region of interest, namely:

- ^{39}Ar
- ^{210}Po
- ^{210}Bi
- ^{11}C
- ^{40}K
- ^{85}Kr
- ^{15}O
- ^{238}U chain, which includes ^{238}U, ^{234}Th, $^{234\mathrm{m}}$Pa, ^{234}U, ^{230}Th, ^{226}Ra, ^{222}Rn, ^{218}Po, ^{214}Pb, ^{214}Bi (α and β branch), ^{214}Po, and ^{210}Tl
- ^{232}Th chain, which includes ^{232}Th, ^{228}Ra, ^{228}Ac, ^{228}Th, ^{224}Ra, ^{220}Rn, ^{216}Po, ^{212}Pb, ^{212}Bi (α and β branch), ^{212}Po, and ^{208}Tl

Many of these are β or $\beta - \gamma$ decays, with some α decays. Some of these, such as ^{238}U and its daughters (including ^{210}Bi and ^{210}Po), ^{232}Th and its daughters, and ^{40}K are primordial isotopes that accumulate in the target media via the dissolution of dust and other particulate matter from air and material contact and which can further contaminate detector components that then leach into the scintillator during processing or operations. Meanwhile, ^{85}Kr is abundant due to nuclear weapons use and dissolves in liquid materials, while ^{39}Ar is produced in the atmosphere in cosmogenic processes and is especially long-lived. Both of these are found in air, emphasizing a need to remove dissolved gasses and isolate the liquid target volume. ^{11}C is a relatively short-lived cosmogenically activated isotope that is a relevant background due to the copious amount of carbon in the scintillator molecules, and ^{15}O is similarly a cosmogenically-activated isotope present in the background spectrum due to the vast quantity of water deployed in a WbLS-based detector. All of the simulated isotopes have endpoints above 0.5 MeV (or, in the case of α decays, an endpoint which produces an equivalent amount of light as a 0.5 MeV β). An example of the energy spectra for these backgrounds, as well as the solar neutrino fluxes (excepting *hep*), subject to an energy smearing based on simulation of earlier WbLS models, can be found in Fig. 7.2.

7.1.3.1 Neutrinoless Double Beta Decay Sensitivity

For the neutrinoless double beta decay study, the purpose is to explore the impact of the angular resolutions determined in Sec. 7.1.2, so in order to test their effect most directly, the assumptions on the target, backgrounds and energy response are kept the same as previous iterations [1]. Thus, the study considers a target of the above-mentioned configuration with 5% natural Te (34.1% ^{130}Te) doped in LAB with 2 g/L PPO, and assumes the $3\%/\sqrt{E}$ energy resolution from [1]. Since the isotope-loaded scintillator will behave differently from the pure scintillator studied in Sec. 7.1.2 given the changed chemical composition, the resolution used previously is more appropriate regardless. While loaded scintillator is not studied in in Sec. 7.1.2, no assumption on angular resolution was directly made in the prior work, either. As such, the angular resolution found for unloaded scintillator is used to extend the previous analysis. This choice of angular resolution is made for being representative of reasonably achievable time profiles for any pure scintillator (loaded or otherwise), and having been subject to the implementation of the more complete optical model and full reconstruction. While the focus on hybrid detetction studies at large scales has mainly been on the use of WbLS, the particular use case of neutrinoless double beta decay requires exquisite energy resolution, something that can only be achieved with the photon yields of a pure scintillator. However, the improved timing precision of hybrid detectors can still yield significant benefit, as seen from the reconstruction results above in terms of improved angular resolution. This approach has now also been buoyed by the Borexino and SNO+ directionality results [183, 201], which rely on hybrid principles to identify directional events in scintillator, as this study sought to examine.

The same assumptions about location and background rates are made as in the previous studies [1]. Namely, the detector was considered, like in the CNO case, to be at Homestake at the 4300 m.w.e. depth with backgrounds that are shown in Sec. 7.1.3.1.

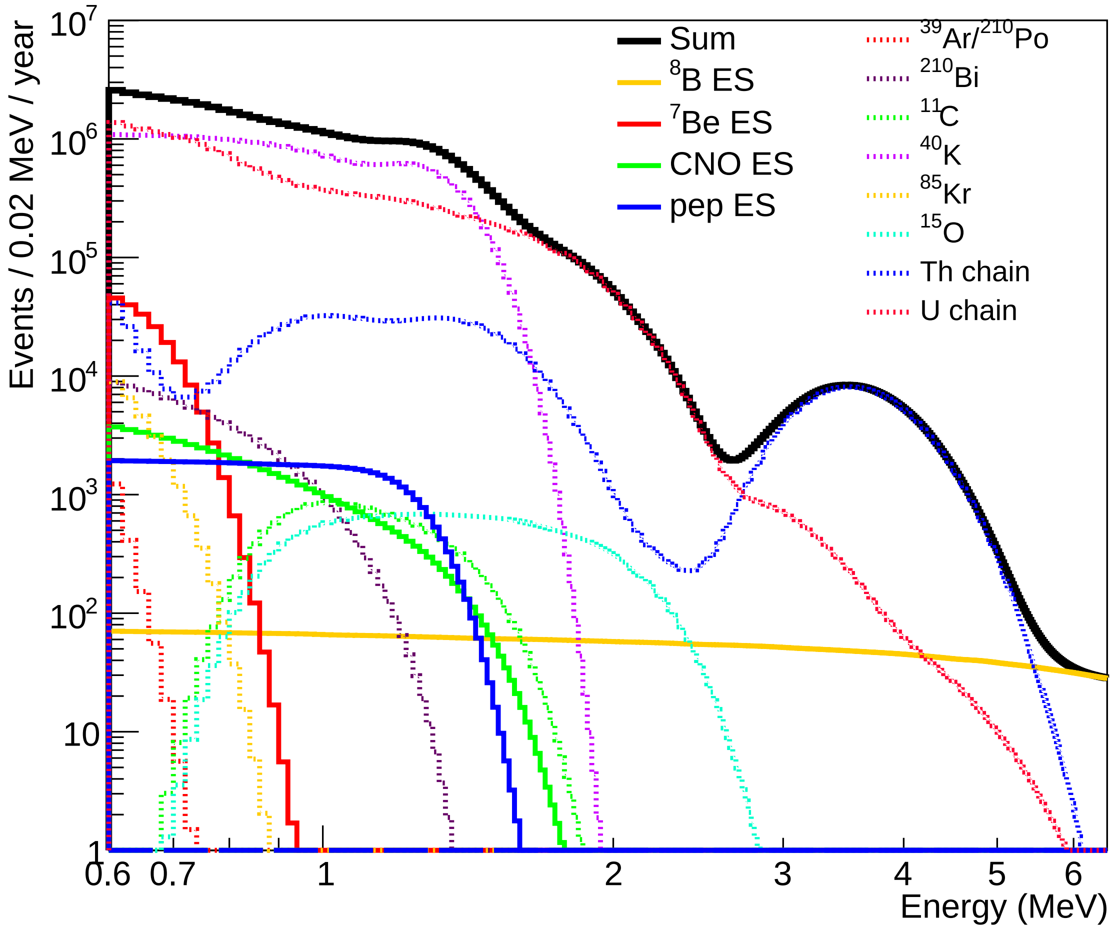

Figure 7.2: Energy spectrum from [1] for solar neutrino signals and radioactive backgrounds for a 25 kt, 5% WbLS detector, with 5 years of datataking and using a simplified lookup-based reconstruction method for energy as discussed in [278].

Table 7.1: Backgrounds assumed for the neutrinoless double beta decay analysis. The events in the ROI/yr are given for a fiducial volume of 7 m and an asymmetric energy range as specified in the text. A rejection factor of 92.5% is applied to ^{10}C, 99.9% to ^{214}Bi and 50% to the balloon backgrounds. Unlike in [1], the full rate for the ^{8}B solar neutrinos is shown, since the rejection calculated from the angular resolution will scale this value.

Source	Target level	Expected events/y	Events/ROI · y
^{10}C		500	2.5
^{8}B neutrinos		2950	27.6
^{130}I		155 (30 from ^{8}B)	8.3
$2\nu\beta\beta$		2.12×10^{9}	8.0
Liquid scintillator	^{214}Bi: 10^{-17} g/g	7300	0.4
	^{208}Tl: 10^{-17} g/g	870	-
Balloon	^{214}Bi: $< 10^{-12}$ g/g	$< 2 \times 10^{5}$	3.0
	^{208}Tl: $< 10^{-12}$ g/g	$< 3 \times 10^{4}$	0.03

Notably, ^{8}B solar neutrino events are the dominant background. Energy cuts were applied to restrict the study to the neutrinoless double beta decay region of interest for ^{130}Te, using a window around the Q-value of the reaction from $Q - \frac{\sigma}{2}$ to $Q + 2\sigma$, with σ is the energy resolution at the Q value. Cuts are applied cuts as a function of reconstructed direction relative to the Sun, $\cos\theta_{\odot}$, having applied a directional smearing according to the angular resolution, in order to reduce the background from directional ^{8}B solar neutrinos. The fraction of ν_e and ν_μ samples for ^{8}B neutrinos surviving these analysis cuts are scaled according to expected event rates on LAB+PPO in order to maintain the correct ratio of ν_e and ν_μ interactions and properly calculate the overall efficiency for rejecting solar neutrino background events and accepting isotropic events such as radioactive decays or $0\nu\beta\beta$. The non-directional signal and backgrounds are assumed to be rejected proportionally to the fraction of angular phase space rejected, and so the values reported from [1] are scaled by the appropriate fraction rather than performing additional calculations or simulation for event rates.

The efficiencies for the cut values were then propagated through the box analysis procedure of [1] to select an optimal cut that yields the best sensitivity. To quote an example, the identified expected sensitivity using the Feldman-Cousins frequentist prescription is $T_{1/2}^{0\nu\beta\beta} > 1.4 \times 10^{28}$ years at 90% CL in the 50 kiloton, LAPPD-instrumented pure LAB+PPO detector with decay time of 2.5 ns and rise time of 1.0 ns after 10 years of data taking. Using the available calculations at the time, this equated to a mass limit of $m_{\beta\beta} < 4.5\,\text{meV} - 11.1\,\text{meV}$, using nuclear matrix elements from [284, 285]. Looking at current scintillator experiments, KamLAND-Zen has placed a limit on the effective Majorana neutrino mass of 36 meV − 156 meV [286] as of 2023 and down to 28 meV − 122 meV [287] with the full dataset in 2024 (though recent nuclear matrix element calculations may result in noticeable deviation). Meanwhile, SNO+ projects a sensitivity of 55 meV − 133 meV [81]. Fig. 19 of [1] shows this result in the context of other proposed future experiments. The detector used to obtain the example half-life limit achieves an angular resolution of roughly 37°. This result is achieved by cutting on a solar angle corresponding to $\cos\theta_{\odot} = 0.7$, which rejects over 65% of the ^{8}B background while keeping 85% of the signal. This increases confidence in assumptions of rejection capability used in [1], which assumed the capacity to reject 50% of solar neutrino events while keeping 70% of the signal. Notably, improving the angular resolution to 30° and performing the same analysis does not yield changes to sensitivity to the leading decimal. Note that this result confirms that of more sophisticated reconstruction techniques, such as that presented in [251], in which similar rejection was demonstrated for a 3 m radius spherical detector. This case serves as a demonstration that such rejection could be preserved even in the much larger detector under consideration here, which is critical for next-generation neutrinoless double beta decay sensitivity.

Several other configurations for the 50-kt detector give results with similar sensitivity. Fig. 7.3 shows the impact of the various photon detector models, with only small losses in sensitivity for the 500 ps (FasterPMT) and 1 ns (FastPMT) models, of less than 1% and approximately 3% in lifetime, respectively. Only standard PMTs show a significant degradation of sensitivity, and this detector is also seen to perform best with no cut on solar angle, due to the degraded direction resolution achieved for this configuration. For the LAPPD-instrumented detector, the impact of scanning the decay time for values from 2.5 to 10 ns for LAB+PPO changes the sensitivity by less than 0.02×10^{28} years, as seen in Fig. 7.4, and the sensitivity improves for slower rise times, but the impact of the change from a rise time of 100 ps to 1 ns is less than 0.04×10^{28} years, as seen in Fig. 7.5.

As such, given the fact that a change in timing parameters would be most observable with faster photosensors, variation of the decay and rise time of the scintillation time profile at the scale examined, without other changes to liquid scintillator optical properties, are not thought to have a large impact on sensitivity to neutrinoless double beta decay. It should be noted that this conclusion is specific to the particular choice of direction reconstruction methodology, and conclusions may differ for other approaches.

7.1.3.2 Precision CNO Measurement

Scenarios for CNO solar neutrino detection were evaluated in a manner akin to the large-scale WbLS detector studies presented in [278] and [1]. The detector location is taken to be Homestake and the background event rates used are the same as in those studies, as in the neutrinoless double beta decay case. The contamination levels for the water and liquid scintillator components are reproduced in Tab. 7.2. The cosmogenic rates assume scaling from measurements done for SuperK for water and Borexino for scintillator, based on the muon rate and energy at Kamioka and Gran Sasso using the methodology developed in [134].

In order to align with the results of this new WbLS model and reconstruction technique, instead of the hit-based lookup reconstruction scheme applied in the prior work, a Gaussian smearing based on the expected number of hits, as determined in Sec. 7.1.2, is used to create a proxy for energy reconstruction. Since quenching effects are fully simulated when accounting for energy deposition that results in scintillation light, only the part of the width in hit-space that is due to photon counting is used in the smearing, so as not to double count the quenching. When applying the energy resolution is scaled with the energy deposition

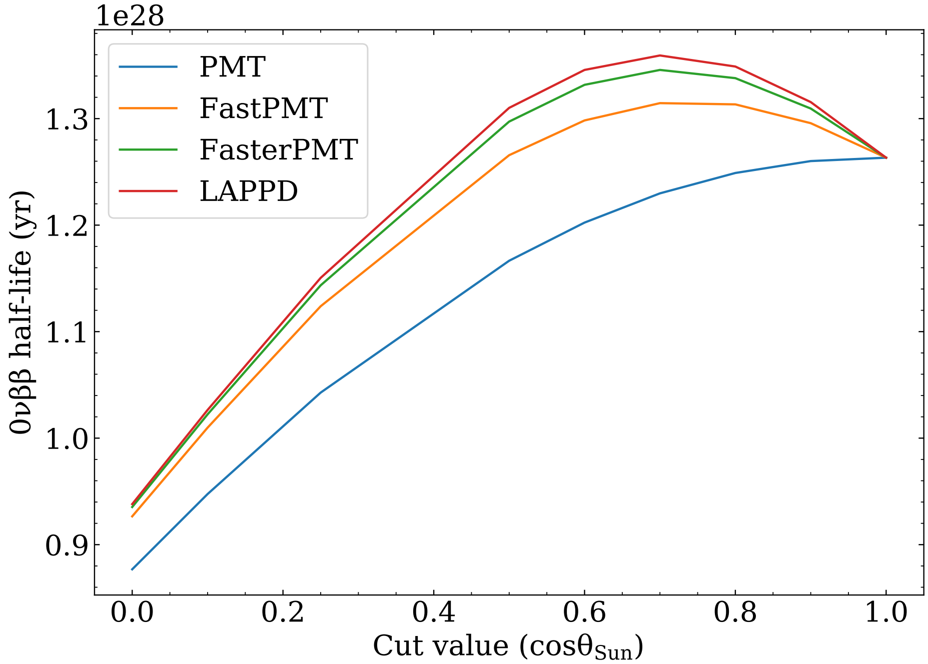

Figure 7.3: Half-life sensitivity for $0\nu\beta\beta$ achieved for a 50-kt pure LS detector with an 8m radius balloon of Te-loaded pure LS at 5% loading, as a function of solar angle cut and photodetector model. Angular resolution is based on that found in Sec. 7.1.2, assuming the as-measured properties of LAB+PPO without considering possible delays to the scintillation profile, and the analysis uses $3\%/\sqrt{E}$ energy resolution, as assumed in [1].

Table 7.2: The radioactive and cosmogenic background concentrations in each WbLS component assumed in the fit explored for the CNO solar neutrino flux precision measurement. The ^{238}U chain (above ^{210} Pb) and ^{234}Th chain are assumed to be in secular equilibrium. For ^{85}Kr, ^{39}Ar, ^{210}Bi and ^{210}Po where no measurement of contamination levels in water exists due to the low threshold, the same concentration as scintillator is assumed.

	H_2O level (g/gH_2O)	LS level (g/gLS)
^{238}U chain	6.6×10^{-15} [288]	1.6×10^{-17} [289]
^{234}Th chain	8.8×10^{-16} [288]	6.8×10^{-18} [289]
^{40}K	6.1×10^{-16} [290]	1.3×10^{-18} [291]
^{85}Kr	2.4×10^{-25} [291]	2.4×10^{-25} [291]
^{39}Ar	2.8×10^{-24} [291]	2.8×10^{-24} [291]
^{210}Bi	3.8×10^{-28} [291]	3.8×10^{-28} [291]
^{210}Po	4.2×10^{-24} [291]	4.2×10^{-24} [291]
^{11}C	100 (event / kt·yr) [134, 135, 292]	2.0×10^{4} (event / kt·yr) [134, 292, 293]
^{15}O	3000 (event / kt·yr) [134, 135, 292]	0

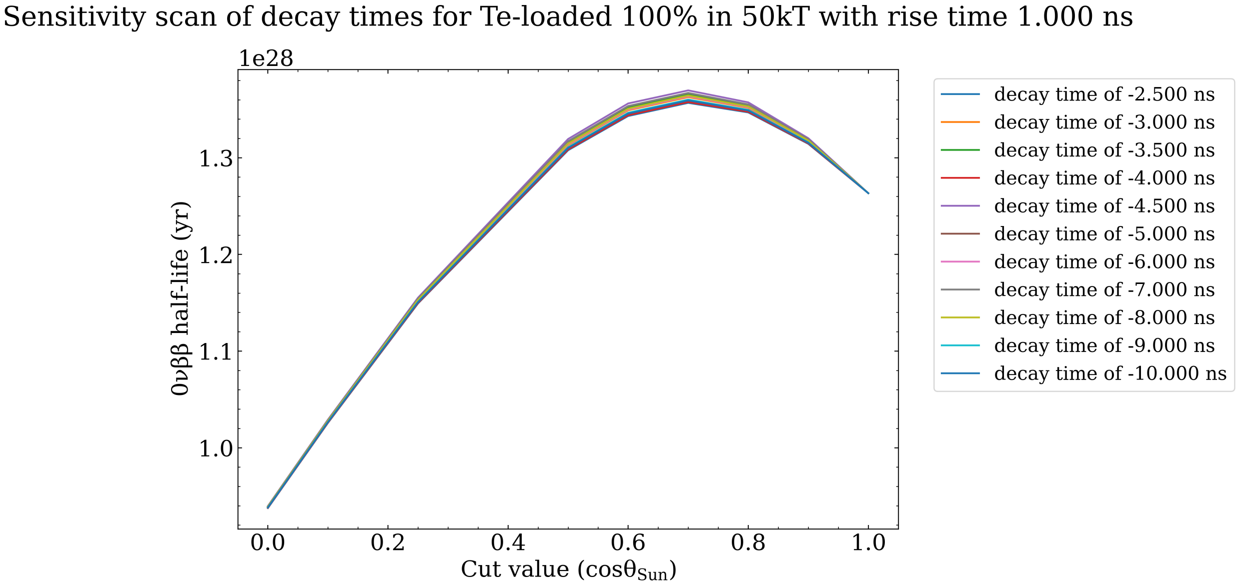

Figure 7.4: Half-life sensitivity for $0\nu\beta\beta$ achieved for a 50-kt pure LS detector with an 8m radius balloon of Te-loaded pure LS at 5% loading, as a function of solar angle cut and listed decay time, with fixed rise time as given. Angular resolution is based on that found in Sec. 7.1.2, assuming the as-measured properties of LAB+PPO without considering possible delays to the scintillation profile, and the analysis uses $3\%/\sqrt{E}$ energy resolution, as assumed in [1].

according to photon statistics. Those previous analyses sampled a variety of potentially representative angular resolutions, but had no strongly motivated basis for them, unlike this study. The CNO sensitivity computed from those studies as a function of scintillator fraction and angular resolution for a 25 kiloton detector can be seen in Fig. 7.6.

Due to the anticipated substantial decrease in the amount of light when assuming rough linearity with respect to energy deposition, the angular resolution evaluated at 2.6 MeV is expected to be much finer than at energies more relevant to the CNO search around the endpoints of the CNO and *pep* fluxes, and the ^{210}Bi endpoint. For this study, unlike Sec. 7.1.2, the angular resolution values were determined using simulated electrons at 1.0 MeV. For consistency, the energy resolution is also recalculated at 1.0 MeV. At this energy, in the 50 kiloton, LAPPD-instrumented detector, the angular resolution achieved by the fitter is 70° for 1% WbLS and 65° for LAB+PPO, as opposed to 40° and 36° respectively at 2.6 MeV. When applying the smearings to individual events, the energy resolution is assumed to vary $\propto 1/\sqrt{E}$ and the angular resolution is assumed to be constant in energy. This does not fully incorporate expected improvements in resolution at higher energies, and degradation at lower energies, but this method should be conservative, as most information in the fit comes from the region around 1.0 MeV where the approximation will most hold. Additionally, this result

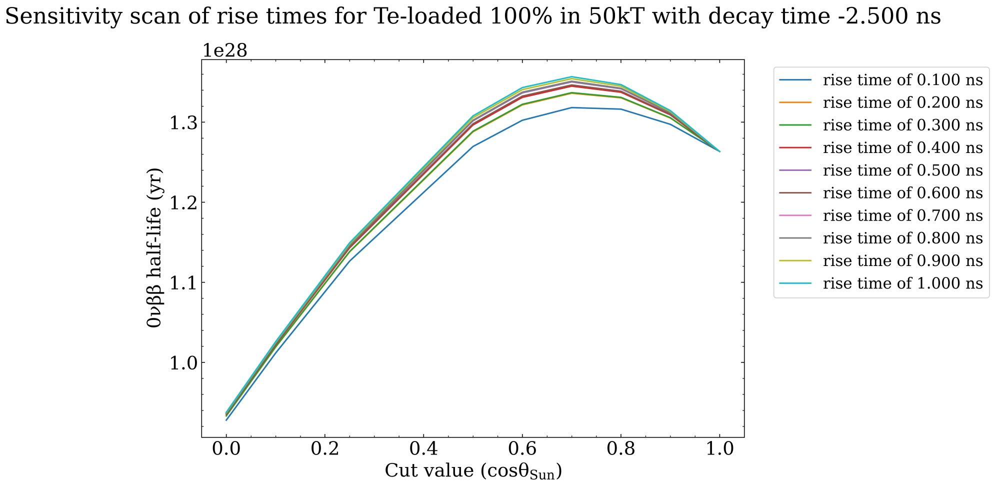

Figure 7.5: Half-life sensitivity for $0\nu\beta\beta$ achieved for a 50-kt pure LS detector with an 8m radius balloon of Te-loaded pure LS at 5% loading, as a function of solar angle cut and listed rise time, with fixed decay time as given. Angular resolution is based on that found in Sec. 7.1.2, assuming the as-measured properties of LAB+PPO without considering possible delays to the scintillation profile, and the analysis uses $3\%/\sqrt{E}$ energy resolution, as assumed in [1].

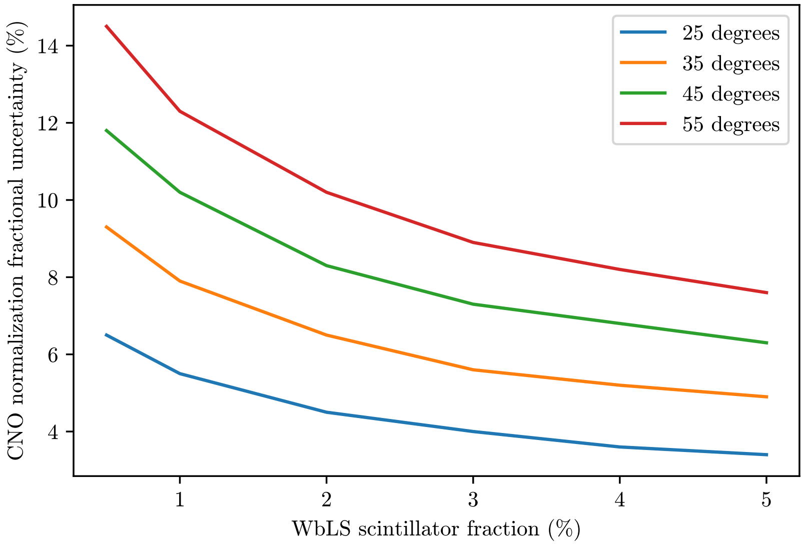

Figure 7.6: The fractional uncertainty on the CNO normalization parameter as a function of the angular resolution, used to smear the event direction, and the scintillator fraction for a 100 kiloton, 90% coverage detector in 5 years of datataking. The fiducial volume used is the inner 60% of the volume, in order to provide a 4 m buffer to mitigate externals.

Table 7.3: The angular resolution in degrees selected with the best t_{prompt} cut for each detector configuration explored, in terms of size and material, and each energy explored.

			Photodetector			
Det. Size (kt)	Energy (MeV)	Material	PMT	FastPMT	FasterPMT	LAPPD
1	1.0	Water	38.5	38.2	37.3	37.7
1	1.0	1% WbLS	68.4	67.8	67.3	64.6
1	1.0	5% WbLS	85.5	85.6	85.9	86.0
1	1.0	10% WbLS	93.1	93.1	92.7	74.8
1	1.0	Pure LS	102.0	85.0	58.8	44.8
1	2.6	Water	32.5	32.5	32.6	32.4
1	2.6	1% WbLS	38.4	37.3	35.6	33.7
1	2.6	5% WbLS	55.1	54.9	54.5	54.2
1	2.6	10% WbLS	68.2	68.0	68.4	63.0
1	2.6	Pure LS	89.5	62.7	32.6	29.4
50	1.0	Water	44.9	43.0	44.7	43.8
50	1.0	1% WbLS	70.2	69.9	70.1	69.9
50	1.0	5% WbLS	86.7	86.3	82.0	73.6
50	1.0	10% WbLS	93.2	92.8	78.8	71.8
50	1.0	Pure LS	85.4	73.6	67.7	64.8
50	2.6	Water	33.1	32.5	33.0	33.0
50	2.6	1% WbLS	40.4	38.4	40.5	40.4
50	2.6	5% WbLS	56.5	55.1	56.3	47.8
50	2.6	10% WbLS	68.1	68.2	53.0	44.7
50	2.6	Pure LS	58.5	89.5	37.8	36.2

is intended to guide the reader as to the capabilities of this style of detector, rather than an exhaustive sensitivity study, especially given the simplified detector model.

It is of interest to see the direction reconstruction performance at these distinct energies, with the acknowledged caveat that improvements are likely possible with more sophisticated analysis techniques. Tab. 7.3 lists the direction resolution achieved for both the 1 kiloton and 50 kiloton detectors, for each target material, with each photon detector model, at both 1 MeV and 2.6 MeV.

The fitting procedure largely follows that described in the mentioned analyses, employing a binned maximum likelihood fit in the reconstructed energy and direction over the signal and background events, which were specified above. The analysis applies a threshold of 0.6 MeV in all cases, and fit to 6.5 MeV at the high end, which is a region where only the ^{8}B solar neutrino flux will be present in any substantial amount as the natural radioactive backgrounds and cosmogenic isotopes of interest all have endpoints at lower energies (some *hep* and atmospheric neutrinos may appear in this region but in greatly lower number). The ^{39}Ar and ^{210}Po parameters are floated together because their similar shapes prove to make the fitted parameters highly covariant given this choice of threshold, and as nuisance parameters their exact value is not strongly important. The ν_e and ν_μ components of each solar neutrino flux are also floated together, as the P_{ee} is held to be independent of the overall flux, meaning that the proportion of flavors should remain fixed. A fiducial volume cut of 50% is used to attenuate the effect of external backgrounds from detector components, which sacrifices statistics but without the addition of a position component to the fit will provide a cleaner sample. Such a dimension could be added to the fit in case where statistics need to be recovered, or datataking could simply be extended, but given that only centrally generated events were studied in Sec. 7.1.2, it stands to reason that applying the same reconstruction performance metrics to events closer to the detector walls would be inappropriate. As a means to reject certain radioactive backgrounds, scaling factors of 95% for α decays, 100% for BiPo decays in separate trigger windows (here taken to be 400 ns), and 95% for BiPo decays in the same trigger window are applied to the appropriate spectra. The capacity to achieve such rejection factors is currently being explored, with significant progress made on studying α rejection, as discussed in Sec. 7.2. While Borexino has demonstrated rejection of ^{11}C using a threefold coincidence technique in pure liquid scintillator to tag the producing muon, associated neutrons, and ^{11}C [294], this is not explored for WbLS in this study, suggesting an area for subsequent investigation. A datataking period of 5 years is assumed, which is a reasonable lower bound for the operation of a detector of this scale. A constraint on the *pep* flux at 1.4% from the global fit analysis of [52], which leverages the information afforded by the full *pp* chain and solar luminosity constraint on the collective experimental data, is used to reduce the correlation between the ^{210}Bi, *pep* and CNO parameters. Application of this constraint follows the methodology of the Borexino CNO discovery [68, 295].

Fig. 7.7 shows the results for the precision with which the CNO flux could be determined in both the 1 kiloton and 50 kiloton detectors, for each combination of target material and photodetector model. The 1 kiloton results are seen to have little dependence on timing resolution for a WbLS deployment. Due to the small target mass (500 ton fiducial volume, after a 50% cut to reject external background events) the sensitivity is significantly reduced in this smaller detector, and the dependence on target material is notably stronger, due to the reduced impact of dispersion for the shorter path lengths. This material dependence is most strongly seen by in the slower timing models moving in the degradation in sensitvity moving from 5% to 10% WbLS, whereas one may naively expect a monotonic improvement in sensitivity. Instead, the degradation in the angular resolution is not outweighed by the improvement in energy resolution from the increased light yield of the material, leading to the poorer result. However, a pure LS detector can still achieve an excellent measurement of CNO neutrinos, with dependence on photodetector model, due to the impact of direction resolution on background rejection efficiency through the fit and its high light yield. Better than 5% uncertainty on the CNO normalization parameter can be achieved in an LAPPD-instrumented detector. In the 50 kiloton detector a stronger dependence on transit time spread is observed across the spectrum of target materials, although the achievable sensitivities are reasonably comparable across different photodetector models, with the largest variations observed for 5% and 10% WbLS, where tradeoffs between angular resolution and light yield become important as well.

From these results, it can be seen that in 5 years of data taking, the CNO flux could be determined to a relative uncertainty of 18% (8%) in the 50 kiloton, LAPPD-instrumented 10% WbLS detector when the *pep* flux is unconstrained (constrained to 1.4%), and to 1% in the same detector filled with LAB+PPO, with the *pep* flux either constrained or unconstrained. For comparison, Borexino's final CNO results, which employed directional information in addition to the fit to the energy spectra used previously, includes an asymmetric 1σ uncertainty of 18% above and 12% below their measured flux, including statistical and systematic uncertainties [69]. This suggests potential improvement is achievable using more robust direction reconstruction techniques. The result for the *pep*-constrained case is not very sensitive to the fraction of scintillator in WbLS (1–10% perform similarly) whereas in the *pep*-unconstrained case the performance degrades with reduced scintillator fraction. This is understood because the angular resolution is found to be similar for different WbLS materials at $1\,\mathrm{MeV}$ (approximately $70°$), so the light yield becomes the critical component in determining performance.

7.2 Case Study: Particle Identification in Hybrid Detectors

The following section details a study of the particle identification capabilities of WbLS of different concentrations and LAB+PPO, given improved benchtop measurements for the light yield and timing for β excitation (which used an LAPPD [243]) and the first such measurements for α excitation in WbLS. This work originally appeared in Eur. Phys. J. C 83 (2023) 11, 1094 [215]. An introduction to the particle identification topic as it relates to hybrid detection is briefly given in Sec. 7.2.1, while the α and β timing and light yield measurements in WbLS to which the author contributed in part are briefly summarized for the benefit of the reader to the extent necessary to understand the final results in Sec. 7.2.2. This author's direct contributions to the publication on the particle identification capabilities in WbLS are restated and expanded upon in Sec. 7.2.3.

7.2.1 Particle Identification Introduction

Radioactive background rejection represents a challenge in addressing many low-energy neutrino physics topics experimentally, typically in the regime around $0.1\,\mathrm{MeV} - 10\,\mathrm{MeV}$. One such class of background is associated with α radiation from decay products in the uranium and thorium decay chains, as discussed in Sec. 7.1.3. Additionally ^{212}Bi-^{212}Po and ^{214}Bi-^{214}Po decays, as well as generic (α, n) reactions on target nuclei [296], constitute time-correlated events, which can mimic inverse-beta decay events used to detect antineutrinos [81, 270].

In liquid scintillators, these events can be classified as α-induced using timing-based particle-identification (PID), which exploits the different scintillation emission time profiles exhibited by particles with different ionization characteristics [297, 298]. This is often achieved with a method known as pulse shape discrimination (PSD), which leverages ratios

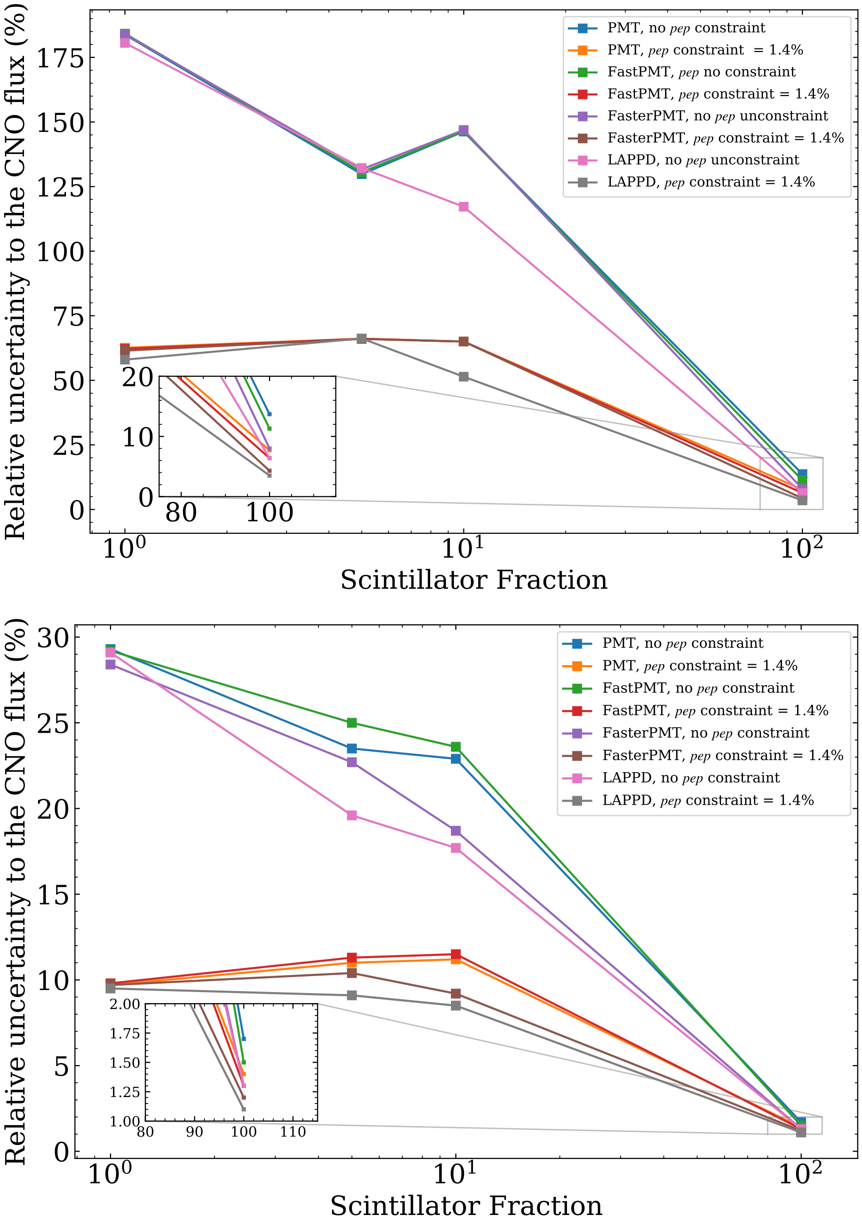

Figure 7.7: (Top) Precision achieved for a measurement of the CNO flux in a 1-kt detector, as a function of the percentage of LS in the target material, where a value of 10^2 refers to pure LS, and of the photodetector model. Detector performance is based on that found in Sec. 7.1.2, assuming the as-measured properties of WbLS and LS, without considering possible delays to the scintillation profile. The angular resolution and energy resolution have been recalculated at 1 MeV, according to the methodology outlined in earlier sections. The inset shows a zoom in on the pure LS sensitivity for the 1-kt detector, to illustrate the importance of photon detector model for this configuration. (Bottom) CNO precision in the 50-kt detector, as a function of %LS and photodetector model.

of the amounts of light observed over different time windows, often computed from a single multiphoton waveform encapsulating an entire event, to classify events as α-like or β-like. This can be extended further by considering the time of each detected photon individually, and using a likelihood-ratio test to compare the α and β hypotheses.

Such timing-based PID has been utilized in past liquid scintillator detectors, for example Borexino, which demonstrated low-energy α/β discrimination on the basis of scintillation timing using a Gatti filter PSD method [191], and in SNO+, which has developed a likelihood-ratio-based discriminant, as discussed in Chapter 4. In a hybrid detector capable of identifying Cherenkov light, additional PID is possible beyond that provided by differences in scintillation emission timing, as heavy ions, including αs and protons, are below the Cherenkov threshold at electron-equivalent energies below the $\sim 100\,\mathrm{MeV}$ scale. Using only timing information, the additional discrimination power available will be limited at low energy, where there are relatively few Cherenkov photons compared to the scintillation light. But future hybrid detectors employing sophisticated Cherenkov tagging through filtering or advanced waveform analysis techniques could use the ratio of the number of detected Cherenkov and scintillation photons as a PID metric, for example to reject hadronic events from atmospheric neutral current reactions, which form a background to antineutrino analyses, as well as to searches for the diffuse supernova neutrino background [1, 271].

7.2.2 Measurements of Timing and Light Yield

The timing properties of WbLS were measured under beta excitation [243] and alpha excitation [215] using fast-timing Hamamatsu H11394-200 PMTs and an LAPPD to achieve exquisite precision, as discussed in Sec. 6.1. For betas, the experimental setup involved placement of a pinhole mask atop the LAPPD face, with a vial containing the target medium on top. The vial is exposed to a disk-shaped radioactive source. The setup is viewed by a "trigger" PMT that is optically coupled to the vessel and the "timing" PMT placed further from the target. The LAPPD setup, aside from the timing PMT, can be see in a simulation rendering in Fig. 7.8. The alpha setup was similar, but did not use the LAPPD and mask and solely relied on the timing PMT. For betas, the deployed source contained ^{90}Sr, which decays to another beta emitter, ^{90}Y. Meanwhile, the alpha-decaying isotope for the subsequent study was ^{210}Po. Waveforms from the LAPPD (both sides of the strip readout) and PMTs were digitized and threshold crossing algorithms applied to them to assign times, using the trigger PMT time to correct for offsets. The photodetectors and experimental setup were calibrated with an LED and by collecting data with a water target under β excitation in order to accurately reproduce the setup in simulation.

The underlying scintillation model is assumed to be a multi-exponential of the form given by

$$S(t) = \sum_{i=0}^{n} A_i \left(\frac{e^{-\frac{t}{\tau_i}} - e^{-\frac{t}{\tau_R}}}{\tau_i - \tau_R}\right), \sum_{i=0}^{n} A_i = 1 \tag{7.2}$$

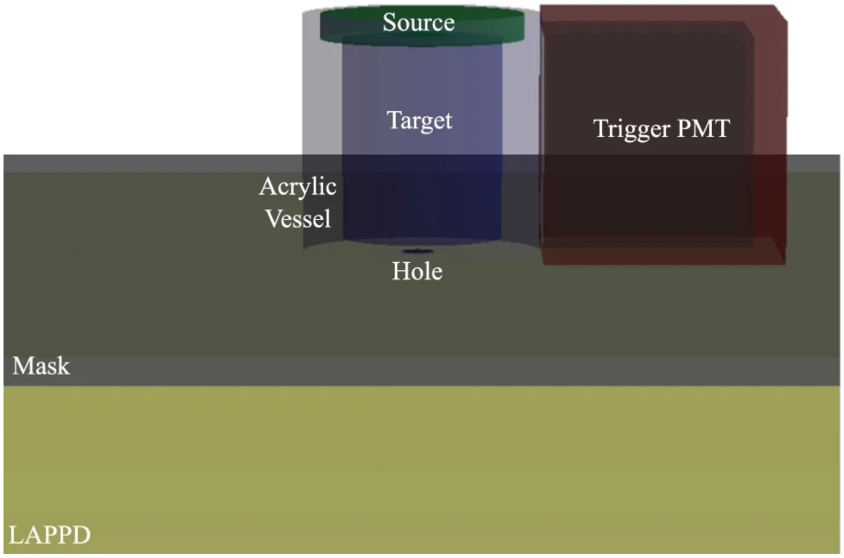

Figure 7.8: The setup used to measure the timing of WbLS subject to electron excitation.

Table 7.4: The timing results for the WbLS mixtures under β and α excitation determined in [243] and [215]. The parameters are defined in Eq. (7.2). Note that $A_{2,\alpha} = 1 - A_{1,\alpha}$ and similarly for the β analogs.

Parameter	5% WbLS	10% WbLS
$\tau_{R,\alpha}$ (ps)	169^{+15}_{-15}	129^{+13}_{-13}
$\tau_{1,\alpha}$ (ns)	$1.82^{+0.01}_{-0.01}$	$1.92^{+0.01}_{-0.01}$
$\tau_{2,\alpha}$ (ns)	$24.7^{+0.8}_{-0.8}$	$26.1^{+0.5}_{-0.5}$
$A_{1,\alpha}$ (%)	$89.7^{+0.2}_{-0.2}$	$86.6^{+0.1}_{-0.1}$
$\tau_{R,\beta}$ (ps)	209^{+10}_{-11}	276^{+7}_{-7}
$\tau_{1,\beta}$ (ns)	$2.25^{+0.01}_{-0.01}$	$2.36^{+0.01}_{-0.01}$
$\tau_{2,\beta}$ (ns)	$23.5^{+1.0}_{-0.9}$	$22.8^{+0.7}_{-0.7}$
$A_{1,\beta}$ (%)	$95.7^{+0.3}_{-0.3}$	$94.8^{+0.1}_{-0.1}$

where τ_i and A_i are the decay time and amplitude of the ith exponential component and τ_R is the single modeled risetime. These parameters are analytically fit subject to more comprehensive models that appropriately account for Cherenkov emission (where applicable), photodetector response and trigger properties, which are detailed in [243] and [215]. Both α and β fits are undertaken with two decay modes allowed, and the results for the parameters of interest are shown in Tab. 7.4 for 5% and 10% WbLS.

A separate setup is used to measure the light yield parameters S and kB for WbLS, which follow from the model of Eq. (3.5). Similarly to the timing setup discussed earlier, the light yield setup images a vessel containing the target that is exposed to a radioactive source, of appropriate particle type. A H11394-200 trigger PMT is again used, with a large-diameter

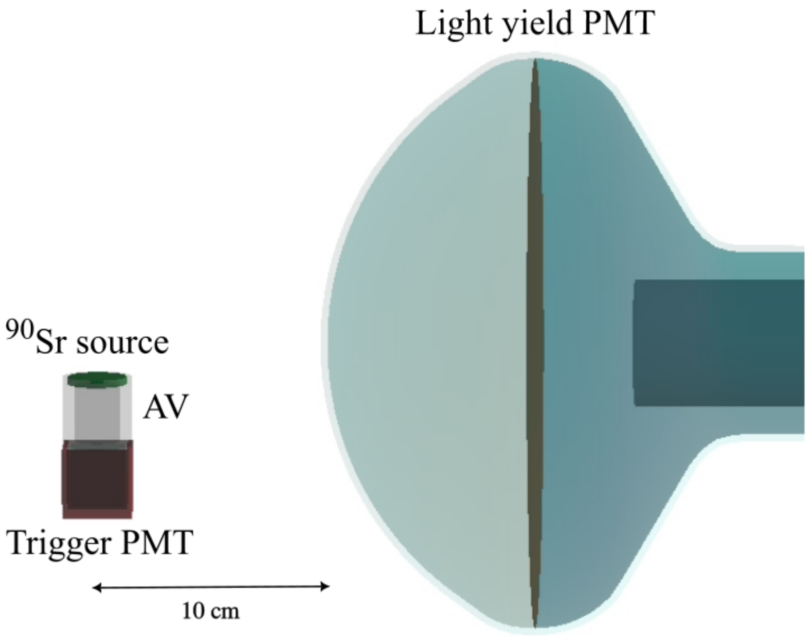

Figure 7.9: The setup used to measure the light yield of WbLS subject to electron and α excitation (when the ^{90}Sr source is exchanged for a ^{210}Po source).

Hamamatsu R7081-100 used to as the "light yield" PMT. A simulated version setup can be viewed in Fig. 7.9.

The charge calculated from integrating around the peaks of the collected waveforms from the light yield PMT. The ensemble of these charges is compared via χ^2 fit to the analogous results gleaned by simulating the experimental setup under different assumptions for the parameters, with the best fit results reported. The simulation is calibrated using a similar LED and Cherenkov-only framework, in order to identify characteristics of the single photoelectron response for the light yield PMT and efficiencies associated with the setup. For β excitation, the kB parameter is not thought to be large enough to produce an appreciable quenching response and is assumed to be equivalent to that measured in LAB+PPO [299] for WbLS. A χ^2 fit between the obtained charge spectrum from data is made with Monte Carlo simulations of the measurement setup using RAT-PAC that explore the S and kB parameter space by varying these parameters at each step. The results for βs are shown in Tab. 7.5. For αs, quenching is significant and the usage of monoenergetic ^{210}Po decays compared to the continuous β spectra means that the two light yield parameters determined for α excitation are degenerate. The results for αs are shown in Fig. 7.10. The full treatment of the fitting procedures and error analysis is discussed in [215].

Table 7.5: The overall light yield parameters measured for 5% WbLS and 10% under the Birks' Law model with kB for βs as measured for LAB+PPO [299].

Material	S [photons/MeV]
5% WbLS	754 ±10 (stat.) $\pm^{73}_{70}$ (syts.)
10% WbLS	1380 ±14 (stat.) $\pm^{134}_{128}$ (syst.)

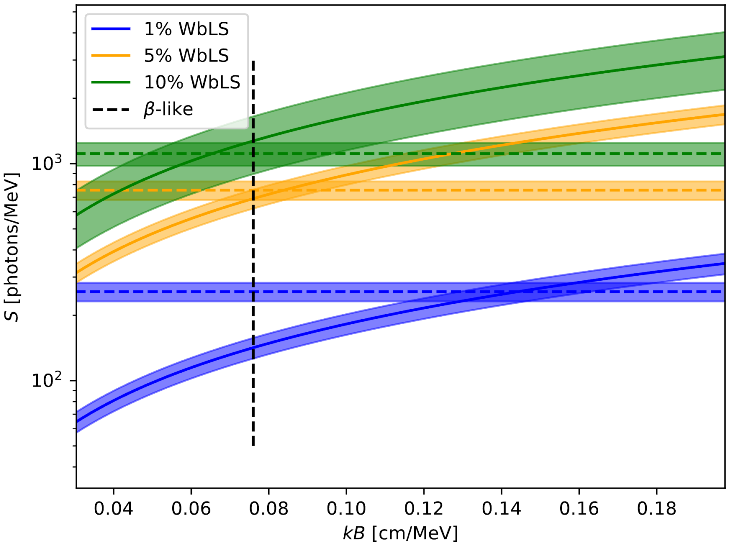

Figure 7.10: Results of the fits for Birks' Law parameters in different WbLS formulations. Solid lines show parameter constraints for α particles obtained from the χ^2 fit procedure. Colored dashed lines show the measured scintillation efficiencies S for electrons, and the vertical black dashed line denotes the value of Birks' constant kB measured for electrons in LAB+PPO, which is assumed also for WbLS in this study. Uncertainty bands contain both statistical and systematic uncertainties.

7.2.3 Particle Identification Performance

As discussed in Sec. 7.2.1, signal and background processes for MeV-scale neutrino physics often arise from different particle species. For example, there is particular interest in the community in rejecting background αs from radioactive decays, thereby improving the selection of electron-like events associated with neutrino interactions.

The properties of Cherenkov radiation and scintillation can be leveraged to attempt separation of event samples by particle type, since Cherenkov emission has a mass-dependent energy threshold below which it does not occur and the scintillation response depends on particle type via quenching mechanisms. Taken together with their underlying characteristics independent of species, Cherenkov and scintillation photons will present differently in timing, wavelength, and angular distributions, as well as in relative proportion as a function of energy, for different types of particles.

This varied response of media to different particle species creates ample potential for PID capabilities. Traditional liquid scintillator detectors rely on timing-based separation mechanisms, but the added lever of finer knowledge of the distinct Cherenkov and scintillation signals has the potential to improve discrimination power even more in WbLS. This is more pertinent at energies relevant to this study where αs will be below Cherenkov threshold. While the technologies discussed in Chapter 6 are being investigated to harness the full potential of the time-based differences using ultra-fast photosensors and precise waveform digitization to allow for performance beyond the single-hit counting regime [243], chromatic differences using spectrally-sorting filters [247], and angular differences using high-coverage detectors with sophisticated reconstruction algorithms [114], this study focuses solely on extending the time-based PID analogy from liquid scintillator detectors to hybrid detectors deploying WbLS and fast-timing PMTs.

In order to understand the impact of the timing and light yield measurements from Sec. 7.2.2 beyond the benchtop scale, the study simulates realistic detector configurations at various sizes. Then, the timing-based PID capabilities of these configurations are assessed to understand the level of background rejection, based on particle type, achievable with WbLS.

7.2.3.1 Simulations

The study explores PID at the 1 t, 1 kt and 100 kt scales with the following configurations:

1. A $\sim$4 t detector of Eos-like geometry [114] (fiducial volume $\sim$1 t), primarily employing Hamamatsu 8-in R14688-100 PMTs [113] with some additional models for a total number of 231 PMTs, yielding a photocoverage of $\sim$40%

2. A $\sim$ 1 kt right cylindrical detector with a 5.4 m radius for the right cylindrical fiducial volume and $\sim$ 54% photocoverage using $\sim$ 3,000 12-in PMTs with equivalent quantum efficiency and time response to the R14688-100

3. A $\sim$ 100 kt right cylindrical detector with a 25.2 m fiducial radius and $\sim$ 85% photocoverage, via $\sim$ 47,000 PMTs of the same hypothetical model as the 1 kt configuration

Table 7.6: The chosen light yield parameters for the three materials of interest used in the particle identification simulations. The scintillation efficiency S is chosen to be the same for both species and is thus listed only once.

Material	S [phMeV]	kB for βs [mm/MeV]	kB for αs [mm/MeV]
5% WbLS	754.0	0.074	0.092
10% WbLS	1380.0	0.074	0.088
LAB+PPO	12200	0.074	0.076

The detector volumes were determined assuming material density equivalent to water (i.e. $1\,\mathrm{g/cm^3}$ under normal conditions) for the given mass in the right cylindrical solid.

Each detector configuration is simulated filled with 5% WbLS, 10% WbLS, and LAB+PPO. 1% WbLS was ignored given the low light yield being prohibitive of the measurement of the excitation properties for αs. The scintillation time profiles and light yields of WbLS are those discussed in Sec. 7.2.2. For LAB+PPO, the time profile under α excitation is used as reported in Sec. 7.2.2, whereas the time profile under β excitation is obtained using similar methodology to [243] and the light yield parameters are obtained from similar methodology to [212] and building on work from the SNO+ collaboration [127]. While Sec. 7.2.2 reports average photon production for α excitation, as opposed to specific model parameters, simulation of large scale detectors requires a definite choice of parameter values. As such, parameters are chosen such that the scintillation efficiency S for electron and α excitation are both equal to the value measured for electrons. These values are listed in Tab. 7.6.

PID performance is determined at the energy of the 5.3 MeV α from the ^{210}Po decay, as this is commonly the most prevalent α background from radioactive contaminants in liquid scintillator experiments. To do so, simulations are performed of the ^{210}Po α decay and monoenergetic βs with kinetic energies that produce an equivalent number of optical photons as the ^{210}Po decays. Comparison of particle types at energies that have dissimilar amounts of photon production will have misleading performance due to the impact of photon statistics. At an even coarser level, energy then can serve as a PID metric given known information about decay spectra, so to restrict to only timing-based PID performance, the matching applied is sensible. The corresponding β energy varies by material due to differences in quenching as modeled in the simulation, and is shown in Tab. 7.7. Several other decays of interest, such as ^{212}Po and ^{214}Po occur at higher energies, and thus the performance determined should be conservative for those decays, as the added light will improve the performance. All events are simulated at the center of the detector configurations and isotropically in direction. Generally, performance will degrade at non-central locations, though the central performance should be representative (performance may peak somewhat higher at an off-center location due to a confluence of factors but will then typically fall off rapidly at the detector edge).

Table 7.7: The kinetic energy of βs corresponding to an equivalent number of optical photons produced as for ^{210}Po α decays in each material.

Material	Equivalent β energy [keV]
5% WbLS	395
10% WbLS	401
LAB+PPO	501

7.2.3.2 Classification Routine

The performance evaluation employs a likelihood-ratio statistic calculated using the hit time residuals for each event, as is done with the analogous approach developed for SNO+ discussed in Chapter 4. The hit time residual is defined as

$$t_{\text{res}} = t_{\text{hit}} - t_{\text{tof}} - t_{\text{vertex}}, \tag{7.3}$$

where t_{hit} is the hit time for the photoelectron (PE) as recorded by the PMT (with time response included), t_{tof} is the estimated time-of-flight from event vertex to PMT and t_{vertex} is the time of the event vertex. For the time-of-flight calculation, in all cases straight line paths from the event vertex to a hit PMT in the target medium are assumed. In other words, no refractions or reflections at interfaces are considered, nor is the effect of scattered light, though these processes are present in the simulation. While the index of refraction is varied appropriately by material and this is taken into account for the light propagation, time-of-flight-calculations assume monochromaticity (at 400 nm) for all photons in evaluating the index of refraction for a given wavelength. Having more information about the wavelength of detected light, for example, from the use of dichroicons as discussed in Chapter 6, may improve the performance of the methods discussed here on real data. Since the emission spectra for β and α particles are the same in simulation, the smearing effect that this assumption has will be like across the timing distribution for the two species. Importantly, this wavelength is near the peaks of both the R14688 quantum efficiency and the scintillation emission spectrum of LAB+PPO and WbLS [113, 252, 278]. At 400 nm, the modeled absorption and scattering lengths of each of the WbLS materials are longer than 10 m.

The classifier value c is defined for an event as the average likelihood-ratio of the observed photon times, comparing the α- and β-hypotheses. That is,

$$c = \frac{1}{N} \sum_{i=0}^{N} [\ln P(t_i|\alpha) - \ln P(t_i|\beta)], \tag{7.4}$$

where the sum is taken over the N distinct photons detected, which, depending on implementation details for a real detector, is generally either the collection of PMTs which were "hit," or the collection of individual photoelectrons detected, subject to cuts on the timing of the hits and other factors. $P(t_i|\alpha)$ is the probability of observing time residual t_i given the event is an α, and $P(t_i|\beta)$ is defined analogously for βs. $P(t|\alpha)$ and $P(t|\beta)$ are probability density functions (PDFs) determined from simulation, as discussed above. Dedicated PDFs are generated for each material and detector configuration. As the classifier is defined as a sample average, the classifier distributions can be understood via the central limit theorem. The mean classifier value for each particle type is the likelihood-ratio as a function of time averaged over the time residual distribution for that particle, and the distribution of classifier values at a given number of hits N is asymptotically Gaussian with standard deviation inversely proportional to $\sqrt{N}$. This naturally facilitates the comparison of different materials and detector configurations, as it decouples the intrinsic classification power (the mean values), driven by the different emission time profiles, from the discrimination power achievable in any particular deployment, which is driven by the amount of light collected.

Time residual PDFs are generated for two extreme photon-counting scenarios: simple "hits," wherein only the time of the first photon incident on a PMT is known, and full photoelectron disambiguation, in which the time of every photoelectron is known, regardless of per-PMT pileup. The scintillation emission time profiles from Sec. 7.2.2 were measured over a $\sim 60\,\text{ns}$ time scale, whereas the event window length in real detectors may be much longer, on the order of $\sim 400\,\text{ns}$. To compromise between these two time scales, an analysis window of $-10\,\text{ns}$ to $220\,\text{ns}$ is defined. This allows for fair inclusion of optical effects, such as Rayleigh scattering, without extending into a regime where unmeasured scintillation decay modes may dominate the detector response. Vertex reconstruction is not performed, and instead the process uses the true position and time of each event in place of the reconstructed vertex, though the effect of smearing this vertex by a characteristic resolution is studied. The emission timing measurements performed in the 60 ns window are used to extrapolate into the longer time window, which is determined to under predict the scintillation timing tail for LAB+PPO in comparison to work that used longer analysis windows [127, 300]. This has less of an impact on the WbLS mixtures, which are significantly faster and emit less light beyond the 60 ns analysis window.

Example of time residual PDFs can be found in Fig. 7.11, which shows the time residuals for each different material in Eos, and in Fig. 7.12, which shows the time residuals for each different detector size with 10% WbLS. The additional peak around 40 ns is caused by PMT late pulsing, typical of large area PMTs. The Eos-like detector, owing to its relatively small size, observes a relatively high proportion of multi-PE PMT hits, which is distinct from the larger detectors which operate primarily in the SPE regime. As such, the difference between "first PE" and "all PE" PDFs, and hence the corresponding PID performance, in the Eos-like detector is larger than for the other two detectors. In particular for LAB+PPO, the "first PE" PDFs in the Eos-like detector are very similar between the two species, resulting in poorer PID performance than would naively be expected for LAB+PPO. This comes as a result of all the PMTs in the detector registering multiple PE, and so the "first PE" PDFs lack a substantial amount of information, particularly from hits coming at later times, as shown in Fig. 7.13. With modern detectors, such as Eos, seeking to differentiate hits at least in the "few PE" regime using photosensors with faster timing and better readout schemes as discussed in Chapter 6, results based on PDFs using all hit times are presented.

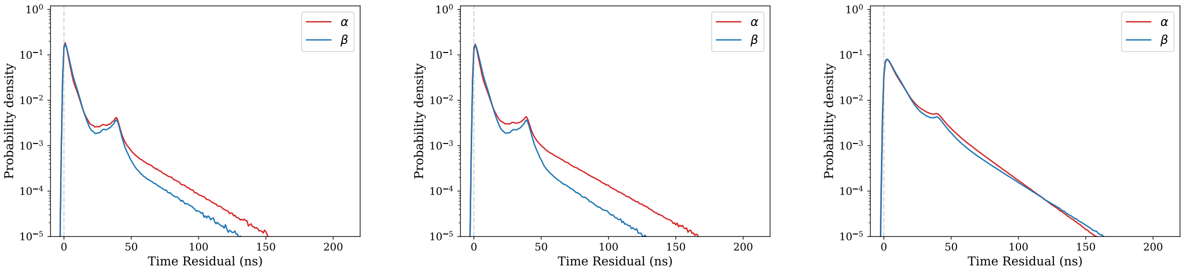

Figure 7.11: Comparisons of the α and β time residuals, using all detected PEs, in the Eos-like detector for 5% WbLS (left), 10% WbLS (middle), and LAB+PPO (right). All events are simulated at the center of the detector, uniformly in direction. The α particles are produced from ^{210}Po decays and the β particles are simulated with energies from Tab. 7.7.

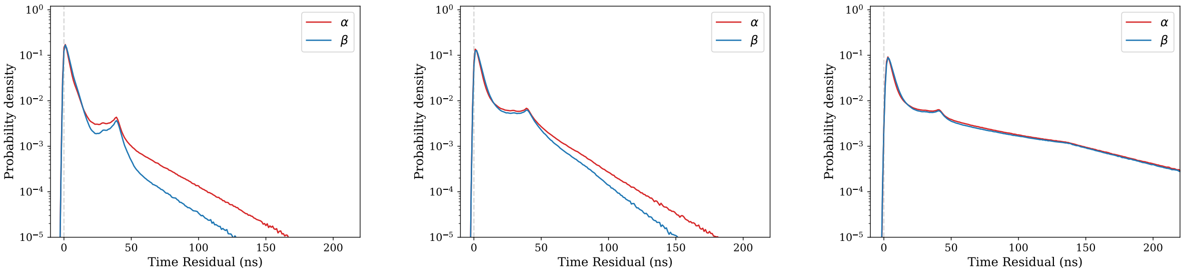

Figure 7.12: Comparisons of the α and β time residuals, using all detected PEs, in an Eos-like detector (left), a 1 kt detector with 54% photocoverage (middle), and a 100 kt detector with 85% photocoverage (right) for 10% WbLS. The α particles are produced from ^{210}Po decays and the β particles are simulated with energies from Tab. 7.7.

7.2.3.3 Analysis Methods

The classifier value is a quantity for which, ideally, the distributions associated with αs and βs have little overlap, which would enable an efficient selection cut to be employed in the course of a physics analysis. As positive values are associated with α-like events, and negative values with β-like events, a simple threshold value can be used to perform classification. These distributions and the resulting classification performance are studied both analytically, and using further simulation.

As described in Sec. 7.2.3.2, these distributions are asymptotically Gaussian, and as such can be summarized at that level by their means and standard deviations. Mathematically, this translates to computing the first and second moments of the log-likelihood ratio: the former is the mean classifier value, and the latter, when scaled by $\sqrt{N}$, is the standard deviation. The values are calculated for each detector configuration via numerical integration (since the likelihood ratios are not in closed form), to offer the asymptotic classifier distributions

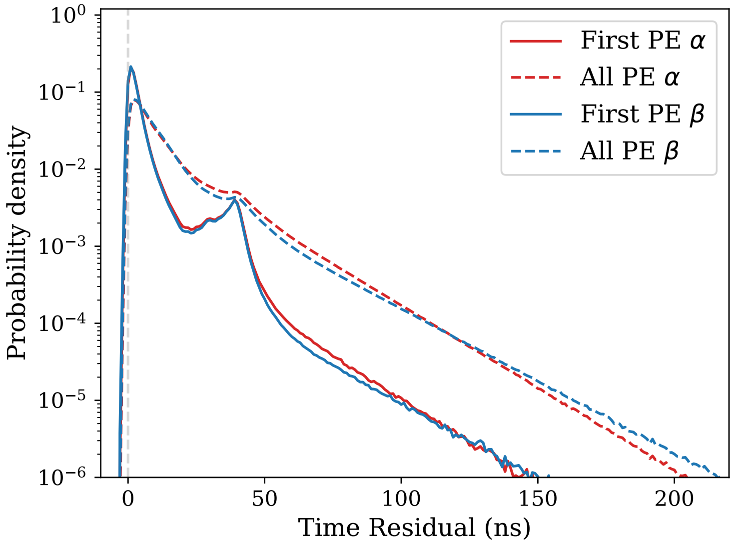

Figure 7.13: Comparison of the "first PE" (solid) and "all PE" (dashed) PDFs for both species in LAB+PPO in the Eos-like detector. This detector configuration is heavily multi-PE, resulting in a significant difference in the shape of the PDFs observed in the two cases. All events are simulated at the center of the detector, uniformly in direction. The α particles are produced from ^{210}Po decays and the β particles are simulated with energies from Tab. 7.7.

in a convenient form. This is designed to easily facilitate follow-on performance studies considering a variety of energies without access to the non-asymptotic classifier distributions that can only be produced through detailed simulations.

Then, using further full MC simulations to sample from the non-asymptotic classifier distributions, various figures of merit are drawn on, which quantify the classification performance, as a function of threshold value chosen for that figure of merit. An example pair of classifier distributions, both sampled from simulation and expressed asymptotically as a Gaussian, can be found in Fig. 7.14, which corresponds to a 10% WbLS-filled Eos-like detector. The two approaches are compared in the leftmost figure, which shows the compatibility of the full MC sampling and asymptotic distributions, indicating that the non-Gaussian components of the classifier distributions at this light level are small.

As electrons are usually considered a "signal" in analysis of neutrino detector data, β events are labelled as signal and α events are labelled as background. The specific classification figures of merit considered are:

1. Sample purity: $N_\beta(c')/N_{\text{tot}}(c')$
2. Signal acceptance: $N_\beta(c')/N_{\beta,\text{tot}}$
3. Background rejection: $N_\alpha(c')/N_{\alpha,\text{tot}}$

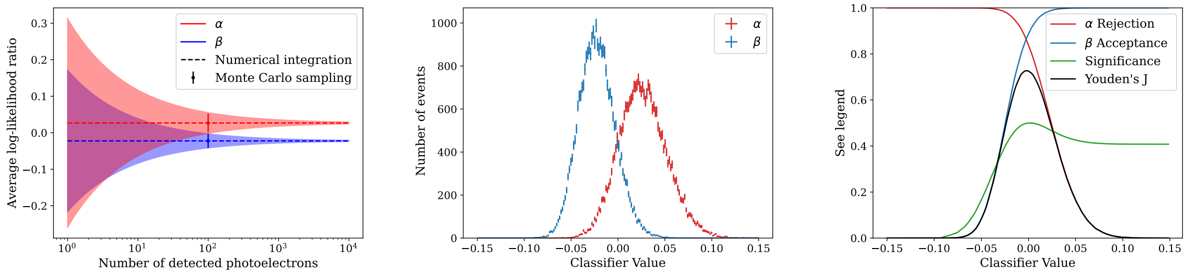

Figure 7.14: Dependence of classifier distributions on the number of photoelectrons detected for α (red) and β (blue) particles (left), nominal classifier distributions for α and β particles (middle), and nominal PID performance figures-of-merit as a function of cut value (right), for 10% WbLS in an Eos-like detector. The shaded bands in the left plot denote the standard deviation of the distributions predicted by numerical integration, and the data points denote the results of explicit Monte Carlo sampling, i.e. the distributions shown in the middle plot. Since the sampled data point occurs at roughly 0.4 MeV per Tab. 7.7, the left plot suggests that substantial improvement should be seen even for αs at slightly higher energies such as that of ^{212}Po, as the 1σ regions cease to overlap just above the sample point, though Sec. 7.2.3.5 examines this in further detail.

4. Significance: $N_\beta(c')/\sqrt{N_\beta(c') + N_\alpha(c')}$
5. Youden's J: $N_\beta(c')/N_{\beta,\mathrm{tot}} - N_\alpha(c')/N_{\alpha,\mathrm{tot}}$

where c' is the cut value on classifier value; $N_\alpha(c')$ and $N_\beta(c')$ are the numbers of α and β events selected from the sample, respectively; $N_{\alpha,\mathrm{tot}}$ and $N_{\beta,\mathrm{tot}}$ are the total numbers of α and β events in the sample, respectively; and $N_{\mathrm{tot}}(c') = N_\alpha(c') + N_\beta(c')$ is the total number of selected events. The selection is performed such that all events with classifier value less than or equal to c' are considered to pass the selection cut, and all those with classifier value greater than c' fail the selection cut. Each of these quantities is computed as function of the cut value c'.

7.2.3.4 Results

The first and second moments of the classifier distributions, i.e. the means and single-sample standard deviations of the log-likelihood ratio, as well as the mean numbers of detected photoelectrons, are listed in Tab. 7.8, Tab. 7.9, and Tab. 7.10. The PID figures of merit for a 10% WbLS-filled Eos-like detector are shown as a function of the classifier cut value in the right panel of Fig. 7.14, and Tab. 7.11 lists the background rejections associated with a 90% signal acceptance for Eos-like detectors of various target media. From Tab. 7.11, the α rejection improves with higher light yields from the increasing scintillator concentration.

Vertex reconstruction resolution is generally robust across different detector sizes as seen from Sec. 7.1.2 [252], and hence the effect of vertex reconstruction error is quantified using

Table 7.8: Mean and single-sample standard deviation of classifier values for the ^{210}Po simulations in the various detectors. These values are determined through numerical integration of the log-likelihood ratio as discussed in the text.

	Mean			Standard deviation		
	5% WbLS	10% WbLS	LAB+PPO	5% WbLS	10% WbLS	LAB+PPO
4 t	1.11×10^{-2}	2.68×10^{-2}	4.42×10^{-3}	1.77×10^{-1}	2.87×10^{-1}	9.58×10^{-2}
1 kt	5.67×10^{-3}	1.32×10^{-2}	2.15×10^{-3}	1.22×10^{-1}	1.68×10^{-1}	6.47×10^{-2}
100 kt	2.70×10^{-3}	5.38×10^{-3}	1.12×10^{-3}	7.27×10^{-2}	1.03×10^{-1}	4.26×10^{-2}

Table 7.9: Mean and single-sample standard deviation of classifier values for the β excitation (energies from Tab. 7.7) in the various detectors. These values are determined through numerical integration of the log-likelihood ratio as discussed in the text.

	Mean			Standard deviation		
	5% WbLS	10% WbLS	LAB+PPO	5% WbLS	10% WbLS	LAB+PPO
4 t	-1.00×10^{-2}	-2.23×10^{-2}	-4.27×10^{-3}	1.36×10^{-1}	1.94×10^{-1}	9.08×10^{-2}
1 kt	-5.53×10^{-3}	-1.24×10^{-2}	-2.25×10^{-3}	1.04×10^{-1}	1.53×10^{-1}	7.09×10^{-2}
100 kt	-2.76×10^{-3}	-5.45×10^{-3}	-1.57×10^{-3}	7.51×10^{-2}	1.05×10^{-1}	8.03×10^{-2}

Table 7.10: The mean detected PE for each detector configuration for the simulated ^{210}Po. Uncertainties are less than 1 PE in all cases.

Nominal mass	Material	Mean N_{PE}
4 t	5% WbLS	52.6
1 kt	5% WbLS	57.5
100 kt	5% WbLS	77.6
4 t	10% WbLS	99.7
1 kt	10% WbLS	108.5
100 kt	10% WbLS	145.6
4 t	LAB+PPO	1039.6
1 kt	LAB+PPO	985.2
100 kt	LAB+PPO	1039.7

Table 7.11: α rejection in Eos-like for various materials, for cut values that yield a β acceptance of 90%. These results use the simulations performed with ^{210}Po and the β particles at energies from Table 7.7.

Material	Cut Value	α Rej. [%]
5% WbLS	0.013	43.1
10% WbLS	0.002	83.2
LAB+PPO	-0.001	96.3

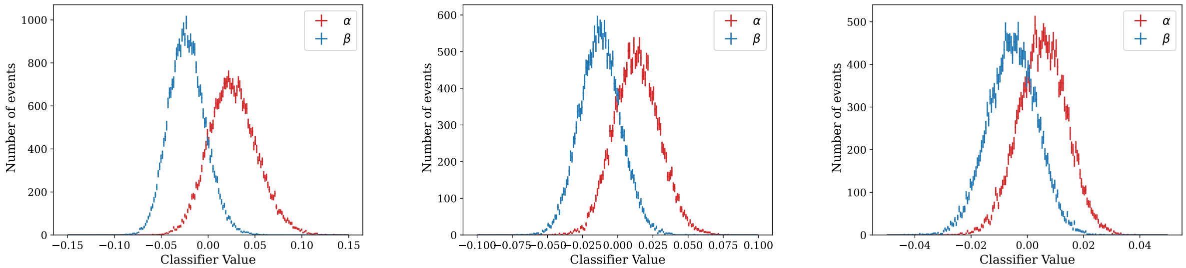

Figure 7.15: Comparisons of the classifier results in an Eos-like detector (left), a 1 kt detector with 54% photocoverage (middle), and a 100 kt detector with 85% photocoverage (right) for 10% WbLS.

a 5% WbLS-filled Eos-like detector, which, owing to its small size, is the most sensitive to the impact of resolution. Applying a 10 cm Gaussian smearing to each Cartesian coordinate of the true vertex position, representative of the achievable position resolution found in Sec. 7.1.2 [252], results in a non-zero but mild loss in performance of less than 0.5% absolute background rejection. The degradation is smaller in larger detectors, where longer nominal photon times-of-flight dominate the fixed uncertainty introduced by finite vertex resolution. This study does not account for possible complicated reconstruction features, such as tails in the vertex reconstruction, which could impact the PID.

The classifier distributions for 10% WbLS for the three detectors are shown in Fig. 7.15. In all cases, the classifier distributions are visibly well-separated around the log-likelihood ratio of 0, with polarity as expected from construction. Tab. 7.12 similarly reports the figures of merit associated with a signal acceptance of 90%. The same trend of increasing performance with increasing scintillator fraction is observed in these detector configurations and is summarized in Fig. 7.16, which shows the α rejection at 90% β acceptance for all three detectors as a function of scintillator fraction of the material.

Higher light yield materials provide better PID performance, as a result of the classifier variance decreasing in accordance with the central limit theorem. As evidenced in Fig. 7.16, scattering and absorption of photons as they propagate through ever-larger detectors can have a substantial impact, as the smaller, lower photocoverage 4 t detector outperforms the

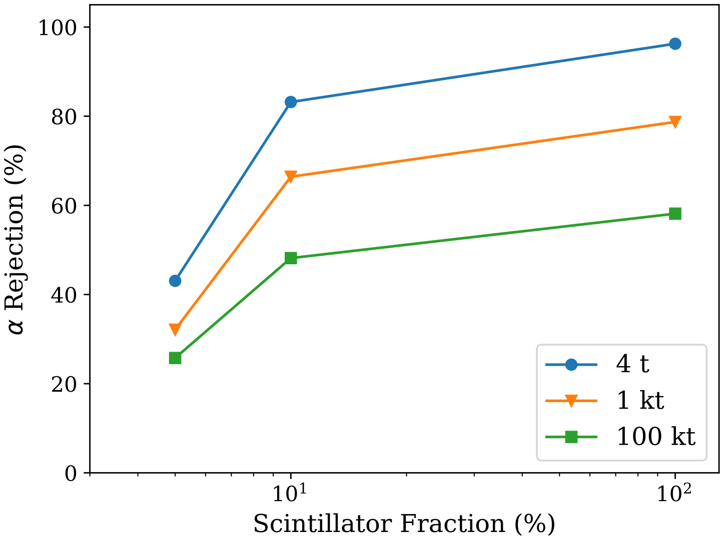

Figure 7.16: Comparison of the α rejection as a function of material scintillator fraction for the three detector concepts, assessed at the 90% β acceptance cut threshold. Notably, as discussed in Sec. 7.2.3.4, using the LAB+PPO emission timing measured in [127] results in 100% separation for all three detector configurations.

Table 7.12: α rejection in 1 kt and 100 kt detectors for various materials, for cut values that yield β acceptances of 90%. These results use the simulations performed with ^{210}Po and the β particles at energies from Tab. 7.7.

Det.	Material	Cut Value	α Rej. [%]
1 kt	5% WbLS	0.012	32.1
1 kt	10% WbLS	0.006	66.4
1 kt	LAB+PPO	0.001	78.7
100 kt	5% WbLS	0.008	25.8
100 kt	10% WbLS	0.006	48.2
100 kt	LAB+PPO	0.001	58.1

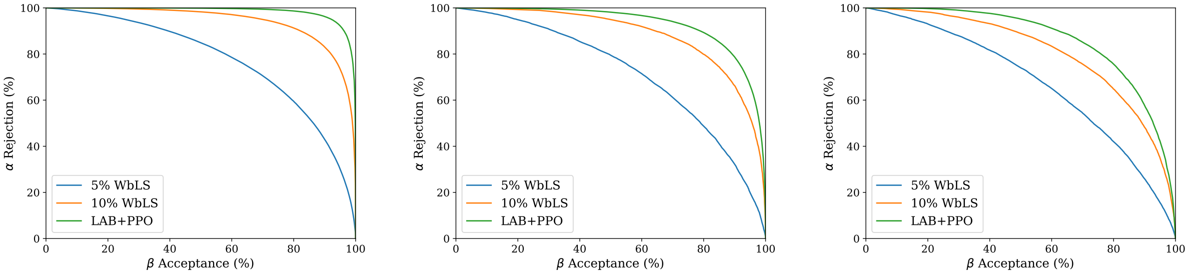

Figure 7.17: Comparisons of the simultaneously achievable β acceptance and α rejection, using all detected PEs, for 5% WbLS, 10% WbLS, and LAB+PPO for the 4 t (left), 1 kt (middle) and 100 kt (right) detectors. All events are simulated at the center of the detector, uniformly in direction. The α particles are produced from ^{210}Po decays and the β particles are simulated with energies from Tab. 7.7.

larger, higher photocoverage kt-scale detectors. This is in accordance with the washing out of features in time residual PDFs for larger detectors (Fig. 7.12) due to smearing from absorption/reemission and optical scattering. Additionally, the particle identification performance ranking of the various detector configurations is robust to the choice of figure of merit used to generate the cuts. Tab. 7.13 shows the performance for 90%, 99%, and 99.9% α rejection to directly compare to existing experiments, such as Borexino [298] and SNO+ [127]. Also, Fig. 7.17 shows the simultaneously achievable β acceptance and α rejection for the examined scenarios.

A consequence of the short time window used to measure the emission timing in Sec. 7.2.2 is an underestimation of the amount of light emitted at late times, beyond 60 ns. This yields a conservative estimation of the expected PID performance for the LAB+PPO, and to a lesser extent, the WbLS. The PID analysis was repeated using the published LAB+PPO emission timing measured by the SNO+ detector [127] for all three detector configurations. These measurements use a longer analysis window and fit using a four-decay exponential model. The finding was that using the SNO+ emission timing results in 100% separation of the α and β particles in all three detector configurations.

7.2.3.5 Discussion

The results presented in Sec. 7.2.3.4 use only timing information, considered over a fixed analysis window. A pertinent question is the role of the Cherenkov light produced by electrons, as its higher proportion in WbLS samples may be expected to contribute to timing-based PID beyond that afforded by differences in scintillation emission time profiles. By ignoring Cherenkov photons in the PID analysis of a 5% WbLS filled EOS-like detector, surprisingly, it is observed that the presence of Cherenkov light degrades α rejection at the level of 1.5%. This is due to the Cherenkov component competing with the scintillation light rise time, which is measured to be larger for βs than for αs. Thus, at ^{210}Po energies, the

Table 7.13: β acceptance in 4 t, 1 kt and 100 kt detectors for various materials, for cut values that yield the stated α rejection. Notably, as discussed in Sec. 7.2.3.4, using the LAB+PPO emission timing measured in [127] results in 100% separation for all three detector configurations.

Det.	Material	Threshold	Cut Value	β Acc. [%]
4 t	5% WbLS	90.0%	-0.016	39.3
4 t	5% WbLS	99.0%	-0.034	8.5
4 t	5% WbLS	99.9%	-0.049	1.3
4 t	10% WbLS	90.0%	-0.005	82.3
4 t	10% WbLS	99.0%	-0.027	40.9
4 t	10% WbLS	99.9%	-0.043	13.4
4 t	LAB+PPO	90.0%	0.001	96.3
4 t	LAB+PPO	99.0%	-0.002	76.8
4 t	LAB+PPO	99.9%	-0.004	48.1
1 kt	5% WbLS	90.0%	-0.012	31.8
1 kt	5% WbLS	99.0%	-0.027	5.9
1 kt	5% WbLS	99.9%	-0.039	0.6
1 kt	10% WbLS	90.0%	-0.007	64.6
1 kt	10% WbLS	99.0%	-0.022	26.1
1 kt	10% WbLS	99.9%	-0.035	5.6
1 kt	LAB+PPO	90.0%	-0.000	79.1
1 kt	LAB+PPO	99.0%	-0.003	40.6
1 kt	LAB+PPO	99.9%	-0.004	16.0
100 kt	5% WbLS	90.0%	-0.008	25.7
100 kt	5% WbLS	99.0%	-0.018	4.0
100 kt	5% WbLS	99.9%	-0.024	0.7
100 kt	10% WbLS	90.0%	-0.006	47.7
100 kt	10% WbLS	99.0%	-0.015	13.6
100 kt	10% WbLS	99.9%	-0.022	3.2
100 kt	LAB+PPO	90.0%	-0.001	61.9
100 kt	LAB+PPO	99.0%	-0.002	29.7
100 kt	LAB+PPO	99.9%	-0.004	13.8

small amount of Cherenkov light emitted for βs causes the effective rise-time to look more similar to αs, degrading the classification power.

At higher light levels, produced by higher energy βs, the larger Cherenkov contribution is sufficient to enact a genuine shape difference in time profiles, and enhances PID performance. For example, at the light levels associated with ^{212}Po α decays, the behavior is reversed, and the Cherenkov light provides a roughly $\sim 1.5\%$ increase in α rejection, absolute. Of course, it should be noted that the measured scintillation rise times may be subject to systematic uncertainties associated with choices in system response modeling, potentially affecting the competition between the Cherenkov component and the scintillation rise times discussed here.

It should be noted that hybrid detectors which leverage dedicated techniques to identify, i.e. “tag,” Cherenkov photons may achieve PID performance beyond that available via the simple likelihood-ratio statistic employed here, owing to the inclusion of other observables. Examples of such observables are angular information and wavelength, employed via the observation of anisotropic photon collection, after performing vertex and direction reconstruction, and spectral photon sorting, respectively. The timing, topological, and spectral information could, in principle, be combined in a joint vertex-direction-PID fit, which inherently determines a particle’s identity based on the interaction geometry. These extensions are promising, but their technical exploration is beyond the scope of this study. Lastly, it is to be expected that the PID would improve in larger detectors, compared to what is shown here, because of the ability to leverage differences in the time profile over a longer time window.

The PID achieved in this study is also less impressive than the rejection factors assumed in Sec. 7.1.3. Given the fact that this method represents a minimal extension and not a full leveraging of hybrid technologies, it remains possible that that 95% assumption for the α rejection may be achievable. While the rejection probability for αs has shown to be weakly correlated with the CNO flux precision for WbLS-based detectors [278], other physics topics may be more attuned to this capability. Further study is needed to explore what is achievable in WbLS and the physics impacts thereof.

Chapter 8

Conclusion

For the past several decades, the neutrino has served as a unique probe into fundamental physics processes, consistently providing long-sought answers to long-asked questions while also opening new lines of inquiry by challenging our understanding of particle physics and the broader Universe. Neutrino detection technologies based on the detection of optical photons have been a mainstay of this field, as discussed in this work, and have enabled the exploration of topics running the gamut from solar neutrinos to reactor antinuetrinos and from accelerator neutrinos to neutrinoless double beta decay, bridging gaps between fundamental particle and nuclear physics and their applications. This thesis has explored the history and state of the art for this form of detector, showcased achievements and advancements being made with the currently-operating SNO+ detector and considered research and development toward the next-generation of this technology in the form of the hybrid paradigm.

SNO+ is a unique optical detector in that it evolved a storied experiment and has gone in a bold new direction, loading with a wholly different target material. Many things that were learned for SNO have provided a strong basis for SNO+, while others have had to be unlearned. This has enabled SNO+ to produce a set of physics results already on topics like nucleon decay and antineutrino detection and has led to development of new methods such as event-by-event direction reconstruction in scintillator, and as displayed in this thesis, classification techniques to remove α and instrumental backgrounds from datasets. This thesis also demonstrated work on ^{8}B solar neutrino detection that has been used to validate understanding of the SNO+ detector's scintillator operations in both unexpected and expected scenarios, and that has joined a burgeoning family of measurements contributing to the global picture of the ^{8}B flux. The final measurement in the fully-filled scintillator phase of $[5.74^{+0.84}_{-0.77}(\text{stat.})] \times 10^{6}$ cm^{-2} s^{-1} using the most reliable fiducial volume can be expanded upon with more scintillator data available to be processed and in future phases of the detector, with the prospect of halving the statistical uncertainty well within the realm of possibility.

With hybrid detectors, there is ample room for growth and investigation of new and exciting technologies to simultaneously detect and exploit light emission from scintillation and Cherenkov processes. From new scintillating materials and photodetection devices to advanced reconstruction algorithms leveraging the latest in computing, the field has been rapidly evolving over the past 10–15 years. These developments have begun to bear fruit in the form of detection testbeds such as Eos. Part and parcel of this growth has been the consistent refinement and testing of models for this technology, which has been presented in this thesis. First, using a comprehensive model of the hybrid WbLS material for the first-time, the physics capabilities for a variety of potential detectors across scales, materials and photodetectors was explored, informed by the use of end-to-end reconstruction. Half-life sensitivity for $0\nu\beta\beta$ for a detector using state of the art photosensors with well-motivated directional resolution was found to push into the inverted mass ordering region. The sensitivity to the CNO solar neutrino flux was similar found to match or exceed the current precision achieved by Borexino by exploiting hybrid technology, potentially entering the realm of sub-10% precision depending on the scenario. These results form the concrete basis for a broad physics program for proposed hybrid detectors like Theia, exhibiting the experimental versatility of hybrid detectors. Additionally, using benchtop measurements of WbLS properties, the particle identification ability in WbLS in large-scale detectors has been probed for the first time. While pure scintillator is found to have superior performance as expected, in a like-for-like comparison, WbLS is shown to provide substantial rejection for α particles while retaining β-like signal using timing-based likelihood ratio approach. With the capacity to include additional pieces of information such as wavelength and deploy a more sophisticated algorithm for PID, there is no doubt that this is a lower limit. The accomplishment here with α particles also underscores the plausability of extension of PID to other types of backgrounds.

Taken together, this thesis has demonstrated that while new detection paradigms may be in vogue in neutrino physics, the tried-and-true optical techniques that date back to the first detection by Cowan and Reines in 1956 still bear extraordinary potential for the discoveries of tomorrow. With the suite of hybrid detection demonstrators coming online in the past few years and advancements like the directional detection capabilities in scintillator recently demonstrated by SNO+ and Borexino, it is a given that these technologies will bear fruit for solar neutrino detection going forward and have broader impacts in neutrino physics. The prospect of determining the CNO flux with high precision, and thereby resolving questions related to solar metallicity, is within reach in the next generation of optical detectors equipped with hybrid approaches. The potential to perform ^{8}B measurements in the range of $2\,\mathrm{MeV} - 5\,\mathrm{MeV}$ at the level needed to resolve remaining questions about the LMA-MSW solution through refinement of solar oscillation parameters and exploration of non-standard interaction models will also be unlocked by hybrid detectors, enabled by the timing and directional resolution explored here. In conjunction with dark matter detectors that have excitingly now reached sensitivity to solar neutrinos [301, 302], this could potentially open the door to boundary-pushing *pp* measurements as well. Beyond solar neutrinos, SNO+ and future hybrid detectors will explore a broad array of MeV-scale physics, moving the bar in fundamental physics forward in neutrinoless double beta decay, nucleon decay and more, with added possibilities for applications to nuclear nonproliferation technologies. Pardon the pun, but the author believes the future of optical neutrino detectors is bright indeed.

Bibliography

[1] M. Askins et al. “THEIA: an advanced optical neutrino detector”. In: *Eur. Phys. J. C* 80.5 (2020), p. 416. DOI: `10.1140/epjc/s10052-020-7977-8`. arXiv: `1911.03501 [physics.ins-det]`.

[2] George F Bertsch, Sharon Bertsch McGrayne, and James Trefil. “atom”. In: *Encyclopedia Britannica*. May 2024.

[3] Sylvia Berryman. “Democritus”. In: *The Stanford Encyclopedia of Philosophy*. Ed. by Edward N. Zalta and Uri Nodelman. Spring 2023. Metaphysics Research Lab, Stanford University, 2023.

[4] Alan Chalmers. “Atomism from the 17th to the 20th Century”. In: *The Stanford Encyclopedia of Philosophy*. Ed. by Edward N. Zalta. Spring 2019. Metaphysics Research Lab, Stanford University, 2019.

[5] Michael Weisberg, Paul Needham, and Robin Hendry. “Philosophy of Chemistry”. In: *The Stanford Encyclopedia of Philosophy*. Ed. by Edward N. Zalta. Spring 2019. Metaphysics Research Lab, Stanford University, 2019.

[6] W. Pauli. “Dear radioactive ladies and gentlemen”. In: *Phys. Today* 31N9 (1978), p. 27.

[7] Edoardo Amaldi. “From the discovery of the neutron to the discovery of nuclear fission”. In: *Physics Reports* 111.1 (1984), pp. 1–331. ISSN: 0370-1573. DOI: `https://doi.org/10.1016/0370-1573(84)90214-X`. URL: `https://www.sciencedirect.com/science/article/pii/037015738490214X`.

[8] C. L. Cowan et al. “Detection of the free neutrino: A Confirmation”. In: *Science* 124 (1956), pp. 103–104. DOI: `10.1126/science.124.3212.103`.

[9] S. L. Glashow. “Partial Symmetries of Weak Interactions”. In: *Nucl. Phys.* 22 (1961), pp. 579–588. DOI: `10.1016/0029-5582(61)90469-2`.

[10] Steven Weinberg. “A Model of Leptons”. In: *Phys. Rev. Lett.* 19 (1967), pp. 1264–1266. DOI: `10.1103/PhysRevLett.19.1264`.

[11] Abdus Salam. “Weak and Electromagnetic Interactions”. In: *Conf. Proc. C* 680519 (1968), pp. 367–377. DOI: `10.1142/9789812795915_0034`.

[12] Murray Gell-Mann. “The Eightfold Way: A Theory of strong interaction symmetry”. In: (Mar. 1961). DOI: `10.2172/4008239`.

[13] Murray Gell-Mann. "A Schematic Model of Baryons and Mesons". In: *Phys. Lett.* 8 (1964), pp. 214–215. DOI: `10.1016/S0031-9163(64)92001-3`.

[14] H. Fritzsch, Murray Gell-Mann, and H. Leutwyler. "Advantages of the Color Octet Gluon Picture". In: *Phys. Lett. B* 47 (1973), pp. 365–368. DOI: `10.1016/0370-2693(73)90625-4`.

[15] David J. Gross and Frank Wilczek. "Ultraviolet Behavior of Nonabelian Gauge Theories". In: *Phys. Rev. Lett.* 30 (1973). Ed. by J. C. Taylor, pp. 1343–1346. DOI: `10.1103/PhysRevLett.30.1343`.

[16] H. David Politzer. "Reliable Perturbative Results for Strong Interactions?" In: *Phys. Rev. Lett.* 30 (1973). Ed. by J. C. Taylor, pp. 1346–1349. DOI: `10.1103/PhysRevLett.30.1346`.

[17] F. Englert and R. Brout. "Broken Symmetry and the Mass of Gauge Vector Mesons". In: *Phys. Rev. Lett.* 13 (1964). Ed. by J. C. Taylor, pp. 321–323. DOI: `10.1103/PhysRevLett.13.321`.

[18] Peter W. Higgs. "Broken Symmetries and the Masses of Gauge Bosons". In: *Phys. Rev. Lett.* 13 (1964). Ed. by J. C. Taylor, pp. 508–509. DOI: `10.1103/PhysRevLett.13.508`.

[19] G. S. Guralnik, C. R. Hagen, and T. W. B. Kibble. "Global Conservation Laws and Massless Particles". In: *Phys. Rev. Lett.* 13 (1964). Ed. by J. C. Taylor, pp. 585–587. DOI: `10.1103/PhysRevLett.13.585`.

[20] R. L. Workman et al. "Review of Particle Physics". In: *PTEP* 2022 (2022), p. 083C01. DOI: `10.1093/ptep/ptac097`.

[21] G. Danby et al. "Observation of High-Energy Neutrino Reactions and the Existence of Two Kinds of Neutrinos". In: *Phys. Rev. Lett.* 9 (1962), pp. 36–44. DOI: `10.1103/PhysRevLett.9.36`.

[22] K. Kodama et al. "Observation of tau neutrino interactions". In: *Phys. Lett. B* 504 (2001), pp. 218–224. DOI: `10.1016/S0370-2693(01)00307-0`. arXiv: `hep-ex/0012035`.

[23] Q. R. Ahmad et al. "Direct evidence for neutrino flavor transformation from neutral current interactions in the Sudbury Neutrino Observatory". In: *Phys. Rev. Lett.* 89 (2002), p. 011301. DOI: `10.1103/PhysRevLett.89.011301`. arXiv: `nucl-ex/0204008 [nucl-ex]`.

[24] Y. Fukuda et al. "Evidence for oscillation of atmospheric neutrinos". In: *Phys. Rev. Lett.* 81 (1998), pp. 1562–1567. DOI: `10.1103/PhysRevLett.81.1562`. arXiv: `hep-ex/9807003`.

[25] K. Eguchi et al. "First results from KamLAND: Evidence for reactor anti-neutrino disappearance". In: *Phys. Rev. Lett.* 90 (2003), p. 021802. DOI: `10.1103/PhysRevLett.90.021802`. arXiv: `hep-ex/0212021`.

[26] Nicola Cabibbo. “Unitary Symmetry and Leptonic Decays”. In: *Phys. Rev. Lett.* 10 (1963), pp. 531–533. DOI: 10.1103/PhysRevLett.10.531.

[27] Makoto Kobayashi and Toshihide Maskawa. “CP Violation in the Renormalizable Theory of Weak Interaction”. In: *Prog. Theor. Phys.* 49 (1973), pp. 652–657. DOI: 10.1143/PTP.49.652.

[28] B. Pontecorvo. “Inverse beta processes and nonconservation of lepton charge”. In: *Zh. Eksp. Teor. Fiz.* 34 (1957), p. 247.

[29] Ziro Maki, Masami Nakagawa, and Shoichi Sakata. “Remarks on the unified model of elementary particles”. In: *Prog. Theor. Phys.* 28 (1962), pp. 870–880. DOI: 10.1143/PTP.28.870.

[30] L. Wolfenstein. “Neutrino Oscillations in Matter”. In: *Phys. Rev. D* 17 (1978), pp. 2369–2374. DOI: 10.1103/PhysRevD.17.2369.

[31] S. P. Mikheev and A. Yu. Smirnov. “Resonant amplification of neutrino oscillations in matter and solar neutrino spectroscopy”. In: *Nuovo Cim. C* 9 (1986), pp. 17–26. DOI: 10.1007/BF02508049.

[32] *Three-neutrino fit based on data available in March 2024 — NuFIT*. [Accessed May 1, 2024]. 2024. URL: http://www.nu-fit.org/?q=node%2F278.

[33] Ivan Esteban et al. “The fate of hints: updated global analysis of three-flavor neutrino oscillations”. In: *JHEP* 09 (2020), p. 178. DOI: 10.1007/JHEP09(2020)178. arXiv: 2007.14792 [hep-ph].

[34] Fengpeng An et al. “Neutrino Physics with JUNO”. In: *J. Phys. G* 43.3 (2016), p. 030401. DOI: 10.1088/0954-3899/43/3/030401. arXiv: 1507.05613.

[35] K. Abe et al. “Physics potential of a long-baseline neutrino oscillation experiment using a J-PARC neutrino beam and Hyper-Kamiokande”. In: *PTEP* 2015 (2015), p. 053C02. DOI: 10.1093/ptep/ptv061. arXiv: 1502.05199 [hep-ex].

[36] B. Abi et al. “Long-baseline neutrino oscillation physics potential of the DUNE experiment”. In: *Eur. Phys. J. C* 80.10 (2020), p. 978. DOI: 10.1140/epjc/s10052-020-08456-z. arXiv: 2006.16043 [hep-ex].

[37] M. Aker et al. “KATRIN: status and prospects for the neutrino mass and beyond”. In: *J. Phys. G* 49.10 (2022), p. 100501. DOI: 10.1088/1361-6471/ac834e. arXiv: 2203.08059 [nucl-ex].

[38] C. Adams et al. “Neutrinoless Double Beta Decay”. In: (Dec. 2022). arXiv: 2212.11099 [nucl-ex].

[39] Steven R. Elliott, Vladimir Gavrin, and Wick Haxton. “The gallium anomaly”. In: *Prog. Part. Nucl. Phys.* 134 (2024), p. 104082. DOI: 10.1016/j.ppnp.2023.104082. arXiv: 2306.03299 [nucl-ex].

[40] M. A. Acero et al. “White Paper on Light Sterile Neutrino Searches and Related Phenomenology”. In: (Mar. 2022). arXiv: 2203.07323 [hep-ex].

[41] A. S. Eddington. *The Internal Constitution of the Stars*. 1926.

[42] H. A. Bethe. "Energy Production in Stars". In: *Phys. Rev.* 55 (5 Mar. 1939), pp. 434–456. DOI: `10.1103/PhysRev.55.434`. URL: `https://link.aps.org/doi/10.1103/PhysRev.55.434`.

[43] Orebi Gann et al. "The Future of Solar Neutrinos". In: *Ann. Rev. Nucl. Part. Sci.* 71 (2021), pp. 491–528. DOI: `10.1146/annurev-nucl-011921-061243`. arXiv: `2107.08613 [hep-ph]`.

[44] John N. Bahcall. "Solar Neutrinos". In: *Phys. Rev. Lett.* 17 (7 Aug. 1966), pp. 398–401. DOI: `10.1103/PhysRevLett.17.398`. URL: `https://link.aps.org/doi/10.1103/PhysRevLett.17.398`.

[45] John N. Bahcall and Roger K. Ulrich. "Solar Models, Neutrino Experiments and Helioseismology". In: *Rev. Mod. Phys.* 60 (1988), pp. 297–372. DOI: `10.1103/RevModPhys.60.297`.

[46] John N. Bahcall. *Neutrino Astrophysics*. 1989.

[47] W.C. Haxton and A.M. Serenelli. "CN-Cycle Solar Neutrinos and Sun's Primordial Core Metalicity". In: *Astrophys. J.* 687 (2008), pp. 678–691. DOI: `10.1086/591787`. arXiv: `0805.2013 [astro-ph]`.

[48] John N. Bahcall, Aldo M. Serenelli, and Sarbani Basu. "10,000 standard solar models: a Monte Carlo simulation". In: *Astrophys. J. Suppl.* 165 (2006), pp. 400–431. DOI: `10.1086/504043`. arXiv: `astro-ph/0511337`.

[49] Aldo Serenelli et al. "New Solar Composition: The Problem With Solar Models Revisited". In: *Astrophys. J. Lett.* 705 (2009), pp. L123–L127. DOI: `10.1088/0004-637X/705/2/L123`. arXiv: `0909.2668 [astro-ph.SR]`.

[50] Aldo M. Serenelli, W.C. Haxton, and Carlos Pena-Garay. "Solar models with accretion. I. Application to the solar abundance problem". In: *Astrophys. J.* 743 (2011), p. 24. DOI: `10.1088/0004-637X/743/1/24`. arXiv: `1104.1639 [astro-ph.SR]`.

[51] Núria Vinyoles et al. "A new Generation of Standard Solar Models". In: *Astrophys. J.* 835.2 (2017), p. 202. DOI: `10.3847/1538-4357/835/2/202`. arXiv: `1611.09867 [astro-ph.SR]`.

[52] Johannes Bergstrom et al. "Updated determination of the solar neutrino fluxes from solar neutrino data". In: *JHEP* 03 (2016), p. 132. DOI: `10.1007/JHEP03(2016)132`. arXiv: `1601.00972 [hep-ph]`.

[53] M. C. Gonzalez-Garcia et al. "Status of direct determination of solar neutrino fluxes after Borexino". In: *JHEP* 02 (2024), p. 064. DOI: `10.1007/JHEP02(2024)064`. arXiv: `2311.16226 [hep-ph]`.

[54] Yago Herrera and Aldo Serenelli. *Standard Solar Models B23 / SF-III*. en. 2023. DOI: `10.5281/ZENODO.10822316`. URL: `https://zenodo.org/doi/10.5281/zenodo.10822316`.

[55] B. Acharya et al. "Solar fusion III: New data and theory for hydrogen-burning stars". In: (May 2024). arXiv: `2405.06470 [astro-ph.SR]`.

[56] M. Asplund, A. M. Amarsi, and N. Grevesse. "The chemical make-up of the Sun: A 2020 vision". In: *Astron. Astrophys.* 653, A141 (Sept. 2021), A141. DOI: `10.1051/0004-6361/202140445`. arXiv: `2105.01661 [astro-ph.SR]`.

[57] Ekaterina Magg et al. "Observational constraints on the origin of the elements - IV. Standard composition of the Sun". In: *Astron. Astrophys.* 661 (2022), A140. DOI: `10.1051/0004-6361/202142971`. arXiv: `2203.02255 [astro-ph.SR]`.

[58] B. Aharmim et al. "A Search for Neutrinos from the Solar hep Reaction and the Diffuse Supernova Neutrino Background with the Sudbury Neutrino Observatory". In: *Astrophys. J.* 653 (2006), pp. 1545–1551. DOI: `10.1086/508768`. arXiv: `hep-ex/0607010`.

[59] M. Agostini et al. "Improved measurement of ^{8}B solar neutrinos with $1.5kty$ of Borexino exposure". In: *Phys. Rev. D* 101.6 (2020), p. 062001. DOI: `10.1103/PhysRevD.101.062001`. arXiv: `1709.00756 [hep-ex]`.

[60] Cleveland et al. "Measurement of the solar electron neutrino flux with the Homestake chlorine detector". In: *Astrophys. J.* 496 (1998), pp. 505–526. DOI: `10.1086/305343`.

[61] J. N. Abdurashitov et al. "Measurement of the solar neutrino capture rate with gallium metal. III: Results for the 2002–2007 data-taking period". In: *Phys. Rev. C* 80 (2009), p. 015807. DOI: `10.1103/PhysRevC.80.015807`. arXiv: `0901.2200 [nucl-ex]`.

[62] K. Abe et al. "Solar neutrino measurements using the full data period of Super-Kamiokande-IV". In: *Phys. Rev. D* 109.9 (2024), p. 092001. DOI: `10.1103/PhysRevD.109.092001`. arXiv: `2312.12907 [hep-ex]`.

[63] B. Aharmim et al. "Combined Analysis of all Three Phases of Solar Neutrino Data from the Sudbury Neutrino Observatory". In: *Phys. Rev. C* 88 (2013), p. 025501. DOI: `10.1103/PhysRevC.88.025501`. arXiv: `1109.0763 [nucl-ex]`.

[64] A. Gando et al. "^{7}Be Solar Neutrino Measurement with KamLAND". In: *Phys. Rev. C* 92.5 (2015), p. 055808. DOI: `10.1103/PhysRevC.92.055808`. arXiv: `1405.6190 [hep-ex]`.

[65] S. Abe et al. "Measurement of the 8B Solar Neutrino Flux with the KamLAND Liquid Scintillator Detector". In: *Phys. Rev. C* 84 (2011), p. 035804. DOI: `10.1103/PhysRevC.84.035804`. arXiv: `1106.0861 [hep-ex]`.

[66] M. Agostini et al. "Comprehensive measurement of *pp*-chain solar neutrinos". In: *Nature* 562.7728 (2018), pp. 505–510. DOI: `10.1038/s41586-018-0624-y`.

[67] M. Anderson et al. "Measurement of the ^{8}B solar neutrino flux in SNO+ with very low backgrounds". In: *Phys. Rev. D* 99.1 (2019), p. 012012. DOI: `10.1103/PhysRevD.99.012012`. arXiv: `1812.03355 [hep-ex]`.

[68] M. Agostini et al. “Experimental evidence of neutrinos produced in the CNO fusion cycle in the Sun”. In: *Nature* 587 (2020), pp. 577–582. DOI: 10.1038/s41586-020-2934-0. arXiv: 2006.15115 [hep-ex].

[69] S. Appel et al. “Improved Measurement of Solar Neutrinos from the Carbon-Nitrogen-Oxygen Cycle by Borexino and Its Implications for the Standard Solar Model”. In: *Phys. Rev. Lett.* 129.25 (2022), p. 252701. DOI: 10.1103/PhysRevLett.129.252701. arXiv: 2205.15975 [hep-ex].

[70] Martin Asplund et al. “The Chemical Composition of the Sun”. In: *Annual Review of Astronomy & Astrophysics* 47.1 (Sept. 2009), pp. 481–522. DOI: 10.1146/annurev.astro.46.060407.145222. arXiv: 0909.0948 [astro-ph.SR].

[71] N. Grevesse and A. J. Sauval. “Standard Solar Composition”. In: *Space Science Reviews* 85 (May 1998), pp. 161–174. DOI: 10.1023/A:1005161325181.

[72] Raymond Davis Jr., Don S. Harmer, and Kenneth C. Hoffman. “Search for neutrinos from the sun”. In: *Phys. Rev. Lett.* 20 (1968), pp. 1205–1209. DOI: 10.1103/PhysRevLett.20.1205.

[73] John N. Bahcall, Neta A. Bahcall, and G. Shaviv. “Present status of the theoretical predictions for the Cl-36 solar neutrino experiment”. In: *Phys. Rev. Lett.* 20 (1968), pp. 1209–1212. DOI: 10.1103/PhysRevLett.20.1209.

[74] John N. Bahcall. “Gallium solar neutrino experiments: Absorption cross-sections, neutrino spectra, and predicted event rates”. In: *Phys. Rev. C* 56 (1997), pp. 3391–3409. DOI: 10.1103/PhysRevC.56.3391. arXiv: hep-ph/9710491.

[75] K. S. Hirata et al. “Observation of ^{8}B solar neutrinos in the Kamiokande-II detector”. In: *Phys. Rev. Lett.* 63 (1 July 1989), pp. 16–19. DOI: 10.1103/PhysRevLett.63.16. URL: https://link.aps.org/doi/10.1103/PhysRevLett.63.16.

[76] Y. Fukuda et al. “Solar Neutrino Data Covering Solar Cycle 22”. In: *Phys. Rev. Lett.* 77 (9 Aug. 1996), pp. 1683–1686. DOI: 10.1103/PhysRevLett.77.1683. URL: https://link.aps.org/doi/10.1103/PhysRevLett.77.1683.

[77] Y. Fukuda et al. “Measurement of the solar neutrino energy spectrum using neutrino electron scattering”. In: *Phys. Rev. Lett.* 82 (1999), pp. 2430–2434. DOI: 10.1103/PhysRevLett.82.2430. arXiv: hep-ex/9812011.

[78] John N. Bahcall et al. “Are Standard Solar Models Reliable?” In: *Phys. Rev. Lett.* 78 (2 Jan. 1997), pp. 171–174. DOI: 10.1103/PhysRevLett.78.171. URL: https://link.aps.org/doi/10.1103/PhysRevLett.78.171.

[79] A. Bellerive et al. “The Sudbury Neutrino Observatory”. In: *Nucl. Phys. B* 908 (2016), pp. 30–51. DOI: 10.1016/j.nuclphysb.2016.04.035. arXiv: 1602.02469 [nucl-ex].

[80] G. Buldgen et al. “Higher metal abundances do not solve the solar problem”. In: *Astronomy & Astrophysics* 669, L9 (Jan. 2023), p. L9. DOI: 10.1051/0004-6361/202245448. arXiv: 2212.06473 [astro-ph.SR].

[81] S. Andringa et al. “Current Status and Future Prospects of the SNO+ Experiment”. In: *Adv. High Energy Phys.* 2016 (2016), p. 6194250. DOI: 10.1155/2016/6194250. arXiv: 1508.05759 [physics.ins-det].

[82] Angel Abusleme et al. “JUNO sensitivity to ^{7}Be, pep, and CNO solar neutrinos”. In: *JCAP* 10 (2023), p. 022. DOI: 10.1088/1475-7516/2023/10/022. arXiv: 2303.03910 [hep-ex].

[83] John F. Beacom et al. “Physics prospects of the Jinping neutrino experiment”. In: *Chin. Phys. C* 41.2 (2017), p. 023002. DOI: 10.1088/1674-1137/41/2/023002. arXiv: 1602.01733 [physics.ins-det].

[84] S.K. Agarwalla et al. “Constraints on flavor-diagonal non-standard neutrino interactions from Borexino Phase-II”. In: *JHEP* 02 (2020), p. 038. DOI: 10.1007/JHEP02(2020)038. arXiv: 1905.03512 [hep-ph].

[85] P. Weatherly et al. “Testing Non-Standard Interactions Between Solar Neutrinos and Quarks with Super-Kamiokande”. In: (Mar. 2022). arXiv: 2203.11772 [hep-ex].

[86] V. V. Barinov et al. “Results from the Baksan Experiment on Sterile Transitions (BEST)”. In: *Phys. Rev. Lett.* 128.23 (2022), p. 232501. DOI: 10.1103/PhysRevLett.128.232501. arXiv: 2109.11482 [nucl-ex].

[87] W. J. Willis and V. Radeka. “Liquid Argon Ionization Chambers as Total Absorption Detectors”. In: *Nucl. Instrum. Meth.* 120 (1974), pp. 221–236. DOI: 10.1016/0029-554X(74)90039-1.

[88] Jay N. Marx and David R. Nygren. “The Time Projection Chamber”. In: *Physics Today* 31.10 (Oct. 1978), pp. 46–53. ISSN: 0031-9228. DOI: 10.1063/1.2994775. eprint: https://pubs.aip.org/physicstoday/article-pdf/31/10/46/8284498/46_1_online.pdf. URL: https://doi.org/10.1063/1.2994775.

[89] F. Arneodo et al. “The ICARUS 50-l LAr TPC in the CERN neutrino beam”. In: *INFN Eloisatron Project: 36th Workshop: New Detectors.* Dec. 1998, pp. 3–12. arXiv: hep-ex/9812006.

[90] R. Acciarri et al. “Design and Construction of the MicroBooNE Detector”. In: *JINST* 12.02 (2017), P02017. DOI: 10.1088/1748-0221/12/02/P02017. arXiv: 1612.05824 [physics.ins-det].

[91] Babak Abi et al. “Deep Underground Neutrino Experiment (DUNE), Far Detector Technical Design Report, Volume I Introduction to DUNE”. In: *JINST* 15.08 (2020), T08008. DOI: 10.1088/1748-0221/15/08/T08008. arXiv: 2002.02967 [physics.ins-det].

[92] M. G. Aartsen et al. “The IceCube Neutrino Observatory: Instrumentation and Online Systems”. In: *JINST* 12.03 (2017). [Erratum: JINST 19, E05001 (2024)], P03012. DOI: 10.1088/1748-0221/12/03/P03012. arXiv: 1612.05093 [astro-ph.IM].

[93] D. Akimov et al. “Observation of Coherent Elastic Neutrino-Nucleus Scattering”. In: *Science* 357.6356 (2017), pp. 1123–1126. DOI: 10.1126/science.aao0990. arXiv: 1708.01294 [nucl-ex].

[94] J. Ashenfelter et al. “The PROSPECT Reactor Antineutrino Experiment”. In: *Nucl. Instrum. Meth. A* 922 (2019), pp. 287–309. DOI: 10.1016/j.nima.2018.12.079. arXiv: 1808.00097 [physics.ins-det].

[95] P. Adamson et al. “Constraints on Oscillation Parameters from ν_e Appearance and ν_μ Disappearance in NOvA”. In: *Phys. Rev. Lett.* 118.23 (2017), p. 231801. DOI: 10.1103/PhysRevLett.118.231801. arXiv: 1703.03328 [hep-ex].

[96] P. A. Cherenkov. “Visible luminescence of pure liquids under the influence of γ-radiation”. In: *Dokl. Akad. Nauk SSSR* 2.8 (1934), pp. 451–454. DOI: 10.3367/UFNr.0093.196710n.0385.

[97] I. M. Frank and I. E. Tamm. “Coherent visible radiation of fast electrons passing through matter”. In: *Compt. Rend. Acad. Sci. URSS* 14.3 (1937). Ed. by V. L. Ginzburg, B. M. Bolotovsky, and I. M. Dremin, pp. 109–114. DOI: 10.3367/UFNr.0093.196710o.0388.

[98] John B. Birks. *The Theory and practice of scintillation counting*. Pergamon Press, 1964. URL: http://www.slac.stanford.edu/spires/find/books/www?cl=QCD928:B52.

[99] B. A. Moffat et al. “Optical calibration hardware for the sudbury neutrino observatory”. In: *Nucl. Instrum. Meth. A* 554 (2005), pp. 255–265. DOI: 10.1016/j.nima.2005.08.029. arXiv: nucl-ex/0507026.

[100] Bryce Anton Moffat. “The optical calibration of the Sudbury Neutrino Observatory”. PhD thesis. Queens University, Canada, Jan. 2001.

[101] M. R. Anderson et al. “Optical calibration of the SNO+ detector in the water phase with deployed sources”. In: *JINST* 16.10 (2021), P10021. DOI: 10.1088/1748-0221/16/10/P10021. arXiv: 2106.03951 [physics.ins-det].

[102] K. Abe et al. “Calibration of the Super-Kamiokande Detector”. In: *Nucl. Instrum. Meth. A* 737 (2014), pp. 253–272. DOI: 10.1016/j.nima.2013.11.081. arXiv: 1307.0162 [physics.ins-det].

[103] S. S. Gokhale et al. “A spectrometric approach to measuring the Rayleigh scattering length for liquid scintillator detectors”. In: *JINST* 16.03 (2021), P03009. DOI: 10.1088/1748-0221/16/03/P03009. arXiv: 2008.08634 [physics.ins-det].

[104] Michael Wurm et al. “Optical Scattering Lengths in Large Liquid-Scintillator Neutrino Detectors”. In: *Rev. Sci. Instrum.* 81 (2010), p. 053301. DOI: 10.1063/1.3397322. arXiv: 1004.0811 [physics.ins-det].

[105] Xiang Zhou et al. “Rayleigh scattering of linear alkylbenzene in large liquid scintillator detectors”. In: *Rev. Sci. Instrum.* 86.7 (2015), p. 073310. DOI: 10.1063/1.4927458. arXiv: 1504.00987 [physics.ins-det].

[106] Guang-You Yu et al. “Some new progress on the light absorption properties of linear alkyl benzene solvent”. In: *Chin. Phys. C* 40.1 (2016), p. 016002. DOI: `10.1088/1674-1137/40/1/016002`. arXiv: `1504.05444 [physics.ins-det]`.

[107] Dewen Cao et al. “Light Absorption Properties of the High Quality Linear Alkylbenzene for the JUNO Experiment”. In: *Nucl. Instrum. Meth. A* 927 (2019), pp. 230–235. DOI: `10.1016/j.nima.2019.01.077`. arXiv: `1801.08363 [physics.ins-det]`.

[108] H. S. Zhang et al. “Refractive index in the JUNO liquid scintillator”. In: (May 2024). arXiv: `2405.19879 [physics.ins-det]`.

[109] H. Wan Chan Tseung and N. Tolich. “Ellipsometric measurements of the refractive indices of linear alkylbenzene and EJ-301 scintillators from 210 to 1000 nm”. In: *Phys. Scripta* 03 (2011), p. 035701. DOI: `10.1088/0031-8949/84/03/035701`. arXiv: `1105.2101 [physics.optics]`.

[110] Lord Rayleigh F.R.S. “XXXIV. On the transmission of light through an atmosphere containing small particles in suspension, and on the origin of the blue of the sky”. In: *Philosophical Magazine Series 1* 47 (1899), pp. 375–384. URL: `https://api.semanticscholar.org/CorpusID:122238555`.

[111] Allan H. Harvey, John S. Gallagher, and J. M. H. Levelt Sengers. “Revised Formulation for the Refractive Index of Water and Steam as a Function of Wavelength, Temperature and Density”. In: *Journal of Physical and Chemical Reference Data* 27.4 (July 1998), pp. 761–774. DOI: `10.1063/1.556029`.

[112] S. D. Biller et al. “Measurements of photomultiplier single photon counting efficiency for the Sudbury Neutrino Observatory”. In: *Nucl. Instrum. Meth. A* 432 (1999), pp. 364–373. DOI: `10.1016/S0168-9002(99)00500-8`.

[113] Hamamatsu. *Photomultiplier tube R14688-100: Hamamatsu Photonics*. `https://www.hamamatsu.com/us/en/product/optical-sensors/pmt/pmt_tube-alone/head-on-type/R14688-100.html`. [Accessed February 3, 2023].

[114] T. Anderson et al. “Eos: conceptual design for a demonstrator of hybrid optical detector technology”. In: *JINST* 18.02 (2023), P02009. DOI: `10.1088/1748-0221/18/02/P02009`. arXiv: `2211.11969 [physics.ins-det]`.

[115] Tanner Kaptanoglu et al. “Characterization of the Hamamatsu 8-inch R14688-100 PMT”. In: *JINST* 19.02 (2024), P02032. DOI: `10.1088/1748-0221/19/02/P02032`. arXiv: `2311.05080 [physics.ins-det]`.

[116] P. DeVore et al. “Light-weight Flexible Magnetic Shields For Large-Aperture Photomultiplier Tubes”. In: *Nucl. Instrum. Meth. A* 737 (2014), pp. 222–228. DOI: `10.1016/j.nima.2013.11.024`. arXiv: `1309.5415 [physics.ins-det]`.

[117] A. Brigatti et al. “The Photomultiplier tube testing facility for the Borexino experiment at LNGS”. In: *Nucl. Instrum. Meth. A* 537 (2005), pp. 521–536. DOI: `10.1016/j.nima.2004.07.248`. arXiv: `physics/0406106`.

[118] S. Ajimura et al. “The JSNS2 detector”. In: *Nucl. Instrum. Meth. A* 1014 (2021), p. 165742. DOI: 10.1016/j.nima.2021.165742. arXiv: 2104.13169.

[119] Angel Abusleme et al. “Mass testing and characterization of 20-inch PMTs for JUNO”. In: *Eur. Phys. J. C* 82.12 (2022), p. 1168. DOI: 10.1140/epjc/s10052-022-11002-8. arXiv: 2205.08629 [physics.ins-det].

[120] Christophe Bronner et al. “Performances of the Hyper-Kamiokande 20” PMT”. In: *JPS Conf. Proc.* 27 (2019), p. 011013. DOI: 10.7566/JPSCP.27.011013.

[121] Aiqiang Zhang et al. “Performance evaluation of the 8-inch MCP-PMT for Jinping Neutrino Experiment”. In: *Nucl. Instrum. Meth. A* 1055 (2023), p. 168506. DOI: 10.1016/j.nima.2023.168506. arXiv: 2303.05373 [hep-ex].

[122] Steve T. Wilson et al. “Characterisation of the temperature-dependent dark rate of Hamamatsu R7081-100 10” photomultiplier tubes”. In: *JINST* 18.08 (2023), P08017. DOI: 10.1088/1748-0221/18/08/P08017. arXiv: 2306.10751 [physics.ins-det].

[123] S. Yamada et al. “Commissioning of the new electronics and online system for the Super-Kamiokande experiment”. In: *IEEE Trans. Nucl. Sci.* 57 (2010). Ed. by Sascha Marc Schmeling, pp. 428–432. DOI: 10.1109/TNS.2009.2034854.

[124] I. Blevis et al. “Measurement of Rn-222 dissolved in water at the Sudbury Neutrino Observatory”. In: *Nucl. Instrum. Meth. A* 517 (2004), pp. 139–153. DOI: 10.1016/j.nima.2003.10.103. arXiv: nucl-ex/0305022.

[125] T. C. Andersen et al. “Measurement of radium concentration in water with Mn coated beads at the Sudbury Neutrino Observatory”. In: *Nucl. Instrum. Meth. A* 501 (2003), pp. 399–417. DOI: 10.1016/S0168-9002(03)00616-8. arXiv: nucl-ex/0208010.

[126] Y. Nakano et al. “Measurement of the radon concentration in purified water in the Super-Kamiokande IV detector”. In: *Nucl. Instrum. Meth. A* 977 (2020), p. 164297. DOI: 10.1016/j.nima.2020.164297. arXiv: 1910.03823 [physics.ins-det].

[127] M. R. Anderson et al. “Development, characterisation, and deployment of the SNO+ liquid scintillator”. In: *JINST* 16.05 (2021), P05009. DOI: 10.1088/1748-0221/16/05/P05009. arXiv: 2011.12924 [physics.ins-det].

[128] M. Balata et al. “The water purification system for the low background counting test facility of the Borexino experiment at Gran Sasso”. In: *Nucl. Instrum. Meth. A* 370 (1996), pp. 605–608. DOI: 10.1016/0168-9002(95)00862-4.

[129] M. G. Giammarchi et al. “The scintillator solvent procurement for the Borexino solar neutrino detector”. In: *Nucl. Instrum. Meth. A* 648 (2011), pp. 100–108. DOI: 10.1016/j.nima.2011.06.003.

[130] J. Benziger et al. “The Scintillator Purification System for the Borexino Solar Neutrino Detector”. In: *Nucl. Instrum. Meth. A* 587 (2008), pp. 277–291. DOI: 10.1016/j.nima.2007.12.043. arXiv: 0709.1503 [physics.ins-det].

[131] M. C. Chu et al. “The radon monitoring system in Daya Bay Reactor Neutrino Experiment”. In: *Nucl. Instrum. Meth. A* 808 (2016), pp. 156–164. DOI: `10.1016/j.nima.2015.11.093`. arXiv: `1601.04885 [physics.ins-det]`.

[132] H. M. O’Keeffe et al. “Four methods for determining the composition of trace radioactive surface contamination of low-radioactivity metal”. In: *Nucl. Instrum. Meth. A* 659 (2011), pp. 182–192. DOI: `10.1016/j.nima.2011.08.060`. arXiv: `1103.5788 [nucl-ex]`.

[133] Xuantong Zhang et al. “Study on the large area MCP-PMT glass radioactivity reduction”. In: *Nucl. Instrum. Meth. A* 898 (2018), pp. 67–71. DOI: `10.1016/j.nima.2018.05.008`. arXiv: `1710.09965 [physics.ins-det]`.

[134] Dongming Mei and A. Hime. “Muon-induced background study for underground laboratories”. In: *Phys. Rev. D* 73 (2006), p. 053004. DOI: `10.1103/PhysRevD.73.053004`. arXiv: `astro-ph/0512125`.

[135] Shirley Weishi Li and John F. Beacom. “First calculation of cosmic-ray muon spallation backgrounds for MeV astrophysical neutrino signals in Super-Kamiokande”. In: *Phys. Rev. C* 89 (2014), p. 045801. DOI: `10.1103/PhysRevC.89.045801`. arXiv: `1402.4687 [hep-ph]`.

[136] DongMei Xia et al. “Temperature dependence of the light yield of the LAB-based and mesitylene-based liquid scintillators”. In: (Feb. 2014). arXiv: `1402.6871`.

[137] D. Bravo-Berguño et al. “The Borexino Thermal Monitoring & Management System and simulations of the fluid-dynamics of the Borexino detector under asymmetrical, changing boundary conditions”. In: *Nucl. Instrum. Meth. A* 885 (2018), pp. 38–53. DOI: `10.1016/j.nima.2017.12.047`. arXiv: `1712.05709 [physics.ins-det]`.

[138] J. D. Wilson. “Thermally-driven scintillator flow in the SNO+ neutrino detector”. In: *Nucl. Instrum. Meth. A* 1055 (2023), p. 168430. DOI: `10.1016/j.nima.2023.168430`. arXiv: `2212.00251 [physics.ins-det]`.

[139] D. G. Michael et al. “The Magnetized steel and scintillator calorimeters of the MINOS experiment”. In: *Nucl. Instrum. Meth. A* 596 (2008), pp. 190–228. DOI: `10.1016/j.nima.2008.08.003`. arXiv: `0805.3170 [physics.ins-det]`.

[140] R. L. Talaga et al. “PVC Extrusion Development and Production for the NOvA Neutrino Experiment”. In: *Nucl. Instrum. Meth. A* 861 (2017), pp. 77–89. DOI: `10.1016/j.nima.2017.03.004`. arXiv: `1601.00908 [physics.ins-det]`.

[141] Annarita Margiotta. “The KM3NeT deep-sea neutrino telescope”. In: *Nucl. Instrum. Meth. A* 766 (2014). Ed. by T. Sumiyoshi et al., pp. 83–87. DOI: `10.1016/j.nima.2014.05.090`. arXiv: `1408.1392 [astro-ph.IM]`.

[142] N. Allemandou et al. “The STEREO Experiment”. In: *JINST* 13.07 (2018), P07009. DOI: `10.1088/1748-0221/13/07/P07009`. arXiv: `1804.09052 [physics.ins-det]`.

[143] R. Becker-Szendy et al. “Neutrino measurements with the IMB detector”. In: *Nucl. Phys. Proc. Suppl.* 38 (1995), pp. 331–336. DOI: `10.1016/0920-5632(94)00765-N`.

[144] Masayuki Nakahata et al. "Atmospheric Neutrino Background and Pion Nuclear Effect for Kamioka Nucleon Decay Experiment". In: *J. Phys. Soc. Jap.* 55 (1986), p. 3786. DOI: `10.1143/JPSJ.55.3786`.

[145] Todd Haines et al. "Neutrinos From SN1987A in the Imb Detector". In: *Nucl. Instrum. Meth. A* 264 (1988). Ed. by K. C. Wali, pp. 28–31. DOI: `10.1016/0168-9002(88)91097-2`.

[146] K. S. Hirata et al. "Observation in the Kamiokande-II Detector of the Neutrino Burst from Supernova SN 1987a". In: *Phys. Rev. D* 38 (1988), pp. 448–458. DOI: `10.1103/PhysRevD.38.448`.

[147] K. Abe et al. "First gadolinium loading to Super-Kamiokande". In: *Nucl. Instrum. Meth. A* 1027 (2022), p. 166248. DOI: `10.1016/j.nima.2021.166248`. arXiv: `2109.00360 [physics.ins-det]`.

[148] K. Abe et al. "Second gadolinium loading to Super-Kamiokande". In: *Nucl. Instrum. Meth. A* 1065 (2024), p. 169480. DOI: `10.1016/j.nima.2024.169480`. arXiv: `2403.07796 [physics.ins-det]`.

[149] M. Jiang et al. "Atmospheric Neutrino Oscillation Analysis with Improved Event Reconstruction in Super-Kamiokande IV". In: *PTEP* 2019.5 (2019), 053F01. DOI: `10.1093/ptep/ptz015`. arXiv: `1901.03230 [hep-ex]`.

[150] K. Abe et al. "Solar Neutrino Measurements in Super-Kamiokande-IV". In: *Phys. Rev. D* 94.5 (2016), p. 052010. DOI: `10.1103/PhysRevD.94.052010`. arXiv: `1606.07538 [hep-ex]`.

[151] A. Takenaka et al. "Search for proton decay via $p \to e^+\pi^0$ and $p \to \mu^+\pi^0$ with an enlarged fiducial volume in Super-Kamiokande I-IV". In: *Phys. Rev. D* 102.11 (2020), p. 112011. DOI: `10.1103/PhysRevD.102.112011`. arXiv: `2010.16098 [hep-ex]`.

[152] R. Matsumoto et al. "Search for proton decay via $p \to \mu^+K^0$ in 0.37 megaton-years exposure of Super-Kamiokande". In: *Phys. Rev. D* 106.7 (2022), p. 072003. DOI: `10.1103/PhysRevD.106.072003`. arXiv: `2208.13188 [hep-ex]`.

[153] M. H. Ahn et al. "Measurement of Neutrino Oscillation by the K2K Experiment". In: *Phys. Rev.* D74 (2006), p. 072003. DOI: `10.1103/PhysRevD.74.072003`. arXiv: `hep-ex/0606032 [hep-ex]`.

[154] K. Abe et al. "Constraint on the matter–antimatter symmetry-violating phase in neutrino oscillations". In: *Nature* 580.7803 (2020). [Erratum: Nature 583, E16 (2020)], pp. 339–344. DOI: `10.1038/s41586-020-2177-0`. arXiv: `1910.03887 [hep-ex]`.

[155] J. A. Formaggio. "Measurement of atmospheric neutrinos at the Sudbury Neutrino Observatory". In: *Nucl. Phys. A* 827 (2009). Ed. by Itzhak Tserruya, Avraham Gal, and Daniel Ashery, pp. 498C–500C. DOI: `10.1016/j.nuclphysa.2009.05.143`.

[156] B. Aharmim et al. "Measurement of Neutron Production in Atmospheric Neutrino Interactions at the Sudbury Neutrino Observatory". In: *Phys. Rev. D* 99.11 (2019), p. 112007. DOI: `10.1103/PhysRevD.99.112007`. arXiv: `1904.01148 [hep-ex]`.

[157] B. Aharmim et al. “Constraints on Neutrino Lifetime from the Sudbury Neutrino Observatory”. In: *Phys. Rev. D* 99.3 (2019), p. 032013. DOI: 10.1103/PhysRevD.99.032013. arXiv: 1812.01088 [hep-ex].

[158] C Athanassopoulos et al. “The Liquid scintillator neutrino detector and LAMPF neutrino source”. In: *Nucl. Instrum. Meth. A* 388 (1997), pp. 149–172. DOI: 10.1016/S0168-9002(96)01155-2. arXiv: nucl-ex/9605002.

[159] A. Aguilar et al. “Evidence for neutrino oscillations from the observation of $\bar{\nu}_e$ appearance in a $\bar{\nu}_\mu$ beam”. In: *Phys. Rev. D* 64 (2001), p. 112007. DOI: 10.1103/PhysRevD.64.112007. arXiv: hep-ex/0104049.

[160] A. A. Aguilar-Arevalo et al. “Improved Search for $\bar{\nu}_\mu \to \bar{\nu}_e$ Oscillations in the MiniBooNE Experiment”. In: *Phys. Rev. Lett.* 110 (2013), p. 161801. DOI: 10.1103/PhysRevLett.110.161801. arXiv: 1303.2588 [hep-ex].

[161] A. A. Aguilar-Arevalo et al. “The MiniBooNE Detector”. In: *Nucl. Instrum. Meth. A* 599 (2009), pp. 28–46. DOI: 10.1016/j.nima.2008.10.028. arXiv: 0806.4201 [hep-ex].

[162] A. A. Aguilar-Arevalo et al. “Updated MiniBooNE neutrino oscillation results with increased data and new background studies”. In: *Phys. Rev. D* 103.5 (2021), p. 052002. DOI: 10.1103/PhysRevD.103.052002. arXiv: 2006.16883 [hep-ex].

[163] Pedro AN Machado, Ornella Palamara, and David W Schmitz. “The Short-Baseline Neutrino Program at Fermilab”. In: *Ann. Rev. Nucl. Part. Sci.* 69 (2019), pp. 363–387. DOI: 10.1146/annurev-nucl-101917-020949. arXiv: 1903.04608 [hep-ex].

[164] K. Eguchi et al. “First results from KamLAND: Evidence for reactor anti-neutrino disappearance”. In: *Phys. Rev. Lett.* 90 (2003), p. 021802. DOI: 10.1103/PhysRevLett.90.021802. arXiv: hep-ex/0212021 [hep-ex].

[165] T. Araki et al. “Experimental investigation of geologically produced antineutrinos with KamLAND”. In: *Nature* 436 (2005), pp. 499–503. DOI: 10.1038/nature03980.

[166] S. Abe et al. “First Search for the Majorana Nature of Neutrinos in the Inverted Mass Ordering Region with KamLAND-Zen”. In: (Mar. 2022). arXiv: 2203.02139 [hep-ex].

[167] G. Alimonti et al. “The Borexino detector at the Laboratori Nazionali del Gran Sasso”. In: *Nucl. Instrum. Meth. A* 600 (2009), pp. 568–593. DOI: 10.1016/j.nima.2008.11.076. arXiv: 0806.2400 [physics.ins-det].

[168] G. Bellini et al. “Observation of Geo-Neutrinos”. In: *Phys. Lett. B* 687 (2010), pp. 299–304. DOI: 10.1016/j.physletb.2010.03.051. arXiv: 1003.0284 [hep-ex].

[169] H. de Kerret et al. “The Double Chooz antineutrino detectors”. In: (Jan. 2022). arXiv: 2201.13285 [physics.ins-det].

[170] F. P. An et al. “The Detector System of The Daya Bay Reactor Neutrino Experiment”. In: *Nucl. Instrum. Meth. A* 811 (2016). DOI: 10.1016/j.nima.2015.11.144. arXiv: 1508.03943 [physics.ins-det].

[171] J. K. Ahn et al. “Observation of Reactor Electron Antineutrino Disappearance in the RENO Experiment”. In: *Phys. Rev. Lett.* 108 (2012), p. 191802. DOI: `10.1103/PhysRevLett.108.191802`. arXiv: `1204.0626 [hep-ex]`.

[172] Chao Zhang, Xin Qian, and Muriel Fallot. “Reactor antineutrino flux and anomaly”. In: *Prog. Part. Nucl. Phys.* 136 (2024), p. 104106. DOI: `10.1016/j.ppnp.2024.104106`. arXiv: `2310.13070 [hep-ph]`.

[173] V. Albanese et al. “The SNO+ experiment”. In: *JINST* 16.08 (2021), P08059. DOI: `10.1088/1748-0221/16/08/P08059`. arXiv: `2104.11687 [physics.ins-det]`.

[174] N. J. T. Smith. “The SNOLAB deep underground facility”. In: *Eur. Phys. J. Plus* 127 (2012), p. 108. DOI: `10.1140/epjp/i2012-12108-9`.

[175] D. J. Auty et al. “A method to load tellurium in liquid scintillator for the study of neutrinoless double beta decay”. In: *Nucl. Instrum. Meth. A* 1051 (2023), p. 168204. DOI: `10.1016/j.nima.2023.168204`. arXiv: `2212.12444 [physics.ins-det]`.

[176] M. Anderson et al. “Search for invisible modes of nucleon decay in water with the SNO+ detector”. In: *Phys. Rev. D* 99.3 (2019), p. 032008. DOI: `10.1103/PhysRevD.99.032008`. arXiv: `1812.05552 [hep-ex]`.

[177] A. Allega et al. “Improved search for invisible modes of nucleon decay in water with the SNO+detector”. In: *Phys. Rev. D* 105.11 (2022), p. 112012. DOI: `10.1103/PhysRevD.105.112012`. arXiv: `2205.06400 [hep-ex]`.

[178] A. Allega et al. “Evidence of Antineutrinos from Distant Reactors using Pure Water at SNO+”. In: *Phys. Rev. Lett.* 130.9 (2023), p. 091801. DOI: `10.1103/PhysRevLett.130.091801`. arXiv: `2210.14154 [nucl-ex]`.

[179] M. R. Anderson et al. “Measurement of neutron-proton capture in the SNO+ water phase”. In: *Phys. Rev. C* 102.1 (2020), p. 014002. DOI: `10.1103/PhysRevC.102.014002`. arXiv: `2002.10351 [physics.ins-det]`.

[180] The SNO+ collaboration. Private communication.

[181] J. Boger et al. “The Sudbury neutrino observatory”. In: *Nucl. Instrum. Meth. A* 449 (2000), pp. 172–207. DOI: `10.1016/S0168-9002(99)01469-2`. arXiv: `nucl-ex/9910016`.

[182] B. Aharmim et al. “Electron energy spectra, fluxes, and day-night asymmetries of B-8 solar neutrinos from measurements with NaCl dissolved in the heavy-water detector at the Sudbury Neutrino Observatory”. In: *Phys. Rev. C* 72 (2005), p. 055502. DOI: `10.1103/PhysRevC.72.055502`. arXiv: `nucl-ex/0502021`.

[183] A. Allega et al. “Event-by-event direction reconstruction of solar neutrinos in a high light-yield liquid scintillator”. In: *Phys. Rev. D* 109.7 (2024), p. 072002. DOI: `10.1103/PhysRevD.109.072002`. arXiv: `2309.06341 [hep-ex]`.

[184] Ana Sofia Carpinteiro Inácio. “Data Analysis of the Water and Scintillator Phases of SNO+: from Solar Neutrino Measurements to Double Beta Decay Sensitivity Studies”. PhD thesis. University of Lisbon, 2022.

[185] A. Allega et al. “Initial measurement of reactor antineutrino oscillation at SNO+”. In: (May 2024). arXiv: 2405.19700 [hep-ex].

[186] Daniel Cookman. “Measurement of Oscillations in Solar Boron-8 Neutrinos and Studies of Optical Scattering in the SNO+ Detector ”. PhD thesis. University of Oxford, 2023.

[187] Edwin Cartlidge. *Chemical spills put Italy’s underground physics lab in jeopardy*. Oct. 2018. DOI: 10.1126/science.aav6712. URL: http://dx.doi.org/10.1126/science.aav6712.

[188] S. Agostinelli et al. “GEANT4–a simulation toolkit”. In: *Nucl. Instrum. Meth. A* 506 (2003), pp. 250–303. DOI: 10.1016/S0168-9002(03)01368-8.

[189] Glenn Horton-Smith et al. *GLG4sim Web Page*. https://www.phys.ksu.edu/personal/gahs/GLG4sim/. [Accessed June 18, 2024]. 2007.

[190] Rene Brun et al. *root-project/root: v6.18/02*. Version v6-18-02. June 2020. DOI: 10.5281/zenodo.3895860. URL: https://doi.org/10.5281/zenodo.3895860.

[191] C. Galbiati, M. Misiaszek, and N. Rossi. “α/β discrimination in Borexino”. In: *Eur. Phys. J. A* 52.4 (2016), p. 86. DOI: 10.1140/epja/i2016-16086-1.

[192] John M. G. Walker. “Study of Invisible Mode Nucleon Decay in the SNO+ Detector”. PhD thesis. University of Liverpool, July 2016.

[193] *Earthquakes Canada*. https://www.earthquakescanada.nrcan.gc.ca/stndon/NEDB-BNDS/bulletin-en.php.

[194] W.T. Winter et al. “The B-8 neutrino spectrum”. In: *Phys. Rev. C* 73 (2006), p. 025503. DOI: 10.1103/PhysRevC.73.025503. arXiv: nucl-ex/0406019.

[195] E. G. Adelberger et al. “Solar fusion cross sections II: the pp chain and CNO cycles”. In: *Rev. Mod. Phys.* 83 (2011), p. 195. DOI: 10.1103/RevModPhys.83.195. arXiv: 1004.2318 [nucl-ex].

[196] B. Longfellow et al. “Determination of the ^{8}B neutrino energy spectrum using trapped ions”. In: *Phys. Rev. C* 107 (3 Mar. 2023), p. L032801. DOI: 10.1103/PhysRevC.107.L032801. URL: https://link.aps.org/doi/10.1103/PhysRevC.107.L032801.

[197] P.A. Zyla et al. “Review of Particle Physics”. In: *PTEP* 2020.8 (2020), p. 083C01. DOI: 10.1093/ptep/ptaa104.

[198] A. Allega et al. “Measurement of the ^{8}B Solar Neutrino Flux Using the Full SNO+ Water Phase”. In: (July 2024). arXiv: 2407.17595 [hep-ex].

[199] Joshua R. Klein et al. “Future Advances in Photon-Based Neutrino Detectors: A SNOWMASS White Paper”. In: (Mar. 2022). arXiv: 2203.07479.

[200] M. Agostini et al. “Correlated and integrated directionality for sub-MeV solar neutrinos in Borexino”. In: *Phys. Rev. D* 105.5 (2022), p. 052002. DOI: 10.1103/PhysRevD.105.052002. arXiv: 2109.04770 [hep-ex].

[201] M. Agostini et al. “First Directional Measurement of Sub-MeV Solar Neutrinos with Borexino”. In: *Phys. Rev. Lett.* 128.9 (2022), p. 091803. DOI: 10.1103/PhysRevLett.128.091803. arXiv: 2112.11816 [hep-ex].

[202] A. Abusleme et al. “Optimization of the JUNO liquid scintillator composition using a Daya Bay antineutrino detector”. In: *Nucl. Instrum. Meth. A* 988 (2021), p. 164823. DOI: 10.1016/j.nima.2020.164823. arXiv: 2007.00314 [physics.ins-det].

[203] Xiongxin Dai et al. “Wavelength Shifters for Water Cherenkov Detectors”. In: *Nucl. Instrum. Meth. A* 589 (2008), pp. 290–295. DOI: 10.1016/j.nima.2008.01.101. arXiv: 0807.2895 [physics.ins-det].

[204] Minfang Yeh et al. “A new water-based liquid scintillator and potential applications”. In: *Nuclear Instruments and Methods in Physics Research Section A-accelerators Spectrometers Detectors and Associated Equipment - NUCL INSTRUM METH PHYS RES A* 660 (Dec. 2011), pp. 51–56. DOI: 10.1016/j.nima.2011.08.040.

[205] Lindsey J. Bignell et al. “Characterization and Modeling of a Water-based Liquid Scintillator”. In: *JINST* 10.12 (2015), P12009. DOI: 10.1088/1748-0221/10/12/P12009. arXiv: 1508.07029 [physics.ins-det].

[206] J. B. Cumming, S. Hans, and M. Yeh. “Improving Light Yield Measurements for Low-Yield Scintillators”. In: *Nucl. Instrum. Meth. A* 925 (2019), pp. 1–5. DOI: 10.1016/j.nima.2019.01.014. arXiv: 1810.02885 [physics.ins-det].

[207] Lindsey J. Bignell et al. “Measurement of Radiation Damage of Water-based Liquid Scintillator and Liquid Scintillator”. In: *JINST* 10.10 (2015), P10027. DOI: 10.1088/1748-0221/10/10/P10027. arXiv: 1508.07023 [physics.med-ph].

[208] R. Zhao et al. “Performance of a ton-scale water-based liquid scintillator detector”. In: *JINST* 19 (2024), P01003.

[209] X. Xiang et al. “Design, construction, and operation of a 1-ton Water-based Liquid scintillator detector at Brookhaven National Laboratory”. In: (Mar. 2024). arXiv: 2403.13231 [physics.ins-det].

[210] J. Caravaca et al. “Experiment to demonstrate separation of Cherenkov and scintillation signals”. In: *Phys. Rev. C* 95.5 (2017), p. 055801. DOI: 10.1103/PhysRevC.95.055801. arXiv: 1610.02029 [physics.ins-det].

[211] J. Caravaca et al. “Cherenkov and Scintillation Light Separation in Organic Liquid Scintillators”. In: *Eur. Phys. J. C* 77.12 (2017), p. 811. DOI: 10.1140/epjc/s10052-017-5380-x. arXiv: 1610.02011 [physics.ins-det].

[212] J. Caravaca et al. “Characterization of water-based liquid scintillator for Cherenkov and scintillation separation”. In: *Eur. Phys. J. C* 80.9 (2020), p. 867. DOI: 10.1140/epjc/s10052-020-8418-4. arXiv: 2006.00173 [physics.ins-det].

[213] Drew R. Onken et al. “Time response of water-based liquid scintillator from X-ray excitation”. In: *Mater. Adv.* 1 (1 2020), pp. 71–76.

[214] Michael J. Ford et al. “Pulse-shape discrimination in water-based scintillators”. In: *Nucl. Instrum. Meth. A* 1036 (2022), p. 166854. DOI: 10.1016/j.nima.2022.166854. arXiv: 2202.07625 [physics.ins-det].

[215] E. J. Callaghan et al. “Characterization of the scintillation response of water-based liquid scintillator to alpha particles, and implications for particle identification”. In: *Eur. Phys. J. C* 83.11 (2023), p. 1094. DOI: 10.1140/epjc/s10052-023-12278-0. arXiv: 2311.16288 [hep-ex].

[216] Lindsey J. Bignell et al. “Characterization and Modeling of a Water-based Liquid Scintillator”. In: *JINST* 10.12 (2015), P12009. DOI: 10.1088/1748-0221/10/12/P12009. arXiv: 1508.07029 [physics.ins-det].

[217] E. J. Callaghan et al. “Measurement of proton light yield of water-based liquid scintillator”. In: *Eur. Phys. J. C* 83.2 (2023), p. 134. DOI: 10.1140/epjc/s10052-023-11242-2. arXiv: 2210.03876 [physics.ins-det].

[218] Mohan Li et al. “Separation of Scintillation and Cherenkov Lights in Linear Alkyl Benzene”. In: *Nucl. Instrum. Meth. A* 830 (2016), pp. 303–308. DOI: 10.1016/j.nima.2016.05.132. arXiv: 1511.09339 [physics.ins-det].

[219] Julieta Gruszko et al. “Detecting Cherenkov light from 1–2 MeV electrons in linear alkylbenzene”. In: *JINST* 14.02 (2019), P02005. DOI: 10.1088/1748-0221/14/02/P02005. arXiv: 1811.11144 [physics.ins-det].

[220] Ziyi Guo et al. “Slow Liquid Scintillator Candidates for MeV-scale Neutrino Experiments”. In: *Astropart. Phys.* 109 (2019), pp. 33–40. DOI: 10.1016/j.astropartphys.2019.02.001. arXiv: 1708.07781 [physics.ins-det].

[221] Jack Dunger, Edward J. Leming, and Steven D. Biller. “Slow-fluor scintillator for low energy solar neutrinos and neutrinoless double beta decay”. In: *Phys. Rev. D* 105.9 (2022), p. 092006. DOI: 10.1103/PhysRevD.105.092006. arXiv: 2203.01147 [physics.ins-det].

[222] Steven D. Biller, Edward J. Leming, and Josephine L. Paton. “Slow fluors for effective separation of Cherenkov light in liquid scintillators”. In: *Nucl. Instrum. Meth. A* 972 (2020), p. 164106. ISSN: 0168-9002. DOI: 10.1016/j.nima.2020.164106.

[223] Hans Th. J. Steiger et al. “Development of a Bi-solvent Liquid Scintillator with Slow Light Emission”. In: (May 2024). arXiv: 2405.01100 [physics.ins-det].

[224] W. C. Haxton. “Salty water Cherenkov detectors for solar neutrinos”. In: *Phys. Rev. Lett.* 76 (1996). [Erratum: Phys.Rev.Lett. 77, 1662 (1996)], pp. 1562–1565. DOI: 10.1103/PhysRevLett.76.1562. arXiv: nucl-th/9511029.

[225] Christian Grieb. “Low energy neutrinos, neutrino luminosity of the Sun & LENS”. In: *Nucl. Phys. B Proc. Suppl.* 168 (2007). Ed. by Paolo Bernardini, Gianluigi Fogli, and Eligio Lisi, pp. 122–124. DOI: 10.1016/j.nuclphysbps.2007.02.017.

[226] Christian Buck and Minfang Yeh. "Metal-loaded organic scintillators for neutrino physics". In: *Journal of Physics G: Nuclear and Particle Physics* 43.9 (Aug. 2016), p. 093001. ISSN: 1361-6471. DOI: 10.1088/0954-3899/43/9/093001. URL: http://dx.doi.org/10.1088/0954-3899/43/9/093001.

[227] J. Ashenfelter et al. "Lithium-loaded Liquid Scintillator Production for the PROSPECT experiment". In: *JINST* 14.03 (2019), P03026. DOI: 10.1088/1748-0221/14/03/P03026. arXiv: 1901.05569 [physics.ins-det].

[228] J. R. Alonso et al. "Advanced Scintillator Detector Concept (ASDC): A Concept Paper on the Physics Potential of Water-Based Liquid Scintillator". In: (Sept. 2014). arXiv: 1409.5864 [physics.ins-det].

[229] Wenhui Shao et al. "The Potential to Probe Solar Neutrino Physics with LiCl Water Solution". In: (Mar. 2022). arXiv: 2203.01860 [hep-ex].

[230] Ayse Bat et al. "Low energy neutrino detection with a compact water-based liquid scintillator detector". In: *Eur. Phys. J. C* 82.8 (2022), p. 734. DOI: 10.1140/epjc/s10052-022-10658-6. arXiv: 2112.03418 [physics.ins-det].

[231] M. Askins et al. "The Physics and Nuclear Nonproliferation Goals of WATCHMAN: A WAter CHerenkov Monitor for ANtineutrinos". In: (Feb. 2015). arXiv: 1502.01132 [physics.ins-det].

[232] A Bernstein. *AIT-WATCHMAN Conceptual Design Review Report*. Tech. rep. Lawrence Livermore National Lab.(LLNL), Livermore, CA (United States), 2019. DOI: 10.2172/1544490.

[233] C. Aberle et al. "Optical Properties of Quantum-Dot-Doped Liquid Scintillators". In: *JINST* 8 (2013), P10015. DOI: 10.1088/1748-0221/8/10/P10015. arXiv: 1307.4742 [physics.ins-det].

[234] L. Winslow and R. Simpson. "Characterizing Quantum-Dot-Doped Liquid Scintillator for Applications to Neutrino Detectors". In: *JINST* 7 (2012), P07010. DOI: 10.1088/1748-0221/7/07/P07010. arXiv: 1202.4733 [physics.ins-det].

[235] Eleanor Graham et al. "Light Yield of Perovskite Nanocrystal-Doped Liquid Scintillator". In: (July 2019). DOI: 10.1088/1748-0221/14/11/P11024. arXiv: 1908.03564 [physics.ins-det].

[236] M. Zhao et al. "Water-based Quantum Dots Liquid Scintillator for Particle Physics". In: (Mar. 2024). arXiv: 2403.10122 [physics.ins-det].

[237] J. Brack et al. "Characterization of the Hamamatsu R11780 12 inch Photomultiplier Tube". In: *Nucl. Instrum. Meth. A* 712 (Oct. 2012). DOI: 10.1016/j.nima.2013.02.022.

[238] N. Barros et al. "Characterization of the ETEL D784UKFLB 11 in. photomultiplier tube". In: *Nucl. Instrum. Meth. A* 852 (2017), pp. 15–19. DOI: 10.1016/j.nima.2017.01.067.

[239] Tanner Kaptanoglu. “Characterization of the Hamamatsu 8” R5912-MOD Photomultiplier Tube”. In: *Nucl. Instrum. Meth. A* 889 (2018), pp. 69–77. DOI: 10.1016/j.nima.2018.01.086. arXiv: 1710.03334 [physics.ins-det].

[240] B. W. Adams et al. “A Brief Technical History of the Large-Area Picosecond Photodetector (LAPPD) Collaboration”. 2016. arXiv: 1603.01843 [physics.ins-det].

[241] A.V. Lyashenko et al. “Performance of Large Area Picosecond Photo-Detectors (LAPPDTM)”. In: *Nucl. Instrum. Meth. A* 958 (Apr. 2020), p. 162834. DOI: 10.1016/j.nima.2019.162834.

[242] B. W. Adams et al. “Timing characteristics of Large Area Picosecond Photodetectors”. In: *Nucl. Instrum. Meth. A* 795 (2015), pp. 1–11. DOI: 10.1016/j.nima.2015.05.027.

[243] T. Kaptanoglu et al. “Cherenkov and scintillation separation in water-based liquid scintillator using an LAPPD^{TM}”. In: *Eur. Phys. J. C* 82.2 (2022), p. 169. DOI: 10.1140/epjc/s10052-022-10087-5. arXiv: 2110.13222 [physics.ins-det].

[244] Marc Breisch. “First results from the LAPPDs in ANNIE”. In: *PoS* TAUP2023 (2024), p. 251. DOI: 10.22323/1.441.0251.

[245] Lin Chen et al. “Large area MCP-PMT design with good time performance”. In: *Opt. Express* 30.14 (July 2022), pp. 25918–25925. DOI: 10.1364/OE.464209. URL: https://opg.optica.org/oe/abstract.cfm?URI=oe-30-14-25918.

[246] Tanner Kaptanoglu, Meng Luo, and Josh Klein. “Cherenkov and Scintillation Light Separation Using Wavelength in LAB Based Liquid Scintillator”. In: *JINST* 14.05 (2019), T05001. DOI: 10.1088/1748-0221/14/05/T05001. arXiv: 1811.11587 [physics.ins-det].

[247] Tanner Kaptanoglu et al. “Spectral Photon Sorting For Large-Scale Cherenkov and Scintillation Detectors”. In: *Phys. Rev. D* 101.7 (2020), p. 072002. DOI: 10.1103/PhysRevD.101.072002. arXiv: 1912.10333 [physics.ins-det].

[248] Björn S. Wonsak et al. “Topological track reconstruction in unsegmented, large-volume liquid scintillator detectors”. In: *JINST* 13.07 (2018), P07005. DOI: 10.1088/1748-0221/13/07/P07005. arXiv: 1803.08802 [physics.ins-det].

[249] C. Aberle et al. “Measuring Directionality in Double-Beta Decay and Neutrino Interactions with Kiloton-Scale Scintillation Detectors”. In: *JINST* 9 (2014), P06012. DOI: 10.1088/1748-0221/9/06/P06012. arXiv: 1307.5813 [physics.ins-det].

[250] Andrey Elagin et al. “Separating Double-Beta Decay Events from Solar Neutrino Interactions in a Kiloton-Scale Liquid Scintillator Detector By Fast Timing”. In: *Nucl. Instrum. Meth. A* 849 (2017), pp. 102–111. DOI: 10.1016/j.nima.2016.12.033. arXiv: 1609.09865 [physics.ins-det].

[251] Runyu Jiang and Andrey Elagin. “Space-Time Discriminant to Separate Double-Beta Decay from ^{8}B Solar Neutrinos in Liquid Scintillator”. In: (Feb. 2019). arXiv: 1902.06912 [physics.ins-det].

[252] B. J. Land et al. "MeV-scale performance of water-based and pure liquid scintillator detectors". In: *Phys. Rev. D* 103.5 (2021), p. 052004. DOI: `10.1103/PhysRevD.103.052004`. arXiv: `2007.14999 [physics.ins-det]`.

[253] Philipp Eller et al. "A flexible event reconstruction based on machine learning and likelihood principles". In: *Nucl. Instrum. Meth. A* 1048 (2023), p. 168011. DOI: `10.1016/j.nima.2023.168011`. arXiv: `2208.10166 [hep-ex]`.

[254] Ayse Bat. "Using machine learning to separate Cherenkov and scintillation light in hybrid neutrino detector". In: *JINST* 19.04 (2024), P04027. DOI: `10.1088/1748-0221/19/04/P04027`. arXiv: `2403.05184 [physics.ins-det]`.

[255] Emrah Tiras et al. "Comprehensive Machine Learning Model Comparison for Cherenkov and Scintillation Light Separation due to Particle Interactions". In: (June 2024). arXiv: `2406.09191 [hep-ex]`.

[256] Austin Mullen et al. "Improvement in light collection of a photomultiplier tube using a wavelength-shifting plate". In: *Nucl. Instrum. Meth. A* 1040 (2022), p. 167207. DOI: `10.1016/j.nima.2022.167207`. arXiv: `2204.05534 [physics.ins-det]`.

[257] M. Ehlert et al. "Proof-of-principle measurements with a liquid-scintillator detector using wavelength-shifting optical modules". In: *JINST* 14.03 (2019), P03021. DOI: `10.1088/1748-0221/14/03/P03021`. arXiv: `1812.06460 [physics.ins-det]`.

[258] Iwan Morton-Blake and Steven D. Biller. "Alternative design for large scale liquid scintillator detectors". In: *Phys. Rev. D* 105.7 (2022), p. 072003. DOI: `10.1103/PhysRevD.105.072003`. arXiv: `2201.06498 [physics.ins-det]`.

[259] Adam Bernstein et al. "A call to Arms Control: Synergies between Nonproliferation Applications of Neutrino Detectors and Large-Scale Fundamental Neutrino Physics Experiments". In: *Snowmass 2021*. Feb. 2022. arXiv: `2203.00042 [physics.ins-det]`.

[260] Liz Kneale. *BUTTON: a technology testbed for future (anti)neutrino detection*. `https://indico.cern.ch/event/1261135/contributions/5333594/attachments/2622769/4535249/BUTTON_technology_testbed_IoP_Kneale.pdf`. [Accessed May 3, 2023]. 2023.

[261] A. R. Back et al. "Accelerator Neutrino Neutron Interaction Experiment (ANNIE): Preliminary Results and Physics Phase Proposal". In: *arXiv:1707.08222 [physics.ins-det]* (2017). arXiv: `1707.08222 [physics.ins-det]`.

[262] A. R. Back et al. "Measurement of Beam-Correlated Background Neutrons from the Fermilab Booster Neutrino Beam in ANNIE Phase-I". In: *JINST* 15.03 (2020), P03011. DOI: `10.1088/1748-0221/15/03/P03011`. arXiv: `1912.03186`.

[263] Emrah Tiras. "Detector R \& D for ANNIE and Future Neutrino Experiments". In: *Meeting of the Division of Particles and Fields of the American Physical Society*. Oct. 2019. arXiv: `1910.08715 [physics.ins-det]`.

[264] M. Ascencio-Sosa et al. "Deployment of Water-based Liquid Scintillator in the Accelerator Neutrino Neutron Interaction Experiment". In: *arXiv:2312.09335* (Dec. 2023).

[265] M. Askins et al. "Letter of interest the rat (-pac) simulation and analysis code base". In: *Snowmass2021* (2020).

[266] *RATPAC-TWO*. https://github.com/rat-pac/ratpac-two.

[267] Michael Wurm et al. "The Physics Potential of the LENA Detector". In: *Acta Phys. Polon. B* 41 (2010). Ed. by Agnieszka Zalewska, pp. 1749–1764. arXiv: 1004.3474 [physics.ins-det].

[268] Michael Wurm et al. "The next-generation liquid-scintillator neutrino observatory LENA". In: *Astropart. Phys.* 35 (2012), pp. 685–732. DOI: 10.1016/j.astropartphys.2012.02.011. arXiv: 1104.5620 [astro-ph.IM].

[269] M. Askins et al. "Theia: Summary of physics program. Snowmass White Paper Submission". In: *Snowmass 2021*. Feb. 2022. arXiv: 2202.12839 [hep-ex].

[270] Stephane Zsoldos et al. "Geo- and reactor antineutrino sensitivity at THEIA". In: *Eur. Phys. J. C* 82.12 (2022), p. 1151. DOI: 10.1140/epjc/s10052-022-11106-1. arXiv: 2204.12278 [hep-ex].

[271] Julia Sawatzki, Michael Wurm, and Daniel Kresse. "Detecting the Diffuse Supernova Neutrino Background in the future Water-based Liquid Scintillator Detector Theia". In: *Phys. Rev. D* 103.2 (2021), p. 023021. DOI: 10.1103/PhysRevD.103.023021. arXiv: 2007.14705 [physics.ins-det].

[272] João Carlos R. Reis et al. "Refractive Index of Liquid Mixtures: Theory and Experiment". In: *ChemPhysChem* 11.17 (2010), pp. 3722–3733. DOI: 10.1002/cphc.201000566.

[273] H. Wan Chan Tseung and N. Tolich. "Ellipsometric measurements of the refractive indices of linear alkylbenzene and EJ-301 scintillators from 210 to 1000 nm". In: *Phys. Scripta* 03 (2011), p. 035701. DOI: 10.1088/0031-8949/84/03/035701. arXiv: 1105.2101 [physics.optics].

[274] Robin M. Pope and Edward S. Fry. "Absorption spectrum (380–700 nm) of pure water. II. Integrating cavity measurements". In: *Appl. Opt.* 36.33 (Nov. 1997), pp. 8710–8723. DOI: 10.1364/AO.36.008710. URL: https://opg.optica.org/ao/abstract.cfm?URI=ao-36-33-8710.

[275] Raymond C. Smith and Karen S. Baker. "Optical properties of the clearest natural waters (200–800 nm)". In: *Appl. Opt.* 20.2 (Jan. 1981), pp. 177–184. DOI: 10.1364/AO.20.000177. URL: https://opg.optica.org/ao/abstract.cfm?URI=ao-20-2-177.

[276] Stan Seibert et al. *RAT User Guide*. https://rat.readthedocs.io/en/latest/. [Accessed June 16, 2022]. 2014.

[277] Hamamatsu Photonics K.K. *Photomultiplier Tubes and Assemblies*. https://www.hamamatsu.com/resources/pdf/etd/High_energy_PMT_TPMZ0003E.pdf. 2017.

[278] R. Bonventre and G. D. Orebi Gann. "Sensitivity of a low threshold directional detector to CNO-cycle solar neutrinos". In: *Eur. Phys. J. C* 78.6 (2018), p. 435. DOI: 10.1140/epjc/s10052-018-5925-7. arXiv: 1803.07109 [physics.ins-det].

[279] B. Aharmim et al. "Determination of the ν_e and total ^{8}B solar neutrino fluxes with the Sudbury neutrino observatory phase I data set". In: *Phys. Rev. C* 75 (2007), p. 045502. DOI: 10.1103/PhysRevC.75.045502. arXiv: nucl-ex/0610020.

[280] O.A. Ponkratenko, V.I. Tretyak, and Yu.G. Zdesenko. "The Event generator DECAY4 for simulation of double beta processes and decay of radioactive nuclei". In: *Phys. Atom. Nucl.* 63 (2000), pp. 1282–1287. DOI: 10.1134/1.855784. arXiv: nucl-ex/0104018.

[281] John N. Bahcall, Marc Kamionkowski, and Alberto Sirlin. "Solar neutrinos: Radiative corrections in neutrino - electron scattering experiments". In: *Phys. Rev. D* 51 (1995), pp. 6146–6158. DOI: 10.1103/PhysRevD.51.6146. arXiv: astro-ph/9502003.

[282] John N. Bahcall, Aldo M. Serenelli, and Sarbani Basu. "New solar opacities, abundances, helioseismology, and neutrino fluxes". In: *Astrophys. J. Lett.* 621 (2005), pp. L85–L88. DOI: 10.1086/428929.

[283] R. Bonventre et al. "Non-Standard Models, Solar Neutrinos, and Large \theta_{13}". In: *Phys. Rev. D* 88.5 (2013), p. 053010. DOI: 10.1103/PhysRevD.88.053010. arXiv: 1305.5835 [hep-ph].

[284] J. Barea, J. Kotila, and F. Iachello. "Nuclear matrix elements for double-β decay". In: *Phys. Rev. C* 87.1 (2013), p. 014315. DOI: 10.1103/PhysRevC.87.014315.

[285] Tomas R. Rodriguez and G. Martinez-Pinedo. "Energy density functional study of nuclear matrix elements for neutrinoless $\beta\beta$ decay". In: *Phys. Rev. Lett.* 105 (2010), p. 252503. DOI: 10.1103/PhysRevLett.105.252503.

[286] S. Abe et al. "Search for the Majorana Nature of Neutrinos in the Inverted Mass Ordering Region with KamLAND-Zen". In: *Phys. Rev. Lett.* 130.5 (2023), p. 051801. DOI: 10.1103/PhysRevLett.130.051801. arXiv: 2203.02139 [hep-ex].

[287] S. Abe et al. "Search for Majorana Neutrinos with the Complete KamLAND-Zen Dataset". In: (June 2024). arXiv: 2406.11438 [hep-ex].

[288] Helen Mary O'Keeffe. "Low Energy Background in the NCD Phase of the Sudbury Neutrino Observatory". PhD thesis. Oxford U., 2008.

[289] C. Arpesella et al. "Direct Measurement of the Be-7 Solar Neutrino Flux with 192 Days of Borexino Data". In: *Phys. Rev. Lett.* 101 (2008), p. 091302. DOI: 10.1103/PhysRevLett.101.091302. arXiv: 0805.3843 [astro-ph].

[290] M. Balata et al. "The water purification system for the low background counting test facility of the Borexino experiment at Gran Sasso". In: *Nucl. Instrum. Meth. A* 370 (1996), pp. 605–608. DOI: 10.1016/0168-9002(95)00862-4.

[291] G. Alimonti et al. “The liquid handling systems for the Borexino solar neutrino detector”. In: *Nucl. Instrum. Meth. A* 609 (2009), pp. 58–78. DOI: 10.1016/j.nima.2009.07.028.

[292] N. Abgrall et al. “Muon Flux Measurements at the Davis Campus of the Sanford Underground Research Facility with the Majorana Demonstrator Veto System”. In: *Astropart. Phys.* 93 (2017), pp. 70–75. DOI: 10.1016/j.astropartphys.2017.01.013. arXiv: 1602.07742 [nucl-ex].

[293] G. Bellini et al. “Cosmic-muon flux and annual modulation in Borexino at 3800 m water-equivalent depth”. In: *JCAP* 05 (2012), p. 015. DOI: 10.1088/1475-7516/2012/05/015. arXiv: 1202.6403 [hep-ex].

[294] M. Agostini et al. “Identification of the cosmogenic ^{11}C background in large volumes of liquid scintillators with Borexino”. In: *Eur. Phys. J. C* 81.12 (2021), p. 1075. DOI: 10.1140/epjc/s10052-021-09799-x. arXiv: 2106.10973 [physics.ins-det].

[295] M. Agostini et al. “Sensitivity to neutrinos from the solar CNO cycle in Borexino”. In: (May 2020). arXiv: 2005.12829 [hep-ex].

[296] Jie Zhao et al. “^{13}C(α,n)^{16}O background in a liquid scintillator based neutrino experiment”. In: *Chin. Phys. C* 38.11 (2014), p. 116201. DOI: 10.1088/1674-1137/38/11/116201. arXiv: 1312.6347 [physics.ins-det].

[297] Gioacchino Ranucci et al. “Scintillation decay time and pulse shape discrimination of binary organic liquid scintillators for the Borexino detector”. In: *Nucl. Instrum. Meth. A* 350 (1994), pp. 338–350. DOI: 10.1016/0168-9002(94)91183-5.

[298] D. Basilico et al. “Novel techniques for alpha/beta pulse shape discrimination in Borexino”. In: (Oct. 2023). arXiv: 2310.11826 [hep-ex].

[299] H. Wan Chan Tseung, J. Kaspar, and N. Tolich. “Measurement of the dependence of the light yields of linear alkylbenzene-based and EJ-301 scintillators on electron energy”. In: *Nucl. Instrum. Meth. A* 654 (2011), pp. 318–323. DOI: 10.1016/j.nima.2011.06.095. arXiv: 1105.2100 [nucl-ex].

[300] Paolo Lombardi et al. “Decay time and pulse shape discrimination of liquid scintillators based on novel solvents”. In: *Nuclear Instruments and Methods in Physics Research Section A: Accelerators, Spectrometers, Detectors and Associated Equipment* 701 (2013), pp. 133–144. ISSN: 0168-9002. DOI: https://doi.org/10.1016/j.nima.2012.10.061. URL: https://www.sciencedirect.com/science/article/pii/S0168900212012077.

[301] Elena Aprile et al. “First Measurement of Solar ^{8}B Neutrinos via Coherent Elastic Neutrino-Nucleus Scattering with XENONnT”. In: (Aug. 2024). arXiv: 2408.02877 [nucl-ex].

[302] Zihao Bo et al. “First Measurement of Solar ^{8}B Neutrino Flux through Coherent Elastic Neutrino-Nucleus Scattering in PandaX-4T”. In: (July 2024). arXiv: 2407.10892 [hep-ex].

Appendix A

Survival Probability

Table A.1: The survival probability P_{ee} as a function of energy in MeV for ^{8}B solar neutrinos. This table was generated with `PSelmaa` using the Barcelona 16 Standard Solar Model evaluation with GS98 metallicity and PDG20 mixing parameters: $\Delta m^2_{21} = 7.53 \times 10^{-5}$, $\sin^2\theta_{12} = 0.307$ and $\sin^2\theta_{13} = 0.0220$. These values are interpolated to provide appropriate weighting for solar neutrino events when building the PDFs for the ^{8}B analysis.

E_ν (MeV)	P_{ee}
0.100000	0.555169
0.200000	0.552170
0.300000	0.549109
0.400000	0.545987
0.500000	0.542805
0.600000	0.539566
0.700000	0.536270
0.800000	0.532919
0.900000	0.529517
1.000000	0.526064
1.100000	0.522565
1.200000	0.519021
1.300000	0.515436
1.400000	0.511814
1.500000	0.508157
1.600000	0.504469
1.700000	0.500755
1.800000	0.497017
1.900000	0.493262
2.000000	0.489492
2.100000	0.485712

2.200000	0.481926
2.300000	0.478139
2.400000	0.474356
2.500000	0.470579
2.600000	0.466815
2.700000	0.463067
2.800000	0.459338
2.900000	0.455634
3.000000	0.451958
3.100000	0.448314
3.200000	0.444706
3.300000	0.441135
3.400000	0.437607
3.500000	0.434123
3.600000	0.430687
3.700000	0.427300
3.800000	0.423965
3.900000	0.420685
4.000000	0.417460
4.100000	0.414293
4.200000	0.411184
4.300000	0.408135
4.400000	0.405147
4.500000	0.402221
4.600000	0.399356
4.700000	0.396554
4.800000	0.393814
4.900000	0.391136
5.000000	0.388521
5.100000	0.385968
5.200000	0.383477
5.300000	0.381047
5.400000	0.378678
5.500000	0.376368
5.600000	0.374118
5.700000	0.371926
5.800000	0.369791
5.900000	0.367713
6.000000	0.365691
6.100000	0.363722
6.200000	0.361807
6.300000	0.359944
6.400000	0.358132

6.500000	0.356369
6.600000	0.354656
6.700000	0.352989
6.800000	0.351370
6.900000	0.349795
7.000000	0.348264
7.100000	0.346776
7.200000	0.345329
7.300000	0.343923
7.400000	0.342557
7.500000	0.341229
7.600000	0.339938
7.700000	0.338683
7.800000	0.337463
7.900000	0.336277
8.000000	0.335124
8.100000	0.334003
8.200000	0.332913
8.300000	0.331854
8.400000	0.330824
8.500000	0.329822
8.600000	0.328847
8.700000	0.327899
8.800000	0.326977
8.900000	0.326080
9.000000	0.325208
9.100000	0.324359
9.200000	0.323532
9.300000	0.322728
9.400000	0.321945
9.500000	0.321183
9.600000	0.320441
9.700000	0.319719
9.800000	0.319015
9.900000	0.318330
10.000000	0.317662
10.100000	0.317012
10.200000	0.316378
10.300000	0.315760
10.400000	0.315159
10.500000	0.314572
10.600000	0.314000
10.700000	0.313442

10.800000	0.312898
10.900000	0.312368
11.000000	0.311850
11.100000	0.311346
11.200000	0.310853
11.300000	0.310372
11.400000	0.309903
11.500000	0.309445
11.600000	0.308998
11.700000	0.308562
11.800000	0.308136
11.900000	0.307719
12.000000	0.307312
12.100000	0.306915
12.200000	0.306527
12.300000	0.306147
12.400000	0.305777
12.500000	0.305414
12.600000	0.305060
12.700000	0.304713
12.800000	0.304374
12.900000	0.304043
13.000000	0.303718
13.100000	0.303401
13.200000	0.303091
13.300000	0.302787
13.400000	0.302490
13.500000	0.302199
13.600000	0.301914
13.700000	0.301635
13.800000	0.301362
13.900000	0.301094
14.000000	0.300832
14.100000	0.300576
14.200000	0.300324
14.300000	0.300078
14.400000	0.299836
14.500000	0.299599
14.600000	0.299367
14.700000	0.299140
14.800000	0.298917
14.900000	0.298698
15.000000	0.298483

15.100000	0.298273
15.200000	0.298066
15.300000	0.297864
15.400000	0.297665
15.500000	0.297470

Appendix B

Partial Fill Analysis Files

Table B.1: Data files used in the ^{8}B partial fill analysis organized by run, subruns of that run, processing pass and processing module.

Run	Subruns	Pass	Module
257693	0-11	0	Analysis40R
257694	0-11	0	Analysis40R
257695	0-11	0	Analysis40R
257697	0-11	0	Analysis40R
257698	0-11	0	Analysis40R
257699	0-11	0	Analysis40R
257700	0-11	0	Analysis40R
257701	0-11	0	Analysis40R
257702	0-11	0	Analysis40R
257703	0-11	0	Analysis40R
257704	0-11	0	Analysis40R
257705	0-11	0	Analysis40R
257706	0-11	0	Analysis40R
257707	0-11	0	Analysis40R
257709	0-11	0	Analysis40R
257710	0-8	0	Analysis40R
257713	0-11	0	Analysis40R
257714	0-11	0	Analysis40R
257715	0-11	0	Analysis40R
257716	0-11	0	Analysis40R
257717	0-11	0	Analysis40R
257718	0-11	0	Analysis40R
257719	0-11	0	Analysis40R
257720	0-11	0	Analysis40R
257721	0-11	0	Analysis40R
257722	0-11	0	Analysis40R
257723	0-11	0	Analysis40R
257724	0-11	0	Analysis40R
257725	0-11	0	Analysis40R
257726	0-11	0	Analysis40R
257727	0-11	0	Analysis40R
257728	0-10	0	Analysis40R
257734	0-11	0	Analysis40R
257735	0-11	0	Analysis40R
257736	0-11	0	Analysis40R
257737	0-11	0	Analysis40R
257738	0-11	0	Analysis40R
257739	0-11	0	Analysis40R
257740	0-11	0	Analysis40R
257741	0-11	0	Analysis40R
257742	0-11	0	Analysis40R
257743	0-11	0	Analysis40R
257744	0-11	0	Analysis40R
257745	0-11	0	Analysis40R
257746	0-11	0	Analysis40R
257747	0-11	0	Analysis40R
257748	0-11	0	Analysis40R
257749	0-11	0	Analysis40R
257750	0-11	0	Analysis40R
257751	0-11	0	Analysis40R
257752	0-11	0	Analysis40R
257753	0-11	0	Analysis40R
257756	0-11	0	Analysis40R
257757	0-11	0	Analysis40R
257758	0-11	0	Analysis40R
257759	0-11	0	Analysis40R
257760	0-11	0	Analysis40R
257761	0-11	0	Analysis40R
257762	0-11	0	Analysis40R
257763	0-11	0	Analysis40R
257764	0-11	0	Analysis40R
257765	0-11	0	Analysis40R
257766	0-11	0	Analysis40R
257767	0-11	0	Analysis40R
257768	0-11	0	Analysis40R
257769	0-11	0	Analysis40R
257770	0-11	0	Analysis40R
257771	0-11	0	Analysis40R
257772	0-11	0	Analysis40R
257773	0-11	0	Analysis40R
257774	0-11	0	Analysis40R
257775	0-11	0	Analysis40R
257776	0-11	0	Analysis40R
257777	0-11	0	Analysis40R
257778	0-11	0	Analysis40R
257779	0-11	0	Analysis40R
257780	0-11	0	Analysis40R
257781	0-11	0	Analysis40R
257782	0-11	0	Analysis40R
257783	0-11	0	Analysis40R
257784	0-11	0	Analysis40R
257785	0-11	0	Analysis40R
257786	0-11	0	Analysis40R
257787	0-11	0	Analysis40R
257788	0-11	0	Analysis40R
257789	0-11	0	Analysis40R
257790	0-11	0	Analysis40R
257791	0-11	0	Analysis40R
257792	0-11	0	Analysis40R
257793	0-11	0	Analysis40R
257794	0-11	0	Analysis40R
257795	0-11	0	Analysis40R
257796	0-11	0	Analysis40R
257797	0-11	0	Analysis40R
257798	0-11	0	Analysis40R
257799	0-11	0	Analysis40R
257800	0-11	0	Analysis40R
257803	0-11	0	Analysis40R
257804	0-11	0	Analysis40R
257805	0-11	0	Analysis40R
257806	0-11	0	Analysis40R
257807	0-11	0	Analysis40R
257808	0-11	0	Analysis40R
257809	0-11	0	Analysis40R
257810	0-11	0	Analysis40R
257811	0-11	0	Analysis40R
257812	0-11	0	Analysis40R
257813	0-11	0	Analysis40R
257814	0-11	0	Analysis40R
257815	0-11	0	Analysis40R
257816	0-11	0	Analysis40R
257817	0-11	0	Analysis40R
257818	0-11	0	Analysis40R
257819	0-11	0	Analysis40R
257820	0-11	0	Analysis40R
257821	0-11	0	Analysis40R
257822	0-11	0	Analysis40R
257824	0-11	0	Analysis40R
257825	0-11	0	Analysis40R
257826	0-11	0	Analysis40R
257827	0-11	0	Analysis40R
257828	0-11	0	Analysis40R

257829	0-11	0	Analysis40R
257830	0-11	0	Analysis40R
257831	0-11	0	Analysis40R
257832	0-11	0	Analysis40R
257833	0-11	0	Analysis40R
257834	0-11	0	Analysis40R
257835	0-11	0	Analysis40R
257836	0-11	0	Analysis40R
257837	0-11	0	Analysis40R
257838	0-11	0	Analysis40R
257839	0-11	0	Analysis40R
257840	0-11	0	Analysis40R
257841	0-11	0	Analysis40R
257842	0-11	0	Analysis40R
257843	0-11	0	Analysis40R
257844	0-11	0	Analysis40R
257845	0-11	0	Analysis40R
257846	0-11	0	Analysis40R
257847	0-11	0	Analysis40R
257848	0-11	0	Analysis40R
257849	0-11	0	Analysis40R
257850	0-11	0	Analysis40R
257851	0-11	0	Analysis40R
257852	0-11	0	Analysis40R
257853	0-11	0	Analysis40R
257854	0-11	0	Analysis40R
257855	0-11	0	Analysis40R
257856	0-11	0	Analysis40R
257857	0-11	0	Analysis40R
257858	0-11	0	Analysis40R
257859	0-11	0	Analysis40R
257860	0-11	0	Analysis40R
257861	0-11	0	Analysis40R
257862	0-11	0	Analysis40R
257863	0-11	0	Analysis40R
257864	0-11	0	Analysis40R
257865	0-11	0	Analysis40R
257866	0-11	0	Analysis40R
257867	0-11	0	Analysis40R
257868	0-11	0	Analysis40R
257870	0-11	0	Analysis40R
257871	0-11	0	Analysis40R
257872	0-11	0	Analysis40R
257873	0-11	0	Analysis40R
257874	0-11	0	Analysis40R
257875	0-11	0	Analysis40R
257876	0-11	0	Analysis40R
257877	0-11	0	Analysis40R
257878	0-11	0	Analysis40R
257879	0-11	0	Analysis40R
257880	0-11	0	Analysis40R
257887	0-11	0	Analysis40R
257888	0-11	0	Analysis40R
257889	0-11	0	Analysis40R
257891	0-11	0	Analysis40R
257892	0-11	0	Analysis40R
257893	0-11	0	Analysis40R
257894	0-11	0	Analysis40R
257895	0-11	0	Analysis40R
257896	0-11	0	Analysis40R
257899	0-11	0	Analysis40R
257900	0-11	0	Analysis40R
257901	0-11	0	Analysis40R
257902	0-11	0	Analysis40R
257903	0-11	0	Analysis40R
257904	0-11	0	Analysis40R
257905	0-11	0	Analysis40R
257906	0-11	0	Analysis40R
257907	0-11	0	Analysis40R
257908	0-11	0	Analysis40R
257910	0-11	0	Analysis40R
257911	0-11	0	Analysis40R
257912	0-11	0	Analysis40R
257913	0-11	0	Analysis40R
257914	0-11	0	Analysis40R
257917	0-11	0	Analysis40R
257918	0-11	0	Analysis40R
257919	0-11	0	Analysis40R
257920	0-11	0	Analysis40R
257921	0-11	0	Analysis40R
257922	0-11	0	Analysis40R
257923	0-11	0	Analysis40R
257924	0-11	0	Analysis40R
257925	0-9	0	Analysis40R
257932	0-7	0	Analysis40R
257934	0-11	0	Analysis40R
257935	0-11	0	Analysis40R
257938	0-11	0	Analysis40R
257939	0-11	0	Analysis40R
257940	0-11	0	Analysis40R
257941	0-11	0	Analysis40R
257942	0-11	0	Analysis40R
257943	0-11	0	Analysis40R
257944	0-11	0	Analysis40R
257945	0-11	0	Analysis40R
257946	0-11	0	Analysis40R
257947	0-11	0	Analysis40R
257954	0-11	0	Analysis40R
257955	0-11	0	Analysis40R
257958	0-11	0	Analysis40R
257959	0-11	0	Analysis40R
257960	0-11	0	Analysis40R
257961	0-11	0	Analysis40R
257962	0-11	0	Analysis40R
257963	0-11	0	Analysis40R
257964	0-11	0	Analysis40R
257965	0-11	0	Analysis40R
257966	0-11	0	Analysis40R
257967	0-11	0	Analysis40R
257968	0-11	0	Analysis40R
257969	0-11	0	Analysis40R
257970	0-11	0	Analysis40R
257971	0-11	0	Analysis40R
257972	0-11	0	Analysis40R
257973	0-11	0	Analysis40R
257974	0-11	0	Analysis40R
257975	0-11	0	Analysis40R
257976	0-11	0	Analysis40R
258002	0-11	0	Analysis40R
258003	0-11	0	Analysis40R
258004	0-11	0	Analysis40R
258005	0-11	0	Analysis40R
258006	0-11	0	Analysis40R
258007	0-11	0	Analysis40R
258008	0-11	0	Analysis40R
258009	0-11	0	Analysis40R
258011	0-11	0	Analysis40R
258012	0-11	0	Analysis40R
258013	0-11	0	Analysis40R
258014	0-11	0	Analysis40R

258015	0-11	0	Analysis40R
258018	0-11	0	Analysis40R
258021	0-11	0	Analysis40R
258023	0-11	0	Analysis40R
258024	0-11	0	Analysis40R
258025	0-11	0	Analysis40R
258026	0-11	0	Analysis40R
258027	0-11	0	Analysis40R
258028	0-11	0	Analysis40R
258029	0-11	0	Analysis40R
258030	0-11	0	Analysis40R
258031	0-11	0	Analysis40R
258032	0-11	0	Analysis40R
258033	0-11	0	Analysis40R
258034	0-11	0	Analysis40R
258035	0-11	0	Analysis40R
258036	0-11	0	Analysis40R
258037	0-11	0	Analysis40R
258038	0-11	0	Analysis40R
258039	0-11	0	Analysis40R
258040	0-11	0	Analysis40R
258041	0-11	0	Analysis40R
258042	0-11	0	Analysis40R
258043	0-11	0	Analysis40R
258044	0-11	0	Analysis40R
258045	0-11	0	Analysis40R
258046	0-11	0	Analysis40R
258047	0-11	0	Analysis40R
258048	0-11	0	Analysis40R
258049	0-11	0	Analysis40R
258050	0-11	0	Analysis40R
258051	0-11	0	Analysis40R
258052	0-11	0	Analysis40R
258053	0-11	0	Analysis40R
258054	0-11	0	Analysis40R
258055	0-11	0	Analysis40R
258056	0-11	0	Analysis40R
258057	0-11	0	Analysis40R
258058	0-11	0	Analysis40R
258059	0-11	0	Analysis40R
258060	0-11	0	Analysis40R
258061	0-11	0	Analysis40R
258062	0-11	0	Analysis40R
258063	0-11	0	Analysis40R
258064	0-11	0	Analysis40R
258065	0-11	0	Analysis40R
258066	0-11	0	Analysis40R
258067	0-11	0	Analysis40R
258068	0-11	0	Analysis40R
258069	0-11	0	Analysis40R
258070	0-11	0	Analysis40R
258071	0-11	0	Analysis40R
258072	0-11	0	Analysis40R
258073	0-11	0	Analysis40R
258074	0-11	0	Analysis40R
258075	0-11	0	Analysis40R
258076	0-11	0	Analysis40R
258077	0-11	0	Analysis40R
258078	0-11	0	Analysis40R
258079	0-11	0	Analysis40R
258080	0-11	0	Analysis40R
258081	0-11	0	Analysis40R
258082	0-11	0	Analysis40R
258083	0-11	0	Analysis40R
258084	0-11	0	Analysis40R
258085	0-11	0	Analysis40R
258086	0-11	0	Analysis40R
258089	0-11	0	Analysis40R
258090	0-11	0	Analysis40R
258091	0-11	0	Analysis40R
258092	0-11	0	Analysis40R
258093	0-11	0	Analysis40R
258094	0-11	0	Analysis40R
258095	0-11	0	Analysis40R
258096	0-11	0	Analysis40R
258097	0-11	0	Analysis40R
258098	0-11	0	Analysis40R
258099	0-11	0	Analysis40R
258100	0-11	0	Analysis40R
258101	0-11	0	Analysis40R
258102	0-11	0	Analysis40R
258103	0-11	0	Analysis40R
258104	0-11	0	Analysis40R
258105	0-11	0	Analysis40R
258106	0-11	0	Analysis40R
258108	0-11	0	Analysis40R
258109	0-11	0	Analysis40R
258110	0-11	0	Analysis40R
258111	0-11	0	Analysis40R
258112	0-11	0	Analysis40R
258113	0-11	0	Analysis40R
258114	0-11	0	Analysis40R
258115	0-11	0	Analysis40R
258116	0-11	0	Analysis40R
258117	0-11	0	Analysis40R
258118	0-11	0	Analysis40R
258119	0-11	0	Analysis40R
258120	0-11	0	Analysis40R
258122	0-7	0	Analysis40R
258133	0-11	0	Analysis40R
258134	0-11	0	Analysis40R
258135	0-11	0	Analysis40R
258136	0-11	0	Analysis40R
258137	0-11	0	Analysis40R
258140	0-7	0	Analysis40R
258141	0-11	0	Analysis40R
258142	0-11	0	Analysis40R
258143	0-11	0	Analysis40R
258144	0-11	0	Analysis40R
258145	0-11	0	Analysis40R
258151	0-5	0	Analysis40R
258154	0-11	0	Analysis40R
258155	0-11	0	Analysis40R
258156	0-14	0	Analysis40R
258158	0-13	0	Analysis40R
258160	0-11	0	Analysis40R
258161	0-11	0	Analysis40R
258162	0-11	0	Analysis40R
258163	0-11	0	Analysis40R
258164	0-11	0	Analysis40R
258165	0-11	0	Analysis40R
258166	0-11	0	Analysis40R
258167	0-11	0	Analysis40R
258168	0-11	0	Analysis40R
258169	0-11	0	Analysis40R
258170	0-11	0	Analysis40R
258171	0-11	0	Analysis40R
258172	0-11	0	Analysis40R
258173	0-11	0	Analysis40R
258174	0-11	0	Analysis40R

258177	0-11	0	Analysis40R
258178	0-11	0	Analysis40R
258181	0-11	0	Analysis40R
258182	0-11	0	Analysis40R
258183	0-11	0	Analysis40R
258184	0-11	0	Analysis40R
258342	0-11	0	Analysis40R
258343	0-11	0	Analysis40R
258344	0-11	0	Analysis40R
258345	0-11	0	Analysis40R
258346	0-11	0	Analysis40R
258347	0-5	0	Analysis40R
258349	0-11	0	Analysis40R
258350	0-11	0	Analysis40R
258351	0-11	0	Analysis40R
258352	0-11	0	Analysis40R
258353	0-11	0	Analysis40R
258354	0-14	0	Analysis40R
258355	0-17	0	Analysis40R
258357	0-11	0	Analysis40R
258358	0-12	0	Analysis40R
258359	0-11	0	Analysis40R
258360	0-11	0	Analysis40R
258361	0-11	0	Analysis40R
258362	0-11	0	Analysis40R
258371	0-11	0	Analysis40R
258372	0-11	0	Analysis40R
258373	0-11	0	Analysis40R
258374	0-11	0	Analysis40R
258375	0-11	0	Analysis40R
258376	0-11	0	Analysis40R
258377	0-11	0	Analysis40R
258378	0-11	0	Analysis40R
258379	0-11	0	Analysis40R
258380	0-11	0	Analysis40R
258381	0-11	0	Analysis40R
258382	0-11	0	Analysis40R
258383	0-11	0	Analysis40R
258384	0-11	0	Analysis40R
258385	0-11	0	Analysis40R
258386	0-11	0	Analysis40R
258387	0-11	0	Analysis40R
258388	0-11	0	Analysis40R
258389	0-11	0	Analysis40R
258390	0-11	0	Analysis40R
258391	0-11	0	Analysis40R
258392	0-11	0	Analysis40R
258393	0-11	0	Analysis40R
258394	0-11	0	Analysis40R
258395	0-11	0	Analysis40R
258396	0-15	0	Analysis40R
258397	0-11	0	Analysis40R
258398	0-11	0	Analysis40R
258399	0-11	0	Analysis40R
258411	0-11	0	Analysis40R
258412	0-11	0	Analysis40R
258413	0-11	0	Analysis40R
258414	0-11	0	Analysis40R
258415	0-11	0	Analysis40R
258416	0-11	0	Analysis40R
258417	0-11	0	Analysis40R
258418	0-11	0	Analysis40R
258419	0-11	0	Analysis40R
258420	0-11	0	Analysis40R
258421	0-11	0	Analysis40R
258422	0-11	0	Analysis40R
258423	0-11	0	Analysis40R
258424	0-11	0	Analysis40R
258425	0-11	0	Analysis40R
258426	0-11	0	Analysis40R
258427	0-11	0	Analysis40R
258428	0-11	0	Analysis40R
258429	0-11	0	Analysis40R
258430	0-11	0	Analysis40R
258431	0-11	0	Analysis40R
258432	0-11	0	Analysis40R
258433	0-11	0	Analysis40R
258434	0-11	0	Analysis40R
258435	0-11	0	Analysis40R
258436	0-11	0	Analysis40R
258437	0-11	0	Analysis40R
258438	0-11	0	Analysis40R
258439	0-11	0	Analysis40R
258440	0-11	0	Analysis40R
258441	0-11	0	Analysis40R
258442	0-11	0	Analysis40R
258443	0-11	0	Analysis40R
258449	0-11	0	Analysis40R
258450	0-11	0	Analysis40R
258451	0-11	0	Analysis40R
258452	0-11	0	Analysis40R
258453	0-11	0	Analysis40R
258454	0-11	0	Analysis40R
258455	0-11	0	Analysis40R
258456	0-11	0	Analysis40R
258457	0-11	0	Analysis40R
258458	0-6	0	Analysis40R
258472	0-11	0	Analysis40R
258480	0-11	0	Analysis40R
258482	0-11	0	Analysis40R
258483	0-11	0	Analysis40R
258484	0-11	0	Analysis40R
258485	0-11	0	Analysis40R
258486	0-11	0	Analysis40R
258488	0-11	0	Analysis40R
258489	0-11	0	Analysis40R
258490	0-11	0	Analysis40R
258491	0-11	0	Analysis40R
258492	0-11	0	Analysis40R
258493	0-11	0	Analysis40R
258494	0-11	0	Analysis40R
258495	0-11	0	Analysis40R
258496	0-11	0	Analysis40R
258497	0-11	0	Analysis40R
258498	0-11	0	Analysis40R
258499	0-11	0	Analysis40R
258500	0-11	0	Analysis40R
258501	0-11	0	Analysis40R
258502	0-11	0	Analysis40R
258503	0-11	0	Analysis40R
258504	0-11	0	Analysis40R
258505	0-11	0	Analysis40R
258506	0-11	0	Analysis40R
258507	0-11	0	Analysis40R
258508	0-11	0	Analysis40R
258509	0-11	0	Analysis40R
258510	0-11	0	Analysis40R
258511	0-11	0	Analysis40R
258512	0-11	0	Analysis40R
258513	0-11	0	Analysis40R

258514	0-11	0	Analysis40R
258515	0-11	0	Analysis40R
258516	0-11	0	Analysis40R
258520	0-11	0	Analysis40R
258521	0-11	0	Analysis40R
258522	0-11	0	Analysis40R
258523	0-11	0	Analysis40R
258524	0-11	0	Analysis40R
258525	0-11	0	Analysis40R
258526	0-11	0	Analysis40R
258527	0-11	0	Analysis40R
258528	0-11	0	Analysis40R
258529	0-11	0	Analysis40R
258530	0-15	0	Analysis40R
258531	0-12	0	Analysis40R
258532	0-11	0	Analysis40R
258538	0-11	0	Analysis40R
258539	0-11	0	Analysis40R
258540	0-11	0	Analysis40R
258541	0-11	0	Analysis40R
258542	0-11	0	Analysis40R
258543	0-11	0	Analysis40R
258555	0-11	0	Analysis40R
258556	0-11	0	Analysis40R
258557	0-11	0	Analysis40R
258558	0-11	0	Analysis40R
258559	0-11	0	Analysis40R
258560	0-11	0	Analysis40R
258561	0-11	0	Analysis40R
258562	0-11	0	Analysis40R
258563	0-11	0	Analysis40R
258729	0-11	1	Analysis40R
258730	0-11	0	Analysis40R
258731	0-11	0	Analysis40R
258732	0-11	0	Analysis40R
258733	0-11	0	Analysis40R
258734	0-11	0	Analysis40R
258735	0-11	0	Analysis40R
258736	0-11	0	Analysis40R
258737	0-11	0	Analysis40R
258738	0-11	0	Analysis40R
258739	0-11	0	Analysis40R
258740	0-11	0	Analysis40R
258741	0-11	0	Analysis40R
258742	0-11	0	Analysis40R
258743	0-11	0	Analysis40R
258744	0-11	0	Analysis40R
258816	0-11	0	Analysis40R
258817	0-11	0	Analysis40R
258818	0-11	0	Analysis40R
258819	0-11	0	Analysis40R
258829	0-11	0	Analysis40R
258830	0-11	0	Analysis40R
258831	0-11	0	Analysis40R
258832	0-6	0	Analysis40R
258833	0-11	0	Analysis40R
258834	0-11	0	Analysis40R
258837	0-11	0	Analysis40R
258838	0-11	0	Analysis40R
258839	0-11	0	Analysis40R
258840	0-11	0	Analysis40R
258841	0-11	0	Analysis40R
258842	0-11	0	Analysis40R
258843	0-11	0	Analysis40R
258844	0-11	0	Analysis40R
258845	0-11	0	Analysis40R
258846	0-11	0	Analysis40R
258847	0-11	0	Analysis40R
258848	0-11	0	Analysis40R
258849	0-11	0	Analysis40R
258850	0-11	0	Analysis40R
258851	0-11	0	Analysis40R
258852	0-11	0	Analysis40R
258853	0-11	0	Analysis40R
258854	0-11	0	Analysis40R
258855	0-11	0	Analysis40R
258856	0-11	0	Analysis40R
258857	0-11	0	Analysis40R
258858	0-11	0	Analysis40R
258859	0-11	0	Analysis40R
258860	0-11	0	Analysis40R
258861	0-11	0	Analysis40R
258862	0-11	0	Analysis40R
258863	0-11	0	Analysis40R
258864	0-11	0	Analysis40R
258865	0-11	0	Analysis40R
258866	0-11	0	Analysis40R
258867	0-11	0	Analysis40R
258870	0-11	0	Analysis40R
258871	0-11	0	Analysis40R
258872	0-11	0	Analysis40R
258873	0-11	0	Analysis40R
258874	0-11	0	Analysis40R
258875	0-11	0	Analysis40R
258876	0-11	0	Analysis40R
258878	0-11	0	Analysis40R
258879	0-11	0	Analysis40R
258880	0-11	0	Analysis40R
258881	0-11	0	Analysis40R
258883	0-11	0	Analysis40R
258884	0-11	0	Analysis40R
258885	0-11	0	Analysis40R
258886	0-11	0	Analysis40R
258887	0-11	0	Analysis40R
258888	0-11	0	Analysis40R
258889	0-11	0	Analysis40R
258890	0-11	0	Analysis40R
258891	0-11	0	Analysis40R
258892	0-11	0	Analysis40R
258893	0-11	0	Analysis40R
258894	0-11	0	Analysis40R
258895	0-11	0	Analysis40R
258896	0-11	0	Analysis40R
258903	0-11	0	Analysis40R
258907	0-11	0	Analysis40R
258908	0-11	0	Analysis40R
258909	0-11	0	Analysis40R
258910	0-11	0	Analysis40R
258911	0-11	0	Analysis40R
258917	0-10	0	Analysis40R
258918	0-10	0	Analysis40R
258919	0-10	0	Analysis40R
258920	0-10	0	Analysis40R
258922	0-10	0	Analysis40R
258924	0-10	0	Analysis40R
258925	0-10	0	Analysis40R
258926	0-10	0	Analysis40R
258927	0-10	0	Analysis40R
258930	0-10	0	Analysis40R
258931	0-10	0	Analysis40R

258932	0-10	0	Analysis40R
258933	0-10	0	Analysis40R
258934	0-10	0	Analysis40R
258935	0-10	0	Analysis40R
258936	0-10	0	Analysis40R
258937	0-6	0	Analysis40R
258939	0-11	0	Analysis40R
258940	0-11	0	Analysis40R
258941	0-11	0	Analysis40R
258942	0-11	0	Analysis40R
258943	0-11	0	Analysis40R
258944	0-11	0	Analysis40R
258945	0-11	0	Analysis40R
258946	0-11	0	Analysis40R
258947	0-11	0	Analysis40R
258948	0-11	0	Analysis40R
258949	0-11	0	Analysis40R
258950	0-11	0	Analysis40R
258952	0-11	0	Analysis40R
258953	0-11	0	Analysis40R
258954	0-11	0	Analysis40R
258955	0-11	0	Analysis40R
258956	0-8	0	Analysis40R
258958	0-11	0	Analysis40R
258959	0-11	0	Analysis40R
258960	0-11	0	Analysis40R
258961	0-11	0	Analysis40R
258962	0-11	0	Analysis40R
258963	0-11	0	Analysis40R
258964	0-11	0	Analysis40R
258965	0-11	0	Analysis40R
258966	0-11	0	Analysis40R
258967	0-8	0	Analysis40R
258968	0-11	0	Analysis40R
258969	0-11	0	Analysis40R
258970	0-11	0	Analysis40R
258971	0-11	0	Analysis40R
258972	0-11	0	Analysis40R
258973	0-11	0	Analysis40R
259959	0-6	0	Analysis40R
259960	0-6	0	Analysis40R
259961	0-6	0	Analysis40R
259962	0-6	0	Analysis40R
259963	0-6	0	Analysis40R
259964	0-6	0	Analysis40R
259965	0-6	0	Analysis40R
259966	0-6	0	Analysis40R
259967	0-6	0	Analysis40R
259968	0-6	0	Analysis40R
259969	0-6	0	Analysis40R
259970	0-6	0	Analysis40R
259971	0-6	0	Analysis40R
259972	0-6	0	Analysis40R
259973	0-6	0	Analysis40R
259974	0-6	0	Analysis40R
259975	0-6	0	Analysis40R
259983	0-6	0	Analysis40R
259984	0-5	0	Analysis40R
259985	0-5	0	Analysis40R
259986	0-3	0	Analysis40R
259993	0-6	0	Analysis40R
259994	0-6	0	Analysis40R
259995	0-6	0	Analysis40R
259996	0-6	0	Analysis40R
259997	0-6	0	Analysis40R
259998	0-6	0	Analysis40R
259999	0-6	0	Analysis40R
260000	0-6	0	Analysis40R
260001	0-6	0	Analysis40R
260002	0-6	0	Analysis40R
260003	0-6	0	Analysis40R
260004	0-6	0	Analysis40R
260005	0-6	0	Analysis40R
260006	0-6	0	Analysis40R
260007	0-6	0	Analysis40R
260008	0-3	0	Analysis40R
260010	0-3	0	Analysis40R
260012	0-3	0	Analysis40R
260025	0-5	0	Analysis40R
260026	0-5	0	Analysis40R
260027	0-5	0	Analysis40R
260028	0-6	0	Analysis40R
260029	0-5	0	Analysis40R
260030	0-5	0	Analysis40R
260031	0-6	0	Analysis40R
260032	0-5	0	Analysis40R
260033	0-5	0	Analysis40R
260034	0-5	0	Analysis40R
260035	0-5	0	Analysis40R
260036	0-5	0	Analysis40R
260037	0-5	0	Analysis40R
260038	0-6	0	Analysis40R
260039	0-5	0	Analysis40R
260040	0-5	0	Analysis40R
260041	0-5	0	Analysis40R
260042	0-5	0	Analysis40R
260043	0-5	0	Analysis40R
260044	0-5	0	Analysis40R
260045	0-5	0	Analysis40R
260046	0-5	0	Analysis40R
260047	0-5	0	Analysis40R
260048	0-5	0	Analysis40R
260049	0-6	0	Analysis40R
260050	0-5	0	Analysis40R
260051	0-5	0	Analysis40R
260052	0-5	0	Analysis40R
260053	0-5	0	Analysis40R
260054	0-5	0	Analysis40R
260055	0-5	0	Analysis40R
260056	0-5	0	Analysis40R
260057	0-5	0	Analysis40R
260058	0-5	0	Analysis40R
260059	0-5	0	Analysis40R
260060	0-5	0	Analysis40R
260061	0-5	0	Analysis40R
260062	0-5	0	Analysis40R
260063	0-6	0	Analysis40R
260064	0-5	0	Analysis40R
260065	0-6	0	Analysis40R
260066	0-5	0	Analysis40R
260067	0-5	0	Analysis40R
260068	0-5	0	Analysis40R
260069	0-5	0	Analysis40R
260070	0-5	0	Analysis40R
260071	0-6	0	Analysis40R
260072	0-5	0	Analysis40R
260073	0-5	0	Analysis40R
260074	0-6	0	Analysis40R
260075	0-5	0	Analysis40R
260076	0-5	0	Analysis40R

260077	0-5	0	Analysis40R
260078	0-5	0	Analysis40R
260079	0-5	0	Analysis40R
260080	0-5	0	Analysis40R
260081	0-5	0	Analysis40R
260082	0-5	0	Analysis40R
260083	0-6	0	Analysis40R
260084	0-5	0	Analysis40R
260085	0-5	0	Analysis40R
260087	0-5	0	Analysis40R
260088	0-6	0	Analysis40R
260089	0-5	0	Analysis40R
260090	0-6	0	Analysis40R
260091	0-5	0	Analysis40R
260101	0-6	0	Analysis40R
260102	0-6	0	Analysis40R
260103	0-6	0	Analysis40R
260104	0-6	0	Analysis40R
260105	0-6	0	Analysis40R
260106	0-6	0	Analysis40R
260107	0-6	0	Analysis40R
260108	0-6	0	Analysis40R
260109	0-6	0	Analysis40R
260110	0-6	0	Analysis40R
260111	0-6	0	Analysis40R
260112	0-6	0	Analysis40R
260113	0-6	0	Analysis40R
260114	0-6	0	Analysis40R
260115	0-6	0	Analysis40R
260116	0-6	0	Analysis40R
260117	0-6	0	Analysis40R
260119	0-6	0	Analysis40R
260120	0-6	0	Analysis40R
260122	0-6	0	Analysis40R
260123	0-6	0	Analysis40R
260125	0-6	0	Analysis40R
260126	0-3	0	Analysis40R
260128	0-6	0	Analysis40R
260129	0-6	0	Analysis40R
260130	0-6	0	Analysis40R
260131	0-6	0	Analysis40R
260132	0-6	0	Analysis40R
260133	0-6	0	Analysis40R
260134	0-6	0	Analysis40R
260135	0-6	0	Analysis40R
260136	0-6	0	Analysis40R
260137	0-6	0	Analysis40R
260138	0-6	0	Analysis40R
260139	0-6	0	Analysis40R
260140	0-6	0	Analysis40R
260141	0-6	0	Analysis40R
260142	0-3	0	Analysis40R
260143	0-6	0	Analysis40R
260144	0-6	0	Analysis40R
260145	0-6	0	Analysis40R
260146	0-6	0	Analysis40R
260147	0-6	0	Analysis40R
260148	0-6	0	Analysis40R
260149	0-3	0	Analysis40R
260156	0-6	0	Analysis40R
260157	0-6	0	Analysis40R
260158	0-6	0	Analysis40R
260160	0-6	0	Analysis40R
260161	0-6	0	Analysis40R
260163	0-6	0	Analysis40R
260164	0-6	0	Analysis40R
260165	0-6	0	Analysis40R
260166	0-6	0	Analysis40R
260167	0-6	0	Analysis40R
260168	0-6	0	Analysis40R
260169	0-6	0	Analysis40R
260170	0-6	0	Analysis40R
260171	0-6	0	Analysis40R
260172	0-6	0	Analysis40R
260173	0-6	0	Analysis40R
260174	0-6	0	Analysis40R
260175	0-6	0	Analysis40R
260176	0-6	0	Analysis40R
260177	0-6	0	Analysis40R
260178	0-6	0	Analysis40R
260179	0-6	0	Analysis40R
260188	0-6	0	Analysis40R
260189	0-6	0	Analysis40R
260190	0-6	0	Analysis40R
260191	0-6	0	Analysis40R
260192	0-6	0	Analysis40R
260193	0-6	0	Analysis40R
260195	0-6	0	Analysis40R
260196	0-4	0	Analysis40R
260199	0-6	0	Analysis40R
260201	0-6	0	Analysis40R
260202	0-6	0	Analysis40R
260203	0-6	0	Analysis40R
260204	0-6	0	Analysis40R
260205	0-6	0	Analysis40R
260206	0-6	0	Analysis40R
260207	0-6	0	Analysis40R
260208	0-6	0	Analysis40R
260209	0-6	0	Analysis40R
260210	0-5	0	Analysis40R
260212	0-6	0	Analysis40R
260213	0-6	0	Analysis40R
260214	0-6	0	Analysis40R
260215	0-6	0	Analysis40R
260216	0-6	0	Analysis40R
260217	0-6	0	Analysis40R
260218	0-6	0	Analysis40R
260219	0-6	0	Analysis40R
260220	0-6	0	Analysis40R
260221	0-6	0	Analysis40R
260222	0-6	0	Analysis40R
260223	0-6	0	Analysis40R
260224	0-6	0	Analysis40R
260225	0-6	0	Analysis40R
260226	0-6	0	Analysis40R
260227	0-6	0	Analysis40R
260228	0-6	0	Analysis40R
260229	0-6	0	Analysis40R
260230	0-6	0	Analysis40R
260231	0-6	0	Analysis40R
260232	0-6	0	Analysis40R
260233	0-6	0	Analysis40R
260234	0-6	0	Analysis40R
260235	0-6	0	Analysis40R
260236	0-6	0	Analysis40R
260237	0-5	0	Analysis40R
260240	0-6	0	Analysis40R
260241	0-6	0	Analysis40R
260242	0-6	0	Analysis40R
260249	0-6	0	Analysis40R

260250	0-6	0	Analysis40R
260251	0-6	0	Analysis40R
260252	0-6	0	Analysis40R
260253	0-6	0	Analysis40R
260255	0-6	0	Analysis40R
260256	0-6	0	Analysis40R
260257	0-6	0	Analysis40R
260258	0-6	0	Analysis40R
260260	0-6	0	Analysis40R
260261	0-6	0	Analysis40R
260262	0-6	0	Analysis40R
260264	0-6	0	Analysis40R
260265	0-6	0	Analysis40R
260266	0-6	0	Analysis40R
260267	0-6	0	Analysis40R
260268	0-6	0	Analysis40R
260269	0-6	0	Analysis40R
260270	0-6	0	Analysis40R
260271	0-6	0	Analysis40R
260272	0-6	0	Analysis40R
260273	0-6	0	Analysis40R
260274	0-6	0	Analysis40R
260275	0-6	0	Analysis40R
260276	0-6	0	Analysis40R
260277	0-6	0	Analysis40R
260278	0-6	0	Analysis40R
260284	0-6	0	Analysis40R
260285	0-6	0	Analysis40R
260286	0-6	0	Analysis40R
260287	0-6	0	Analysis40R
260288	0-6	0	Analysis40R
260289	0-6	0	Analysis40R
260290	0-6	0	Analysis40R
260291	0-6	0	Analysis40R
260292	0-6	0	Analysis40R
260293	0-6	0	Analysis40R
260294	0-6	0	Analysis40R
260296	0-6	0	Analysis40R
260297	0-6	0	Analysis40R
260298	0-6	0	Analysis40R
260299	0-5	0	Analysis40R
260306	0-11	0	Analysis40R
260307	0-11	0	Analysis40R
260308	0-11	0	Analysis40R
260309	0-11	0	Analysis40R
260312	0-11	0	Analysis40R
260313	0-11	0	Analysis40R
260314	0-11	0	Analysis40R
260315	0-11	0	Analysis40R
260316	0-11	0	Analysis40R
260317	0-11	0	Analysis40R
260318	0-11	0	Analysis40R
260319	0-11	0	Analysis40R
260320	0-11	0	Analysis40R
260323	0-11	0	Analysis40R
260324	0-11	0	Analysis40R
260325	0-11	0	Analysis40R
260326	0-11	0	Analysis40R
260327	0-11	0	Analysis40R
260328	0-11	0	Analysis40R
260329	0-11	0	Analysis40R
260330	0-11	0	Analysis40R
260331	0-11	0	Analysis40R
260332	0-11	0	Analysis40R
260333	0-11	0	Analysis40R
260334	0-11	0	Analysis40R
260335	0-11	0	Analysis40R
260336	0-11	0	Analysis40R
260337	0-11	0	Analysis40R
260338	0-11	0	Analysis40R
260339	0-11	0	Analysis40R
260341	0-11	0	Analysis40R
260342	0-11	0	Analysis40R
260343	0-11	0	Analysis40R
260344	0-11	0	Analysis40R
260345	0-11	0	Analysis40R
260346	0-11	0	Analysis40R
260347	0-11	0	Analysis40R
260348	0-11	0	Analysis40R
260349	0-11	0	Analysis40R
260350	0-11	0	Analysis40R
260352	0-11	0	Analysis40R
260353	0-11	0	Analysis40R
260354	0-11	0	Analysis40R
260356	0-8	0	Analysis40R
260362	0-11	0	Analysis40R
260363	0-11	0	Analysis40R
260364	0-11	0	Analysis40R
260365	0-11	0	Analysis40R
260367	0-11	0	Analysis40R
260368	0-11	0	Analysis40R
260378	0-11	0	Analysis40R
260381	0-11	0	Analysis40R
260382	0-11	0	Analysis40R
260383	0-11	0	Analysis40R
260388	0-11	0	Analysis40R
260389	0-11	0	Analysis40R
260390	0-11	0	Analysis40R
260392	0-11	0	Analysis40R
260393	0-11	0	Analysis40R
260397	0-11	0	Analysis40R
260399	0-12	0	Analysis40R
260407	0-11	0	Analysis40R
260408	0-11	0	Analysis40R
260409	0-11	0	Analysis40R
260410	0-11	0	Analysis40R
260411	0-11	0	Analysis40R
260412	0-11	0	Analysis40R
260418	0-11	0	Analysis40R
260419	0-11	0	Analysis40R
260420	0-11	0	Analysis40R
260421	0-11	0	Analysis40R
260422	0-11	0	Analysis40R
260423	0-11	0	Analysis40R
260424	0-11	0	Analysis40R
260430	0-11	0	Analysis40R
260431	0-11	0	Analysis40R
260432	0-11	0	Analysis40R
260433	0-11	0	Analysis40R
260434	0-11	0	Analysis40R
260435	0-11	0	Analysis40R
260437	0-11	0	Analysis40R
260438	0-11	0	Analysis40R
260439	0-11	0	Analysis40R
260440	0-11	0	Analysis40R
260441	0-11	0	Analysis40R
260442	0-11	0	Analysis40R
260443	0-11	0	Analysis40R
260456	0-11	0	Analysis40R
260457	0-11	0	Analysis40R

260458	0-11	0	Analysis40R
260459	0-11	0	Analysis40R
260460	0-11	0	Analysis40R
260461	0-11	0	Analysis40R
260462	0-11	0	Analysis40R
260463	0-11	0	Analysis40R
260464	0-11	0	Analysis40R
260467	0-11	0	Analysis40R
260468	0-11	0	Analysis40R
260469	0-11	0	Analysis40R
260480	0-11	0	Analysis40R
260483	0-7	0	Analysis40R
260484	0-11	0	Analysis40R
260485	0-11	0	Analysis40R
260491	0-11	0	Analysis40R
260494	0-11	0	Analysis40R
260495	0-11	0	Analysis40R
260496	0-11	0	Analysis40R
260498	0-11	0	Analysis40R
260499	0-11	0	Analysis40R
260500	0-11	0	Analysis40R
260501	0-6	0	Analysis40R
260502	0-5	0	Analysis40R
260503	0-5	0	Analysis40R
260504	0-5	0	Analysis40R
260505	0-5	0	Analysis40R
260506	0-5	0	Analysis40R
260507	0-5	0	Analysis40R
260508	0-5	0	Analysis40R
260509	0-5	0	Analysis40R
260510	0-5	0	Analysis40R
260511	0-5	0	Analysis40R
260512	0-5	0	Analysis40R
260513	0-5	0	Analysis40R
260514	0-5	0	Analysis40R
260515	0-5	0	Analysis40R
260527	0-5	0	Analysis40R
260528	0-5	0	Analysis40R
260532	0-5	0	Analysis40R
260536	0-5	0	Analysis40R
260541	0-5	0	Analysis40R
260545	0-5	0	Analysis40R
260546	0-5	0	Analysis40R
260547	0-5	0	Analysis40R
260549	0-5	0	Analysis40R
260550	0-5	0	Analysis40R
260566	0-5	0	Analysis40R
260569	0-5	0	Analysis40R
260576	0-5	0	Analysis40R
260577	0-5	0	Analysis40R
260579	0-5	0	Analysis40R
260580	0-5	0	Analysis40R
260584	0-5	0	Analysis40R
260585	0-5	0	Analysis40R
260586	0-5	0	Analysis40R
260587	0-5	0	Analysis40R
260588	0-5	0	Analysis40R
260591	0-5	0	Analysis40R
260593	0-5	0	Analysis40R
260594	0-5	0	Analysis40R
260595	0-5	0	Analysis40R
260596	0-5	0	Analysis40R
260597	0-5	0	Analysis40R
260598	0-5	0	Analysis40R
260599	0-5	0	Analysis40R
260600	0-5	0	Analysis40R
260601	0-5	0	Analysis40R
260602	0-5	0	Analysis40R
260603	0-5	0	Analysis40R
260604	0-5	0	Analysis40R
260605	0-5	0	Analysis40R
260606	0-5	0	Analysis40R
260607	0-5	0	Analysis40R
260608	0-5	0	Analysis40R
260609	0-5	0	Analysis40R
260610	0-5	0	Analysis40R
260611	0-5	0	Analysis40R
260612	0-5	0	Analysis40R
260613	0-5	0	Analysis40R
260614	0-5	0	Analysis40R
260615	0-5	0	Analysis40R
260616	0-5	0	Analysis40R
260617	0-5	0	Analysis40R
260620	0-5	0	Analysis40R
260621	0-5	0	Analysis40R
260622	0-5	0	Analysis40R
260623	0-5	0	Analysis40R
260624	0-5	0	Analysis40R
260625	0-5	0	Analysis40R
260626	0-5	0	Analysis40R
260627	0-5	0	Analysis40R
260628	0-5	0	Analysis40R
260629	0-5	0	Analysis40R
260630	0-5	0	Analysis40R
260631	0-5	0	Analysis40R
260632	0-5	0	Analysis40R
260633	0-5	0	Analysis40R
260635	0-5	0	Analysis40R
260636	0-5	0	Analysis40R
260637	0-5	0	Analysis40R
260638	0-5	0	Analysis40R
260639	0-5	0	Analysis40R
260641	0-5	0	Analysis40R
260642	0-5	0	Analysis40R
260643	0-5	0	Analysis40R
260675	0-5	0	Analysis40R
260688	0-5	0	Analysis40R
260709	0-5	0	Analysis40R
260779	0-5	0	Analysis40R
260787	0-5	0	Analysis40R
260800	0-5	0	Analysis40R
260801	0-5	0	Analysis40R
260820	0-5	0	Analysis40R
260821	0-5	0	Analysis40R
260828	0-5	0	Analysis40R
260834	0-5	0	Analysis40R
260869	0-5	0	Analysis40R
260873	0-5	0	Analysis40R
260874	0-5	0	Analysis40R
260875	0-5	0	Analysis40R
260876	0-5	0	Analysis40R
260877	0-5	0	Analysis40R
260878	0-5	0	Analysis40R
260879	0-5	0	Analysis40R
260880	0-5	0	Analysis40R
260881	0-5	0	Analysis40R
260882	0-5	0	Analysis40R
260883	0-5	0	Analysis40R
260884	0-5	0	Analysis40R
260885	0-5	0	Analysis40R

260886	0-5	0	Analysis40R
260887	0-5	0	Analysis40R
260888	0-5	0	Analysis40R
260889	0-5	0	Analysis40R
260890	0-5	0	Analysis40R
260891	0-5	0	Analysis40R
260892	0-5	0	Analysis40R
260893	0-5	0	Analysis40R
260894	0-5	0	Analysis40R
260895	0-5	0	Analysis40R
260896	0-5	0	Analysis40R
260897	0-5	0	Analysis40R
260898	0-5	0	Analysis40R
260899	0-5	0	Analysis40R
260900	0-5	0	Analysis40R
260901	0-5	0	Analysis40R
260902	0-5	0	Analysis40R
260903	0-5	0	Analysis40R
260904	0-5	0	Analysis40R
260905	0-5	0	Analysis40R
260906	0-5	0	Analysis40R
260907	0-5	0	Analysis40R
260908	0-5	0	Analysis40R
260909	0-5	0	Analysis40R
260910	0-5	0	Analysis40R
260911	0-5	0	Analysis40R
260912	0-5	0	Analysis40R
260913	0-5	0	Analysis40R
260914	0-5	0	Analysis40R
260915	0-5	0	Analysis40R
260916	0-5	0	Analysis40R
260917	0-5	0	Analysis40R
260918	0-5	0	Analysis40R
260919	0-5	0	Analysis40R
260920	0-5	0	Analysis40R
260922	0-6	0	Analysis40R
260923	0-5	0	Analysis40R
260924	0-5	0	Analysis40R
260925	0-5	0	Analysis40R
260927	0-5	0	Analysis40R
260928	0-5	0	Analysis40R
260929	0-5	0	Analysis40R
260930	0-5	0	Analysis40R
260931	0-5	0	Analysis40R
260932	0-5	0	Analysis40R
260933	0-5	0	Analysis40R
260934	0-5	0	Analysis40R
260935	0-5	0	Analysis40R
260936	0-5	0	Analysis40R
260937	0-5	0	Analysis40R
260938	0-5	0	Analysis40R
260939	0-5	0	Analysis40R
260940	0-5	0	Analysis40R
260941	0-5	0	Analysis40R
260942	0-5	0	Analysis40R
260943	0-5	0	Analysis40R
260944	0-5	0	Analysis40R
260945	0-5	0	Analysis40R
260946	0-5	0	Analysis40R
260947	0-5	0	Analysis40R
260948	0-5	0	Analysis40R
260949	0-5	0	Analysis40R
260951	0-5	0	Analysis40R
260952	0-5	0	Analysis40R
260953	0-5	0	Analysis40R
260954	0-5	0	Analysis40R
260955	0-5	0	Analysis40R
260956	0-5	0	Analysis40R
260958	0-5	0	Analysis40R
260959	0-5	0	Analysis40R
260960	0-5	0	Analysis40R
260962	0-5	0	Analysis40R
260963	0-5	0	Analysis40R
260964	0-5	0	Analysis40R
260965	0-5	0	Analysis40R
260966	0-5	0	Analysis40R
260967	0-5	0	Analysis40R
260968	0-5	0	Analysis40R
260969	0-5	0	Analysis40R
260973	0-5	0	Analysis40R
260974	0-5	0	Analysis40R
260975	0-5	0	Analysis40R
260976	0-5	0	Analysis40R
260977	0-5	0	Analysis40R
260978	0-5	0	Analysis40R
260979	0-5	0	Analysis40R
260980	0-5	0	Analysis40R
260981	0-5	0	Analysis40R
260982	0-5	0	Analysis40R
260983	0-5	0	Analysis40R
260984	0-5	0	Analysis40R
260985	0-5	0	Analysis40R
260986	0-5	0	Analysis40R
260987	0-5	0	Analysis40R
260988	0-5	0	Analysis40R
260989	0-5	0	Analysis40R
260990	0-5	0	Analysis40R
260991	0-5	0	Analysis40R
260992	0-5	0	Analysis40R
260993	0-5	0	Analysis40R
260994	0-5	0	Analysis40R
260995	0-5	0	Analysis40R
260996	0-5	0	Analysis40R
260997	0-5	0	Analysis40R
260998	0-5	0	Analysis40R
260999	0-5	0	Analysis40R
261000	0-5	0	Analysis40R
261001	0-5	0	Analysis40R
261002	0-5	0	Analysis40R
261003	0-5	0	Analysis40R
261004	0-5	0	Analysis40R
261005	0-5	0	Analysis40R
261006	0-5	0	Analysis40R
261007	0-5	0	Analysis40R
261008	0-5	0	Analysis40R
261394	0-5	0	Analysis40RP
261395	0-5	0	Analysis40RP
261396	0-5	0	Analysis40RP
261397	0-5	0	Analysis40RP
261398	0-5	0	Analysis40RP
261399	0-5	0	Analysis40RP
261400	0-5	0	Analysis40RP
261401	0-5	0	Analysis40RP
261402	0-5	0	Analysis40RP
261403	0-5	0	Analysis40RP
261404	0-5	0	Analysis40RP
261405	0-5	0	Analysis40RP
261406	0-5	0	Analysis40RP
261407	0-5	0	Analysis40RP
261408	0-5	0	Analysis40RP

261409	0-5	0	Analysis40RP
261410	0-5	0	Analysis40RP
261411	0-5	0	Analysis40RP
261412	0-5	0	Analysis40RP
261413	0-5	0	Analysis40RP
261414	0-5	0	Analysis40RP
261415	0-5	0	Analysis40RP
261416	0-5	0	Analysis40RP
261417	0-5	0	Analysis40RP
261418	0-5	0	Analysis40RP
261419	0-5	0	Analysis40RP
261420	0-5	0	Analysis40RP
261421	0-5	0	Analysis40RP
261422	0-5	0	Analysis40RP
261423	0-5	0	Analysis40RP
261424	0-5	0	Analysis40RP
261425	0-5	0	Analysis40RP
261426	0-5	0	Analysis40RP
261427	0-5	0	Analysis40RP
261428	0-5	0	Analysis40RP
261429	0-5	0	Analysis40RP
261430	0-5	0	Analysis40RP
261431	0-5	0	Analysis40RP
261432	0-5	0	Analysis40RP
261433	0-5	0	Analysis40RP
261434	0-5	0	Analysis40RP
261435	0-5	0	Analysis40RP
261436	0-5	0	Analysis40RP
261437	0-5	0	Analysis40RP
261438	0-5	0	Analysis40RP
261439	0-5	0	Analysis40RP
261440	0-5	0	Analysis40RP
261441	0-5	0	Analysis40RP
261442	0-5	0	Analysis40RP
261443	0-5	0	Analysis40RP
261444	0-5	0	Analysis40RP
261445	0-5	0	Analysis40RP
261446	0-5	0	Analysis40RP
261447	0-5	0	Analysis40RP
261448	0-5	0	Analysis40RP
261449	0-5	0	Analysis40RP
261450	0-5	0	Analysis40RP
261451	0-5	0	Analysis40RP
261452	0-5	0	Analysis40RP
261453	0-5	0	Analysis40RP
261455	0-5	0	Analysis40RP
261456	0-5	0	Analysis40RP
261457	0-5	0	Analysis40RP
261458	0-5	0	Analysis40RP
261459	0-5	0	Analysis40RP
261460	0-5	0	Analysis40RP
261461	0-5	0	Analysis40RP
261462	0-5	0	Analysis40RP
261463	0-5	0	Analysis40RP
261464	0-5	0	Analysis40RP
261465	0-5	0	Analysis40RP
261466	0-5	0	Analysis40RP
261467	0-5	0	Analysis40RP
261468	0-5	0	Analysis40RP
261469	0-5	0	Analysis40RP
261470	0-5	0	Analysis40RP
261471	0-5	0	Analysis40RP
261472	0-5	0	Analysis40RP
261473	0-5	0	Analysis40RP
261474	0-5	0	Analysis40RP
261475	0-5	0	Analysis40RP
261476	0-5	0	Analysis40RP
261477	0-5	0	Analysis40RP
261478	0-5	0	Analysis40RP
261479	0-5	0	Analysis40RP
261480	0-5	0	Analysis40RP
261481	0-5	0	Analysis40RP
261482	0-5	0	Analysis40RP
261483	0-5	0	Analysis40RP
261484	0-5	0	Analysis40RP
261485	0-5	0	Analysis40RP
261486	0-5	0	Analysis40RP
261487	0-5	0	Analysis40RP
261488	0-5	0	Analysis40RP
261489	0-5	0	Analysis40RP
261490	0-5	0	Analysis40RP
261491	0-5	0	Analysis40RP
261492	0-5	0	Analysis40RP
261493	0-5	0	Analysis40RP
261494	0-5	0	Analysis40RP
261495	0-5	0	Analysis40RP
261496	0-5	0	Analysis40RP
261497	0-5	0	Analysis40RP
261498	0-5	0	Analysis40RP
261499	0-5	0	Analysis40RP
261500	0-5	0	Analysis40RP
261501	0-5	0	Analysis40RP
261502	0-5	0	Analysis40RP
261503	0-5	0	Analysis40RP
261504	0-5	0	Analysis40RP
261505	0-5	0	Analysis40RP
261506	0-5	0	Analysis40RP
261507	0-5	0	Analysis40RP
261508	0-5	0	Analysis40RP
261509	0-5	0	Analysis40RP
261510	0-5	0	Analysis40RP
261511	0-5	0	Analysis40RP
261512	0-5	0	Analysis40RP
261513	0-5	0	Analysis40RP
261514	0-5	0	Analysis40RP
261515	0-5	0	Analysis40RP
261516	0-5	0	Analysis40RP
261517	0-5	0	Analysis40RP
261518	0-5	0	Analysis40RP
261519	0-5	0	Analysis40RP
261520	0-5	0	Analysis40RP
261521	0-5	0	Analysis40RP
261522	0-5	0	Analysis40RP
261523	0-5	0	Analysis40RP
261524	0-5	0	Analysis40RP
261525	0-5	0	Analysis40RP
261526	0-5	0	Analysis40RP
261527	0-5	0	Analysis40RP
261528	0-5	0	Analysis40RP
261529	0-5	0	Analysis40RP
261530	0-5	0	Analysis40RP
261531	0-5	0	Analysis40RP
261532	0-5	0	Analysis40RP
261533	0-5	0	Analysis40RP
261534	0-5	0	Analysis40RP
261536	0-5	0	Analysis40RP
261537	0-5	0	Analysis40RP
261538	0-5	0	Analysis40RP
261539	0-5	0	Analysis40RP
261540	0-5	0	Analysis40RP

261541	0-5	0	Analysis40RP
261542	0-5	0	Analysis40RP
261543	0-5	0	Analysis40RP
261544	0-5	0	Analysis40RP
261545	0-5	0	Analysis40RP
261546	0-5	0	Analysis40RP
261547	0-5	0	Analysis40RP
261562	0-5	0	Analysis40RP
261563	0-5	0	Analysis40RP
261564	0-5	0	Analysis40RP
261565	0-5	0	Analysis40RP
261566	0-5	0	Analysis40RP
261567	0-5	0	Analysis40RP
261568	0-5	0	Analysis40RP
261569	0-5	0	Analysis40RP
261570	0-5	0	Analysis40RP
261571	0-5	0	Analysis40RP
261572	0-5	0	Analysis40RP
261573	0-5	0	Analysis40RP
261574	0-5	0	Analysis40RP
261575	0-5	0	Analysis40RP
261576	0-5	0	Analysis40RP
261577	0-5	0	Analysis40RP
261578	0-5	0	Analysis40RP
261579	0-5	0	Analysis40RP
261580	0-5	0	Analysis40RP
261581	0-5	0	Analysis40RP
261582	0-5	0	Analysis40RP
261583	0-5	0	Analysis40RP
261584	0-5	0	Analysis40RP
261585	0-5	0	Analysis40RP
261586	0-5	0	Analysis40RP
261587	0-5	0	Analysis40RP
261588	0-5	0	Analysis40RP
261589	0-5	0	Analysis40RP
261590	0-5	0	Analysis40RP
261591	0-5	0	Analysis40RP
261593	0-5	0	Analysis40RP
261594	0-5	0	Analysis40RP
261595	0-5	0	Analysis40RP
261596	0-5	0	Analysis40RP
261597	0-5	0	Analysis40RP
261598	0-5	0	Analysis40RP
261599	0-5	0	Analysis40RP
261600	0-5	0	Analysis40RP
261601	0-5	0	Analysis40RP
261602	0-5	0	Analysis40RP
261603	0-5	0	Analysis40RP
261604	0-5	0	Analysis40RP
261605	0-5	0	Analysis40RP
261606	0-5	0	Analysis40RP
261607	0-5	0	Analysis40RP
261608	0-5	0	Analysis40RP
261609	0-5	0	Analysis40RP
261610	0-5	0	Analysis40RP
261611	0-5	0	Analysis40RP
261612	0-5	0	Analysis40RP
261613	0-5	0	Analysis40RP
261614	0-5	0	Analysis40RP
261615	0-5	0	Analysis40RP
261616	0-5	0	Analysis40RP
261617	0-5	0	Analysis40RP
261618	0-5	0	Analysis40RP
261619	0-5	0	Analysis40RP
261624	0-5	0	Analysis40RP
261625	0-5	0	Analysis40RP
261626	0-5	0	Analysis40RP
261627	0-5	0	Analysis40RP
261628	0-5	0	Analysis40RP
261629	0-5	0	Analysis40RP
261630	0-5	0	Analysis40RP
261631	0-5	0	Analysis40RP
261632	0-5	0	Analysis40RP
261633	0-5	0	Analysis40RP
261635	0-5	0	Analysis40RP
261636	0-5	0	Analysis40RP
261637	0-5	0	Analysis40RP
261638	0-5	0	Analysis40RP
261639	0-5	0	Analysis40RP
261640	0-5	0	Analysis40RP
261641	0-5	0	Analysis40RP
261642	0-5	0	Analysis40RP
261643	0-5	0	Analysis40RP
261644	0-5	0	Analysis40RP
261645	0-5	0	Analysis40RP
261646	0-5	0	Analysis40RP
261647	0-5	0	Analysis40RP
261648	0-5	0	Analysis40RP
261649	0-5	0	Analysis40RP
261650	0-5	0	Analysis40RP
261651	0-5	0	Analysis40RP
261652	0-5	0	Analysis40RP
261653	0-5	0	Analysis40RP
261654	0-5	0	Analysis40RP
261655	0-5	0	Analysis40RP
261656	0-8	0	Analysis40RP
261657	0-5	0	Analysis40RP
261659	0-8	0	Analysis40RP
261660	0-5	0	Analysis40RP
261661	0-5	0	Analysis40RP
261662	0-5	0	Analysis40RP
261663	0-5	0	Analysis40RP
261664	0-5	0	Analysis40RP
261665	0-5	0	Analysis40RP
261666	0-5	0	Analysis40RP
261667	0-5	0	Analysis40RP
261668	0-5	0	Analysis40RP
261669	0-5	0	Analysis40RP
261670	0-5	0	Analysis40RP
261671	0-5	0	Analysis40RP
261672	0-5	0	Analysis40RP
261673	0-5	0	Analysis40RP
261674	0-5	0	Analysis40RP
261675	0-5	0	Analysis40RP
261676	0-5	0	Analysis40RP
261677	0-5	0	Analysis40RP
261678	0-5	0	Analysis40RP
261679	0-5	0	Analysis40RP
261680	0-5	0	Analysis40RP
261681	0-5	0	Analysis40RP
261682	0-5	0	Analysis40RP
261683	0-5	0	Analysis40RP
261684	0-5	0	Analysis40RP
261685	0-5	0	Analysis40RP
261686	0-5	0	Analysis40RP
261687	0-5	0	Analysis40RP
261689	0-5	0	Analysis40RP
261690	0-5	0	Analysis40RP
261691	0-5	0	Analysis40RP
261692	0-5	0	Analysis40RP

261693	0-5	0	Analysis40RP
261694	0-5	0	Analysis40RP
261695	0-5	0	Analysis40RP
261696	0-5	0	Analysis40RP
261698	0-5	0	Analysis40RP
261699	0-5	0	Analysis40RP
261700	0-5	0	Analysis40RP
261701	0-5	0	Analysis40RP
261702	0-5	0	Analysis40RP
261703	0-5	0	Analysis40RP
261704	0-5	0	Analysis40RP
261705	0-5	0	Analysis40RP
261706	0-5	0	Analysis40RP
261707	0-5	0	Analysis40RP
261709	0-5	0	Analysis40RP
261710	0-5	0	Analysis40RP
261711	0-5	0	Analysis40RP
261712	0-5	0	Analysis40RP
261713	0-5	0	Analysis40RP
261714	0-5	0	Analysis40RP
261715	0-5	0	Analysis40RP
261716	0-5	0	Analysis40RP
261717	0-5	0	Analysis40RP
261718	0-5	0	Analysis40RP
261719	0-5	0	Analysis40RP
261720	0-5	0	Analysis40RP
261721	0-5	0	Analysis40RP
261722	0-5	0	Analysis40RP
261723	0-5	0	Analysis40RP
261724	0-5	0	Analysis40RP
261739	0-5	0	Analysis40RP
261741	0-5	0	Analysis40RP
261743	0-5	0	Analysis40RP
261747	0-5	0	Analysis40RP
261749	0-5	0	Analysis40RP
261752	0-5	0	Analysis40RP
261755	0-5	0	Analysis40RP
261756	0-5	0	Analysis40RP
261757	0-5	0	Analysis40RP
261758	0-5	0	Analysis40RP
261759	0-5	0	Analysis40RP
261760	0-5	0	Analysis40RP
261761	0-5	0	Analysis40RP
261762	0-5	0	Analysis40RP
261763	0-5	0	Analysis40RP
261764	0-5	0	Analysis40RP
261765	0-5	0	Analysis40RP
261766	0-5	0	Analysis40RP
261767	0-5	0	Analysis40RP
261768	0-5	0	Analysis40RP
261769	0-5	0	Analysis40RP
261770	0-5	0	Analysis40RP
261771	0-5	0	Analysis40RP
261772	0-5	0	Analysis40RP
261773	0-5	0	Analysis40RP
261774	0-5	0	Analysis40RP
261775	0-5	0	Analysis40RP
261776	0-5	0	Analysis40RP
261777	0-5	0	Analysis40RP
261778	0-5	0	Analysis40RP
261779	0-5	0	Analysis40RP
261780	0-5	0	Analysis40RP
261781	0-5	0	Analysis40RP
261782	0-5	0	Analysis40RP
261783	0-5	0	Analysis40RP
261784	0-5	0	Analysis40RP
261785	0-5	0	Analysis40RP
261786	0-5	0	Analysis40RP
261787	0-5	0	Analysis40RP
261788	0-5	0	Analysis40RP
261789	0-5	0	Analysis40RP
261790	0-5	0	Analysis40RP
261791	0-5	0	Analysis40RP
261792	0-5	0	Analysis40RP
261793	0-5	0	Analysis40RP
261794	0-5	0	Analysis40RP
261795	0-5	0	Analysis40RP
261796	0-5	0	Analysis40RP
261797	0-5	0	Analysis40RP
261798	0-5	0	Analysis40RP
261799	0-5	0	Analysis40RP
261800	0-5	0	Analysis40RP
261801	0-5	0	Analysis40RP
261802	0-5	0	Analysis40RP
261803	0-5	0	Analysis40RP
261804	0-5	0	Analysis40RP
261805	0-5	0	Analysis40RP
261806	0-5	0	Analysis40RP
261807	0-5	0	Analysis40RP
261808	0-5	0	Analysis40RP
261809	0-5	0	Analysis40RP
261810	0-5	0	Analysis40RP
261811	0-5	0	Analysis40RP
261812	0-5	0	Analysis40RP
261820	0-5	0	Analysis40RP
261821	0-5	0	Analysis40RP
261822	0-5	0	Analysis40RP
261823	0-5	0	Analysis40RP
261824	0-5	0	Analysis40RP
261825	0-5	0	Analysis40RP
261826	0-5	0	Analysis40RP
261827	0-5	0	Analysis40RP
261828	0-5	0	Analysis40RP
261829	0-5	0	Analysis40RP
261830	0-5	0	Analysis40RP
261831	0-5	0	Analysis40RP
261832	0-5	0	Analysis40RP
261833	0-5	0	Analysis40RP
261834	0-5	0	Analysis40RP
261835	0-5	0	Analysis40RP
261836	0-5	0	Analysis40RP
261837	0-5	0	Analysis40RP
261838	0-5	0	Analysis40RP
261839	0-5	0	Analysis40RP
261840	0-5	0	Analysis40RP
261841	0-5	0	Analysis40RP
261842	0-5	0	Analysis40RP
261843	0-5	0	Analysis40RP
261844	0-5	0	Analysis40RP
261845	0-5	0	Analysis40RP
261846	0-5	0	Analysis40RP
261847	0-5	0	Analysis40RP
261848	0-5	0	Analysis40RP
261849	0-5	0	Analysis40RP
261850	0-5	0	Analysis40RP
261851	0-5	0	Analysis40RP
261852	0-5	0	Analysis40RP
261853	0-5	0	Analysis40RP
261854	0-5	0	Analysis40RP
261855	0-5	0	Analysis40RP

261858	0-5	0	Analysis40RP
261859	0-5	0	Analysis40RP
261860	0-5	0	Analysis40RP
261861	0-5	0	Analysis40RP
261862	0-5	0	Analysis40RP
261863	0-5	0	Analysis40RP
261864	0-5	0	Analysis40RP
261865	0-5	0	Analysis40RP
261866	0-5	0	Analysis40RP
261867	0-5	0	Analysis40RP
261868	0-5	0	Analysis40RP
261869	0-5	0	Analysis40RP
261870	0-5	0	Analysis40RP
261871	0-5	0	Analysis40RP
261872	0-5	0	Analysis40RP
261873	0-5	0	Analysis40RP
261875	0-5	0	Analysis40RP
261876	0-5	0	Analysis40RP
261877	0-5	0	Analysis40RP
261878	0-5	0	Analysis40RP
261879	0-5	0	Analysis40RP
261880	0-5	0	Analysis40RP
261881	0-5	0	Analysis40RP
261882	0-5	0	Analysis40RP
261883	0-5	0	Analysis40RP
261884	0-5	0	Analysis40RP
261885	0-5	0	Analysis40RP
261886	0-5	0	Analysis40RP
261887	0-5	0	Analysis40RP
261888	0-5	0	Analysis40RP
261889	0-5	0	Analysis40RP
261890	0-5	0	Analysis40RP
261891	0-5	0	Analysis40RP
261892	0-5	0	Analysis40RP
261893	0-5	0	Analysis40RP
261894	0-5	0	Analysis40RP
261908	0-5	0	Analysis40RP
261909	0-5	0	Analysis40RP
261911	0-5	0	Analysis40RP
261912	0-5	0	Analysis40RP
261913	0-5	0	Analysis40RP
261914	0-5	0	Analysis40RP
261915	0-5	0	Analysis40RP
261916	0-5	0	Analysis40RP
261917	0-5	0	Analysis40RP
261918	0-5	0	Analysis40RP
261919	0-5	0	Analysis40RP
261920	0-5	0	Analysis40RP
261921	0-5	0	Analysis40RP
261922	0-5	0	Analysis40RP
261923	0-5	0	Analysis40RP
261924	0-5	0	Analysis40RP
261925	0-5	0	Analysis40RP
261926	0-5	0	Analysis40RP
261927	0-5	0	Analysis40RP
261928	0-5	0	Analysis40RP
261929	0-5	0	Analysis40RP
261930	0-5	0	Analysis40RP
261931	0-5	0	Analysis40RP
261932	0-5	0	Analysis40RP
261933	0-5	0	Analysis40RP
261934	0-5	0	Analysis40RP
261935	0-5	0	Analysis40RP
261936	0-5	0	Analysis40RP
261937	0-5	0	Analysis40RP
261938	0-5	0	Analysis40RP
261939	0-5	0	Analysis40RP
261940	0-5	0	Analysis40RP
261941	0-5	0	Analysis40RP
261942	0-5	0	Analysis40RP
261943	0-5	0	Analysis40RP
261944	0-5	0	Analysis40RP
261945	0-5	0	Analysis40RP
261946	0-5	0	Analysis40RP
261947	0-5	0	Analysis40RP
261948	0-5	0	Analysis40RP
261949	0-5	0	Analysis40RP
261950	0-5	0	Analysis40RP
261951	0-5	0	Analysis40RP
261952	0-5	0	Analysis40RP
261953	0-5	0	Analysis40RP
261954	0-5	0	Analysis40RP
261955	0-5	0	Analysis40RP
261956	0-5	0	Analysis40RP
261957	0-5	0	Analysis40RP
261958	0-5	0	Analysis40RP
261959	0-5	0	Analysis40RP
261960	0-5	0	Analysis40RP
261961	0-5	0	Analysis40RP
261962	0-5	0	Analysis40RP
261963	0-5	0	Analysis40RP
261964	0-5	0	Analysis40RP
261965	0-5	0	Analysis40RP
261969	0-5	0	Analysis40RP
261970	0-4	0	Analysis40RP
261978	0-5	0	Analysis40RP
261990	0-5	0	Analysis40RP
261993	0-5	0	Analysis40RP
261994	0-5	0	Analysis40RP
261995	0-5	0	Analysis40RP
261996	0-5	0	Analysis40RP
261997	0-5	0	Analysis40RP
261998	0-5	0	Analysis40RP
262000	0-5	0	Analysis40RP
262001	0-5	0	Analysis40RP
263473	0-5	0	Analysis40RP
263477	0-5	0	Analysis40RP
263478	0-5	0	Analysis40RP
263479	0-5	0	Analysis40RP
263480	0-5	0	Analysis40RP
263481	0-5	0	Analysis40RP
263482	0-5	0	Analysis40RP
263483	0-5	0	Analysis40RP
263484	0-5	0	Analysis40RP
263491	0-5	0	Analysis40RP
263492	0-5	0	Analysis40RP
263493	0-5	0	Analysis40RP
263494	0-5	0	Analysis40RP
263495	0-5	0	Analysis40RP
263496	0-5	0	Analysis40RP
263497	0-5	0	Analysis40RP
263498	0-5	0	Analysis40RP
263499	0-5	0	Analysis40RP
263500	0-5	0	Analysis40RP
263501	0-5	0	Analysis40RP
263502	0-5	0	Analysis40RP
263503	0-5	0	Analysis40RP
263504	0-5	0	Analysis40RP
263505	0-5	0	Analysis40RP
263506	0-5	0	Analysis40RP

263507	0-5	0	Analysis40RP
263508	0-5	0	Analysis40RP
263509	0-5	0	Analysis40RP
263510	0-5	0	Analysis40RP
263511	0-5	0	Analysis40RP
263512	0-5	0	Analysis40RP
263513	0-5	0	Analysis40RP
263514	0-5	0	Analysis40RP
263515	0-5	0	Analysis40RP
263516	0-5	0	Analysis40RP
263517	0-7	0	Analysis40RP
263518	0-5	0	Analysis40RP
263519	0-5	0	Analysis40RP
263520	0-5	0	Analysis40RP
263521	0-5	0	Analysis40RP
263522	0-5	0	Analysis40RP
263523	0-5	0	Analysis40RP
263524	0-5	0	Analysis40RP
263525	0-5	0	Analysis40RP
263526	0-5	0	Analysis40RP
263527	0-5	0	Analysis40RP
263528	0-5	0	Analysis40RP
263529	0-5	0	Analysis40RP
263530	0-5	0	Analysis40RP
263531	0-5	0	Analysis40RP
263532	0-5	0	Analysis40RP
263533	0-5	0	Analysis40RP
263534	0-5	0	Analysis40RP
263535	0-5	0	Analysis40RP
263536	0-5	0	Analysis40RP
263537	0-5	0	Analysis40RP
263538	0-5	0	Analysis40RP
263539	0-5	0	Analysis40RP
263540	0-5	0	Analysis40RP
263541	0-5	0	Analysis40RP
263542	0-6	0	Analysis40RP
263543	0-5	0	Analysis40RP
263544	0-5	0	Analysis40RP
263547	0-5	0	Analysis40RP
263548	0-5	0	Analysis40RP
263549	0-5	0	Analysis40RP
263550	0-5	0	Analysis40RP
263551	0-5	0	Analysis40RP
263552	0-5	0	Analysis40RP
263553	0-5	0	Analysis40RP
263554	0-5	0	Analysis40RP
263555	0-5	0	Analysis40RP
263556	0-5	0	Analysis40RP
263557	0-5	0	Analysis40RP
263558	0-5	0	Analysis40RP
263559	0-5	0	Analysis40RP
263560	0-5	0	Analysis40RP
263561	0-5	0	Analysis40RP
263562	0-5	0	Analysis40RP
263563	0-5	0	Analysis40RP
263564	0-5	0	Analysis40RP
263565	0-5	0	Analysis40RP
263566	0-5	0	Analysis40RP
263567	0-5	0	Analysis40RP
263568	0-5	0	Analysis40RP
263569	0-5	0	Analysis40RP
263570	0-5	0	Analysis40RP
263571	0-5	0	Analysis40RP
263572	0-5	0	Analysis40RP
263573	0-5	0	Analysis40RP
263574	0-5	0	Analysis40RP
263575	0-5	0	Analysis40RP
263576	0-5	0	Analysis40RP
263577	0-5	0	Analysis40RP
263578	0-5	0	Analysis40RP
263583	0-5	0	Analysis40RP
263584	0-5	0	Analysis40RP
263585	0-5	0	Analysis40RP
263586	0-5	0	Analysis40RP
263587	0-5	0	Analysis40RP
263588	0-5	0	Analysis40RP
263589	0-5	0	Analysis40RP
263590	0-5	0	Analysis40RP
263591	0-5	0	Analysis40RP
263593	0-5	0	Analysis40RP
263594	0-5	0	Analysis40RP
263595	0-5	0	Analysis40RP
263596	0-5	0	Analysis40RP
263597	0-5	0	Analysis40RP
263598	0-5	0	Analysis40RP
263599	0-5	0	Analysis40RP
263600	0-5	0	Analysis40RP
263601	0-5	0	Analysis40RP
263602	0-5	0	Analysis40RP
263603	0-5	0	Analysis40RP
263604	0-5	0	Analysis40RP
263605	0-5	0	Analysis40RP
263606	0-5	0	Analysis40RP
263607	0-5	0	Analysis40RP
263608	0-5	0	Analysis40RP
263609	0-5	0	Analysis40RP
263610	0-5	0	Analysis40RP
263611	0-5	0	Analysis40RP
263612	0-5	0	Analysis40RP
263613	0-5	0	Analysis40RP
263614	0-5	0	Analysis40RP
263615	0-5	0	Analysis40RP
263616	0-5	0	Analysis40RP
263617	0-5	0	Analysis40RP
263618	0-5	0	Analysis40RP
263619	0-5	0	Analysis40RP
263620	0-5	0	Analysis40RP
263621	0-5	0	Analysis40RP
263622	0-5	0	Analysis40RP
263623	0-5	0	Analysis40RP
263624	0-5	0	Analysis40RP
263625	0-5	0	Analysis40RP
263626	0-5	0	Analysis40RP
263627	0-5	0	Analysis40RP
263628	0-5	0	Analysis40RP
263629	0-5	0	Analysis40RP
263630	0-5	0	Analysis40RP
263639	0-5	0	Analysis40RP
263640	0-5	0	Analysis40RP
263641	0-5	0	Analysis40RP
263642	0-5	0	Analysis40RP
263643	0-5	0	Analysis40RP
263644	0-5	0	Analysis40RP
263645	0-5	0	Analysis40RP
263646	0-5	0	Analysis40RP
263647	0-5	0	Analysis40RP
263648	0-5	0	Analysis40RP
263649	0-5	0	Analysis40RP
263650	0-5	0	Analysis40RP
263651	0-5	0	Analysis40RP

263652	0-5	0	Analysis40RP
263653	0-5	0	Analysis40RP
263654	0-5	0	Analysis40RP
263655	0-5	0	Analysis40RP
263656	0-5	0	Analysis40RP
263657	0-5	0	Analysis40RP
263658	0-5	0	Analysis40RP
263659	0-5	0	Analysis40RP
263660	0-5	0	Analysis40RP
263661	0-5	0	Analysis40RP
263662	0-5	0	Analysis40RP
263663	0-5	0	Analysis40RP
263664	0-5	0	Analysis40RP
263665	0-5	0	Analysis40RP
263666	0-5	0	Analysis40RP
263667	0-5	0	Analysis40RP
263668	0-5	0	Analysis40RP
263669	0-5	0	Analysis40RP
263670	0-5	0	Analysis40RP
263671	0-5	0	Analysis40RP
263672	0-5	0	Analysis40RP
263673	0-5	0	Analysis40RP
263674	0-5	0	Analysis40RP
263675	0-5	0	Analysis40RP
263676	0-5	0	Analysis40RP
263677	0-5	0	Analysis40RP
263678	0-5	0	Analysis40RP
263679	0-5	0	Analysis40RP
263680	0-5	0	Analysis40RP
263681	0-5	0	Analysis40RP
263682	0-5	0	Analysis40RP
263683	0-5	0	Analysis40RP
263684	0-5	0	Analysis40RP
263685	0-5	0	Analysis40RP
263701	0-10	0	Analysis40RP
263702	0-10	0	Analysis40RP
263703	0-10	0	Analysis40RP
263704	0-10	0	Analysis40RP
263705	0-10	0	Analysis40RP
263706	0-8	0	Analysis40RP
263722	0-10	0	Analysis40RP
263728	0-6	0	Analysis40RP
263732	0-10	0	Analysis40RP
263733	0-10	0	Analysis40RP
263734	0-10	0	Analysis40RP
263735	0-10	0	Analysis40RP
263736	0-10	0	Analysis40RP
263740	0-10	0	Analysis40RP
263741	0-10	0	Analysis40RP
263752	0-10	0	Analysis40RP
263756	0-10	0	Analysis40RP
263757	0-8	0	Analysis40RP
263761	0-10	0	Analysis40RP
263762	0-10	0	Analysis40RP
263763	0-10	0	Analysis40RP
263764	0-10	0	Analysis40RP
263765	0-10	0	Analysis40RP
263767	0-10	0	Analysis40RP
263768	0-10	0	Analysis40RP
263769	0-10	0	Analysis40RP
263776	0-10	0	Analysis40RP
263777	0-10	0	Analysis40RP
263778	0-10	0	Analysis40RP
263779	0-10	0	Analysis40RP
263780	0-10	0	Analysis40RP
263781	0-10	0	Analysis40RP
263782	0-10	0	Analysis40RP
263783	0-10	0	Analysis40RP
263784	0-10	0	Analysis40RP
263786	0-10	0	Analysis40RP
263787	0-10	0	Analysis40RP
263788	0-10	0	Analysis40RP
263789	0-10	0	Analysis40RP
263790	0-10	0	Analysis40RP
263792	0-10	0	Analysis40RP
263793	0-10	0	Analysis40RP
263794	0-10	0	Analysis40RP
263795	0-10	0	Analysis40RP
263796	0-10	0	Analysis40RP
263797	0-10	0	Analysis40RP
263798	0-10	0	Analysis40RP
263799	0-10	0	Analysis40RP
263801	0-10	0	Analysis40RP
263802	0-10	0	Analysis40RP
263803	0-10	0	Analysis40RP
263804	0-10	0	Analysis40RP
263805	0-10	0	Analysis40RP
263806	0-10	0	Analysis40RP
263807	0-10	0	Analysis40RP
263808	0-10	0	Analysis40RP
263809	0-10	0	Analysis40RP
263810	0-10	0	Analysis40RP
263811	0-10	0	Analysis40RP
263812	0-10	0	Analysis40RP
263813	0-10	0	Analysis40RP
263814	0-10	0	Analysis40RP
263815	0-10	0	Analysis40RP
263816	0-10	0	Analysis40RP
263817	0-10	0	Analysis40RP
263818	0-10	0	Analysis40RP
263819	0-10	0	Analysis40RP
263820	0-10	0	Analysis40RP
263821	0-10	0	Analysis40RP
263822	0-10	0	Analysis40RP
263823	0-10	0	Analysis40RP
263825	0-10	0	Analysis40RP
263826	0-10	0	Analysis40RP
263827	0-10	0	Analysis40RP
263828	0-10	0	Analysis40RP
263829	0-10	0	Analysis40RP
263830	0-10	0	Analysis40RP
263831	0-10	0	Analysis40RP
263832	0-10	0	Analysis40RP
263833	0-10	0	Analysis40RP
263834	0-5	0	Analysis40RP
263836	0-10	0	Analysis40RP
263837	0-10	0	Analysis40RP
263838	0-10	0	Analysis40RP
263839	0-10	0	Analysis40RP
263840	0-10	0	Analysis40RP
263841	0-10	0	Analysis40RP
263842	0-10	0	Analysis40RP
263843	0-10	0	Analysis40RP
263844	0-10	0	Analysis40RP
263845	0-10	0	Analysis40RP
263846	0-10	0	Analysis40RP
263847	0-10	0	Analysis40RP
263849	0-10	0	Analysis40RP
263850	0-10	0	Analysis40RP
263851	0-10	0	Analysis40RP

263852	0-10	0	Analysis40RP	263964	0-11	0	Analysis40RP
263853	0-10	0	Analysis40RP	263965	0-11	0	Analysis40RP
263854	0-10	0	Analysis40RP	263966	0-11	0	Analysis40RP
263855	0-10	0	Analysis40RP	263967	0-11	0	Analysis40RP
263856	0-10	0	Analysis40RP	263968	0-11	0	Analysis40RP
263857	0-10	0	Analysis40RP	263970	0-11	0	Analysis40RP
263858	0-10	0	Analysis40RP	263971	0-11	0	Analysis40RP
263859	0-10	0	Analysis40RP	263972	0-11	0	Analysis40RP
263860	0-10	0	Analysis40RP	263973	0-14	0	Analysis40RP
263861	0-10	0	Analysis40RP	263974	0-11	0	Analysis40RP
263862	0-10	0	Analysis40RP	263975	0-11	0	Analysis40RP
263863	0-10	0	Analysis40RP	263976	0-11	0	Analysis40RP
263864	0-10	0	Analysis40RP	263977	0-11	0	Analysis40RP
263865	0-10	0	Analysis40RP	263978	0-11	0	Analysis40RP
263866	0-8	0	Analysis40RP	263979	0-11	0	Analysis40RP
263868	0-10	0	Analysis40RP	263980	0-11	0	Analysis40RP
263869	0-10	0	Analysis40RP	263981	0-11	0	Analysis40RP
263870	0-10	0	Analysis40RP	263982	0-11	0	Analysis40RP
263871	0-10	0	Analysis40RP	263983	0-11	0	Analysis40RP
263872	0-10	0	Analysis40RP	263984	0-11	0	Analysis40RP
263873	0-10	0	Analysis40RP	263985	0-11	0	Analysis40RP
263874	0-10	0	Analysis40RP	263986	0-11	0	Analysis40RP
263876	0-10	0	Analysis40RP	263987	0-11	0	Analysis40RP
263877	0-10	0	Analysis40RP	263988	0-11	0	Analysis40RP
263879	0-10	0	Analysis40RP	263989	0-11	0	Analysis40RP
263881	0-10	0	Analysis40RP	263990	0-11	0	Analysis40RP
263883	0-10	0	Analysis40RP	264001	0-11	0	Analysis40RP
263886	0-10	0	Analysis40RP	264002	0-11	0	Analysis40RP
263887	0-10	0	Analysis40RP	264003	0-11	0	Analysis40RP
263889	0-10	0	Analysis40RP	264004	0-11	0	Analysis40RP
263891	0-8	0	Analysis40RP	264005	0-11	0	Analysis40RP
263892	0-7	0	Analysis40RP	264007	0-11	0	Analysis40RP
263902	0-11	0	Analysis40RP	264009	0-11	0	Analysis40RP
263903	0-11	0	Analysis40RP	264011	0-11	0	Analysis40RP
263909	0-10	0	Analysis40RP	264013	0-11	0	Analysis40RP
263910	0-10	0	Analysis40RP	264015	0-11	0	Analysis40RP
263911	0-10	0	Analysis40RP	264016	0-11	0	Analysis40RP
263912	0-7	0	Analysis40RP	264017	0-11	0	Analysis40RP
263913	0-11	0	Analysis40RP	264018	0-11	0	Analysis40RP
263914	0-10	0	Analysis40RP	264019	0-11	0	Analysis40RP
263915	0-10	0	Analysis40RP	264021	0-11	0	Analysis40RP
263916	0-10	0	Analysis40RP	264023	0-11	0	Analysis40RP
263917	0-10	0	Analysis40RP	264024	0-11	0	Analysis40RP
263932	0-8	0	Analysis40RP	264026	0-11	0	Analysis40RP
263934	0-11	0	Analysis40RP	264027	0-11	0	Analysis40RP
263935	0-10	0	Analysis40RP	264029	0-11	0	Analysis40RP
263936	0-10	0	Analysis40RP	264030	0-11	0	Analysis40RP
263937	0-11	0	Analysis40RP	264031	0-11	0	Analysis40RP
263938	0-10	0	Analysis40RP	264032	0-11	0	Analysis40RP
263939	0-11	0	Analysis40RP	264033	0-11	0	Analysis40RP
263940	0-10	0	Analysis40RP	264035	0-11	0	Analysis40RP
263941	0-10	0	Analysis40RP	264036	0-11	0	Analysis40RP
263942	0-11	0	Analysis40RP	264038	0-11	0	Analysis40RP
263943	0-10	0	Analysis40RP	264042	0-11	0	Analysis40RP
263944	0-11	0	Analysis40RP	264044	0-11	0	Analysis40RP
263945	0-10	0	Analysis40RP	264045	0-11	0	Analysis40RP
263946	0-10	0	Analysis40RP	264047	0-11	0	Analysis40RP
263947	0-10	0	Analysis40RP	264048	0-11	0	Analysis40RP
263948	0-10	0	Analysis40RP	264049	0-11	0	Analysis40RP
263949	0-10	0	Analysis40RP	264050	0-11	0	Analysis40RP
263950	0-10	0	Analysis40RP	264054	0-11	0	Analysis40RP
263951	0-6	0	Analysis40RP	264057	0-11	0	Analysis40RP
263961	0-11	0	Analysis40RP	264058	0-11	0	Analysis40RP
263962	0-11	0	Analysis40RP	264060	0-11	0	Analysis40RP
263963	0-11	0	Analysis40RP	264065	0-11	0	Analysis40RP

264066	0-11	0	Analysis40RP
264067	0-11	0	Analysis40RP
264068	0-11	0	Analysis40RP
264069	0-11	0	Analysis40RP
264070	0-11	0	Analysis40RP
264072	0-11	0	Analysis40RP
264073	0-11	0	Analysis40RP
264074	0-11	0	Analysis40RP
264075	0-11	0	Analysis40RP
264076	0-11	0	Analysis40RP
264077	0-11	0	Analysis40RP
264078	0-11	0	Analysis40RP
264079	0-11	0	Analysis40RP
264080	0-11	0	Analysis40RP
264081	0-11	0	Analysis40RP
264082	0-11	0	Analysis40RP
264083	0-11	0	Analysis40RP
264084	0-7	0	Analysis40RP
264096	0-11	0	Analysis40RP
264097	0-11	0	Analysis40RP
264102	0-11	0	Analysis40RP
264103	0-11	0	Analysis40RP
264108	0-11	0	Analysis40RP
264109	0-11	0	Analysis40RP
264110	0-11	0	Analysis40RP
264111	0-11	0	Analysis40RP
264112	0-11	0	Analysis40RP
264113	0-11	0	Analysis40RP
264114	0-11	0	Analysis40RP
264115	0-11	0	Analysis40RP
264116	0-11	0	Analysis40RP
264117	0-11	0	Analysis40RP
264118	0-11	0	Analysis40RP
264119	0-11	0	Analysis40RP
264120	0-11	0	Analysis40RP
264121	0-11	0	Analysis40RP
264126	0-11	0	Analysis40RP
264127	0-11	0	Analysis40RP
264128	0-11	0	Analysis40RP
264129	0-11	0	Analysis40RP
264130	0-11	0	Analysis40RP
264131	0-11	0	Analysis40RP
264145	0-11	0	Analysis40RP
264146	0-11	0	Analysis40RP
264147	0-11	0	Analysis40RP
264148	0-11	0	Analysis40RP
264149	0-10	0	Analysis40RP
264156	0-11	0	Analysis40RP
264157	0-11	0	Analysis40RP
264158	0-11	0	Analysis40RP
264159	0-11	0	Analysis40RP
264160	0-11	0	Analysis40RP
264161	0-11	0	Analysis40RP
264167	0-11	0	Analysis40RP
264168	0-11	0	Analysis40RP
264169	0-11	0	Analysis40RP
264170	0-11	0	Analysis40RP
264171	0-11	0	Analysis40RP
264172	0-11	0	Analysis40RP
264173	0-11	0	Analysis40RP
264174	0-11	0	Analysis40RP
264175	0-11	0	Analysis40RP
264176	0-11	0	Analysis40RP
264177	0-11	0	Analysis40RP
264178	0-11	0	Analysis40RP
264179	0-11	0	Analysis40RP
264180	0-11	0	Analysis40RP
264181	0-11	0	Analysis40RP
264182	0-11	0	Analysis40RP
264183	0-11	0	Analysis40RP
264185	0-11	0	Analysis40RP
264188	0-11	0	Analysis40RP
264189	0-11	0	Analysis40RP
264191	0-11	0	Analysis40RP
264193	0-7	0	Analysis40RP
264195	0-11	0	Analysis40RP
264196	0-11	0	Analysis40RP
264197	0-11	0	Analysis40RP
264198	0-11	0	Analysis40RP
264199	0-11	0	Analysis40RP
264202	0-11	0	Analysis40RP
264203	0-11	0	Analysis40RP
264204	0-11	0	Analysis40RP
264205	0-11	0	Analysis40RP
264206	0-11	0	Analysis40RP
264213	0-11	0	Analysis40RP
264215	0-11	0	Analysis40RP
264216	0-11	0	Analysis40RP
264217	0-11	0	Analysis40RP
264218	0-11	0	Analysis40RP
264219	0-11	0	Analysis40RP
264220	0-10	0	Analysis40RP
264221	0-11	0	Analysis40RP
264222	0-11	0	Analysis40RP
264223	0-11	0	Analysis40RP
264224	0-11	0	Analysis40RP
264225	0-11	0	Analysis40RP
264226	0-11	0	Analysis40RP
264227	0-11	0	Analysis40RP
264228	0-11	0	Analysis40RP
264229	0-11	0	Analysis40RP
264230	0-11	0	Analysis40RP
264232	0-11	0	Analysis40RP
264233	0-11	0	Analysis40RP
264234	0-11	0	Analysis40RP
264236	0-11	0	Analysis40RP
264237	0-11	0	Analysis40RP
264238	0-11	0	Analysis40RP
264239	0-11	0	Analysis40RP
264240	0-11	0	Analysis40RP
264241	0-11	0	Analysis40RP
264242	0-8	0	Analysis40RP
264247	0-11	0	Analysis40RP
264248	0-11	0	Analysis40RP
264249	0-11	0	Analysis40RP
264250	0-11	0	Analysis40RP
264251	0-11	0	Analysis40RP
264252	0-11	0	Analysis40RP
264253	0-11	0	Analysis40RP
264255	0-11	0	Analysis40RP
264256	0-11	0	Analysis40RP
264257	0-11	0	Analysis40RP
264258	0-11	0	Analysis40RP
264259	0-10	0	Analysis40RP
264260	0-11	0	Analysis40RP
264261	0-11	0	Analysis40RP
264262	0-11	0	Analysis40RP
264263	0-11	0	Analysis40RP
264264	0-11	0	Analysis40RP
264265	0-11	0	Analysis40RP

264266	0-11	0	Analysis40RP
264267	0-11	0	Analysis40RP
264268	0-5	0	Analysis40RP
264269	0-11	0	Analysis40RP
264270	0-11	0	Analysis40RP
264271	0-11	0	Analysis40RP
264272	0-11	0	Analysis40RP
264273	0-11	0	Analysis40RP
264274	0-11	0	Analysis40RP
264275	0-11	0	Analysis40RP
264276	0-11	0	Analysis40RP
264277	0-11	0	Analysis40RP
264278	0-11	0	Analysis40RP
264279	0-11	0	Analysis40RP
264280	0-11	0	Analysis40RP
264281	0-7	0	Analysis40RP
264284	0-11	0	Analysis40RP
264285	0-11	0	Analysis40RP
264286	0-11	0	Analysis40RP
264287	0-11	0	Analysis40RP
264288	0-10	0	Analysis40RP
264289	0-11	0	Analysis40RP
264292	0-11	0	Analysis40RP
264293	0-11	0	Analysis40RP
264298	0-11	0	Analysis40RP
264299	0-11	0	Analysis40RP
264301	0-11	0	Analysis40RP
264302	0-11	0	Analysis40RP
264303	0-11	0	Analysis40RP
264304	0-11	0	Analysis40RP
264305	0-11	0	Analysis40RP
264306	0-11	0	Analysis40RP
264307	0-11	0	Analysis40RP
264308	0-10	0	Analysis40RP
264309	0-11	0	Analysis40RP
264310	0-11	0	Analysis40RP
264311	0-11	0	Analysis40RP
264312	0-11	0	Analysis40RP
264313	0-11	0	Analysis40RP
264314	0-11	0	Analysis40RP
264316	0-11	0	Analysis40RP
264317	0-10	0	Analysis40RP
264318	0-11	0	Analysis40RP
264320	0-11	0	Analysis40RP
264321	0-11	0	Analysis40RP
264322	0-11	0	Analysis40RP
264323	0-11	0	Analysis40RP
264324	0-11	0	Analysis40RP
264325	0-11	0	Analysis40RP
264326	0-11	0	Analysis40RP
264327	0-11	0	Analysis40RP
264328	0-11	0	Analysis40RP
264329	0-11	0	Analysis40RP
264330	0-11	0	Analysis40RP
264331	0-5	0	Analysis40RP
264332	0-11	0	Analysis40RP
264333	0-11	0	Analysis40RP
264334	0-11	0	Analysis40RP
264335	0-11	0	Analysis40RP
264336	0-11	0	Analysis40RP
264337	0-11	0	Analysis40RP
264338	0-11	0	Analysis40RP
264339	0-11	0	Analysis40RP
264340	0-11	0	Analysis40RP
264341	0-11	0	Analysis40RP
264342	0-11	0	Analysis40RP
264343	0-11	0	Analysis40RP
264344	0-11	0	Analysis40RP
264345	0-11	0	Analysis40RP
264346	0-11	0	Analysis40RP
264347	0-11	0	Analysis40RP
264348	0-11	0	Analysis40RP
264349	0-11	0	Analysis40RP
264350	0-11	0	Analysis40RP
264351	0-11	0	Analysis40RP
264352	0-11	0	Analysis40RP
264353	0-11	0	Analysis40RP
264354	0-11	0	Analysis40RP
264355	0-11	0	Analysis40RP
264356	0-11	0	Analysis40RP
264357	0-11	0	Analysis40RP
264358	0-11	0	Analysis40RP
264359	0-11	0	Analysis40RP
264360	0-11	0	Analysis40RP
264361	0-11	0	Analysis40RP
264362	0-11	0	Analysis40RP
264363	0-11	0	Analysis40RP
264364	0-11	0	Analysis40RP
264365	0-11	0	Analysis40RP
264366	0-11	0	Analysis40RP
264367	0-11	0	Analysis40RP
264368	0-11	0	Analysis40RP
264369	0-11	0	Analysis40RP
264370	0-11	0	Analysis40RP
264371	0-11	0	Analysis40RP
264372	0-11	0	Analysis40RP
264373	0-11	0	Analysis40RP
264374	0-11	0	Analysis40RP
264375	0-11	0	Analysis40RP
264376	0-11	0	Analysis40RP
264377	0-11	0	Analysis40RP
264381	0-11	0	Analysis40RP
264382	0-11	0	Analysis40RP
264383	0-11	0	Analysis40RP
264384	0-11	0	Analysis40RP
264386	0-11	0	Analysis40RP
264387	0-11	0	Analysis40RP
264388	0-11	0	Analysis40RP
264389	0-11	0	Analysis40RP
264390	0-11	0	Analysis40RP
264391	0-11	0	Analysis40RP
264392	0-11	0	Analysis40RP
264393	0-11	0	Analysis40RP
264394	0-11	0	Analysis40RP
264395	0-11	0	Analysis40RP
264396	0-11	0	Analysis40RP
264397	0-11	0	Analysis40RP
264398	0-11	0	Analysis40RP
264399	0-11	0	Analysis40RP
264400	0-11	0	Analysis40RP
264401	0-11	0	Analysis40RP
264402	0-11	0	Analysis40RP
264403	0-11	0	Analysis40RP
264404	0-11	0	Analysis40RP
264405	0-11	0	Analysis40RP
264406	0-11	0	Analysis40RP
264407	0-11	0	Analysis40RP
264408	0-11	0	Analysis40RP
264409	0-11	0	Analysis40RP
264410	0-11	0	Analysis40RP

264411	0-11	0	Analysis40RP
264412	0-11	0	Analysis40RP
264413	0-11	0	Analysis40RP
264414	0-11	0	Analysis40RP
264432	0-11	0	Analysis40RP
264434	0-11	0	Analysis40RP
264436	0-11	0	Analysis40RP
264437	0-11	0	Analysis40RP
264438	0-11	0	Analysis40RP
264439	0-11	0	Analysis40RP
264440	0-11	0	Analysis40RP
264441	0-11	0	Analysis40RP
264442	0-11	0	Analysis40RP
264443	0-11	0	Analysis40RP
264444	0-11	0	Analysis40RP
264445	0-11	0	Analysis40RP
264446	0-11	0	Analysis40RP
264447	0-11	0	Analysis40RP
264448	0-11	0	Analysis40RP
264449	0-11	0	Analysis40RP
264450	0-11	0	Analysis40RP
264451	0-11	0	Analysis40RP
264452	0-11	0	Analysis40RP
264453	0-11	0	Analysis40RP
264456	0-11	0	Analysis40RP
264457	0-11	0	Analysis40RP
264458	0-11	0	Analysis40RP
264459	0-11	0	Analysis40RP
264460	0-11	0	Analysis40RP
264461	0-11	0	Analysis40RP
264462	0-11	0	Analysis40RP
264463	0-11	0	Analysis40RP
264464	0-11	0	Analysis40RP
264465	0-11	0	Analysis40RP
264466	0-11	0	Analysis40RP
264467	0-11	0	Analysis40RP
264468	0-11	0	Analysis40RP
264474	0-11	0	Analysis40RP
264478	0-11	0	Analysis40RP
264479	0-11	0	Analysis40RP
264480	0-6	0	Analysis40RP
264500	0-11	0	Analysis40RP
264501	0-11	0	Analysis40RP
264502	0-11	0	Analysis40RP
264503	0-11	0	Analysis40RP
264504	0-11	0	Analysis40RP
264505	0-11	0	Analysis40RP
264506	0-11	0	Analysis40RP
264507	0-11	0	Analysis40RP
264508	0-11	0	Analysis40RP
264509	0-11	0	Analysis40RP
264510	0-11	0	Analysis40RP
264512	0-11	0	Analysis40RP
264513	0-11	0	Analysis40RP
264514	0-11	0	Analysis40RP
264515	0-11	0	Analysis40RP
264516	0-11	0	Analysis40RP
264517	0-11	0	Analysis40RP
264518	0-11	0	Analysis40RP
264519	0-11	0	Analysis40RP
264520	0-11	0	Analysis40RP
264521	0-11	0	Analysis40RP
264522	0-11	0	Analysis40RP
264523	0-11	0	Analysis40RP
264525	0-11	0	Analysis40RP
264526	0-11	0	Analysis40RP
264527	0-11	0	Analysis40RP
264528	0-11	0	Analysis40RP
264529	0-11	0	Analysis40RP
264530	0-11	0	Analysis40RP
264531	0-11	0	Analysis40RP
264532	0-11	0	Analysis40RP
264533	0-11	0	Analysis40RP
264534	0-11	0	Analysis40RP
264535	0-11	0	Analysis40RP
264536	0-11	0	Analysis40RP
264537	0-11	0	Analysis40RP
264538	0-11	0	Analysis40RP
264539	0-11	0	Analysis40RP
264540	0-11	0	Analysis40RP
264541	0-11	0	Analysis40RP
264542	0-9	0	Analysis40RP
264543	0-11	0	Analysis40RP
264544	0-11	0	Analysis40RP
264545	0-11	0	Analysis40RP
264546	0-11	0	Analysis40RP
264547	0-11	0	Analysis40RP
264548	0-11	0	Analysis40RP
264551	0-11	0	Analysis40RP
264552	0-11	0	Analysis40RP
264553	0-11	0	Analysis40RP
264554	0-11	0	Analysis40RP
264555	0-11	0	Analysis40RP
264556	0-11	0	Analysis40RP
264557	0-11	0	Analysis40RP
264558	0-11	0	Analysis40RP
264559	0-11	0	Analysis40RP
264560	0-11	0	Analysis40RP
264561	0-11	0	Analysis40RP
264562	0-11	0	Analysis40RP
264563	0-11	0	Analysis40RP
264564	0-11	0	Analysis40RP
264565	0-11	0	Analysis40RP
264566	0-11	0	Analysis40RP
264567	0-11	0	Analysis40RP
264568	0-11	0	Analysis40RP
264569	0-11	0	Analysis40RP
264570	0-11	0	Analysis40RP
264571	0-11	0	Analysis40RP
264572	0-11	0	Analysis40RP
264573	0-11	0	Analysis40RP
264574	0-11	0	Analysis40RP
264575	0-11	0	Analysis40RP
264576	0-11	0	Analysis40RP
264577	0-6	0	Analysis40RP
264578	0-11	0	Analysis40RP
264579	0-11	0	Analysis40RP
264580	0-11	0	Analysis40RP
264581	0-11	0	Analysis40RP
264582	0-11	0	Analysis40RP
264583	0-11	0	Analysis40RP
264584	0-7	0	Analysis40RP
264589	0-11	0	Analysis40RP
264590	0-11	0	Analysis40RP
264591	0-10	0	Analysis40RP
264593	0-11	0	Analysis40RP
264597	0-11	0	Analysis40RP
264598	0-11	0	Analysis40RP
264599	0-11	0	Analysis40RP
264600	0-11	0	Analysis40RP

264601	0-11	0	Analysis40RP
264602	0-11	0	Analysis40RP
264603	0-11	0	Analysis40RP
264604	0-11	0	Analysis40RP
264605	0-11	0	Analysis40RP
264606	0-11	0	Analysis40RP
264607	0-11	0	Analysis40RP
264608	0-11	0	Analysis40RP
264609	0-11	0	Analysis40RP
264610	0-11	0	Analysis40RP
264611	0-9	0	Analysis40RP
264613	0-11	0	Analysis40RP
264614	0-9	0	Analysis40RP
264621	0-11	0	Analysis40RP
264622	0-11	0	Analysis40RP
264623	0-11	0	Analysis40RP
264624	0-11	0	Analysis40RP
264625	0-11	0	Analysis40RP
264626	0-11	0	Analysis40RP
264627	0-11	0	Analysis40RP
264628	0-11	0	Analysis40RP
264629	0-11	0	Analysis40RP
264630	0-11	0	Analysis40RP
264631	0-11	0	Analysis40RP
264632	0-11	0	Analysis40RP
264633	0-11	0	Analysis40RP
264634	0-11	0	Analysis40RP
264635	0-11	0	Analysis40RP
264636	0-11	0	Analysis40RP
264637	0-11	0	Analysis40RP
264638	0-11	0	Analysis40RP
264639	0-11	0	Analysis40RP
264640	0-11	0	Analysis40RP
264641	0-11	0	Analysis40RP
264642	0-11	0	Analysis40RP
264643	0-11	0	Analysis40RP
264648	0-7	0	Analysis40RP
264650	0-11	0	Analysis40RP
264651	0-11	0	Analysis40RP
264652	0-11	0	Analysis40RP
264653	0-11	0	Analysis40RP
264654	0-11	0	Analysis40RP
264655	0-11	0	Analysis40RP
264656	0-11	0	Analysis40RP
264657	0-11	0	Analysis40RP
264658	0-11	0	Analysis40RP
264659	0-11	0	Analysis40RP
264660	0-11	0	Analysis40RP
264661	0-11	0	Analysis40RP
264662	0-11	0	Analysis40RP
264663	0-11	0	Analysis40RP
264664	0-11	0	Analysis40RP
264665	0-11	0	Analysis40RP
264666	0-11	0	Analysis40RP
264667	0-11	0	Analysis40RP
264668	0-11	0	Analysis40RP
264669	0-11	0	Analysis40RP
264670	0-11	0	Analysis40RP
264671	0-11	0	Analysis40RP
264672	0-11	0	Analysis40RP
264673	0-11	0	Analysis40RP
264674	0-11	0	Analysis40RP
264675	0-11	0	Analysis40RP
264676	0-11	0	Analysis40RP
264677	0-11	0	Analysis40RP
264678	0-11	0	Analysis40RP
264679	0-11	0	Analysis40RP
264680	0-11	0	Analysis40RP
264681	0-11	0	Analysis40RP
264682	0-11	0	Analysis40RP
264683	0-11	0	Analysis40RP
264684	0-11	0	Analysis40RP
264685	0-11	0	Analysis40RP
264686	0-11	0	Analysis40RP
264687	0-11	0	Analysis40RP
264688	0-11	0	Analysis40RP
264689	0-11	0	Analysis40RP
264690	0-11	0	Analysis40RP
264691	0-11	0	Analysis40RP
264692	0-11	0	Analysis40RP
264693	0-11	0	Analysis40RP
264694	0-11	0	Analysis40RP
264695	0-11	0	Analysis40RP
264696	0-11	0	Analysis40RP
264697	0-11	0	Analysis40RP
264698	0-11	0	Analysis40RP
264699	0-11	0	Analysis40RP
264700	0-11	0	Analysis40RP
264701	0-11	0	Analysis40RP
264702	0-11	0	Analysis40RP
264703	0-11	0	Analysis40RP
264704	0-11	0	Analysis40RP
264705	0-11	0	Analysis40RP
264706	0-11	0	Analysis40RP
264707	0-11	0	Analysis40RP
264708	0-11	0	Analysis40RP
264709	0-11	0	Analysis40RP
264710	0-11	0	Analysis40RP
264712	0-11	0	Analysis40RP
264713	0-11	0	Analysis40RP
264714	0-11	0	Analysis40RP
264716	0-11	0	Analysis40RP

Table B.2: MC files used in the ^{8}B partial fill analysis. All files use the PartialScint module and all are the scintillator ("ScintRun") component only unless otherwise stated. The pass number is indicated by entries in each column, with X indicating a missing file corresponding to that run for a particular signal. While the full internal ^{238}U and ^{232}Th chain signal contributions are used in the analysis, files for signals with no events passing cuts in any of the corresponding files are excluded for brevity.

Runs	^{8}B ν_e	^{8}B ν_μ	^{212}BiPo	^{214}BiPo	^{208}Tl	^{210}Tl
257694	0	0	0	0	0	0
257702	0	0	0	0	0	0
257710	0	0	0	0	0	0
257719	0	0	0	0	0	0
257726	0	0	0	0	0	0
257738	0	0	0	0	0	0
257745	0	0	0	0	0	0
257752	0	0	0	0	0	0
257761	0	0	0	0	0	0
257768	0	0	0	0	0	0
257775	0	0	0	0	0	0
257782	0	0	0	0	0	0
257789	0	0	0	0	0	0
257796	0	0	0	0	0	0
257805	0	0	0	0	0	0
257812	0	0	1	2	1	1
257819	0	0	0	0	0	0
257827	0	0	0	0	0	0
257834	0	0	0	0	0	0
257841	0	0	0	0	0	0
257848	0	0	0	0	0	0
257855	0	0	0	0	0	0
257862	0	0	0	0	0	0
257870	0	0	0	0	0	0
257877	0	0	0	0	0	0
257891	0	0	0	0	0	0
257900	0	0	0	0	0	0
257907	0	0	0	0	0	0
257917	0	0	0	0	0	0
257924	0	0	0	0	0	0
257940	0	0	0	0	0	0
257947	0	0	1	2	1	2
257962	0	0	0	0	0	0
257969	0	0	0	0	0	0
257976	0	0	0	0	0	0
258008	0	0	0	0	0	0
258018	0	0	0	0	0	0
258028	0	0	0	0	0	0
258035	0	0	0	0	0	0
258042	0	0	0	0	0	0
258049	0	0	0	0	0	0
258056	0	0	0	0	0	0
258063	0	0	1	4	1	1
258070	0	0	0	0	0	0
258077	0	0	0	0	0	0
258084	0	0	1	2	1	1
258093	0	0	0	0	0	0
258100	0	0	0	0	0	0
258108	0	0	0	0	0	0
258115	0	0	1	2	1	1
258133	0	0	0	0	0	0
258142	0	0	0	0	0	0

258156	0	0	0	0	0	0
258165	0	0	0	0	0	0
258172	0	0	0	0	0	0
258183	0	0	0	0	0	0
258347	0	0	0	0	0	0
258355	0	0	0	0	0	0
258371	0	0	0	0	0	0
258378	0	0	1	2	1	1
258385	0	0	0	0	0	0
258392	0	0	0	0	0	0
258399	0	0	1	2	1	1
258417	0	0	0	0	0	0
258424	0	0	0	0	0	0
258431	0	0	0	0	0	0
258438	0	0	0	0	0	0
258450	0	0	0	0	0	0
258457	0	0	0	0	0	0
258485	0	0	0	0	0	0
258493	0	0	0	0	0	0
258500	0	0	0	0	0	0
258507	0	0	0	0	0	0
258514	0	0	0	0	0	0
258524	0	0	0	0	0	0
258531	0	0	0	0	0	0
258543	0	0	0	0	0	0
258561	0	0	1	2	1	1
258733	0	0	0	0	0	0
258740	0	0	0	0	0	0
258818	0	0	0	0	0	0
258834	0	0	0	0	0	0
258843	0	0	0	0	0	0
258850	0	0	0	0	0	0
258857	0	0	0	0	0	0
258864	0	0	1	2	1	1
258873	0	0	1	2	1	1
258881	0	0	0	0	0	0
258889	0	0	0	0	0	0
258896	0	0	0	0	0	0
258917	0	0	0	0	0	0
258926	0	0	0	0	0	0
258935	0	0	0	0	0	0
258943	0	0	0	0	0	0
258950	0	0	0	0	0	0
258959	0	0	0	0	0	0
258966	0	0	0	0	0	0
258973	0	0	0	0	0	0
259965	0	0	0	0	0	0
259972	0	0	0	0	0	0
259986	0	0	0	0	0	0
259999	0	0	0	0	0	0
260006	0	0	0	0	0	0
260027	0	0	0	0	0	0
260034	0	0	0	0	0	0
260041	0	0	0	0	0	0
260048	0	0	0	0	0	0
260055	0	0	0	0	0	0
260062	0	0	0	0	0	0
260069	0	0	0	0	0	0
260076	0	0	0	0	0	0
260083	0	0	0	0	0	0
260091	0	0	0	0	0	0
260107	0	0	0	0	0	0
260114	0	0	0	0	0	0
260123	0	0	0	0	0	0
260132	0	0	0	0	0	0

260139	0	0	0	0	0	0
260146	0	0	0	0	0	0
260160	0	0	0	0	0	0
260168	0	0	0	0	0	0
260175	0	0	0	0	0	0
260190	0	0	0	0	0	0
260201	0	0	0	0	0	0
260208	0	0	0	0	0	0
260216	0	0	0	0	0	0
260223	0	0	0	0	0	0
260230	0	0	0	0	0	0
260237	0	0	0	0	0	0
260252	0	0	0	0	0	0
260261	0	0	0	0	0	0
260270	0	0	0	0	0	0
260277	0	0	0	0	0	0
260289	0	0	0	0	0	0
260297	0	0	0	0	0	0
260312	0	0	0	0	0	0
260319	0	0	0	0	0	0
260328	0	0	0	0	0	0
260335	0	0	1	2	1	1
260343	0	0	0	0	0	0
260350	0	0	0	0	0	0
260364	0	0	0	0	0	0
260383	0	0	0	0	0	0
260399	0	0	0	0	0	0
260418	0	0	0	0	0	0
260430	0	0	1	4	2	1
260438	0	0	0	0	0	0
260457	0	0	0	0	0	0
260464	0	0	0	0	0	0
260485	0	0	0	0	0	0
260500	0	0	0	0	0	0
260507	0	0	0	0	0	0
260514	0	0	0	0	0	0
260545	0	0	0	0	0	0
260576	0	0	0	0	0	0
260587	0	0	0	0	0	0
260597	0	0	0	0	0	0
260604	0	0	0	0	0	0
260611	0	0	0	0	0	0
260620	0	0	0	0	0	0
260627	0	0	0	0	0	0
260635	0	0	0	0	0	0
260643	0	0	0	0	0	0
260801	0	0	0	0	0	0
260874	0	0	0	0	0	0
260881	0	0	0	0	0	0
260888	0	0	0	0	0	0
260895	0	0	0	0	0	0
260902	0	0	0	0	0	0
260909	0	0	0	0	0	0
260916	0	0	0	0	0	0
260924	0	0	0	0	0	0
260932	0	0	0	0	0	0
260939	0	0	0	0	0	0
260946	0	0	0	0	0	0
260954	0	0	0	0	0	0
260963	0	0	0	0	0	0
260973	0	0	0	0	0	0
260980	0	0	0	0	0	0
260987	0	0	0	0	0	0
260994	0	0	0	0	0	0
261001	0	0	0	0	0	0

261008	0	0	0	0	0	0
261399	0	0	0	0	0	0
261406	0	0	0	0	0	0
261413	0	0	0	0	0	0
261420	0	0	0	0	0	0
261427	0	0	0	0	0	0
261434	0	0	0	0	0	0
261441	0	0	0	0	0	0
261448	0	0	0	0	0	0
261456	0	0	0	0	0	0
261463	0	0	0	0	0	0
261470	0	0	0	0	0	0
261477	0	0	0	0	0	0
261484	0	0	0	0	0	0
261491	0	0	0	0	0	0
261498	0	0	0	0	0	0
261505	0	0	0	0	0	0
261512	0	0	0	0	0	0
261519	0	0	0	0	0	0
261526	0	0	0	0	0	0
261533	0	0	0	0	0	0
261541	0	0	0	0	0	0
261562	0	0	0	0	0	0
261569	0	0	0	0	0	0
261576	0	0	0	0	1	0
261583	0	0	0	0	0	0
261590	0	0	0	0	0	0
261598	0	0	0	0	0	0
261605	0	0	0	0	0	0
261612	0	0	0	0	0	0
261619	0	0	0	0	0	0
261630	0	0	0	0	0	0
261638	0	0	0	0	0	0
261645	0	0	0	0	0	0
261652	0	0	0	0	0	0
261660	0	0	0	0	0	0
261667	0	0	0	0	0	0
261674	0	0	0	0	0	0
261681	0	0	0	0	0	0
261689	0	0	0	0	0	0
261696	0	0	0	0	0	0
261704	0	0	0	0	0	0
261712	0	0	0	0	0	0
261719	0	0	0	0	0	0
261741	0	0	0	0	0	0
261757	0	0	0	0	0	0
261764	0	0	0	0	0	0
261771	0	0	0	0	0	0
261778	0	0	0	0	0	0
261785	0	0	0	0	0	0
261792	0	0	0	0	0	0
261799	0	0	0	0	0	0
261806	0	0	0	0	0	0
261820	0	0	0	0	0	0
261827	0	0	0	0	0	0
261834	0	0	0	0	0	0
261841	0	0	0	0	0	0
261848	0	0	0	0	0	0
261855	0	0	0	0	0	0
261864	0	0	0	0	0	0
261871	0	0	0	0	0	0
261879	0	0	0	0	0	0
261886	0	0	0	0	0	0
261893	0	0	0	0	0	0
261914	0	0	0	0	0	0

261921	0	0	0	0	0	0
261928	0	0	0	0	0	0
261935	0	0	0	0	0	0
261942	0	0	0	0	0	0
261949	0	0	0	0	0	0
261956	0	0	0	0	0	0
261963	0	0	0	0	0	0
261993	0	0	0	0	0	0
262001	0	0	0	0	0	0
263482	0	0	0	0	0	0
263495	0	0	0	0	0	0
263502	0	0	0	0	0	0
263509	0	0	0	0	0	0
263516	0	0	0	0	0	0
263523	0	0	0	0	0	0
263530	0	0	0	0	0	0
263537	0	0	0	0	0	0
263544	0	0	0	0	0	0
263553	0	0	0	0	0	0
263560	0	0	0	0	0	0
263567	0	0	0	0	0	0
263574	0	0	0	0	0	0
263585	0	0	0	0	0	0
263593	0	0	0	0	0	0
263600	0	0	0	0	0	0
263607	0	0	0	0	0	0
263614	0	0	0	0	0	0
263621	0	0	0	0	0	0
263628	0	0	0	0	0	0
263643	0	0	0	0	0	0
263650	0	0	0	0	0	0
263657	0	0	0	0	0	0
263664	0	0	0	0	0	0
263671	0	0	0	0	0	0
263678	0	0	0	0	0	0
263685	0	0	0	0	0	0
263722	0	0	0	0	0	1
263740	0	0	0	0	0	0
263763	0	0	0	0	0	0
263777	0	0	0	0	0	0
263784	0	0	0	0	0	0
263793	0	0	0	0	0	0
263801	0	0	0	0	0	0
263808	0	0	0	0	0	0
263815	0	0	0	0	0	0
263822	0	0	0	0	0	0
263830	0	0	0	0	0	0
263838	0	0	0	0	0	0
263845	0	0	0	0	0	0
263853	0	0	0	1	0	0
263860	0	0	0	0	0	0
263868	0	0	0	0	0	0
263876	0	0	0	0	0	0
263889	0	0	0	0	0	0
263911	0	0	0	0	0	0
263932	0	0	0	0	0	0
263940	0	0	0	0	0	0
263947	0	0	0	0	0	0
263963	0	0	0	0	0	0
263971	0	0	0	0	0	0
263978	0	0	0	0	0	0
263985	0	0	0	0	0	0
264002	0	0	0	0	0	0
264013	0	0	0	0	0	0
264023	0	0	0	0	0	0

264032	0	0	0	0	0	0
264045	0	0	0	0	0	0
264058	0	0	0	0	0	0
264070	0	0	0	0	0	0
264078	0	0	0	0	0	0
264096	0	0	0	0	0	0
264111	0	0	0	0	0	0
264118	0	0	0	0	0	0
264129	0	0	0	0	0	0
264149	0	0	0	0	0	0
264167	0	0	0	0	0	0
264174	0	0	0	0	0	0
264181	0	0	0	0	0	0
264193	0	0	0	0	0	0
264203	0	0	0	0	0	0
264217	0	0	0	0	0	0
264224	0	0	0	0	0	0
264232	0	0	0	0	0	0
264240	0	0	0	0	0	0
264251	0	0	0	0	0	0
264259	0	0	0	0	0	0
264266	0	0	0	0	0	0
264273	0	0	0	0	0	0
264280	0	0	0	0	0	0
264289	0	0	0	0	0	0
264303	0	0	0	0	0	0
264310	0	0	0	0	0	0
264318	0	0	0	0	0	0
264326	0	0	0	0	0	0
264333	0	0	0	0	0	0
264340	0	0	0	0	0	0
264347	0	0	0	0	0	0
264354	0	0	0	0	0	0
264361	0	0	0	0	0	0
264368	0	0	0	0	0	0
264375	0	0	0	0	0	0
264386	0	0	0	0	0	0
264393	0	0	0	0	0	0
264400	0	0	0	0	0	0
264407	0	0	0	0	0	0
264414	0	0	0	0	0	0
264440	0	0	0	0	0	0
264447	0	0	0	0	0	0
264456	0	0	0	0	0	0
264463	0	0	0	0	0	0
264478	0	0	0	0	0	0
264504	0	0	0	0	0	0
264512	0	0	0	0	0	0
264519	0	0	0	0	0	0
264527	0	0	0	0	0	0
264534	0	0	0	0	0	0
264541	0	0	0	0	0	0
264548	0	0	0	0	0	0
264557	0	0	0	0	0	0
264564	0	0	0	0	0	0
264571	0	0	0	0	0	0
264578	0	0	0	0	0	0
264589	0	0	0	0	0	0
264600	0	0	0	0	0	0
264607	0	0	0	0	0	0
264621	0	0	0	0	0	0
264628	0	0	0	0	0	0
264635	0	0	0	0	0	0
264642	0	0	0	0	0	0
264654	0	0	0	0	0	0

264661	0	X	0	0	0	0
264668	0	0	0	0	0	0
264675	0	0	0	0	0	0
264682	0	0	0	0	0	0
264689	0	0	0	0	0	0
264696	0	0	0	0	0	0
264703	0	0	0	0	0	0
264710	0	0	0	0	0	0

Appendix C

Partial Fill Event Selection Cut Efficiencies

Signal	Number of physics events simulated	Triggered events (eff.)	Fitted events (eff.)	skyShine events (eff.)	FV events (eff.)	Energy events (eff.)	Inwindow events (eff.)	Tagged events (eff.)	Overall efficiency
Bi214_beta	1378862	4.78954e+06 (347.354%)	4.78522e+06 (99.9099%)	4.24629e+06 (88.7376%)	897969 (21.1471%)	44 (0.00489995%)	25 (56.8182%)	4 (16%)	0.000290094%
B8_Solar_Nue	424324	254696 (60.024%)	254360 (99.8678%)	217620 (85.556%)	48471.6 (22.2735%)	22036.9 (45.4635%)	22036.9 (100%)	22035.9 (100%)	5.19318%
B8_Solar_Numu	225921	252129 (111.601%)	251753 (99.8506%)	215566 (85.6262%)	47896 (22.2187%)	20874.3 (43.5826%)	20874.3 (100%)	20874.3 (100%)	9.23966%
Tl208	1151077	2.12844e+06 (184.908%)	2.12748e+06 (99.955%)	1.80935e+06 (85.0467%)	377904 (20.8862%)	303857 (80.4059%)	303857 (100%)	303854 (100%)	26.3974%
Tl210	1149803	2.13114e+06 (185.348%)	2.12983e+06 (99.9385%)	1.80182e+06 (84.5992%)	375623 (20.8469%)	220815 (58.7863%)	220815 (100%)	220815 (100%)	19.2046%

Table C.1: For each signal, in the 4.5m FV, the number of surviving events from MC after each successive cut and the associated efficiency. The events include any trigger stemming from a simulated physics events, hence the number of triggers possibly being higher than the number of simulated events. Note that the solar neutrino signals have P_{ee} weighting applied, leading to fractional values.

Signal	Number of physics events simulated	Triggered events (eff.)	Fitted events (eff.)	skyShine events (eff.)	FV events (eff.)	Energy events (eff.)	Inwindow events (eff.)	Tagged events (eff.)	Overall efficiency
Bi214_beta	1378862	4.78954e+06 (347.354%)	4.78522e+06 (99.9099%)	4.24629e+06 (88.7376%)	1.29018e+06 (30.3837%)	51 (0.00395293%)	29 (56.8627%)	6 (20.6897%)	0.000435141%
B8_Solar_Nue	424324	254696 (60.024%)	254360 (99.8678%)	217620 (85.556%)	69403.8 (31.8922%)	31119.4 (44.8382%)	31119.4 (100%)	31118.1 (100%)	7.33358%
B8_Solar_Numu	225921	252129 (111.601%)	251753 (99.8506%)	215566 (85.6262%)	68752.9 (31.8941%)	29606.5 (43.0622%)	29606.5 (100%)	29606.5 (100%)	13.1048%
Tl208	1151077	2.12844e+06 (184.908%)	2.12748e+06 (99.955%)	1.80935e+06 (85.0467%)	539934 (29.8413%)	416849 (77.2037%)	416849 (100%)	416845 (100%)	36.2135%
Tl210	1149803	2.13114e+06 (185.348%)	2.12983e+06 (99.9385%)	1.80182e+06 (84.5992%)	539253 (29.9283%)	307049 (56.9397%)	307049 (100%)	307049 (100%)	26.7045%

Table C.2: For each signal, in the 5.0m FV, the number of surviving events from MC after each successive cut and the associated efficiency. The events include any trigger stemming from a simulated physics events, hence the number of triggers possibly being higher than the number of simulated events. Note that the solar neutrino signals have P_{ee} weighting applied, leading to fractional values.

Signal	Number of physics events simulated	Triggered events (eff.)	Fitted events (eff.)	skyShine events (eff.)	FV events (eff.)	Energy events (eff.)	Inwindow events (eff.)	Tagged events (eff.)	Overall efficiency
Bi214_beta	1378862	4.78954e+06 (347.354%)	4.78522e+06 (99.9099%)	4.24629e+06 (88.7376%)	1.76748e+06 (41.624%)	51 (0.00288547%)	29 (56.8627%)	6 (20.6897%)	0.000435141%
B8_Solar_Nue	424324	254696 (60.024%)	254360 (99.8678%)	217620 (85.556%)	94487.7 (43.4187%)	41308.3 (43.7182%)	41308.3 (100%)	41307 (100%)	9.73478%
B8_Solar_Numu	225921	252129 (111.601%)	251753 (99.8506%)	215566 (85.6262%)	93872.7 (43.547%)	39358.3 (41.9273%)	39358.3 (100%)	39357.6 (100%)	17.421%
Tl208	1151077	2.12844e+06 (184.908%)	2.12748e+06 (99.955%)	1.80935e+06 (85.0467%)	740754 (40.9403%)	509799 (68.8216%)	509799 (100%)	509795 (100%)	44.2885%
Tl210	1149803	2.13114e+06 (185.348%)	2.12983e+06 (99.9385%)	1.80182e+06 (84.5992%)	739058 (41.0174%)	385535 (52.1657%)	385535 (100%)	385535 (100%)	33.5305%

Table C.3: For each signal, in the 5.5m FV, the number of surviving events from MC after each successive cut and the associated efficiency. The events include any trigger stemming from a simulated physics events, hence the number of triggers possibly being higher than the number of simulated events. Note that the solar neutrino signals have P_{ee} weighting applied, leading to fractional values.

Appendix D

Full Fill Analysis Files

Table D.1: Data files used in the ^{8}B full fill analysis organized by run, subruns of that run, and processing pass. The processing module used was Analysis 20R.

Run	Subruns	Pass
300733	0-14	0
300734	0-14	0
300735	0-14	0
300736	0-14	0
300737	0-14	0
300738	0-14	0
300739	0-14	0
300740	0-14	0
300741	0-14	0
300742	0-14	0
300743	0-14	0
300744	0-14	0
300767	0-14	0
300768	0-14	0
300770	0-14	0
300772	0-14	0
300773	0-14	0
300775	0-14	0
300776	0-14	0
300777	0-14	0
300778	0-14	0
300779	0-14	0
300780	0-14	0
300781	0-14	0
300782	0-14	0
300783	0-14	0
300804	0-14	0
300809	0-14	0
300814	0-14	0
300815	0-14	0
300817	0-14	0
300819	0-14	0
300822	0-14	0
300823	0-14	0
300824	0-14	0
300825	0-14	0
300826	0-14	0
300827	0-14	0
300828	0-14	0
300829	0-14	0
300830	0-14	0
300831	0-14	0
300832	0-14	0
300833	0-14	0
300834	0-14	0
300835	0-14	0
300836	0-14	0
300839	0-14	0
300840	0-14	0
300841	0-14	0
300843	0-14	0
300844	0-14	0
300845	0-14	0
300846	0-14	0
300847	0-14	0
300849	0-14	0
300850	0-14	0
300851	0-14	0
300852	0-14	0
300853	0-14	0
300854	0-14	0
300856	0-14	0
300857	0-14	0
300858	0-14	0
300859	0-14	0
300860	0-14	0
300861	0-14	0
300862	0-14	0
300863	0-14	0
300864	0-14	0
300865	0-14	0
300866	0-14	0
300867	0-14	0
300868	0-14	0
300869	0-14	0
300870	0-14	0
300871	0-14	0
300872	0-14	0
300873	0-14	0
300874	0-14	0
300875	0-14	0
300876	0-14	0
300877	0-14	0
300878	0-14	0
300879	0-14	0
300880	0-14	0
300881	0-14	0
300882	0-14	0
300883	0-14	0
300884	0-14	0
300885	0-14	0
300886	0-14	0
300887	0-14	0
300888	0-14	0
300889	0-14	0
300890	0-14	0
300891	0-14	0
300892	0-14	0
300894	0-14	0
300897	0-14	0
300899	0-14	0
300900	0-14	0
300901	0-14	0
300902	0-14	0
300903	0-14	0
300904	0-14	0
300905	0-14	0
300906	0-14	0
300907	0-14	0
300908	0-14	0
300909	0-14	0
300910	0-14	0
300911	0-14	0
300912	0-14	0
300913	0-14	0
300914	0-14	0
300916	0-14	0
300917	0-14	0
300918	0-14	0
300920	0-14	0
300922	0-14	0
300925	0-14	0
300926	0-14	0
300929	0-14	0
300932	0-14	0
300933	0-14	0
300934	0-14	0
300935	0-14	0
300936	0-14	0
300943	0-14	0
300944	0-14	0
300945	0-14	0
300946	0-14	0
300947	0-14	0
300948	0-14	0
300949	0-14	0
300950	0-14	0
300951	0-14	0
300952	0-14	0
300953	0-14	0
300954	0-9	0
300990	0-14	0
300991	0-14	0
300993	0-14	0
300994	0-14	0
300995	0-14	0
300996	0-14	0
300997	0-14	0
300998	0-14	0
300999	0-14	0
301000	0-14	0
301001	0-14	0
301002	0-14	0
301003	0-14	0
301004	0-14	0
301005	0-14	0
301006	0-14	0
301007	0-14	0
301008	0-14	0
301009	0-14	0
301010	0-14	0
301011	0-14	0
301012	0-14	0
301013	0-14	0
301014	0-14	0
301015	0-14	0
301016	0-14	0
301017	0-14	0
301018	0-14	0
301019	0-14	0
301020	0-14	0
301021	0-14	0
301022	0-14	0
301023	0-14	0
301024	0-14	0
301025	0-14	0
301026	0-14	0
301027	0-14	0
301028	0-14	0
301029	0-14	0
301030	0-14	0
301032	0-14	0

301033	0-14	0	
301034	0-14	0	
301035	0-14	0	
301036	0-14	0	
301037	0-14	0	
301038	0-14	0	
301039	0-14	0	
301040	0-14	0	
301041	0-14	0	
301042	0-14	0	
301043	0-14	0	
301044	0-14	0	
301045	0-14	0	
301046	0-14	0	
301047	0-14	0	
301048	0-14	0	
301049	0-14	0	
301050	0-14	0	
301051	0-14	0	
301052	0-14	0	
301053	0-14	0	
301054	0-14	0	
301055	0-14	0	
301056	0-14	0	
301057	0-14	0	
301058	0-14	0	
301059	0-14	0	
301060	0-14	0	
301061	0-14	0	
301062	0-14	0	
301066	0-14	0	
301067	0-14	0	
301068	0-14	0	
301069	0-14	0	
301070	0-14	0	
301071	0-14	0	
301072	0-14	0	
301073	0-14	0	
301074	0-14	0	
301075	0-14	0	
301076	0-14	0	
301077	0-14	0	
301078	0-14	0	
301079	0-14	0	
301080	0-14	0	
301081	0-14	0	
301082	0-14	0	
301083	0-14	0	
301084	0-14	0	
301085	0-14	0	
301086	0-14	0	
301088	0-14	0	
301089	0-14	0	
301090	0-14	0	
301091	0-14	0	
301092	0-14	0	
301093	0-14	0	
301094	0-14	0	
301095	0-14	0	
301096	0-14	0	
301097	0-14	0	
301098	0-14	0	
301099	0-14	0	
301100	0-14	0	
301101	0-14	0	
301102	0-14	0	
301103	0-14	0	
301104	0-14	0	
301108	0-14	0	
301109	0-14	0	
301110	0-14	0	
301111	0-14	0	
301112	0-14	0	
301113	0-14	0	
301114	0-14	0	
301115	0-14	0	
301116	0-14	0	
301117	0-14	0	
301118	0-14	0	
301119	0-14	0	
301120	0-14	0	
301121	0-14	0	
301122	0-14	0	
301123	0-14	0	
301124	0-14	0	
301125	0-14	0	
301126	0-14	0	
301127	0-14	0	
301128	0-14	0	
301129	0-14	0	
301130	0-14	0	
301131	0-14	0	
301132	0-14	0	
301133	0-14	0	
301134	0-14	0	
301135	0-14	0	
301137	0-14	0	
301138	0-14	0	
301139	0-14	0	
301140	0-12	0	
301143	0-14	0	
301144	0-14	0	
301145	0-14	0	
301148	0-14	0	
301178	0-9	0	
301188	0-14	0	
301189	0-14	0	
301190	0-14	0	
301191	0-14	0	
301192	0-14	0	
301193	0-14	0	
301194	0-14	0	
301204	0-14	0	
301205	0-14	0	
301206	0-14	0	
301207	0-14	0	
301208	0-14	0	
301210	0-14	0	
301211	0-14	0	
301212	0-14	0	
301213	0-14	0	
301214	0-14	0	
301215	0-14	0	
301216	0-14	0	
301217	0-14	0	
301218	0-14	0	
301219	0-14	0	
301220	0-14	0	
301221	0-14	0	
301222	0-14	0	
301223	0-14	0	
301225	0-14	0	
301226	0-14	0	
301227	0-14	0	
301228	0-14	0	
301229	0-14	0	
301230	0-14	0	
301231	0-14	0	
301232	0-14	0	
301233	0-14	0	
301234	0-14	0	
301235	0-14	0	
301236	0-14	0	
301237	0-14	0	
301238	0-14	0	
301239	0-14	0	
301240	0-14	0	
301241	0-14	0	
301242	0-14	0	
301246	0-14	0	
301247	0-14	0	
301248	0-14	0	
301249	0-14	0	
301250	0-14	0	
301251	0-14	0	
301252	0-14	0	
301253	0-14	0	
301254	0-14	0	
301255	0-14	0	
301256	0-14	0	
301257	0-14	0	
301258	0-14	0	
301259	0-14	0	
301260	0-14	0	
301261	0-14	0	
301262	0-14	0	
301263	0-14	0	
301264	0-14	0	
301265	0-14	0	
301266	0-14	0	
301267	0-14	0	
301268	0-14	0	
301269	0-14	0	
301270	0-14	0	
301271	0-14	0	
301272	0-14	0	
301273	0-14	0	
301274	0-14	0	
301275	0-14	0	
301276	0-14	0	
301277	0-14	0	
301279	0-14	0	
301280	0-14	0	
301281	0-14	0	
301282	0-14	0	
301286	0-14	0	
301288	0-10	0	
301290	0-14	0	
301299	0-14	0	
301300	0-14	0	
301301	0-14	0	
301302	0-14	0	
301303	0-14	0	
301304	0-14	0	
301305	0-14	0	

301306	0-14	0
301307	0-14	0
301308	0-14	0
301309	0-14	0
301310	0-14	0
301311	0-14	0
301312	0-14	0
301313	0-14	0
301314	0-14	0
301315	0-14	0
301316	0-14	0
301317	0-14	0
301318	0-14	0
301319	0-14	0
301320	0-14	0
301321	0-14	0
301322	0-14	0
301323	0-14	0
301324	0-14	0
301327	0-14	0
301328	0-14	0
301329	0-14	0
301330	0-14	0
301331	0-14	0
301332	0-14	0
301333	0-14	0
301334	0-14	0
301335	0-14	0
301337	0-14	0
301338	0-14	0
301339	0-14	0
301340	0-14	0
301341	0-14	0
301342	0-14	0
301343	0-14	0
301346	0-14	0
301347	0-14	0
301348	0-14	0
301350	0-14	0
301351	0-14	0
301352	0-14	0
301353	0-14	0
301354	0-14	0
301355	0-14	0
301356	0-14	0
301357	0-14	0
301358	0-14	0
301359	0-14	0
301360	0-14	0
301361	0-14	0
301362	0-14	0
301363	0-14	0
301364	0-14	0
301365	0-14	0
301366	0-14	0
301375	0-10	0
301377	0-13	0
301378	0-14	0
301379	0-13	0
301380	0-14	0
301381	0-13	0
301382	0-13	0
301383	0-14	0
301384	0-14	0
301385	0-14	0
301386	0-14	0
301387	0-14	0
301388	0-14	0
301389	0-14	0
301390	0-14	0
301391	0-14	0
301392	0-14	0
301393	0-14	0
301394	0-14	0
301395	0-14	0
301396	0-14	0
301397	0-14	0
301398	0-14	0
301399	0-14	0
301400	0-14	0
301403	0-14	0
301404	0-14	0
301407	0-14	0
301408	0-14	0
301409	0-14	0
301410	0-14	0
301411	0-14	0
301412	0-14	0
301413	0-14	0
301414	0-14	0
301415	0-14	0
301416	0-14	0
301417	0-14	0
301418	0-14	0
301419	0-14	0
301420	0-14	0
301421	0-14	0
301422	0-14	0
301423	0-14	0
301424	0-14	0
301425	0-14	0
301426	0-14	0
301427	0-14	0
301428	0-14	0
301429	0-14	0
301430	0-14	0
301431	0-14	0
301432	0-14	0
301433	0-14	0
301434	0-14	0
301435	0-14	0
301436	0-14	0
301437	0-14	0
301438	0-14	0
301439	0-14	0
301440	0-14	0
301441	0-14	0
301442	0-14	0
301443	0-14	0
301444	0-14	0
301475	0-14	0
301476	0-14	0
301477	0-14	0
301478	0-14	0
301479	0-14	0
301480	0-14	0
301481	0-14	0
301482	0-14	0
301483	0-14	0
301484	0-14	0
301485	0-14	0
301486	0-14	0
301487	0-14	0
301488	0-14	0
301489	0-14	0
301490	0-14	0
301491	0-14	0
301492	0-14	0
301493	0-14	0
301494	0-14	0
301495	0-14	0
301496	0-14	0
301497	0-14	0
301498	0-14	0
301499	0-14	0
301500	0-14	0
301501	0-14	0
301502	0-14	0
301503	0-14	0
301504	0-14	0
301505	0-14	0
301506	0-14	0
301507	0-14	0
301509	0-14	0
301510	0-14	0
301511	0-14	0
301512	0-14	0
301514	0-14	0
301515	0-14	0
301516	0-14	0
301517	0-14	0
301518	0-14	0
301519	0-14	0
301520	0-14	0
301522	0-14	0
301524	0-14	0
301525	0-14	0
301526	0-14	0
301527	0-14	0
301528	0-14	0
301529	0-14	0
301530	0-14	0
301555	0-12	0
301560	0-14	0
301561	0-14	0
301575	0-14	0
301576	0-14	0
301577	0-14	0
301578	0-14	0
301579	0-14	0
301580	0-14	0
301581	0-14	0
301582	0-14	0
301584	0-14	0
301585	0-14	0
301586	0-14	0
301587	0-14	0
301588	0-14	0
301589	0-14	0
301590	0-14	0
301591	0-14	0
301592	0-7	0
301594	0-14	0
301597	0-14	0
301598	0-14	0

301599	0-14	0
301600	0-14	0
301601	0-14	0
301602	0-14	0
301603	0-14	0
301604	0-14	0
301605	0-14	0
301606	0-14	0
301607	0-14	0
301608	0-14	0
301609	0-14	0
301610	0-14	0
301611	0-14	0
301612	0-14	0
301613	0-14	0
301614	0-14	0
301615	0-14	0
301616	0-14	0
301617	0-14	0
301618	0-14	0
301619	0-14	0
301620	0-14	0
301621	0-14	0
301622	0-14	0
301623	0-14	0
301624	0-14	0
301625	0-14	0
301626	0-14	0
301627	0-14	0
301628	0-14	0
301629	0-14	0
301630	0-14	0
301631	0-14	0
301632	0-14	0
301634	0-14	0
301635	0-14	0
301636	0-14	0
301637	0-14	0
301638	0-14	0
301639	0-14	0
301640	0-14	0
301641	0-14	0
301642	0-14	0
301643	0-14	0
301644	0-14	0
301645	0-14	0
301646	0-14	0
301647	0-14	0
301648	0-14	0
301649	0-14	0
301650	0-14	0
301651	0-14	0
301652	0-14	0
301653	0-14	0
301654	0-14	0
301655	0-14	0
301656	0-14	0
301657	0-14	0
301658	0-14	0
301659	0-14	0
301660	0-14	0
301661	0-14	0
301663	0-14	0
301664	0-14	0
301665	0-14	0
301666	0-14	0
301667	0-14	0
301668	0-14	0
301669	0-14	0
301670	0-14	0
301671	0-14	0
301672	0-14	0
301673	0-14	0
301674	0-14	0
301675	0-14	0
301676	0-14	0
301677	0-14	0
301680	0-14	0
301682	0-14	0
301683	0-14	0
301684	0-14	0
301685	0-14	0
301687	0-14	0
301688	0-14	0
301689	0-14	0
301698	0-14	0
301699	0-14	0
301704	0-10	0
301705	0-14	0
301706	0-14	0
301707	0-14	0
301708	0-14	0
301709	0-14	0
301710	0-14	0
301711	0-14	0
301712	0-14	0
301713	0-14	0
301714	0-14	0
301715	0-14	0
301716	0-14	0
301717	0-14	0
301718	0-14	0
301719	0-14	0
301720	0-14	0
301721	0-14	0
301722	0-14	0
301723	0-14	0
301724	0-14	0
301725	0-14	0
301726	0-14	0
301727	0-14	0
301728	0-14	0
301729	0-14	0
301730	0-14	0
301731	0-14	0
301732	0-14	0
301733	0-14	0
301734	0-14	0
301735	0-14	0
301736	0-14	0
301737	0-14	0
301738	0-14	0
301739	0-14	0
301740	0-14	0
301741	0-14	0
301743	0-14	0
301744	0-14	0
301745	0-14	0
301748	0-14	0
301758	0-14	0
301759	0-14	0
301761	0-14	0
301762	0-14	0
301763	0-14	0
301764	0-14	0
301765	0-14	0
301766	0-14	0
301767	0-14	0
301768	0-14	0
301769	0-14	0
301770	0-14	0
301771	0-14	0
301772	0-14	0
301773	0-14	0
301774	0-11	0
301778	0-12	0
301781	0-14	0
301782	0-14	0
301783	0-7	0
301786	0-14	0
301787	0-14	0
301789	0-14	0
301790	0-14	0
301791	0-14	0
301792	0-14	0
301793	0-14	0
301794	0-14	0
301795	0-14	0
301796	0-14	0
301797	0-14	0
301798	0-14	0
301799	0-14	0
301800	0-14	0
301801	0-14	0
301802	0-14	0
301803	0-14	0
301804	0-14	0
301805	0-14	0
301806	0-14	0
301807	0-14	0
301808	0-14	0
301809	0-14	0
301810	0-11	0
301812	0-11	0
301813	0-14	0
301814	0-14	0
301815	0-14	0
301816	0-14	0
301817	0-14	0
301819	0-14	0
301820	0-14	0
301821	0-14	0
301822	0-14	0
301823	0-14	0
301883	0-14	0
301887	0-9	0
301889	0-13	0
301891	0-7	0
301892	0-14	0
301893	0-14	0
301894	0-14	0
301895	0-14	0
301896	0-14	0
301897	0-14	0
301898	0-14	0

301899	0-14	0
301900	0-14	0
301901	0-14	0
301902	0-14	0
301903	0-14	0
301904	0-14	0
301905	0-14	0
301909	0-14	0
301910	0-14	0
301911	0-14	0
301912	0-14	0
301913	0-14	0
301914	0-14	0
301915	0-14	0
301916	0-14	0
301917	0-14	0
301919	0-14	0
301920	0-14	0
301922	0-14	0
301923	0-14	0
301924	0-14	0
301925	0-14	0
301926	0-14	0
301927	0-14	0
301928	0-14	0
301929	0-14	0
301930	0-11	0
301939	0-14	0
301947	0-14	0
301949	0-14	0
301950	0-14	0
301951	0-14	0
301952	0-14	0
301953	0-14	0
301954	0-14	0
301955	0-14	0
301956	0-14	0
301957	0-14	0
301958	0-14	0
301959	0-14	0
301960	0-14	0
301961	0-14	0
301962	0-14	0
301963	0-14	0
301964	0-14	0
301965	0-14	0
301966	0-14	0
301967	0-14	0
301968	0-14	0
301970	0-14	0
301971	0-14	0
301972	0-14	0
301973	0-14	0
301974	0-14	0
301975	0-14	0
301976	0-14	0
301977	0-14	0
301978	0-14	0
301979	0-14	0
301980	0-14	0
301981	0-14	0
301982	0-14	0
301983	0-14	0
301984	0-14	0
301985	0-14	0
301986	0-14	0
301987	0-14	0
301988	0-14	0
301989	0-14	0
301990	0-14	0
301991	0-14	0
301992	0-14	0
301993	0-14	0
301994	0-14	0
302000	0-14	0
302002	0-14	0
302003	0-14	0
302004	0-14	0
302005	0-14	0
302006	0-14	0
302007	0-14	0
302008	0-14	0
302009	0-14	0
302010	0-14	0
302011	0-14	0
302012	0-14	0
302013	0-14	0
302014	0-14	0
302015	0-14	0
302016	0-14	0
302017	0-14	0
302018	0-14	0
302019	0-14	0
302020	0-14	0
302021	0-14	0
302022	0-14	0
302023	0-14	0
302024	0-14	0
302025	0-14	0
302026	0-14	0
302027	0-14	0
302028	0-14	0
302029	0-14	0
302030	0-14	0
302031	0-14	0
302032	0-14	0
302033	0-14	0
302034	0-14	0
302035	0-14	0
302036	0-14	0
302037	0-14	0
302038	0-14	0
302039	0-14	0
302040	0-14	0
302041	0-14	0
302042	0-14	0
302043	0-14	0
302044	0-14	0
302045	0-14	0
302046	0-14	0
302047	0-14	0
302048	0-14	0
302049	0-14	0
302050	0-14	0
302051	0-14	0
302052	0-14	0
302053	0-14	0
302054	0-14	0
302055	0-14	0
302056	0-14	0
302057	0-14	0
302058	0-14	0
302059	0-14	0
302060	0-14	0
302061	0-14	0
302062	0-14	0
302063	0-14	0
302064	0-14	0
302065	0-14	0
302066	0-14	0
302067	0-14	0
302068	0-14	0
302814	0-13	0
302816	0-8	0
302818	0-13	0
302819	0-14	0
302821	0-13	0
302823	0-13	0
302882	0-13	0
302889	0-13	0
302891	0-13	0
302895	0-12	0
302909	0-13	0
302910	0-13	0
302911	0-9	0
302918	0-13	0
302920	0-13	0
302922	0-13	0
302925	0-13	0
302928	0-13	0
302933	0-13	0
303031	0-13	0
303032	0-13	0
303033	0-11	0
303037	0-13	0
303038	0-13	0
303039	0-13	0
303049	0-14	0
303050	0-13	0
303051	0-8	0
303052	0-14	0
303060	0-14	0
303070	0-14	0
303071	0-13	0
303073	0-13	0
303074	0-10	0
303075	0-14	0
303076	0-13	0
303078	0-13	0
303079	0-13	0
303080	0-13	0
303081	0-13	0
303082	0-13	0
303083	0-13	0
303084	0-13	0
303085	0-13	0
303086	0-13	0
303087	0-13	0
303088	0-13	0
303089	0-13	0
303090	0-14	0
303091	0-14	0
303092	0-13	0
303093	0-14	0
303094	0-13	0

303095	0-13	0	
303096	0-13	0	
303097	0-13	0	
303098	0-13	0	
303099	0-14	0	
303100	0-13	0	
303101	0-13	0	
303102	0-14	0	
303103	0-14	0	
303104	0-13	0	
303105	0-13	0	
303106	0-13	0	
303107	0-13	0	
303108	0-13	0	
303109	0-13	0	
303110	0-13	0	
303111	0-14	0	
303112	0-13	0	
303113	0-13	0	
303114	0-13	0	
303115	0-13	0	
303116	0-13	0	
303117	0-13	0	
303118	0-13	0	
303119	0-13	0	
303120	0-13	0	
303122	0-13	0	
303125	0-13	0	
303126	0-13	0	
303127	0-13	0	
303128	0-13	0	
303130	0-13	0	
303131	0-13	0	
303132	0-13	0	
303133	0-13	0	
303134	0-13	0	
303135	0-13	0	
303136	0-13	0	
303137	0-13	0	
303138	0-13	0	
303139	0-13	0	
303140	0-13	0	
303141	0-13	0	
303142	0-13	0	
303143	0-13	0	
303144	0-13	0	
303147	0-9	0	
303152	0-13	0	
303153	0-7	0	
303155	0-13	0	
303156	0-13	0	
303157	0-13	0	
303161	0-13	0	
303162	0-13	0	
303163	0-13	0	
303164	0-13	0	
303167	0-13	0	
303168	0-13	0	
303169	0-13	0	
303170	0-13	0	
303171	0-13	0	
303172	0-13	0	
303173	0-13	0	
303174	0-13	0	
303175	0-13	0	
303176	0-13	0	
303177	0-13	0	
303185	0-13	0	
303189	0-13	0	
303190	0-9	0	
303210	0-13	0	
303211	0-13	0	
303212	0-13	0	
303213	0-13	0	
303214	0-13	0	
303215	0-13	0	
303216	0-13	0	
303217	0-13	0	
303218	0-13	0	
303219	0-13	0	
303220	0-13	0	
303221	0-13	0	
303222	0-13	0	
303223	0-13	0	
303224	0-13	0	
303225	0-13	0	
303228	0-13	0	
303229	0-13	0	
303230	0-13	0	
303231	0-13	0	
303232	0-13	0	
303233	0-13	0	
303234	0-13	0	
303235	0-13	0	
303236	0-13	0	
303238	0-13	0	
303239	0-13	0	
303240	0-13	0	
303241	0-13	0	
303242	0-13	0	
303243	0-13	0	
303244	0-13	0	
303245	0-13	0	
303246	0-13	0	
303247	0-13	0	
303248	0-13	0	
303249	0-13	0	
303250	0-13	0	
303252	0-13	0	
303253	0-13	0	
303254	0-13	0	
303255	0-13	0	
303256	0-13	0	
303363	0-13	0	
303364	0-13	0	
303365	0-13	0	
303366	0-13	0	
303367	0-13	0	
303368	0-13	0	
303369	0-13	0	
303370	0-13	0	
303371	0-13	0	
303372	0-13	0	
303373	0-13	0	
303374	0-13	0	
303375	0-13	0	
303376	0-13	0	
303385	0-13	0	
303386	0-13	0	
303387	0-13	0	
303388	0-13	0	
303389	0-13	0	
303390	0-13	0	
303391	0-13	0	
303392	0-13	0	
303393	0-13	0	
303394	0-13	0	
303395	0-13	0	
303396	0-13	0	
303397	0-13	0	
303398	0-13	0	
303399	0-13	0	
303400	0-13	0	
303401	0-13	0	
303402	0-13	0	
303403	0-13	0	
303404	0-13	0	
303406	0-13	0	
303407	0-13	0	
303408	0-13	0	
303409	0-13	0	
303410	0-13	0	
303411	0-13	0	
303412	0-13	0	
303413	0-13	0	
303414	0-13	0	
303415	0-13	0	
303416	0-13	0	
303417	0-13	0	
303418	0-13	0	
303419	0-13	0	
303420	0-13	0	
303421	0-13	0	
303422	0-13	0	
303423	0-13	0	
303424	0-13	0	
303425	0-13	0	
303426	0-13	0	
303427	0-13	0	
303428	0-13	0	
303429	0-13	0	
303430	0-13	0	
303431	0-13	0	
303432	0-13	0	
303433	0-13	0	
303434	0-13	0	
303435	0-13	0	
303436	0-13	0	
303437	0-13	0	
303438	0-13	0	
303441	0-13	0	
303442	0-13	0	
303443	0-13	0	
303444	0-13	0	
303446	0-13	0	
303447	0-13	0	
303448	0-13	0	
303449	0-13	0	
303450	0-13	0	
303451	0-13	0	
303452	0-13	0	
303453	0-13	0	
303454	0-13	0	
303455	0-13	0	
303456	0-13	0	

303457	0-13	0
303458	0-13	0
303459	0-13	0
303460	0-13	0
303461	0-13	0
303462	0-13	0
303464	0-13	0
303465	0-13	0
303466	0-13	0
303467	0-13	0
303468	0-13	0
303469	0-13	0
303470	0-13	0
303471	0-13	0
303472	0-13	0
303473	0-13	0
303474	0-13	0
303475	0-13	0
303476	0-13	0
303477	0-13	0
303478	0-13	0
303479	0-13	0
303480	0-13	0
303490	0-13	0
303497	0-13	0
303498	0-9	0
303502	0-13	0
303503	0-13	0
303504	0-13	0
303505	0-13	0
303506	0-13	0
303507	0-13	0
303509	0-13	0
303510	0-13	0
303511	0-9	0
303547	0-13	0
303548	0-13	0
303549	0-13	0
303550	0-9	0
303727	0-13	0
303728	0-13	0
303729	0-13	0
303730	0-13	0
303731	0-13	0
303732	0-13	0
303733	0-13	0
303734	0-13	0
303735	0-13	0
303736	0-13	0
303737	0-13	0
303738	0-13	0
303739	0-13	0
303740	0-13	0
303741	0-13	0
303742	0-13	0
303751	0-13	0
303752	0-13	0
303753	0-13	0
303754	0-13	0
303755	0-13	0
303756	0-13	0
303757	0-13	0
303758	0-13	0
303759	0-13	0
303760	0-13	0
303761	0-13	0
303762	0-13	0
303763	0-13	0
303764	0-13	0
303765	0-13	0
303766	0-13	0
303767	0-13	0
303768	0-13	0
303769	0-13	0
303770	0-13	0
303771	0-13	0
303772	0-13	0
303773	0-6	0
303776	0-13	0
303777	0-13	0
303778	0-13	0
303779	0-13	0
303783	0-13	0
303784	0-13	0
303785	0-13	0
303786	0-13	0
303787	0-13	0
303788	0-13	0
303789	0-13	0
303790	0-13	0
303791	0-13	0
303792	0-13	0
303793	0-13	0
303794	0-13	0
303795	0-13	0
303796	0-13	0
303797	0-13	0
303798	0-13	0
303799	0-13	0
303800	0-13	0
303801	0-13	0
303802	0-13	0
303803	0-13	0
303804	0-13	0
303805	0-13	0
303806	0-13	0
303807	0-13	0
303808	0-13	0
303809	0-13	0
303810	0-13	0
303811	0-13	0
303812	0-13	0
303813	0-13	0
303814	0-13	0
303815	0-13	0
303816	0-13	0
303817	0-13	0
303818	0-13	0
303819	0-13	0
303820	0-13	0
303821	0-13	0
303822	0-13	0
303824	0-13	0
303825	0-13	0
303826	0-13	0
303827	0-13	0
303828	0-13	0
303829	0-13	0
303830	0-13	0
303831	0-13	0
303832	0-13	0
303833	0-13	0
303834	0-13	0
303835	0-13	0
303836	0-13	0
303837	0-13	0
303838	0-13	0
303839	0-13	0
303840	0-13	0
303841	0-13	0
303842	0-13	0
303843	0-13	0
303844	0-13	0
303847	0-13	0
303849	0-13	0
303850	0-13	0
303851	0-13	0
303852	0-13	0
303853	0-13	0
303854	0-13	0
303855	0-13	0
303856	0-13	0
303857	0-13	0
303858	0-13	0
303859	0-13	0
303860	0-13	0
303861	0-13	0
303862	0-13	0
303863	0-13	0
303864	0-13	0
303865	0-13	0
303866	0-13	0
303867	0-13	0
303868	0-13	0
303869	0-13	0
303870	0-7	0
303876	0-13	0
303877	0-13	0
303878	0-13	0
303879	0-13	0
303880	0-13	0
303881	0-13	0
303882	0-13	0
303883	0-13	0
303884	0-13	0
303885	0-13	0
303886	0-13	0
303887	0-13	0
303888	0-13	0
303889	0-13	0
303890	0-13	0
303891	0-13	0
303892	0-6	0
303903	0-13	0
303904	0-13	0
303905	0-13	0
303906	0-13	0
303907	0-13	0
303908	0-13	0
303909	0-13	0
303911	0-13	0
303940	0-13	0
303941	0-13	0
303942	0-13	0
303943	0-13	0

303944	0-13	0
303945	0-13	0
303946	0-13	0
303947	0-13	0
303948	0-13	0
303949	0-13	0
303951	0-13	0
303952	0-13	0
303953	0-13	0
303954	0-13	0
303955	0-13	0
303958	0-13	0
303959	0-13	0
303960	0-13	0
303961	0-13	0
303962	0-13	0
303963	0-13	0
303964	0-13	0
303965	0-13	0
303966	0-13	0
303967	0-13	0
303968	0-13	0
303969	0-13	0
303970	0-13	0
303971	0-13	0
303972	0-13	0
303973	0-13	0
303974	0-13	0
303975	0-13	0
303976	0-13	0
303977	0-13	0
303978	0-13	0
303979	0-13	0
303980	0-13	0
303981	0-13	0
303982	0-13	0
303983	0-13	0
303984	0-13	0
303985	0-13	0
303986	0-13	0
303987	0-13	0
303988	0-13	0
303990	0-13	0
303991	0-13	0
303992	0-13	0
303993	0-13	0
303994	0-13	0
303995	0-13	0
303996	0-13	0
303997	0-13	0
303998	0-13	0
303999	0-13	0
304000	0-13	0
304001	0-13	0
304002	0-13	0
304003	0-13	0
304004	0-13	0
304005	0-13	0
304006	0-13	0
304010	0-13	0
304011	0-13	0
304012	0-13	0
304013	0-13	0
304014	0-13	0
304015	0-13	0
304016	0-13	0
304017	0-13	0
304018	0-13	0
304019	0-13	0
304020	0-13	0
304021	0-13	0
304024	0-13	0
304025	0-13	0
304026	0-13	0
304027	0-13	0
304028	0-13	0
304029	0-13	0
304030	0-13	0
304031	0-13	0
304032	0-13	0
304033	0-13	0
304034	0-13	0
304035	0-13	0
304036	0-13	0
304037	0-13	0
304038	0-13	0
304039	0-13	0
304040	0-13	0
304041	0-13	0
304042	0-13	0
304043	0-13	0
304044	0-13	0
304045	0-13	0
304046	0-13	0
304047	0-13	0
304048	0-13	0
304049	0-13	0
304050	0-13	0
304051	0-13	0
304052	0-13	0
304053	0-13	0
304054	0-13	0
304055	0-13	0
304057	0-13	0
304058	0-13	0
304059	0-13	0
304060	0-13	0
304061	0-13	0
304062	0-13	0
304063	0-13	0
304064	0-13	0
304065	0-13	0
304066	0-13	0
304067	0-13	0
304068	0-13	0
304071	0-7	0
304075	0-11	0
304083	0-13	0
304084	0-13	0
304085	0-13	0
304086	0-13	0
304087	0-13	0
304088	0-13	0
304089	0-13	0
304090	0-13	0
304091	0-13	0
304092	0-13	0
304093	0-13	0
304094	0-13	0
304095	0-13	0
304096	0-13	0
304097	0-13	0
304098	0-13	0
304099	0-13	0
304100	0-13	0
304101	0-13	0
304103	0-13	0
304104	0-13	0
304108	0-13	0
304109	0-13	0
304110	0-13	0
304111	0-13	0
304112	0-13	0
304113	0-13	0
304114	0-13	0
304115	0-13	0
304116	0-13	0
304117	0-13	0
304118	0-13	0
304119	0-13	0
304120	0-13	0
304121	0-13	0
304133	0-13	0
304134	0-13	0
304135	0-13	0
304136	0-13	0
304140	0-13	0
304141	0-13	0
304142	0-13	0
304143	0-13	0
304144	0-13	0
304145	0-13	0
304146	0-13	0
304147	0-13	0
304149	0-13	0
304150	0-13	0
304151	0-13	0
304155	0-13	0
304156	0-13	0
304157	0-13	0
304158	0-13	0
304159	0-13	0
304160	0-13	0
304161	0-13	0
304162	0-13	0
304163	0-13	0
304164	0-13	0
304165	0-13	0
304166	0-13	0
304167	0-13	0
304168	0-13	0
304169	0-13	0
304170	0-13	0
304171	0-13	0
304172	0-13	0
304173	0-13	0
304174	0-13	0
304176	0-13	0
304179	0-13	0
304181	0-13	0
304190	0-13	0
304191	0-13	0
304194	0-13	0
304195	0-13	0
304196	0-13	0

304197	0-13	0	
304198	0-13	0	
304199	0-13	0	
304200	0-13	0	
304744	0-9	0	
304748	0-7	0	
304749	0-13	0	
304752	0-11	0	
304754	0-10	0	
304761	0-13	0	
304762	0-13	0	
304763	0-13	0	
304764	0-13	0	
304765	0-13	0	
304766	0-13	0	
304785	0-7	0	
304789	0-13	0	
304790	0-13	0	
304791	0-13	0	
304792	0-13	0	
304793	0-13	0	
304794	0-13	0	
304795	0-13	0	
304801	0-13	0	
304802	0-13	0	
304803	0-13	0	
304804	0-13	0	
304805	0-13	0	
304806	0-11	0	
304817	0-13	0	
304822	0-13	0	
304823	0-13	0	
304826	0-11	0	
304828	0-13	0	
304844	0-13	0	
304845	0-13	0	
304846	0-13	0	
304847	0-13	0	
304848	0-13	0	
304849	0-13	0	
304850	0-11	0	
304852	0-13	0	
304853	0-12	0	
304871	0-13	0	
304872	0-13	0	
304873	0-13	0	
304874	0-13	0	
304875	0-13	0	
304876	0-13	0	
304877	0-13	0	
304878	0-13	0	
304882	0-13	0	
304883	0-13	0	
304884	0-13	0	
304885	0-13	0	
304887	0-13	0	
304888	0-13	0	
304889	0-13	0	
304899	0-13	0	
304900	0-13	0	
304901	0-13	0	
304902	0-13	0	
304903	0-13	0	
304904	0-13	0	
304905	0-13	0	
304906	0-13	0	
304907	0-13	0	
304908	0-13	0	
304909	0-13	0	
304910	0-13	0	
304911	0-13	0	
304912	0-13	0	
304913	0-13	0	
304914	0-13	0	
304916	0-13	0	
304917	0-13	0	
304918	0-13	0	
304919	0-13	0	
304924	0-13	0	
304925	0-13	0	
304926	0-13	0	
304927	0-13	0	
304928	0-13	0	
304929	0-13	0	
304930	0-13	0	
304937	0-13	0	
304938	0-13	0	
304939	0-13	0	
304940	0-13	0	
304941	0-13	0	
304942	0-13	0	
304943	0-13	0	
304944	0-13	0	
304945	0-13	0	
304946	0-13	0	
304947	0-13	0	
304948	0-13	0	
304949	0-13	0	
304950	0-13	0	
304951	0-13	0	
304952	0-13	0	
304953	0-13	0	
304954	0-13	0	
304955	0-13	0	
304956	0-13	0	
304957	0-13	0	
304958	0-9	0	
304968	0-13	0	
304969	0-13	0	
304970	0-13	0	
304971	0-13	0	
304972	0-13	0	
304973	0-13	0	
304974	0-13	0	
304975	0-13	0	
304976	0-13	0	
304977	0-13	0	
304978	0-7	0	
304980	0-13	0	
304981	0-13	0	
304982	0-13	0	
304983	0-13	0	
304984	0-10	0	
305026	0-13	0	
305028	0-13	0	
305029	0-13	0	
305030	0-13	0	
305031	0-13	0	
305032	0-13	0	
305033	0-6	0	
305035	0-13	0	
305036	0-13	0	
305037	0-13	0	
305038	0-13	0	
305039	0-13	0	
305040	0-13	0	
305041	0-13	0	
305042	0-13	0	
305043	0-13	0	
305044	0-13	0	
305048	0-13	0	
305049	0-13	0	
305054	0-13	0	
305055	0-13	0	
305063	0-13	0	
305064	0-13	0	
305065	0-13	0	
305066	0-13	0	
305067	0-13	0	
305068	0-13	0	
305069	0-13	0	
305070	0-13	0	
305071	0-13	0	
305072	0-13	0	
305073	0-13	0	
305074	0-13	0	
305075	0-13	0	
305076	0-13	0	
305077	0-13	0	
305078	0-13	0	
305087	0-13	0	
305088	0-13	0	
305089	0-13	0	
305090	0-13	0	
305096	0-13	0	
305099	0-13	0	
305131	0-13	0	
305132	0-8	0	
305134	0-13	0	
305137	0-13	0	
305138	0-13	0	
305139	0-13	0	
305140	0-13	0	
305141	0-13	0	
305142	0-13	0	
305143	0-13	0	
305144	0-13	0	
305148	0-13	0	
305149	0-13	0	
305150	0-13	0	
305197	0-13	0	
305198	0-13	0	
305199	0-13	0	
305200	0-13	0	
305201	0-13	0	
305202	0-13	0	
305203	0-13	0	
305204	0-13	0	
305205	0-13	0	
305215	0-13	0	
305216	0-13	0	
305217	0-13	0	
305218	0-13	0	
305219	0-13	0	
305229	0-13	0	

305230	0-13	0	
305231	0-13	0	
305232	0-13	0	
305233	0-13	0	
305234	0-13	0	
305235	0-13	0	
305236	0-13	0	
305237	0-13	0	
305238	0-13	0	
305239	0-13	0	
305240	0-13	0	
305241	0-13	0	
305242	0-13	0	
305293	0-13	0	
305294	0-13	0	
305295	0-13	0	
305296	0-13	0	
305297	0-13	0	
305298	0-13	0	
305299	0-13	0	
305300	0-13	0	
305301	0-13	0	
305302	0-13	0	
305303	0-13	0	
305304	0-13	0	
305305	0-13	0	
305306	0-13	0	
305366	0-13	0	
305367	0-13	0	
305368	0-13	0	
305375	0-13	0	
305376	0-13	0	
305380	0-13	0	
305381	0-13	0	
305382	0-13	0	
305383	0-13	0	
305384	0-13	0	
305385	0-13	3	
305386	0-13	0	
305387	0-13	0	
305388	0-13	0	
305389	0-13	0	
305390	0-13	0	
305391	0-13	0	
305392	0-13	0	
305393	0-13	0	
305394	0-13	0	
305395	0-13	0	
305396	0-13	0	
305397	0-13	0	
305398	0-7	0	
305401	0-13	0	
305402	0-13	0	
305403	0-13	0	
305404	0-13	0	
305405	0-13	0	
305406	0-13	0	
305407	0-13	0	
305408	0-13	0	
305409	0-13	0	
305410	0-13	0	
305411	0-13	0	
305412	0-13	0	
305413	0-13	0	
305414	0-13	0	
305415	0-13	0	
305419	0-13	0	
305420	0-13	0	
305421	0-13	0	
305422	0-13	0	
305423	0-13	0	
305424	0-13	0	
305425	0-13	0	
305426	0-13	0	
305427	0-13	0	
305428	0-13	0	
305429	0-13	0	
305430	0-13	0	
305431	0-13	0	
305432	0-13	0	
305433	0-13	0	
305434	0-13	0	
305435	0-13	0	
305436	0-13	0	
305437	0-13	0	
305438	0-13	0	
305439	0-6	0	
305447	0-13	0	
305448	0-13	0	
305449	0-13	0	
305450	0-13	0	
305451	0-13	0	
305452	0-13	0	
305453	0-13	0	
305454	0-13	0	
305455	0-13	0	
305456	0-13	0	
305457	0-13	0	
305458	0-13	0	
305459	0-13	0	
305460	0-13	0	
305461	0-13	0	
305462	0-13	0	
305465	0-13	0	
305468	0-13	0	
305470	0-13	0	
305471	0-13	0	
305472	0-13	0	
305473	0-13	0	
305474	0-7	0	
305478	0-13	0	
305479	0-13	0	
305480	0-13	0	
305481	0-13	0	
305495	0-13	0	
305496	0-11	0	
305500	0-13	0	
305501	0-13	0	
305505	0-13	0	
305507	0-13	0	
305509	0-13	0	
305516	0-13	0	
305519	0-13	0	
305520	0-13	0	
305521	0-6	0	
305527	0-13	0	
305528	0-13	0	
305529	0-13	0	
305530	0-13	0	
305531	0-13	0	
305532	0-13	0	
305533	0-13	0	
305536	0-13	0	
305537	0-13	0	
305538	0-13	0	
305539	0-13	0	
305540	0-13	0	
305541	0-13	0	
305542	0-13	0	
305543	0-13	0	
305544	0-13	0	
305545	0-13	0	
305546	0-13	0	
305547	0-13	0	
305548	0-13	0	
305549	0-13	0	
305550	0-13	0	
305551	0-13	0	
305552	0-13	0	
305553	0-13	0	
305554	0-13	0	
305555	0-13	0	
305556	0-13	0	
305557	0-13	0	
305560	0-13	0	
305561	0-13	0	
305562	0-13	0	
305563	0-13	0	
305564	0-13	0	
305565	0-13	0	
305566	0-13	0	
305572	0-13	0	
305573	0-13	0	
305580	0-13	0	
305581	0-13	0	
305582	0-13	0	
305584	0-15	0	
305586	0-15	0	
305588	0-14	0	
305597	0-13	0	
305598	0-13	0	
305599	0-13	0	
305600	0-13	0	
305601	0-13	0	
305602	0-13	0	
305603	0-13	0	
305606	0-13	0	
305610	0-13	0	
305612	0-6	0	
305614	0-13	0	
305615	0-9	0	
305621	0-13	0	
305622	0-13	0	
305625	0-13	0	
305626	0-13	0	
305627	0-13	0	
305629	0-13	0	
305633	0-13	0	
305634	0-13	0	
305637	0-13	0	
305638	0-13	0	
305641	0-13	0	
305642	0-13	0	
305645	0-13	0	
305649	0-13	0	

305650	0-13	0
305651	0-13	0
305652	0-13	0
305653	0-13	0
305654	0-13	0
305655	0-13	0
305659	0-13	0
305662	0-13	0
305663	0-13	0
305664	0-13	0
305665	0-13	0
305668	0-13	0
305671	0-13	0
305672	0-13	0
305673	0-13	0
305674	0-13	0
305675	0-13	0
305676	0-13	0
305677	0-13	0
305678	0-13	0
305679	0-13	0
305680	0-13	0
305681	0-13	0
305682	0-13	0
305683	0-13	0
305684	0-13	0
305685	0-13	0
305686	0-13	0
305687	0-13	0
305688	0-13	0
305689	0-13	0
305690	0-13	0
305692	0-13	0
305693	0-13	0
305695	0-13	0
305696	0-13	0
305697	0-13	0
305698	0-13	0
305699	0-13	0
305700	0-13	0
305701	0-13	0
305702	0-13	0
305703	0-13	0
305704	0-13	0
305705	0-13	0
305706	0-13	0
305707	0-13	0
305708	0-13	0
305709	0-13	0
305710	0-13	0
305711	0-13	0
305912	0-13	0
305913	0-13	0
305914	0-13	0
305915	0-13	0
305916	0-13	0
305917	0-13	0
305918	0-13	0
305919	0-13	0
305920	0-9	0
305947	0-13	0
305952	0-13	0
305953	0-13	0
305956	0-13	0
305957	0-13	0
305958	0-13	0
305959	0-13	0
305960	0-13	0
305961	0-13	0
305962	0-13	0
305963	0-13	0
305964	0-13	0
305965	0-13	0
305966	0-13	0
305967	0-13	0
305968	0-13	0
305969	0-13	0
305970	0-13	0
305971	0-13	0
305972	0-13	0
305973	0-6	0
305976	0-9	0
305978	0-13	0
305979	0-13	0
305980	0-13	0
305981	0-13	0
305982	0-13	0
305983	0-13	0
305984	0-13	0
305985	0-13	0
305986	0-13	0
305987	0-13	0
305988	0-13	0
305989	0-13	0
305990	0-13	0
305991	0-13	0
305992	0-13	0
305993	0-13	0
305994	0-13	0
305995	0-13	0
305996	0-13	0
305997	0-13	0
305998	0-13	0
305999	0-13	0
306000	0-13	0
306001	0-13	0
306002	0-13	0
306303	0-13	0
306304	0-13	0
306305	0-13	0
306306	0-13	0
306309	0-13	0
306310	0-13	0
306311	0-13	0
306312	0-13	0
306313	0-13	0
306314	0-13	0
306315	0-13	0
306316	0-13	0
306317	0-13	0
306318	0-13	0
306319	0-13	0
306320	0-13	0
306321	0-13	0
306322	0-13	0
306332	0-13	0
306333	0-13	0
306334	0-10	0
306340	0-13	0
306341	0-13	0
306342	0-13	0
306343	0-13	0
306344	0-13	0
306345	0-13	0
306347	0-13	0
306348	0-13	0
306349	0-13	0
306350	0-13	0
306351	0-13	0
306352	0-13	0
306353	0-13	0
306354	0-13	0
306355	0-13	0
306356	0-13	0
306357	0-13	0
306358	0-13	0
306359	0-13	0
306360	0-13	0
306361	0-13	0
306362	0-13	0
306363	0-13	0
306365	0-13	0
306366	0-13	0
306367	0-13	0
306368	0-13	0
306369	0-13	0
306370	0-13	0
306371	0-13	0
306372	0-13	0
306373	0-13	0
306374	0-13	0
306375	0-13	0
306376	0-13	0
306377	0-13	0
306378	0-13	0
306379	0-13	0
306380	0-13	0
306381	0-13	0
306382	0-13	0
306383	0-13	0
306384	0-13	0
306385	0-13	0
306386	0-13	0
306387	0-13	0
306388	0-13	0
306389	0-13	0
306390	0-13	0
306391	0-13	0
306392	0-13	0
306393	0-13	0
306394	0-13	0
306395	0-13	0
306396	0-13	0
306397	0-13	0
306398	0-13	0
306410	0-13	0
306427	0-13	0
306429	0-13	0
306437	0-13	0
306441	0-8	0
306454	0-13	0
306458	0-13	0
306460	0-13	0
306466	0-13	0
306498	0-13	0